

University of Southampton Research Repository  
ePrints Soton

Copyright © and Moral Rights for this thesis are retained by the author and/or other copyright owners. A copy can be downloaded for personal non-commercial research or study, without prior permission or charge. This thesis cannot be reproduced or quoted extensively from without first obtaining permission in writing from the copyright holder/s. The content must not be changed in any way or sold commercially in any format or medium without the formal permission of the copyright holders.

When referring to this work, full bibliographic details including the author, title, awarding institution and date of the thesis must be given e.g.

AUTHOR (year of submission) "Full thesis title", University of Southampton, name of the University School or Department, PhD Thesis, pagination

# **UNIVERSITY OF SOUTHAMPTON**

FACULTY OF PHYSICAL SCIENCES AND ENGINEERING

Physics and Astronomy

DNA-directed assembly of inorganic nanoparticles

by

**Pascal Khalid Harimech**

Thesis for the degree of Doctor of Philosophy

June 2016



UNIVERSITY OF SOUTHAMPTON

## **ABSTRACT**

FACULTY OF PHYSICAL SCIENCES AND ENGINEERING

Physics and Astronomy

Doctor of Philosophy

### **DNA-directed assembly of inorganic nanoparticles**

by

**Pascal Khalid Harimech**

In the last two decades, inorganic nanoparticles have become an active field of research due to their unique physical properties. The advancements in the control over size, shape and composition opened up many potential applications in a wide range of fields from optoelectronics to medicine. A lot of research focusses on the controlled assembly of nanoparticles into larger pre-defined structures. A very successful approach uses DNA-functionalised nanoparticles as building blocks, which are capable of self-assembly driven by the DNA design. Such nanoparticle assemblies can infer new optical properties like circular dichroism or make multi-functional materials for advanced applications.

In this work, a novel tool for the ligation of nanoparticle assemblies with DNA is presented. The UV-responsive molecule 3-cyanovinyl carbazole was embedded in DNA strands as a crosslinker for the covalent linkage of dsDNA. The covalent bond significantly increases the stability of dsDNA even in unfavourable conditions allowing a wider range of applicability. Unlike with other crosslinking techniques, already formed interstrand bonds can be reversed with UV-B light as an external stimulus. The efficient application of 3-cyanovinyl carbazole in tetrahedral gold nanoparticle assemblies is demonstrated for the first time. In addition, limitations of the strain-promoted azide-alkyne click reaction in the same system are revealed.

DNA-directed hetero-assemblies consisting of CdSe/ZnS quantum dots and upconversion nanoparticles are presented. The results suggest that energy transfer from excited upconversion nanoparticles to quantum dots occurs upon self-assembly with short oligonucleotides. This example shows the potential of using DNA-based assembly as a general technique for creating novel materials helping to gain a fundamental understanding about nanoparticle interactions.

In addition, lead halide perovskite nanoparticles are introduced. A modified synthesis protocol is demonstrated, which significantly increases the processability of such nanoparticles.



## Table of Contents

ABSTRACT .....	iii
Table of Figures .....	iv
List of Equations.....	xiv
List of Tables.....	xiv
Acknowledgements .....	xviii
Abbreviations .....	xx
Chapter 1. Introduction .....	1
Chapter 2. Background.....	5
2.1 Colloidal nanoparticles .....	5
2.1.1 Synthesis of gold and silver nanoparticles.....	5
2.1.2 Optical properties of gold and silver nanoparticles .....	10
2.1.3 Synthesis of semiconductor quantum dots .....	14
2.1.4 Optical properties of semiconductor quantum dots.....	16
2.1.5 Synthesis of upconversion nanoparticles.....	19
2.1.6 Optical properties of upconversion nanoparticles.....	20
2.1.7 Lead halide perovskite nanoparticles .....	23
2.2 Functionalisation of nanoparticles.....	25
2.3 Nanoparticle growth models and DLVO theory .....	28
2.3.1 LaMer model.....	28
2.3.2 Size-focussing and broadening regime.....	29
2.3.3 DLVO model.....	31
2.4 DNA as a tool in nanotechnology .....	34
2.4.1 Structure and properties of DNA.....	34
2.4.2 DNA crosslinking.....	38
2.5 Self-assembly of nanoparticles .....	43
Chapter 3. Experimental.....	49

3.1 Nanoparticle synthesis and functionalisation.....	49
3.1.1 Gold and silver nanoparticles.....	49
3.1.2 Synthesis of $\text{Cd}_{1-x}\text{Se}_x\text{Zn}_{1-y}\text{S}_y$ quantum dots.....	51
3.1.3 Synthesis of Upconversion nanoparticles.....	52
3.1.4 Synthesis of lead halide perovskite nanoparticles.....	52
3.2 Nanoparticle functionalisation .....	53
3.2.1 Gold and silver nanoparticles.....	53
3.2.2 Semiconductor quantum dots .....	55
3.2.3 Upconversion nanoparticles.....	55
3.3 DNA hybridisation and assembly of DNA-NP conjugates.....	56
3.3.1 DNA hybridisation and crosslinking .....	56
3.3.1 Gold nanoparticle assemblies.....	57
3.3.2 Assemblies of upconversion nanoparticle and quantum dots.....	58
3.4 Characterisation techniques .....	58
3.4.1 Ultraviolet-Visible spectroscopy .....	58
3.4.2 Fluorescence spectroscopy.....	59
3.4.3 Surface enhance Raman spectroscopy.....	60
3.4.4 Transmission Electron Microscopy (TEM) .....	61
3.4.5 Energy dispersive X-ray spectroscopy (EDX) .....	61
3.4.6 Gel electrophoresis .....	63
3.4.7 Dynamic light scattering (DLS).....	65
3.4.8 Zeta-potential.....	66
Chapter 4. Results on nanoparticle synthesis and characterisation .....	67
4.1 Plasmonic nanoparticles.....	67
4.1.1 Gold nanoparticles.....	67
4.1.2 Silver nanoparticles .....	73
4.2 Semiconductor quantum dots.....	77
4.3 Upconversion nanoparticles.....	83

---

4.4 Lead halide perovskite nanoparticles.....	90
4.5 DNA-functionalisation of nanoparticles .....	96
4.5.1 Gold nanoparticles .....	97
4.5.2 Silver nanoparticles.....	100
4.5.3 Quantum dots and upconversion nanoparticles .....	102
4.6 Summary .....	103
Chapter 5. Formation and Ligation of AuNP-DNA assemblies .....	107
5.1 Characteristics of employed oligonucleotides .....	107
5.1.1 Design, modification and melting temperature .....	107
5.1.2 Polyacrylamide gel electrophoresis.....	111
5.2 Directed gold nanoparticle assembly .....	120
5.2.1 Unmodified oligonucleotides.....	121
5.2.2 Azide/BCN-modified oligonucleotides .....	128
5.2.3 3-cyanovinyl carbazole-modified oligonucleotides .....	133
5.3 Nanoparticle assemblies for SER(R)S.....	144
5.4 Summary.....	149
Chapter 6. Upconversion nanoparticle-Quantum dot hetero-assemblies.....	151
6.1 Introduction.....	151
6.2 Assembly of UCNP and QDs with short DNA .....	152
Chapter 7. Summary and Outlook .....	161
7.1 Summary of results.....	161
7.2 Outlook to future work .....	163
A. Appendix.....	167
A.1 List of reagents and suppliers.....	167
A.2 Calculation of nanoparticle concentration.....	167
A.3 Sequences of unmodified and Azide/BCN-modified DNA.....	170
A.4 Determination of the PLQY .....	172
A.5 Extinction and PL spectral overlap .....	173

References.....	175
-----------------	-----

## Table of Figures

Figure 2.1: Reaction mechanism of the gold nanoparticle synthesis with the Turkevich method. Adapted from ref. [43].....	6
Figure 2.2: The protonation and hydrolysis of citrate and gold chloride. The pH is an important factor for the reactivity of the precursors and the electrostatic stabilisation. Adapted from ref. [55].....	8
Figure 2.3: The localised surface plasmon resonance (LSPR) of gold nanoparticles. The collective displacement of conduction electrons leads to large absorption and scattering coefficients.....	11
Figure 2.4: Typical setup for the synthesis of nanoparticles with the hot-injection method...	15
Figure 2.5: Illustration of the difference between the bulk and the nano-regime of semiconductors. The energy gap is increasing and the quasi-continuous energy states in the valence and conduction band become discrete due to the quantum size effect [130].....	18
Figure 2.6: Illustration of three different multi-photon excitation pathways. (a) Two-photon absorption, (b) excited state absorption and (c) energy transfer upconversion. G = ground state; E1,E2 = excited state; VS = virtual state. The red, blue and green arrows represent photon absorption, energy transfer and radiative emission, respectively.....	21
Figure 2.7: Scheme of the relevant energy levels of rare-earth elements used in upconversion nanoparticles. The large coloured arrows indicate radiative relaxation of the visible emissions. Reprinted from ref. [144] with permission from Elsevier, Copyright 2005.....	22
Figure 2.8: Visualisation of the APbX <sub>3</sub> (A: monovalent cation, X: halide) perovskite crystal structure.....	25
Figure 2.9: Functionalisation of nanoparticles by attachment of molecules such as PEG or DNA on the surface via functional groups.....	26
Figure 2.10: Post-functionalisation of nanoparticles via ligand exchange. (1) Complete ligand exchange by a binding group with higher affinity towards the surface and (2) partial exchange by molecules with the same binding group.....	27
Figure 2.11: Illustration of the precursor concentration changing with time according to the LaMer model. At stage I, there is an increase in monomer concentration until a critical supersaturation $c_{\text{crit}}$ is reached. At this point rapid nucleation occurs, which relieves the saturation (stage II). In stage III, the nuclei grow by a diffusion-limited process until the saturation concentration $c_s$ is reached. Adapted from ref. [50].....	28
Figure 2.12: The change of the free energy depending on the radius of nanoparticles formed from monomers in solution according to equation 2.6. The surface tension imposes an energy	

barrier, which is overcome once the particle reaches the critical radius $r_c$ and spontaneous growth commences.....	30
Figure 2.13: The interaction between two particles in solution. Attractive Van-der-Waals forces and repulsive electrostatic forces determine the colloidal stability according to the DLVO theory.....	31
Figure 2.14: The interaction between Van-der-Waals attraction and electric repulsion as described by the DLVO theory for two spheres. An energy barrier is imposed by the electric force.....	33
Figure 2.15: Structure of double stranded DNA. The specific complementarity of the two base pairs adenine-thymine and guanine-cytosine leads to hybridisation with a double helical conformation.....	35
Figure 2.16: Extinction spectra of the four DNA nucleobases [202].....	37
Figure 2.17: Illustration of the absorption at 260 nm during DNA melting experiments. An increase of the absorption indicates the dehybridisation of dsDNA due to the hyperchromic effect. The melting temperature is defined at the point of inflection of the sigmoidal curve.	38
Figure 2.18: Scheme of the structure of SNS monomers and the polymerisation reaction yielding crosslinked DNA strands by enzymatic ligation. ....	39
Figure 2.19: Structure of 5-Methoxypsonalen and its UV-mediated reaction with thymine bases.....	40
Figure 2.20: Reaction of 3-cyanovinyl carbazole with a thymine base under UV-A irradiation forming a cyclobutane bridge via a [2+2]-photocycloaddition.....	41
Figure 2.21: Reaction mechanism of the [2+2]-photocycloaddition between thymine and 3-cyanovinyl carbazole. ....	41
Figure 2.22: Reaction mechanism for the strain-promoted 1,3-dipolar cycloaddition between BCN and an azide.....	42
Figure 2.23: An overview about different parameters that can be used to trigger self-assembly of molecules and nanoparticles in ordered structures. Reprinted with permission from ref. [8]. Copyright 2010, American Chemical Society.....	44
Figure 2.24: Energy splitting due to plasmon coupling of two spherical nanoparticles. Reprinted with permission from ref. [253], Copyright 2013, Elsevier.....	46
Figure 2.25: Concepts of a “new” periodic table. Nanoparticles act as atoms depending on the size, shape and composition and DNA plays the role of the bond forming electrons connecting the atoms to form “artificial” molecules. Re-printed with permission from ref. [262], Copyright 2013, John Wiley and Sons.....	47
Figure 3.1: Set-up for upconversion detection. The light of a laser diode (980 nm, 500 mW) is focussed by a lens into the sample in a transparent cuvette. The emitted light is collected with a spectrometer using a second lens. Scattered light from the laser diode is removed by a filter in front of the detector. ....	60

Figure 3.2: Home-built setup for Raman scattering measurements. Laser light (532 nm, 50 mW) is first filtered with a bandpass filter and focussed using an objective (NA = 0.5). The backscattered light is filtered twice before entering the spectrometer. ....	61
Figure 3.3: Illustration of the principle of the generation of characteristic X-ray radiation used in EDX analysis. Electrons are removed from the atom by excitation with light or energetic electrons leaving a gap behind. These are filled by other electrons under emission of a photon. The transitions are named according to the shell with the gap (K, L, M...) and the electron filling the gap ( $\alpha, \beta, \gamma$ ). ....	62
Figure 3.4: Formation of a polyacrylamide gel matrix from the two precursors acrylamide and <i>N,N'</i> -Methylenebisacrylamide. ....	64
Figure 3.5: Chemical structure of agarose. ....	65
Figure 4.1: (A) TEM image of $15 \pm 1$ nm gold nanoparticles synthesised with the citrate reduction method. (B) Statistical analysis of the gold nanoparticle diameters. ....	67
Figure 4.2: Functionalisation of citrate-coated gold nanoparticles with BSPP via a ligand exchange reaction. ....	68
Figure 4.3: Extinction spectra of citrate- and BSPP-functionalised $15 \pm 1$ nm gold nanoparticles. The peak of the LSPR is shifted from 519 nm to 522 nm after ligand exchange. ....	69
Figure 4.4: Zeta-potential of citrate- and BSPP-coated gold nanoparticles. After functionalisation with BSPP the increased value from -28.4 mV to -44.4 mV indicates the successful capping and enhanced colloidal stability. ....	69
Figure 4.5: Extinction spectra of citrate-coated gold nanoparticles as-synthesised and in 0.5xTBE buffer. The aggregation of the gold nanoparticles leads to a shoulder in the spectrum caused by plasmon coupling. ....	70
Figure 4.6: UV-Vis spectra of citrate-coated gold nanoparticles synthesised with the growth method from Bastús <i>et al.</i> Both, the shift of the plasmon peak and the changing ratio $A_{400}/A_{\max}$ indicate the growth of the nanoparticles. ....	71
Figure 4.7: Stability of $30 \pm 3$ nm BSPP-functionalised gold nanoparticles (g3) against NaCl. While there is no significant change in the UV-Vis spectra at 30 mM NaCl after 2 hours (left), aggregation is indicated by a shoulder at 620 nm and a decrease of the main peak after 5 minutes at 40 mM NaCl (right). The photographs show the colour change from red to blue due to agglomeration/aggregation of the gold nanoparticles. ....	72
Figure 4.8: A representative TEM image and the size distribution of $7 \pm 1.5$ nm AuNPs. ....	73
Figure 4.9: Extinction spectrum of BSPP-coated $7 \pm 1.5$ nm gold nanoparticles. ....	73
Figure 4.10: Photograph (left), representative TEM image (middle) and size distribution of as-synthesised silver nanoparticles. ....	74
Figure 4.11: UV-Vis spectra of $22.5 \pm 2.5$ nm citrate-coated AgNP without (black) and with 50 mM NaCl (red). The arrow indicates the development of a shoulder due to aggregation. ....	74

Figure 4.12: Zeta potentials of citrate- and SH-mPEG-coated silver nanoparticles. The significant reduction of the zeta potential from -48.7 mV to -6.9 mV indicates the ligand exchange with SH-mPEG.....	75
Figure 4.13: UV-Vis spectra of $22.5 \pm 2.5$ nm SH-mPEG and citrate functionalised silver nanoparticles.....	76
Figure 4.14: UV-Vis spectra of $22.5 \pm 2.5$ nm folic acid-functionalised and citrate-capped silver nanoparticles.....	77
Figure 4.15: Illustration of the composition gradient in $\text{Cd}_{1-x}\text{Se}_x\text{Zn}_{1-y}\text{S}_y$ quantum dots. The core (yellow) consists of CdSe and the outer shell layers of ZnS.....	78
Figure 4.16: Representative transmission electron micrograph of $\text{Cd}_{1-x}\text{Se}_x\text{Zn}_{1-y}\text{S}_y$ quantum dots (QD520) and their size distribution.....	78
Figure 4.17: EDX spectrum of semiconductor quantum dots (QD520). .....	79
Figure 4.18: Extinction and fluorescence spectra of different $\text{Cd}_{1-x}\text{Se}_x\text{Zn}_{1-y}\text{S}_y$ quantum dots. The excitation was at 400 nm.....	80
Figure 4.19: Photographs of quantum dots (QD480-QD580) under ambient light and under UV irradiation.....	80
Figure 4.20: Top: Activation of L-lipoic acid by cleaving the dithiolane bond with UV-A irradiation. Bottom: In the course of the reaction the absorption peak at 333 nm drops indicating the opening of the ring structure. The photographs show the colour change from yellow to colourless due to the opening of the ring.....	81
Figure 4.21: Fluorescence spectra of QD520 in hexane and after transfer to water. The extinction spectrum was acquired in water. The excitation was at 400 nm. ....	82
Figure 4.22: Zeta potential of L-lipoic acid-functionalised quantum dots in water. ....	83
Figure 4.23: TEM micrograph of quantum dots (QD520) functionalised with lipoic acid.....	83
Figure 4.24: TEM micrograph and size distribution of $\text{NaYF}_4:\text{Yb,Tm}$ upconversion nanoparticles. ....	85
Figure 4.25: EDX spectrum of $\text{NaYF}_4:\text{Yb,Tm}$ upconversion nanoparticles.....	85
Figure 4.26: EDX spectrum of $\text{NaYF}_4:\text{Yb,Er}$ upconversion nanoparticles.....	86
Figure 4.27: Emission spectrum of $\text{NaYF}_4:\text{Yb,Er}$ upconversion nanoparticles. The excitation wavelength was 980 nm.....	87
Figure 4.28: Emission spectrum of $\text{NaYF}_4:\text{Yb,Tm}$ upconversion nanoparticles doped with 20% Yb,2% Tm (spectrum A) and 30% Yb,0.2% Tm (spectrum B). The excitation wavelength was 980 nm. ....	88
Figure 4.29: Zeta potential of PAA-coated upconversion nanoparticles in water. ....	89
Figure 4.30: TEM micrograph of PAA-coated upconversion nanoparticles in water.....	90
Figure 4.31: TEM micrograph and size distribution of $\text{CH}_3\text{NH}_3\text{PbBr}_3$ nanoparticles synthesised with a re-precipitation method. ....	91

Figure 4.32: Fluorescence spectrum (top), extinction spectrum (middle) and photoluminescence excitation spectrum (bottom) of $\text{CH}_3\text{NH}_3\text{PbBr}_3$ nanoparticles synthesised with a re-precipitation method.....	92
Figure 4.33: TEM micrograph and size distribution of $\text{CH}_3\text{NH}_3\text{PbBr}_3$ nanoparticles synthesised with CTAB.....	93
Figure 4.34: Fluorescence spectrum (top), extinction spectrum (middle) and photoluminescence excitation spectrum (bottom) of $\text{CH}_3\text{NH}_3\text{PbBr}_3$ nanoparticles synthesised via re-precipitation with CTAB.....	94
Figure 4.35: TEM micrograph of $\text{CsPbBr}_3$ nanoparticles synthesised via a hot-injection method. The nanoparticle sizes were measured in terms of the diagonal. ....	95
Figure 4.36: Photographs of $\text{CsPbX}_3$ nanoparticles under ambient light and under illumination with UV-A light.....	95
Figure 4.37: Extinction and fluorescence spectra of $\text{CsPbX}_3$ nanoparticles with different halide mixtures.....	96
Figure 4.38: Structure of the thiol-linker used as oligonucleotide modification for the attachment of DNA to nanoparticles.....	97
Figure 4.39: Illustration of the disulphide cleavage with BSPP.....	98
Figure 4.40: Separation of $15 \pm 1$ nm AuNP-DNA conjugates (SA1) by the number of attached oligonucleotides with agarose gel electrophoresis (2.25% w/v). Lane 1: AuNP reference, Lane 2: AuNP mixed with DNA. The necessary band is then extracted from the gel by soaking the gel in buffer.....	99
Figure 4.41: $7 \pm 1.5$ nm AuNP-DNA conjugate (SA1) separation in an agarose gel (3% w/v). .....	100
Figure 4.42: Extinction spectra of $15 \pm 1$ nm BSPP-AuNPs mixed with $22.5 \pm 2.5$ nm AgNPs monitored at different times. The arrows indicate that the AgNP plasmon peak is decreasing and the AuNP plasmon peak is increasing with time.....	101
Figure 4.43: 2% Agarose gel containing $22.5 \pm 2.5$ nm silver nanoparticles incubated with oligonucleotides (SC1) without de-protection. Lane 1: AgNP reference; Lane 2: AgNP 1 hour incubation; Lane 3: AgNP 6 hours incubation; Lane 4: AgNP 24 hours incubation.....	102
Figure 4.44: Illustration of a coupling reaction between a carboxylic acid and a primary amine with EDC and Sulfo-NHS. First, the carboxylic acid is activated with EDC formation an unstable o-Acylisourea intermediate. This intermediate then readily reacts with a primary amine coupling it to the carboxylic acid via an amide bond. The stability can be improved by addition of Sulfo-NHS, which forms a semi-stable ester with the carboxylic acid. Adapted from ref. [301]. .....	103
Figure 5.1: Illustration of different assemblies from different combinations of oligonucleotides are mixed. A: S1+S3, B: S1+S3, C: S1-S3, D: S1-S4. The spheres indicate the positions of the nanoparticles in NP-DNA assemblies.....	108

Figure 5.2: Illustration of the tetrahedron formed by directed folding of all four oligonucleotides from Table 5.1. The 5'-end is at the thiol-modification. The three thymine bases (TTT) in between the different sections were omitted. Each oligonucleotide is coloured with a single colour (SC1: red, SC2: blue, SC3: green, SC4: yellow). The boxes indicate the 3-cyanovinyl carbazole crosslinking sites.....	109
Figure 5.3: Melting curve of oligonucleotide dimers (SA1+SA2). The curve was determined as an average from 3 complete cycles. The melting temperature was determined at the point of inflection as 74°C.....	111
Figure 5.4: 6% native polyacrylamide gel of different DNA mixtures without crosslinking groups (SA1-SA4). The gel was stained with ethidium bromide. Lane 1: Single strand; Lanes 2-3: DNA dimers (SA1+SA3 and SA1+SA4); Lanes 4-7: DNA trimers; Lane 8: DNA tetramers. The different bands were labelled as single strands (a), DNA dimers (b), DNA trimers (c) and DNA tetrahedra (d).....	112
Figure 5.5: 6% native polyacrylamide gel containing different DNA dimer mixtures with unmodified and azide/BCN-modified oligonucleotides. Lane 1: Single strand reference; Lane 2: SA1+SA4; Lane 3: SA1+SA3; Lane 4: SB1+SB3; Lane 5: SB1+SB4. The different bands were labelled as single strands (a), dimers (b+c), and higher order complexes (d, indicated with arrows).....	114
Figure 5.6: 6% native polyacrylamide gel of different DNA mixtures. Lane D: Cyanol xylene reference; Lane 1: DNA dimers (SB1+SB3) with 100 mM NaCl; Lane 2: DNA dimers (SB1+SB3) with 200mM NaCl; Lane 3: DNA tetrahedra (SB1-SB4) with 200 mM NaCl. The different bands were labelled as single strands (a), DNA dimers (b), and higher order complexes (c, black arrows). The red arrow indicates DNA residue, which did not pass into the gel.....	115
Figure 5.7: 6% native polyacrylamide gel of DNA dimers (SB1+SB3) hybridised at different temperatures. Lane D: Cyanol xylene reference; Lane 1: 55°C; Lane 2: 60°C; Lane 3: 65°C; Lane 4: 70°C. The different bands were labelled as single strands (a), DNA dimers (b), and higher order complexes (c).....	116
Figure 5.8: 6% native polyacrylamide gel of carbazole-modified and unmodified oligonucleotides. The odd lanes contain the carbazole strands and the even lanes the unmodified strands. The gel was stained with ethidium bromide. Lanes 1+2: single strand (SA1,SC1); Lanes 3+4: two strands (SA1+SA2,SC1+SC2); Lanes 5+6: three strands (SA1-3,SC1-3); lanes 7+8: all four strands (SA1-4,SC1-4). The bands are labelled as single strands (a), dimers (b), trimers (c) and tetrahedra (d).....	117
Figure 5.9: 6% native polyacrylamide gel with carbazole-modified oligonucleotide dimers (SC1+SC2) after different times of UV-A irradiation. The gel was stained with ethidium bromide. Lane 1: 300 s; Lane 2: 240 s; Lane 3: 120 s; Lane 4: 60 s; Lane 5: 30 s. The bands a	

labelled as degraded single strand (a), single strand (b), degraded dimer (c) and dimer (d). .....	118
Figure 5.10: 6% denaturing polyacrylamide gel with 3-cyanovinyl carbazole-modified and cross-linked oligonucleotides. The gel was stained with ethidium bromide Lane 1: Single strand (SC1); Lane 2: two oligonucleotides (SC1+SC2); Lane 3: three oligonucleotides (SC1-3); Lane 4: All four oligonucleotides (SC1-4). The bands were labelled as single strands (a), dimers (b), trimers (c) and tetrahedra (d). .....	120
Figure 5.11: 2% agarose gel of 15nm gold nanoparticle dimers (SA1+SA2) hybridised at different temperatures. The buffer used was phosphate buffer (20 mM, pH 7.4) and the final NaCl concentration was 60 mM. Lane 1: 75°C, Lane 2: 70°C, Lane 3: 65°C, Lane 4: 60°C. The lanes are labelled as single AuNPs (a) and AuNP dimers (b). .....	122
Figure 5.12: 2% agarose gel of 15nm gold nanoparticle dimers (SA1+SA2) hybridised with different sodium chloride concentrations. The hybridisation temperature was 65°C and the buffer was phosphate buffer (20 mM, pH 7.4) with varying NaCl contents. Lane 1: Monoconj. reference; Lane 2: 100 mM NaCl; Lane 3: 80 mM NaCl; Lane 4: 60 mM NaCl; Lane 5: 40 mM NaCl; Lane 6: 10 mM NaCl. The lanes are labelled as single AuNPs (a) and AuNP dimers (b). .....	123
Figure 5.13: 2% agarose gel of 15 nm gold nanoparticle dimers (SA1+SA2) hybridised with different conditions. The buffer was phosphate buffer (20 mM, pH 7.4) with 50 mM NaCl. Lane 1: Monoconj. reference; Lane 2: Hybr. Temp = 65°C, shaken for 2h at 50°C; Lane 3: Hybr. Temp = 65°C for 1 h; Lane 4: Hybr. Temp = 50°C, shaken for 2 h at 50°C. The lanes are labelled as single AuNPs (a) and AuNP dimers (b). .....	124
Figure 5.14: 2% agarose gel of all four AuNP-DNA monoconjugates (SA1-SA4) hybridised at different conditions. In all samples PBS (20 mM, pH 7.4) with the indicated sodium chloride concentration was used. Lane 1: Monoconjugate reference; Lane 2: 60°C, 65 mM; Lane 3: 60°C, 50 mM; Lane 4: 60°C, 50 mM, 24h; Lane 5: 55°C, 50 mM, shaken. ....	126
Figure 5.15: Representative TEM micrograph of gold nanoparticle dimers purified by agarose gel electrophoresis.....	126
Figure 5.16: Representative TEM micrograph of gold nanoparticle trimers purified by agarose gel electrophoresis.....	127
Figure 5.17: Representative TEM micrograph of gold nanoparticle tetramers purified by agarose gel electrophoresis.....	127
Figure 5.18: Agarose gel of hybridised AuNP-monoconjugates with azide/BCN-modified oligonucleotides (SB1-SB4). The hybridisation temperature was 65°C. Phosphate buffer (20 mM, pH 7.4) and two different salt concentrations were used. Lane 1: 50 mM NaCl; Lane 2: 65 mM NaCl. The bands correspond to monoconjugates (a), dimers (b), trimers (c), tetramers (d) and higher ordered structures (e). .....	129

Figure 5.19: Representative TEM micrograph of the AuNP dimer band made with azide/BCN-modified DNA (SB1-SB4) after gel electrophoresis (see Figure 81, lane 2, band <i>b</i> ).....	129
Figure 5.20: Representative TEM micrograph of the AuNP trimer band made with azide/BCN-modified DNA (SB1-SB4) after gel electrophoresis (see Figure 81, lane 2, band <i>c</i> ).....	130
Figure 5.21: Representative TEM micrograph of the AuNP tetramer band made with azide/BCN-modified DNA (SB1-SB4) after gel electrophoresis (see Figure 81, lane 2, band <i>d</i> ).....	130
Figure 5.22: Agarose gel of gold nanoparticle dimers. The DNA pairs containing the same clicking groups were utilised. Lane 1: Monoconjugate; Lane 2: SB1+SB2 (azide); Lane 3: SB3+SB4 (BCN). The bands are labelled as monoconjugates (a) and dimers (b). .....	132
Figure 5.23: TEM image of AuNP dimers. The contents are from the agarose gel in Figure 5.22 (Lane 2, band <i>b</i> ).....	133
Figure 5.24: Illustration of DNA cross-linking and de-crosslinking on gold nanoparticle dimers. Gold nanoparticles conjugated with complementary oligonucleotides are hybridized to form dimers. One of the oligonucleotides contains a 3-cyanovinyl carbazole group, which can react with an adjacent thymine, in the opposite strand, upon light irradiation. Irradiation with UV-A light allows the formation of a cyclobutane bridge between the opposite thymine base as indicated by the red box. After cross-linking, the dimers remain intact even under denaturing conditions. The crosslinked DNA strands can be reversibly de-crosslinked with UV-B light irradiation. ....	134
Figure 5.25: UV-Vis spectra of $15 \pm 1$ nm gold nanoparticles before and after irradiation with UV-A (365 nm) and UV-B light (312 nm) for 15 minutes. The perfect overlap of the spectra indicates that there is no change of the gold nanoparticles during UV irradiation.....	135
Figure 5.26: 2% agarose gel of non-crosslinked (nc) and crosslinked (c) gold nanoparticle dimers (SC1+SC2). Lane 1: monoconjugates native; Lane 2: dimers native; Lane 3: monoconjugates formamide (30%); Lane 4: dimers (nc) formamide (30%); Lane 5: dimers (c) formamide (30%); Lane 6: monoconjugates formamide (50%); Lane 7: dimers (nc) formamide (50%); Lane 8: dimers (c) formamide (50%). The percentages are given as final v/v %. The bands are labelled as monoconjugates (a) and dimers (b). .....	137
Figure 5.27: Agarose gel electrophoresis of gold nanoparticle dimers (SC1+SC2) under denaturing conditions showing the reversibility of the photo-crosslinking reaction. Lane 1: Mono-conjugates as reference; Lane 2: Cross-linked dimers; Lane 3: De-crosslinked dimers running as mono-conjugate band; Lane 4: Re-crosslinked dimers.....	138
Figure 5.28: Representative TEM images of crosslinked and de-crosslinked 13 nm gold nanoparticle assemblies. The samples were deposited on the grids under DNA denaturing conditions. Photo-crosslinked gold nanoparticle dimers (A), de-crosslinked nanoparticle dimers, which disassemble to mono-conjugates (B), and re-crosslinked dimers (C).....	139

Figure 5.29: Illustration of the trimer and tetrahedron formation with three and four oligonucleotides. The arrows and black lines indicate the position of the 3-cyanovinyl carbazole groups.....	139
Figure 5.30: An agarose gel comparing crosslinked and de-crosslinked trimers (SC1-3) with mono-conjugates and dimers in denaturing conditions. Lane 1: reference mono-conjugates; Lane 2: reference dimers; Lane 3: crosslinked trimers; Lane 4: de-crosslinked trimers; Lane 5: re-crosslinked trimers.....	140
Figure 5.31: TEM images of crosslinked trimers, de-crosslinked trimers and re-crosslinked trimers.....	141
Figure 5.32: An agarose gel comparing crosslinked and de-crosslinked tetramers (SC1-4) with mono-conjugates, dimers and trimers in denaturing conditions. Lane 1: reference mono-conjugates; Lane 2: reference dimers; Lane 3: reference trimers; Lane 4: crosslinked tetramers; Lane 5: de-crosslinked tetramers; Lane 6: re-crosslinked Tetramers.....	141
Figure 5.33: TEM images of crosslinked tetrahedra, de-crosslinked tetrahedra and re-crosslinked tetrahedra.....	142
Figure 5.34: Dynamic light scattering spectra of gold nanoparticle monomers (red), dimers (green), trimers (blue), tetrahedra (black). The peaks of the hydrodynamic diameters are at 16.06 nm (single NP), 27.74 nm (dimers), 40.31 nm (trimers) and 45.41 nm (tetrahedra). .....	142
Figure 5.35: UV-Visible spectrum of gold nanoparticle mono-conjugates, dimers, trimers and tetrahedral structures.....	143
Figure 5.36: Principle of (non-)resonant Raman scattering. An incident photon has a small probability of interacting with molecules so that they are excited to a virtual excited state (VS). The molecule then either re-emits a photon of the same energy (Rayleigh scattering), of lower energy (Stokes scattering) or of higher energy (anti-Stokes scattering, not shown). If the molecule has an electronic transition at the wavelength of the incident light ( $E_0 \rightarrow S_1$ ), the excitation is in resonance leading to larger scattering probabilities. ....	145
Figure 5.37: Extinction spectra of $30 \pm 3$ nm AuNPs and dimers purified after gel electrophoresis. The broadening of the plasmon bands indicates a plasmonic interaction between the two nanoparticles in the dimer. ....	146
Figure 5.38: Raman spectra of an empty reference glass slide (A) and an acridine orange solution (5mg/mL) deposited on a glass slide (B) and on a PTFE-Au substrate (C). Raman peaks appear in the acridine orange sample at 630, 1222, 1314 and $1360\text{ cm}^{-1}$ .....	147
Figure 5.39: Raman spectra of 30nm gold nanoparticles (A) and 30nm gold nanoparticle dimers (B) with acridine orange at a concentration of $10^{-8}$ M. While the single nanoparticles show no Raman peaks, several peaks at 635, 1228, 1321, 1370, 1526, 1569 and $1632\text{ cm}^{-1}$ are present in the dimer sample.....	149

---

Figure 6.1: Illustration of an upconversion nanoparticle-quantum dot FRET system. The rare-earth doped upconversion nanoparticles (UCNP) absorb light in the infrared (980 nm) and emit light $\lambda_{em} - \text{UCNP}$ . Some of the energy is transferred to quantum dots in close proximity via FRET, which leads to emission at a different wavelength $\lambda_{QD} - \text{FRET}$ . This system utilises DNA as linker between the nanoparticles and enables control of the distance between the donor (UCNP) and the acceptor (QD).....	153
Figure 6.2: Quantum dots (QD540) before and after attachment of DNA (Seq1-Cy3) with EDC/Sulfo-NHS coupling. I: QD540 without DNA, II: QD540 coupled with phosphate buffer, III: QD540 coupled with MES buffer. The pink colour indicates the presence of Seq1-Cy3 on the nanoparticle surface. ....	155
Figure 6.3: Quantum dots (QD540) illuminated with UV-A light after EDC/Sulfo-NHS coupling. Left: QD540 without DNA; Middle: QD540 coupled with phosphate buffer; Right: QD540 coupled with MES buffer.....	155
Figure 6.4: Extinction spectra of QD540 before and after coupling with Seq1-Cy3 using phosphate buffer or MES buffer.....	156
Figure 6.5: Fluorescence spectra of QD540 with Cy3-DNA coupling by two different methods via EDC/NHS chemistry.....	157
Figure 6.6: Photoluminescence spectra of UCNP ( $\text{NaYF}_4:\text{Yb,Tm}$ ) mixed with QDs (QD580) and without DNA functionalisation to determined potential reabsorption from the QDs. The UCNP concentration was 1 nM. At a ratio of UCNP:QD of 1:100, there is no emission from the QDs (red curve). At a ratio of UCNP:QD of 1: $10^5$ , the QD spectrum is clearly obtained and the blue emission of the UCNP quenched (red curve).....	158
Figure 6.7: Photoluminescence spectra obtained from UCNP-QD580 assemblies. No PL was obtained from QDs under irradiation with 980 nm light (black curve). Hybridised assemblies showed quantum dot PL depending on the ratio UCNP:QD due to energy transfer from the UCNPs (1:10 green, 1:25 red, 1:100 blue).....	159
Figure A1: Extinction spectrum of QD520 in water. The first exciton peak is used to determine the concentration of the quantum dots. ....	169
Figure A2: Three-dimensional representation of the tetrahedron formed by hybridisation of all four oligonucleotides SB1-SB4 and the positions of the clicking groups (see Table A2). 171	171
Figure A3: The emission spectrum of QD540 (red curve) and the absorption of Cy3 (blue curve) have a large overlap allowing FRET to occur, which results in emission from the Cy3 dye (pink curve). .....	174
Figure A4: The emission spectrum of $\text{NaYF}_4:\text{Yb,Tm}$ UCNP (blue curve) and the absorption of QD580 (red curve) have a complete overlap allowing FRET to occur, which results in emission from QD580 (orange curve). .....	174

## List of Equations

Equation 2.1: Polarizability of a metal sphere in the quasi-static approximation.....	11
Equations 2.2: Scattering and absorption cross-sections of spherical metal particles in the quasi-static approximation. ....	11
Equation 2.3: The condition on the real part of the dielectric function for plasmon resonance (Fröhlich condition).....	12
Equation 2.4: The change in the energy of the first exciton in a quantum dot due to the quantum size effect. ....	18
Equation 2.5: The change in the free energy G for n atoms forming a cluster in solution....	29
Equation 2.6: The change in the free energy G considering spherical particles.....	30
Equation 2.7: Attractive Van-der-Waals interaction (top) and repulsive double layer interaction (bottom) between two spheres in solution resulting from DLVO theory. ....	32
Equation 3.1: Beer-Lambert's law for dilute solutions.....	59
Equation A1: Definition of the photoluminescence quantum yield.....	172
Equation A2: Formula for the calculation of the quantum yield $\phi$ .....	172

## List of Tables

Table 3.1: Influence of the amount selenium on the emission of $\text{Cd}_{1-x}\text{Se}_x\text{Zn}_{1-y}\text{S}_y$ quantum dots.....	51
Table 5.1: Oligonucleotide sequences modified with 3-cyanovinyl carbazole. The colours indicate the complementarity between the DNA strands. The X denotes the 3-cyanovinyl carbazole modification within the DNA strands. ....	108
Table 6.1: Oligonucleotide sequences employed for the assembly of upconversion nanoparticles and quantum dots. The sequences Seq1 and Seq2 are completely complementary. The sequence Seq1-Cy3 is equal to Seq1 but contains a Cy3 label at the 3'-end.....	153
Table A1: Oligonucleotide sequences without cross-linker modifications.....	170
Table A2: Oligonucleotide sequences modified with azide (labelled with X) and BCN moieties (labelled with Y). ....	171
Table A3: Calculated and literature quantum yields for different nanoparticles.....	173



# DECLARATION OF AUTHORSHIP

I, Pascal Khalid Harimech,

declare that this thesis and the work presented in it are my own and has been generated by me as the result of my own original research.

## DNA-directed assembly of inorganic nanoparticles

I confirm that:

1. This work was done wholly or mainly while in candidature for a research degree at this university;
2. Where any part of this thesis has previously been submitted for a degree or any other qualification at this University or any other institution, this has been clearly stated;
3. Where I have consulted the published work of others, this is always clearly attributed;
4. Where I have quoted from the work of others, the source is always given. With the exception of such quotations, this thesis is entirely my own work;
5. I have acknowledged all main sources of help;
6. Where the thesis is based on work done by myself jointly with others, I have made clear exactly what was done by others and what I have contributed myself;
7. Parts of this work have been published as:

### Articles in academic press:

1. Heuer-Jungemann, A.; Harimech, P. K.; Brown, T.; Kanaras, A. G. "Gold Nanoparticles and Fluorescently-Labelled DNA as a Platform for Biological Sensing", *Nanoscale*, **2013**, 5, 9503-9510.
2. Harimech, P. K.; Gerrard, S. R.; El-Sagheer, A. H.; Brown, T.; Kanaras, A. G. "Reversible Ligation of Programmed DNA-Gold Nanoparticle Assemblies", *Journal of the American Chemistry Society*, **2015**, 137, 9242-9245.

### Other publications:

3. Harimech, P. K.; Hartmann, R.; Rejman, J.; del Pino, P.; Rivera-Gil P.; Parak, W. J. "Encapsulated enzymes with integrated fluorescence-control of enzymatic activity", *Journal of Materials Chemistry B*, **2015**, 3, 2801-2807.

### Abstracts, Posters and Presentations at Conferences:

1. HINT Cost Training school MP1201 (March 2013, Bordeaux, France)

2. E-MRS Spring Meeting (May 2014, Lille, France)
3. E-MRS Spring Meeting (May 2015, Lille, France)
4. HINT Cost Training school MP1201 (May 2015, Ljubljana, Slovenia)

## Acknowledgements

I would like to thank my supervisor Dr. Antonios Kanaras for the opportunity to work on a very interesting research project, which allowed me to gain a deep understanding of current developments in the field of nanotechnology. The constant feedback and guidance throughout the PhD is very much appreciated and helped me to develop myself as a researcher. I also would like to thank my second supervisor Prof. Tom Brown for many insightful discussions and ideas and constant support during the PhD. I am very grateful for the support from Dr. Simon Gerrard who helped me in many ways. Thanks to Dr. Afaf El-Sagheer who helped me in the beginning of my PhD project with lots of advice. Many thanks to Dr. Mauro Chiacchia and Dr. Jordi Aguilera Sigalat for interesting discussions. Furthermore, I would like to thank the people from the Biological Imaging Unit who were always helpful about microscopy related topics. The help from Prof. Muskens (and his group) is very much appreciated.

The University of Southampton and ATDBio are gratefully acknowledged for my PhD studentship.

Many, many thanks are going out to the beloved members of my research group: Dr. Amelie Heuer-Jungemann, Johanna Midelet, Patrick Vilela and Marilena Kyriazi. You guys cheered me up a lot even in the most stressful times and made the time in the lab much more enjoyable. I also would like to thank all the other people who became friends with me during the PhD.

I want to thank my invaluable friends Lars Peters, Lena Schätzel, Eric Sander, Eugen Heinrich, David Steinfeld (and many more) who also provided me a lot of support during my PhD. Special thanks are reserved for Daniel Sasse and Oliver Hübner who became very important people in my life for many reasons.

I would like to thank my parents Elke and Makhlof Harimech as well as my whole family for their encouragement and support.



## Abbreviations

A – Adenine

ADC – Acetone dicarboxylate

APS – Ammonium persulfate

APTES - (3-aminopropyl)-triethoxysilane

BCN - Bicyclo[6.1.0]nonyne

BSPP – bis(p-sulfonatophenyl)phenylphosphine

C – Cytosine

CR – Cross relaxation

CSU – Cooperative sensitisation upconversion

CuAAC – Copper-promoted alkyne-azide cycloaddition

DIBO – Dibenzocyclooctyne

DMF – *N,N*'-dimethylformamide

DNA – Desoxyribonucleic acid

dsDNA – Double stranded DNA

DTT – Dithiothreitol

DLVO - Derjaguin-Landau-Verwey-Overbeek

EDC - 1-Ethyl-3-(3-dimethylaminopropyl)carbodiimide

ESA – Excited-state absorption

ETU – Energy transfer upconversion

eV - Electronvolt

FWHM – Full width of half maximum

G – Guanine

g – Gram

h - Hour

LA – L-lipoic acid

LSPR – Localised surface plasmon resonance

m – metre

m- – milli-

min – minute

*n*- – nano-

$\mu$ - – micro-

M – Molar (mol/L)

MES – 2-(*N*-morpholino)ethanesulfonic acid

MPTMS – (3-mercaptopropyl)-trimethoxysilane  
NHS - N-Hydroxysuccinimide  
NP – Nanoparticle  
OA – Oleic acid  
OAm – Oleylamine  
ODE – 1-octadecene  
PA – Photon avalanche  
PAA – Polyacrylic acid  
QD – Quantum dot  
PAGE – Polyacrylamide gel electrophoresis  
PEG – Polyethylene glycol  
PVP – Polyvinylpyrrolidone  
rpm – revolutions per minute  
s – Second  
SAM – Self-assembled monolayer  
SAXS – Small-angle X-ray scattering  
SERS – Surface enhanced Raman scattering  
SNS - 2,5-bis(2-thienyl)pyrrole  
ssDNA – Single stranded DNA  
SPAAC – Strain-promoted alkyne-azide cycloaddition  
SPANC – Strain-promoted alkyne-nitrone cycloaddition  
T – Thymine  
TEMED – Tetramethylethylenediamine  
TEOS – Tetraethyl orthosilicate  
TMAH – Tetramethylammonium hydroxide  
TMS - Trimethylsilyl  
TOP(O) – Trioctylphosphine (oxide)  
UCNP – Upconversion nanoparticle  
UV – Ultraviolet  
V – Volts  
Vis – Visible  
VS – Virtual state  
W – Watt  
XANES – X-ray absorption near-edge spectroscopy



## Chapter 1. Introduction

More than five decades ago, the famous physicist Richard Feynman envisioned the miniaturisation of machines down to the nanoscale [1, 2]. About three centuries later, inorganic nanoparticles were recognised as extremely useful materials with interesting physical and chemical properties [3, 4]. Their potential led to manifold chemical procedures to generate size- and shape-controlled nanocrystals, which are nowadays the foundation for the development of new materials and technologies at the nanoscale [5-7].

A lot of research in the field of nanotechnology focusses on the assembly of these nanoparticles to form larger regular structures in an automated manner [8-10]. The combination of different nanoparticles allows creating multi-functional materials with a wide range of potential applications. It has been shown in the past that new physical properties can be inferred by nanoparticle assembly through coupling between the constituents, which can lead to a different collective behaviour [11, 12]. An example is the creation of circular dichroism by arranging non-chiral nanoparticles in a chiral structure. One of first and most promising approaches for nanoparticle self-assembly is the utilisation of DNA due to its exceptional properties [13, 14]. DNA acts as a scaffold for the controlled positioning of nanoparticles in complex structures [15]. Its natural recognition capabilities through Watson-Crick base pairing is a big advantage over other approaches like pH or solvent-mediated assembly, which are typically much less specific [16].

Even though the first examples of nanoparticle assemblies using DNA were presented already two decades ago, this research field is still in its infancy [17]. The aim of this work was to further develop the assembly of inorganic nanoparticles with DNA. One of the major drawbacks of utilising DNA is that proper conditions for base pairing need to be maintained in order to avoid disassembly. In addition, depending on the approach, this problem might cause low hybridisation yields of nanoparticle assemblies [18, 19]. In order to increase the stability of such nanoparticle assemblies, DNA crosslinking strategies leading to a permanent connection between two DNA strands have been developed [20, 21]. Following previous work, the use of the well-known strain-promoted azide-alkyne click reaction (SPAAC) between cyclooctynes and azides, which has already been applied successfully in the past, was further investigated [22, 23]. Besides that, the UV-sensitive molecule 3-cyanovinyl

carbazole was employed for the first time in conjunction with gold nanoparticle assemblies [24]. This molecule allows to crosslink DNA reversibly via an external stimulus, which provides a novel tool for spatially and temporally manipulation of nanoparticle assemblies.

Moreover, DNA-directed formation of CdSe/ZnS quantum dot and upconversion nanoparticle hetero-assemblies is presented. The combination of different nanoparticles allows to generate multifunctional materials with the properties of the individual constituents. Both types of particles exhibit well-known photoluminescence properties [25, 26]. While quantum dots have been widely applied in many fields for many years, the use of upconversion nanoparticles has emerged only recently [27, 28]. Even though there have been tremendous advancements in the formation of nanoparticle assemblies, there are still comparably little examples of hetero-assemblies [29-31]. Therefore, the aim of this study was to show the feasibility of creating a new system, which could be the starting point for further research.

In addition, results from the research on lead halide perovskite nanoparticles are presented. Lead halide perovskites have sparked an extraordinary interest in the last years because of their successful implementation in photovoltaics [32]. Very recently, lead halide perovskite nanoparticles have been synthesised for the first time with very promising photoluminescence properties, which have been exploited in LEDs [33, 34]. A modification of the synthesis protocol led to nanoparticle dispersions with a significantly increased processability while maintaining the optical properties.

**Chapter 2** and **Chapter 3** describe the theoretical background as well as the experimental procedures of this work.

In **Chapter 4**, the different inorganic nanoparticles employed in this work are characterised with different techniques. Their surface functionalisation with different ligands as well as oligonucleotides is discussed. Furthermore, the optical properties of lead halide nanoparticles are shown at the end of the chapter.

In **Chapter 5**, the crosslinking of tetrahedral DNA-gold nanoparticles assemblies is presented. The combination of more than one azide- and bicyclononyne-modification per oligonucleotides causes problems in the hybridisation process. On the other

hand, 3-cyanovinyl carbazole as UV-responsive molecule is shown to form at least four reversible crosslinks in one DNA structure in high yields. The crosslinked assemblies are stable even in very unfavourable conditions, i.e. denaturing conditions.

**Chapter 6** contains a preliminary study on the DNA-directed assembly of CdSe/ZnS quantum dots and upconversion nanoparticles. The functionalisation of these nanoparticles with DNA using EDC coupling chemistry as well as the analysis of the combined system will be presented.

**Chapter 7** provides a conclusion of the results. In addition, remarks and ideas for future work are suggested.



## Chapter 2. Background

The synthetic methods and properties of the various types of nanoparticles employed in this work are described in **section 2.1**. Then nanoparticle functionalization will be discussed in **section 2.2** followed by an introduction to DNA as a tool in nanotechnology in **section 2.3**. Finally, an overview about DNA-based nanoparticle assemblies will be given in **section 2.4** on which the experimental work in this project mainly focusses.

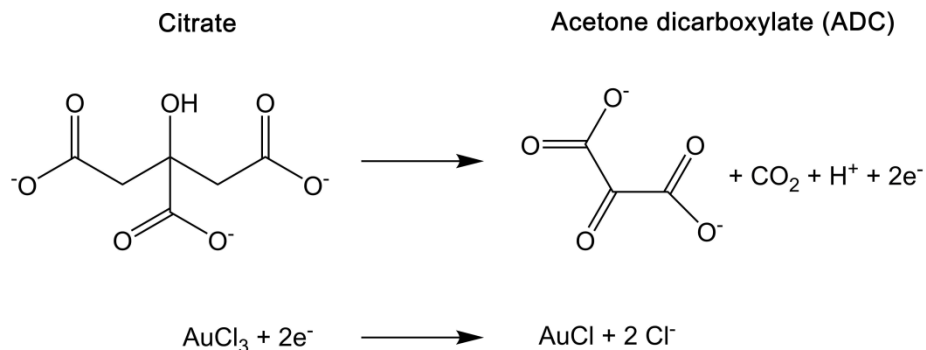
### 2.1 Colloidal nanoparticles

#### 2.1.1 Synthesis of gold and silver nanoparticles

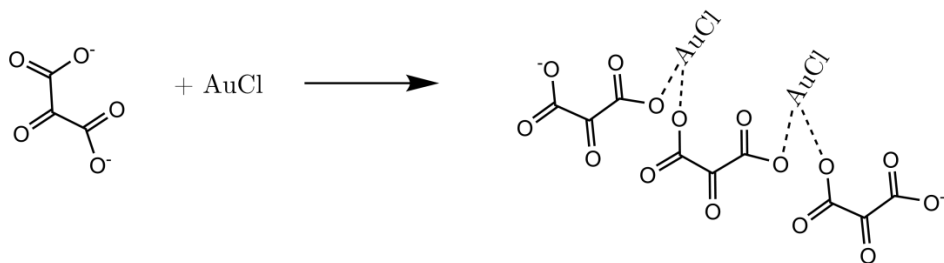
For more than a millennium, metals such as gold and silver were used in glass staining because of the resulting brilliant and tuneable colours [35]. A famous example is the Lycurgus cup, which dates back to the 4<sup>th</sup> century and exhibits different colours depending on the direction of illumination [36]. Besides those optical effects, gold has played a role in medicine for many centuries [37]. In the last twenty years, gold and silver nanoparticle research has become very popular because of several unique and controllable chemical and physical properties [38]. As a result, nanoparticles are foreseen to be a key technology for manifold applications in different fields of nanotechnology [39]. The synthesis of nanoparticles and their optical properties will be described in the following sections.

A synthesis method of gold nanoparticles, which is still the most prominent nowadays, was reported by Turkevich *et al.* in the 1950's [40]. They studied the nucleation and growth of gold nanoparticles using a variety of reducing agents. The importance of trisodium citrate as a reducing agent has been highlighted because of the uniform size distribution created by its use. Around 20 years later, the Turkevich method was re-visited by Frens who re-fined the method based on trisodium citrate [41, 42]. Therefore, this method is nowadays named after Turkevich and Frens. The reaction relies on the reduction of a gold chloride precursor with trisodium citrate in a boiling aqueous solution. The proposed mechanism is shown in **Figure 2.1** [43].

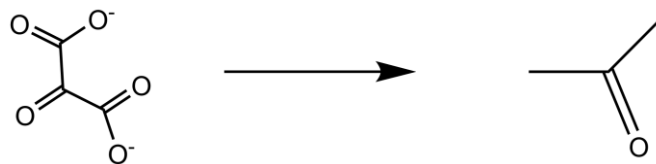
**Reaction A: Redox reaction between gold precursor and citrate**



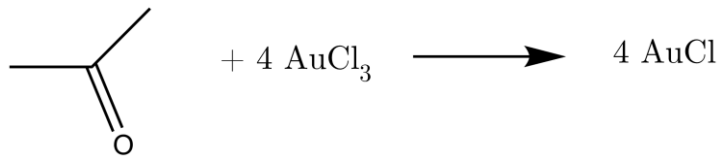
**Reaction B: Complexation of ADC and AuCl**



**Reaction C: Decomposition of ADC into acetone**



**Reaction D: Redox reaction between  $\text{AuCl}_3$  and acetone**



**Reaction E: Disproportionation of AuCl**

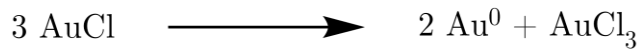


Figure 2.1: Reaction mechanism of the gold nanoparticle synthesis with the Turkevich method. Adapted from ref. [43].

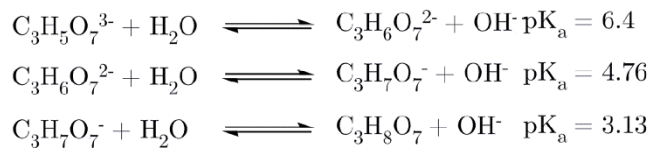
The synthesis starts with a redox reaction where a citrate anion is oxidised to acetone dicarboxylate (ADC) donating two electrons to Au(III), which is reduced to Au(I) (**Reaction A**). In an intermediate step, ADC forms macromolecular complexes with the Au(I) species (**Reaction B**). Finally, precursor particles (nuclei) are formed by coagulation of the complexes and disproportionation of AuCl to Au(0) (**Reaction E**). These nuclei induce an autocatalytic reaction with further AuCl molecules attaching to the nuclei leading to the growth of gold nanoparticles. However, a side reaction occurs simultaneously. Besides forming complexes with Au(I), ADC can decompose into acetone (**Reaction C**) and reduce Au(III) to Au(I) (**Reaction D**). The mechanistic study of the gold nanoparticle synthesis by citrate reduction is not trivial due to the different steps involved. Nevertheless, the reaction mechanism was derived from the conclusions of different authors [44-49].

The formation of nanoparticles consists generally of nucleation and growth by addition of monomers from solution onto the nuclei. In the case of gold nanoparticles, Au(0) are nuclei and Au(I) are the monomers. It is clear that a fast nucleation step, which is separated from the growth, needs to be generated to achieve a narrow size distribution as described by the LaMer model (see **section 2.3.1**) [50]. Privman *et al.* have demonstrated that rapid coagulation of the macromolecular complexes is necessary for the formation of monodisperse nanoparticles [47]. Thus, Xia *et al.* hypothesised that a larger amount of initial ADC should accelerate the formation and coagulation of Au-ADC complexes [43]. In their work, they employed an Ag(I)-assisted generation of ADC and showed that the amount of ADC is a key parameter for a fast nucleation and homogenous growth [51, 52]. Similar results were obtained by the group of Puntes who induced a pre-oxidation of sodium citrate to ADC at high temperature by changing the sequence of precursor addition [53]. Kumar *et al.* discuss that the second reaction between acetone and Au(III) precursor molecules only plays a role in the growth process when low concentrations of citrate are used. This is because of the slow reduction compared to citrate [49].

A systematic series of experiments conducted by Ji *et al.* revealed that the citrate molecule has three roles in the Turkevich method [54]. First, citrate acts as a mild reducing agent through the formation to ADC [44]. Secondly, citrate binds electrostatically on the nanoparticle surface and stabilises the nanoparticle colloid

[45, 46]. Finally, citrate acts as a buffer influencing the pH of the reaction solution, which was overlooked for a long time. The pH is an important parameter because the gold precursor becomes less reactive at higher pH values and de-protonation of the citrate molecule increases the stability of the nanoparticles through electrostatic repulsion (Figure 2.2) [54, 55]. Schulz *et al.* used the inversion method reported by Puntes and reported that accurate control of the pH using citrate buffer improves the size distribution of the AuNP synthesis [55].

#### Citrate protonation at different pH values



#### Hydrolysis of the gold precursor at different pH values

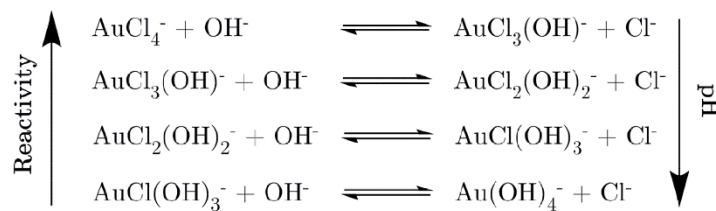


Figure 2.2: The protonation and hydrolysis of citrate and gold chloride. The pH is an important factor for the reactivity of the precursors and the electrostatic stabilisation. Adapted from ref. [55].

Another interesting aspect of the Turkevich method is the colour change during the gold nanoparticle synthesis. The yellow gold chloride precursor solution rapidly turns colourless upon addition of the citrate indicating the reduction of Au(III) to Au(I). Then, the solution becomes purple for several seconds to minutes before turning wine red. Pong *et al.* investigated the purple transition and reported that small gold clusters coagulate and form a network of nanowires, which eventually collapses into small pieces with gold nanospheres as the final product [56]. However, even though those nanowires species were visualised with transmission electron microscopy, Polte *et al.* did not detect these intermediates using *in situ* small-angle X-ray scattering (SAXS) and X-ray absorption near edge structure (XANES) [57]. It is evident from all the different results that this seemingly simple reaction is highly non-trivial and therefore still under debate to date [58].

A drawback of the Turkevich method is that it only yields rather monodisperse gold nanoparticles for diameters between 10-20 nm [41]. In order to synthesise larger nanoparticles with similar dispersions (standard deviation  $\sigma \leq 10\%$ ), seeded-growth approaches have been applied [59-61]. These methods rely on the growth of pre-formed nanoparticle seeds by mild reduction of additionally injected Au(III) precursor, e.g. with hydroxylamine or ascorbic acid. The reduction needs to be performed in such a way that no new nuclei are formed but Au(III) becomes Au(I) so that it can attach on the nanoparticle surface. Bastús *et al.* performed a kinetic study on the evolution of gold nanoparticle growth yielding uniformly shaped and sized gold nanoparticles up to 150 nm [62]. The difficulty of the seeded-growth approach is that the ratio of seeds to additional gold precursor needs to be tuned carefully in order to prevent new nucleation or irregular growth due to Ostwald ripening (see **section 2.3.2**). They found out that lowering the temperature to 80-90°C and controlling the added amount of gold salt by successive injections prevents new nucleation and leads to monodisperse gold nanoparticles.

The previously presented and discussed Turkevich method can only be used to synthesise nanoparticles with diameters of at least 10 nm. In order to prepare smaller particles, a strong reducing agent like sodium borohydride needs to be utilised for the rapid formation of neutral metal species [63, 64]. In addition, by using a strong reducing agent a larger number of nuclei is produced, which in turn leads to a smaller nanoparticle size due to a limited amount of precursor material. Polte *et al.* investigated the gold nanoparticle formation with sodium borohydride [57]. They discovered that the reduced gold atoms ( $\text{Au}^{3+} \rightarrow \text{Au}^0$ ) rapidly form clusters in less than 200 ms. Subsequently, those clusters coalesce to nanoparticles with growth decaying exponentially in time. Furthermore, different from the citrate reduction method, the growth by attachment of monomers from the solution is very limited. Therefore, nanoparticles can be extracted when they are still small in size. A related synthesis is the famous Brust-Schiffrin method, which produces very stable nanoparticles in the organic [64].

*Silver nanoparticles:* Apart from the synthesis of gold nanoparticles, the Turkevich method has been employed for the synthesis of silver nanoparticles [65-67]. After having developed their successful growing method for gold nanoparticles, Bastús *et al.* used their approach for the synthesis of monodisperse silver nanoparticles with

sizes up to 200 nm [68]. Similarly, the formation of silver nanoparticles is a multistep reaction [68, 69]. First,  $\text{Ag}^+$  is reduced to  $\text{Ag}^0$ , which then forms a dimer  $\text{Ag}_2^+$  with an unreacted silver cation [70, 71]. Further dimerization of these species leads to  $\text{Ag}_4^{2+}$ , which acts as a monomer for nanoparticles formation. In their work, Bastús *et al.* discuss that a small addition of tannic acid favour fast nucleation leading to monodisperse silver nanoparticles. The multi-step procedure outlined earlier has successfully been applied to achieve large silver nanoparticles with size distributions of about 10% standard deviation.

*Ligand capping:* After the synthesis of gold nanoparticles and silver nanoparticles with the citrate reduction method, their surface is covered with citrate anions. These ions are only labile bound via electrostatic interaction of the carboxylic groups with the nanoparticle surface and can be replaced by other stronger binding ligands such as phosphines, amines or thiols, which will be discussed in **section 2.3**.

### 2.1.2 Optical properties of gold and silver nanoparticles

The properties of gold nanoparticles are very different from the bulk material. While the bulk exhibits the well-known metallic gloss paired with a yellowish colour, nano-sized gold has different brilliant colours ranging from wine red to deep blue [72]. Michael Faraday was the first scientist to report that the colours arise from the small sizes of the gold particles [73].

The physical mechanism behind the different colours is the so-called localised surface plasmon resonance (LSPR) [74]. Plasmons are quantised collective oscillations of free electrons in metals that can be induced by electromagnetic waves. This process can be explained in a semi-classical model where the conduction electrons are displaced against the fixed positive cores leading to polarisation and an inner restoring force. The result is a driven harmonic oscillation, also known as plasma oscillation, where the intensity is largest when the excitation is in resonance with the plasma frequency of the electron gas. The plasma frequency depends on several factors such as electron density and charge distribution [75, 76]. Because the resonance lies in the visible range of the light for gold and silver nanoparticles, the brilliant colours observed.

For nanoparticles with diameters below 40 nm the quasi-static approximation, i.e. the phase of the electric field is considered constant throughout the particle, can be

applied to model the oscillation. In this way, excellent agreements with experimental results have been reported [77, 78]. The dipole excitation of the electron cloud by an external electromagnetic wave is illustrated in **Figure 2.3**.

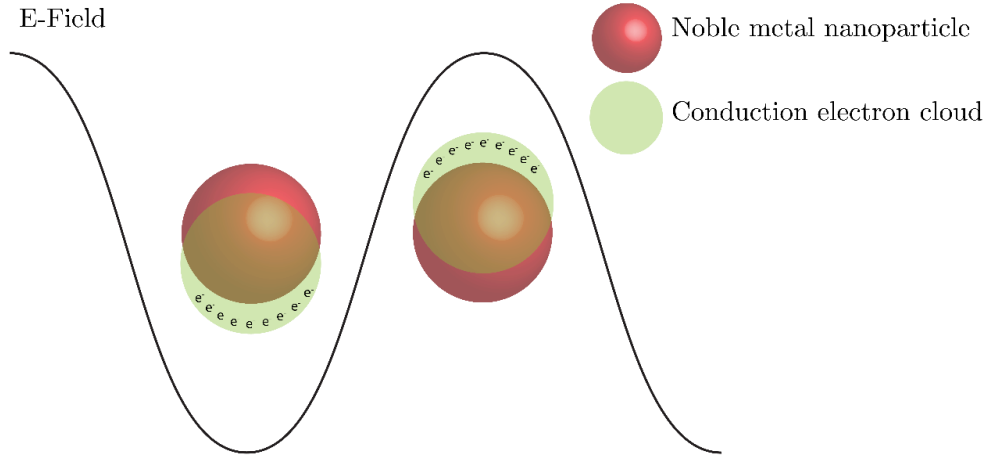


Figure 2.3: The localised surface plasmon resonance (LSPR) of gold nanoparticles. The collective displacement of conduction electrons leads to large absorption and scattering coefficients.

Considering the quasi-static approximation, the equations for the absorption and scattering coefficients can be calculated from simple electrostatics [75, 79]. The polarizability  $\alpha$  of a metal sphere, describing how well charges in a molecule can be separated, is related with its dielectric function via the Clausius-Mossotti relation as follows:

$$\alpha = 3\epsilon_0 V \cdot \frac{\epsilon_r(\omega) - 1}{\epsilon_r(\omega) + 2},$$

Equation 2.1: Polarizability of a metal sphere in the quasi-static approximation.

where  $\epsilon_0$  is the vacuum permittivity and  $\epsilon_r(\omega) = \epsilon'_r(\omega) + i \cdot \epsilon''_r(\omega) = \epsilon_{\text{metal}}/\epsilon_{\text{medium}}$  is the complex dielectric function of the metal divided by the dielectric constant of the surrounding medium. From the polarizability it is possible to obtain the absorption and scattering cross-sections according to Bohren and Huffman [80]:

$$C_{sca} = \frac{k^4}{6\pi} \cdot \left| \frac{\alpha}{\epsilon_0} \right|^2 = \frac{k^4 \cdot 9V^2}{6\pi} \frac{(\epsilon'_r - 1)^2 + \epsilon''_r^2}{(\epsilon'_r + 2)^2 + \epsilon''_r^2}$$

$$C_{abs} = k \cdot \Im(\alpha/\epsilon_0) = k \cdot 3V \frac{\epsilon''_r}{(\epsilon'_r + 2)^2 + \epsilon''_r^2}$$

Equations 2.2: Scattering and absorption cross-sections of spherical metal particles in the quasi-static approximation.

where  $k = 2\pi/\lambda$  is the wave vector and  $\Im$  denotes the imaginary part. From these equations it follows that resonance occurs when the denominator is minimised, i.e. the so-called Fröhlich condition is met [81]:

$$\Re(\varepsilon_r) = -2$$

**Equation 2.3: The condition on the real part of the dielectric function for plasmon resonance (Fröhlich condition).**

When the imaginary part of the dielectric function is small and only weakly dependent on the frequency, then the denominator may approach zero leading to a very large polarizability and extinction cross-sections. There are important characteristics that can be extracted directly from the two **equations 2.1 and 2.2**. The scattering dominates the absorption with increasing particle size because of the quadratic dependence in the volume, i.e.  $C_{\text{sca}} \sim r^6$  whereas  $C_{\text{abs}} \sim r^3$ . The  $r^6$  dependence is in particular important for dynamic light scattering (DLS) where the size of a solute is measured by scattering (see **section 3.4.7**). Nevertheless, both scattering and absorption are strongly enhanced at the resonance because both denominators are minimised at the Fröhlich condition. Another result from these equations is the dependence of the resonance on the dielectric constant of the surrounding medium  $\varepsilon_m$ . As  $\varepsilon_m$  increases the plasmon resonance shifts to longer wavelengths (red-shift), which has been experimentally verified in many examples. This includes the solvent as well as the surface ligands, which are bound to the nanoparticles. The dependence can be used for sensing applications, e.g. detection of biomolecules [78, 82, 83].

It should be noted that the dielectric function has no explicit dependence on the radius in the dipole approximation, i.e.  $\varepsilon = \varepsilon(\omega)$ . This is contrary to an experimentally observed broadening of the bandwidth as well as a LSPR peak shift with decreasing nanoparticle sizes for diameters smaller than 10 nm [84]. A model suggested by Kreibig and Genzel renders the dielectric function size dependent by considering the spatial constraint of electrons in small nanoparticles [85]. Because the free-mean path of the electrons is larger than the nanoparticle dimension, surface scattering accounts for a  $1/R$ -dependence of the dielectric function, which is in agreement with experimental results [85-87].

This simple theory predicts a plasmon resonance for gold nanoparticles suspended in water at around  $\lambda = 520$  nm and  $\lambda = 400$  nm for silver nanoparticles. These

predictions use the experimentally determined bulk dielectric functions for gold and silver from Johnson and Christy or Weaver *et al.* [88, 89]. The predicted values are in good agreement with real nanoparticle dispersions. However, for nanoparticles with larger diameters ( $d \geq 40$  nm), the quasi-static approximation is not valid anymore because the phase inside the nanoparticles becomes variable and higher order modes are excited (quadrupolar etc.). Since the higher order modes have a lower energy, the overall plasmon resonance shifts to larger wavelengths (red-shift) as the nanoparticles become larger.

A theory about scattering and absorption of spherical nanoparticles with an exact solution has been published by Mie in 1908 [90]. This work was a milestone for the description of optical phenomena in colloidal systems. The author used a rigorous approach starting from the Maxwell equations and solving them with appropriate boundary conditions. The result yields expressions for the scattering and extinction cross-sections that involve an infinite series of Riccati-Bessel functions containing information about all possible excited modes [91]. When only the dipole term is considered, the same solution as for the quasi-static approximation is obtained justifying this approximation. However, as the nanoparticles increase in size the contributions from higher order excitations (quadrupole, octupole) become non-negligible. Different from the dipole mode, these higher modes contain the size-dependence needed to predict the red-shift of the plasmon resonance for increasing nanoparticle sizes. This has been experimentally verified in numerous examples [92, 93].

A few years later, the theory was expanded for ellipsoidal gold particles by Richard Gans in 1912 and for silver nanoparticles in 1915 [94, 95]. The solutions are useful for the prediction of the LSPR of elongated nanoparticles such as nanorods [96, 97]. An interesting outcome is that the plasmon resonance of elongated nanoparticles depends on the aspect ratio of length to width. This allows for tuning the plasmon resonance of gold nanorods from about 600-1200 nm. The extended range into the near-infrared (NIR) make these particles particularly interesting for biological applications because NIR light has deeper penetration depths in tissue [98, 99]. In addition, there are possibilities to apply these nanoparticles in optoelectronic devices such as solar cells or lasers [100, 101].

In summary, the plasmonic properties of gold and silver nanoparticles are stemming from the reduction of the spatial dimensions to much less than the wavelength of light. The LSPR makes them attractive for several research fields. It should be noted that in the past much more research has been conducted on gold nanoparticles than silver nanoparticles. The main reasons are that gold is chemically much less reactive and reliable synthesis methods were mainly developed for these nanoparticles. On the other hand, silver nanoparticles are much more sensitive to oxidation, which may result in ligand stripping and dissolution of the nanoparticles. Nevertheless, silver nanoparticles are of interest due to much higher extinction coefficients of one to two orders of magnitude compared with gold nanoparticles making them attractive for applications such as surface enhanced Raman scattering (SERS) [102, 103].

### 2.1.3 Synthesis of semiconductor quantum dots

Semiconductor nanoparticles or quantum dots (QDs) are a class of materials that sparked extraordinary interest in the scientific community due to their remarkable properties and have been subject to extensive research since the 1990's [26]. The most prominent property is the fluorescence of these particles, which can be tuned over the whole visible spectrum by controlling their size [104]. Significant work about their synthesis was conducted by Steigerwald and Brus *et al.* using wet chemistry methods involving precursors in aqueous solution with surfactants in a reverse micelle approach [105]. In 1993, the hot-injection solvothermal approach was published by Murray *et al.*, which had a significant impact on the synthesis of nanoparticles in general [106]. In this method, organometallic precursors are quickly injected into a high boiling point solvent at high temperature. Immediately after injection, a sudden nucleation burst occurs due to super-saturation leading to monodisperse nuclei, which are then accumulating further material from the solution by diffusion according to the LaMer model (see **section 2.3.1**).

In the first protocols trioctylphosphine (TOP) and trioctylphosphine oxide (TOPO) were utilised as coordinating solvents and organometallic precursors like diethyl zinc and bis(trimethylsilyl) sulfide ((TMS)<sub>2</sub>S) used, which are toxic and highly flammable. Therefore, necessary precautions needed to be taken and typically the reaction was carried out in a glove box under nitrogen atmosphere. Fatty acids and fatty amines such as oleic acid (OA) or oleylamine (OAm) in a non-coordinating high boiling point solvent like 1-octadecene (ODE) have been proven to be advantageous

for several reasons [107]. Firstly, diethyl zinc and bis(trimethylsilyl) sulfide ((TMS)<sub>2</sub>S) can be excluded from the reaction by *in situ* or *ex situ* preparation of metal oleate precursors like zinc oleate. Since metal oleates are easily synthesised and purified, this approach is more universal and allowed the development of many precursor materials. Secondly, the growth dynamics are improved leading to narrower size distributions of nanoparticles [108]. Finally, better surface passivation is achieved giving rise to enhanced optical properties [109].

A generic setup for the hot-injection method is shown in **Figure 2.4**. Typically, three-neck flasks sealed with septa are used as the reaction vessel. One arm is equipped with a thermometer or thermocouple. The top opening is equipped with a condenser together with a supply of inert gas. The other arm is used for the injection of the precursor with a syringe. The reaction vessel can be heated in an oil-bath or with a heating mantle. This setup allows for controlling the temperature as well as avoiding humidity and oxygen in the reaction, which are two factors commonly influencing the reaction negatively.

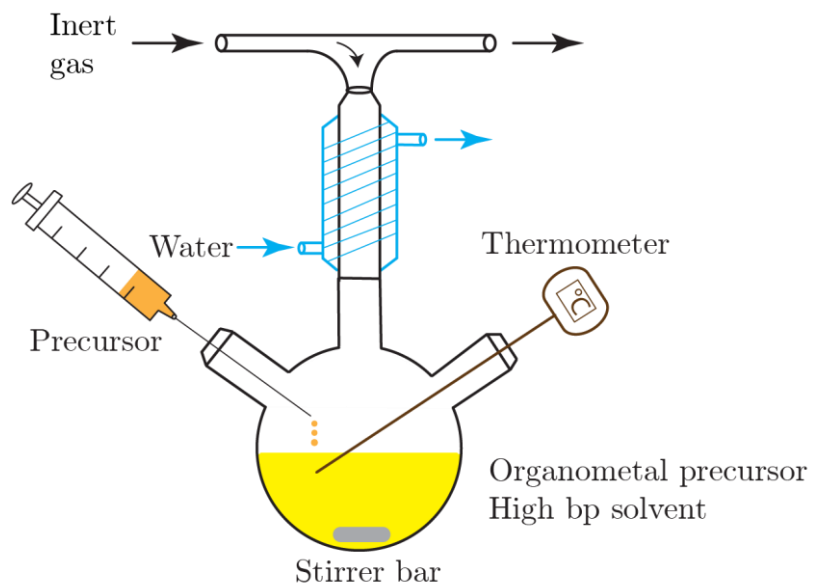


**Figure 2.4:** Typical setup for the synthesis of nanoparticles with the hot-injection method.

The hot-injection method produces highly monodisperse nanoparticles simply by controlling the reaction temperature and the mixtures of organics [110]. Soon after the synthesis of the first II-VI semiconductor nanoparticles (CdSe, CdS, CdTe), the solvothermal method was adopted for the synthesis of III-V materials (InAs, InP,

GaP) and IV-VI materials (PbS, PbSe, PbTe) that extended the photoluminescence range of semiconductor nanoparticles from the visible into the infrared [111].

In the beginning the photoluminescence quantum yields (PLQY) of the synthesised quantum dots were rather low and its improvement became subject of research. The PLQY is a measure of radiative emission and defined as the number of photons emitted divided by the number of photons absorbed (see **Appendix A.4**). It became clear that the surface capping had a significant influence on the quantum yield of the nanoparticles. This was attributed to the non-radiative surface traps stemming from surface defects, which had a significant influence due to the large surface to volume ratio of small nanoparticles [112-114]. The first attempts to minimise the surface defects focussed on the growth of an inorganic shell of zinc sulfide around the nanoparticles [104]. ZnS has a larger band gap than CdSe, which is necessary for improving the luminescence by confining the electrons and holes to the core [115]. While the growth of a shell with few monolayers (1-3) significantly increased the quantum yield, larger shells resulted in a reduction of the yield. The reason is that new trap states are formed at the core/shell interface or in the shell itself because the lattice mismatch of about 12% between CdSe and ZnS induces strain [116]. Even though pure CdSe nanoparticles with quantum yields up to 85% have been synthesised, the inorganic capping increases the stability of the quantum dots significantly against environmental influences and photo-degradation [117]. In a more recent work by the group of Klimov, an alloying strategy for CdSe nanoparticles such as  $\text{CdSe}/\text{CdSe}_{x}\text{S}_{1-x}/\text{CdS}$  or  $\text{Cd}_x\text{Se}_{1-x}\text{Zn}_y\text{S}_{1-y}$  has been developed [118, 119]. This approach leads to quick and facile protocols for the synthesis of quantum dots with high quantum yields (>50%) and the aforementioned stability in a one-step reaction.

#### 2.1.4 Optical properties of semiconductor quantum dots

The genuine optical properties of quantum dots are a result of them being a nano-sized semiconductor material, which leads to quantum size effects [120, 121]. The origin will be explained in the following [122]. In the bulk of solids, large numbers of atoms are arranged in a periodic lattice and hybridisation of the atomic orbitals leads to delocalisation of the valence electrons. An electron is then described for example according to the Kronig-Penney model, where its wave function is considered in a periodic arrangement of rectangular potential wells [123]. The Bloch

theorem then allows for solving the Schrödinger equation and as a result, continuous energy bands with allowed and forbidden electron energies in the system are obtained. The physical properties are ruled by the highest fully occupied band (valence band) and the next energetically higher band (conduction band).

While the valence and conduction band are overlapping in metals, there is a band gap of few electronvolts ( $0 < E_g < 3$  eV) between them in semiconductor materials. This means that electron-hole pairs can be generated by the absorption of visible light (1.65-2.75 eV) with energies larger than the bandgap. On the other hand, recombination of an electron with a hole creates photon emission corresponding to the band gap energy. Further distinction involves the classification into direct or indirect band gap semiconductors. In indirect semiconductors, the energy valley of the conduction band is not in line with the apex of the valence band in the band diagram. As a consequence, a phonon (collective vibrational motion of the lattice) is needed to assist radiative relaxation in order to fulfil the conservation of momentum. Because this process is much less probable, the vast majority of the transitions are non-radiative. The opposite is true for direct band gap semiconductors where radiative recombination is not limited by phonons but occurs readily as there is no external momentum needed. This criterion of a direct or indirect bandgap is still important at the nanoscale. For instance, even though silicon nanocrystals were found to exhibit increased luminescence compared to its bulk counterpart, it still remains a challenge to make them efficient emitters [124-127]. On the other hand, certain semiconductor quantum dots such as CdSe belong to the class of direct bandgap materials, which explains their inherently stronger luminescence.

As the spatial dimensions of the bulk semiconductor are decreased in all directions to only few nanometres, the so-called strong confinement regime is reached [128]. The actual range of this regime is determined by the material-dependent exciton Bohr radius, which describes the size of a bound electron-hole pair [129]. In this regime, the electronic bands become quantised because the electron and hole wave functions become spatially confined by the quantum dot boundaries. This can be modelled with the ‘particle-in-a-sphere’ model where a particle is confined in an infinitely large potential well with spherical symmetry. As a result, the smaller the confinement space the larger the energy gaps becomes. Therefore, smaller nanoparticles exhibit a blue-shifted absorption and emission compared to larger particles. **Figure 2.5** shows

the effect on the band gap and the discretisation of the energy states due to the quantum size effect in the strong confinement regime [130]. The correlation between the size and the emission wavelength has been verified experimentally for many materials. The Brus equation allows to calculate the first exciton energy depending on the size of the quantum dot [131]:

$$E^* = E_{gap} + \frac{\hbar^2 \pi^2}{2r^2} \left( \frac{1}{m_e^*} + \frac{1}{m_h^*} \right) - \frac{1.8e^2}{\epsilon \cdot r}$$

Equation 2.4: The change in the energy of the first exciton in a quantum dot due to the quantum size effect.

$E_{gap}$  is the band gap energy of the bulk material,  $r$  is the radius of the quantum dot,  $m_e^*$  and  $m_h^*$  are the effective electron and hole masses of the material, respectively and  $\epsilon$  is the dielectric constant of the material. The second term is associated with the confinement energy and the third term describes the coulomb interaction of the exciton.

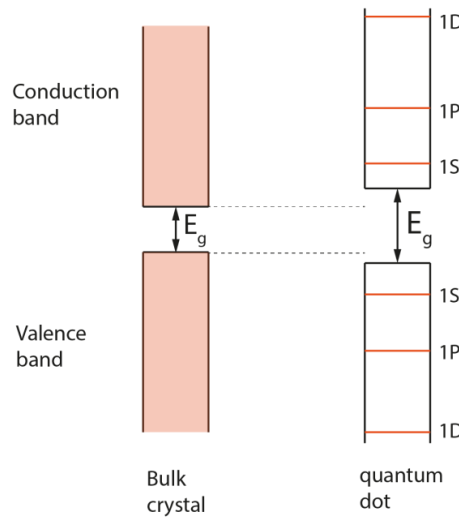


Figure 2.5: Illustration of the difference between the bulk and the nano-regime of semiconductors. The energy gap is increasing and the quasi-continuous energy states in the valence and conduction band become discrete due to the quantum size effect [130].

To conclude, the luminescence properties of semiconductor quantum dots are a result of the intrinsic band gap of several electronvolts and the quantisation of the energy states as the strong confined regime is approached. By choosing an appropriate material as well as controlling its size, the emission wavelength can be tuned over the whole visible range and into the infrared.

Comparing quantum dots with organic fluorophores like laser dyes, e.g. fluorescein or rhodamines, there are several differences [132]. While organic dyes often have very high QYs of around 90%, typical values for CdSe/ZnS quantum dots are 40-70%. However, their molar absorption coefficient  $\epsilon$  is typically one to two orders of larger than for dyes. Furthermore, QDs exhibit a Gaussian emission profile without tails at longer wavelengths, which is common for organic dyes. This allows for better multiplexing with QDs because signal crossover is reduced. In addition, the photostability of QDs can be several orders of magnitude larger compared to organic dyes. Importantly, quantum dots can be modified relatively easily using appropriate surface chemistry leading to functional probes. These advantages make quantum dots particularly interesting for optical applications like photovoltaics or LEDs [27, 133]. Much research is also conducted in the field of biology where organic dyes are still the standard due to established methods and the unknown toxicity of quantum dots [134].

In the next section, upconversion nanoparticles as another class of luminescent nanoparticles will be described.

### 2.1.5 Synthesis of upconversion nanoparticles

Another class of materials, which gained recent research interest, are the so-called upconversion nanoparticles. The name stems from the fact that these particles absorb light at a higher wavelength (usually near-infrared (NIR)) and emit photons at lower wavelengths (anti-Stokes type emission). This is achieved by doping transition metals and lanthanides in a low-phonon host matrix, which facilitates efficient energy transfer between the doped atoms (see **section 2.1.6**). Due to the advances in nanoparticle synthesis in the 1990's, nano-sized upconversion nanocrystals became available and have since then been studied thoroughly [28]. Similar to the synthesis of quantum dots (see **section 2.1.3**), solvothermal methods are used for the synthesis of monodisperse and size-tunable upconversion nanoparticles. A vast range of host matrices, e.g.  $\text{NaYF}_4$ ,  $\text{NaGdF}_4$  or  $\text{La}_2\text{O}_2\text{S}$  have been employed so far.

Among several initial strategies to synthesise matrices for upconversion nanoparticles, the group of Yan *et al.* were the first to establish a simple solvothermal protocol using a single precursor  $\text{La}(\text{CF}_3\text{COO})_3$  together with OA in ODE at 280°C yielding monodisperse  $\text{LaF}_3$  nanoparticles [135]. This approach has become a common synthesis method for the synthesis of monodisperse nanoparticles of

different compositions and a variety of shapes such as spheres, cubes, rods and hexagonal prisms [136]. However, this protocol raised safety concerns because the decomposition of the fluoride reactants could create toxic fluorinated species and even HF by hydrolysis. Therefore, Li and Zhang developed another two-step procedure for the synthesis of  $\text{NaYF}_4$  where yttrium oleate precursor was formed *in situ* with subsequent addition of  $\text{NH}_4\text{F}$  and  $\text{NaOH}$  in methanol [137]. Then, the reaction temperature is increased to 300°C yielding uniform crystalline nanoparticles successively over one hour. In order to create upconversion nanoparticles, the host matrices are doped with different rare-earth elements. Typical lanthanides are ytterbium ( $\text{Yb}^{3+}$ ) as an absorber (also called antenna) and erbium ( $\text{Er}^{3+}$ ) or thulium ( $\text{Tm}^{3+}$ ) as emitters. These lanthanides are mixed in desired ratios with the host matrix precursors to create doped nanoparticles. Different contents from 10-90%  $\text{Yb}^{3+}$  and 0.1-10%  $\text{Er}^{3+}$  or  $\text{Tm}^{3+}$  change both the photoluminescence quantum yields and the emission spectra [138] (see **section 2.1.6**).

The as-synthesised upconversion nanoparticles are like quantum dots stabilised by fatty amines or fatty acids as surface ligands. Similarly, upconversion quantum yields are influenced by surface defects and several methods for surface modification have been applied [139]. Ligand exchange reactions, silanization or core-shell type of approaches have been successfully performed, which will be discussed in **section 2.2**.

### 2.1.6 Optical properties of upconversion nanoparticles

The anti-Stokes emission of upconversion nanoparticles is rather peculiar, which is one of the reasons why a lot of research on these materials is still being conducted [140]. The main principle of upconversion photoluminescence is the ability of the material to absorb several photons of lower energy before radiative or non-radiative relaxation occurs. An example is two-photon absorption, which has been observed in quantum dots and is still under investigation [141]. However, two-photon absorption is an inefficient non-linear process, which requires high photon densities achieved only with ultrashort pulse lasers [142]. The excitation by two photons is only possible via virtual states (VS), i.e. a very short-lived quantum state, which renders such a transition very unlikely (**Figure 2.6a**). On the other hand, lanthanide-doped upconversion nanoparticles can be tailored in such a way that the lifetimes of the excited states are long enough to allow multiple photon absorption. Different

from quantum dots, these particles have real ladder-like energy states, which makes the process several orders of magnitude more efficient (Figure 2.6b). Therefore, the combination of lanthanide ions creates a rather efficient platform for anti-Stokes photoluminescence that is not limited by costly pulsed lasers but can readily be exploited with relatively low-priced continuous-wave photodiodes.

Besides multi-photon absorption or excited state absorption (ESA), other important energy transfer mechanisms have been identified [25]. Energy transfer upconversion (ETU), cooperative sensitisation upconversion (CSU), cross relaxation (CR) and photon avalanche (PA) are all upconversion processes that have a certain significance depending on the dopant combination or the concentration of the dopants [143]. The most crucial process for the  $\text{Yb}^{3+}/\text{Er}^{3+}$  and  $\text{Yb}^{3+}/\text{Tm}^{3+}$  pairs employed in this work is ETU (Figure 2.6c). In this process a sensitizer ion (Ion1) is excited into a metastable excited state (E1) by the absorption of a photon. The energy is then transferred to a second ion (Ion2) which is excited to its first excited state whereas the sensitizer relaxes back to its ground state (G). Several of these excitations lead to an excitation of ion2 into higher states (E2), which can radiatively relax.

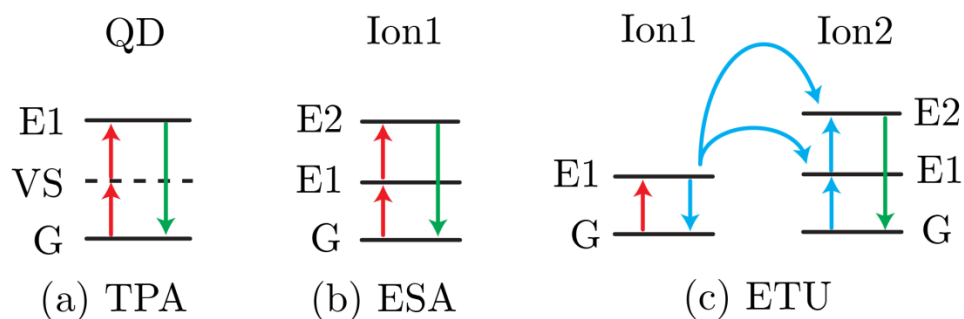
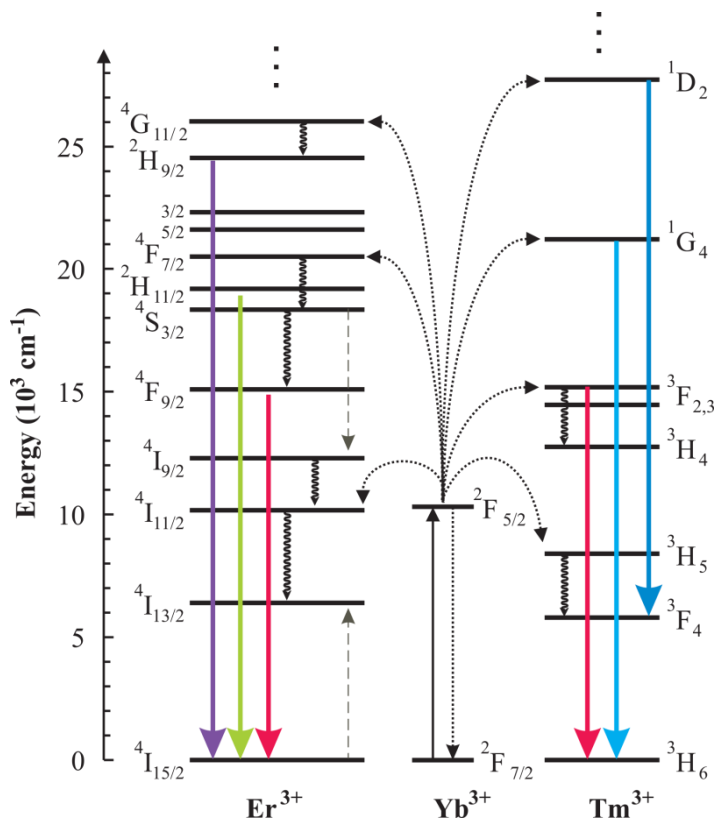


Figure 2.6: Illustration of three different multi-photon excitation pathways. (a) Two-photon absorption, (b) excited state absorption and (c) energy transfer upconversion. G = ground state; E1,E2 = excited state; VS = virtual state. The red, blue and green arrows represent photon absorption, energy transfer and radiative emission, respectively.

In a series of experiments, Suyver *et al.* determined the exact transitions of ytterbium and erbium respectively thulium co-doped  $\text{NaYF}_4$  nanoparticles [144]. Figure 2.7 shows the specific energy level diagram describing the interaction between the sensitisier ( $\text{Yb}^{3+}$ ) and the acceptor ions ( $\text{Er}^{3+}$ ,  $\text{Tm}^{3+}$ ). The upconversion relies on 4f-4f transitions, which are dipole forbidden and therefore have long lifetimes facilitating multi-photon transfer. The ytterbium ion has a two-level system with an absorption

maximum at around 980 nm. The energy from an excited ytterbium atom is then transferred to the co-doped rare-earth atoms via ETU, which relax by emitting photons of different wavelengths as indicated in **Figure 2.7**. The relative proportions of the different emission channels can be influenced by changing the relative dopant concentrations. For example, Quintanilla *et al.* described that the emission spectrum of thulium-doped UCNPs blue-shifts with decreasing thulium content (0.1%-2%) and increasing ytterbium content (2%-30%) [145]. This effect can be explained by the multi-photon nature of the process. The lower the thulium concentration, the more probable it is to populate the higher energy states because the same amount of energy is transferred to less ions for a given ytterbium concentration. Additionally,  $Tm^{3+}$  ions have been shown to exhibit effective cross-relaxation processes that depopulate the  $^3H_4$  level and therefore inhibiting the excitation into the  $^1G_4$  level. At the same time, red emission is increased.



**Figure 2.7:** Scheme of the relevant energy levels of rare-earth elements used in upconversion nanoparticles. The large coloured arrows indicate radiative relaxation of the visible emissions. Reprinted from ref. [144] with permission from Elsevier, Copyright 2005.

Upconversion nanoparticles have been promoted as potentially useful for biological imaging [25]. One reason is the excitation with NIR light, which penetrates biological tissue much deeper than visible light (biological window) [146].

Furthermore, fluorescence techniques are ubiquitous in bio-sciences so that upconversion nanoparticles are of interest for replacing other dyes. Advantages are their resistance against photobleaching and a large reduction of autofluorescence of biological species due to the NIR excitation [147]. Another potential application for upconversion nanoparticles is the gathering and conversion of infrared light in solar cells [148, 149].

In the next section a brief description of very recently developed lead halide perovskite nanoparticles will be given.

### 2.1.7 Lead halide perovskite nanoparticles

Lead halide perovskites with the chemical formula  $APbX_3$  ( $A = CH_3NH_3^+$ ,  $Cs^+$ ;  $X = Cl$ ,  $Br$ ,  $I$ ) have gained a lot of attraction in the field of photovoltaics in recent years [32]. While these materials have been known for several decades, it was not until 2009 when they have first been applied in solar cells. These materials led very rapidly to conversion efficiencies from 3.8% in 2009 to 20.1% in 2014, which is the fastest development in the field of photovoltaics to date [33]. The advantage of these perovskite materials is the possibility to manufacture relatively efficient solar cells at very low cost with very basic thin film technologies such as spin coating [150].

Films of lead halide perovskites are readily forming when a precursor solution is dried on a substrate. In a typical procedure, lead halide salts (e.g.  $PbBr_2$ ) and methylammonium halide salts (e.g.  $CH_3NH_3Br$ ) are dissolved in a polar organic solvent such as  $N,N'$ -dimethylformamide (DMF) and then cast on a substrate. Spin coating then spreads the solution over the whole substrate and heat is used to evaporate the solvent leading to the formation of perovskite films. This basic procedure was refined in the past and several other processing strategies were developed [151].

In 2009, Kojima *et al.* found perovskite nanoparticles for the first time after spin-coating a methyl ammonium lead bromide solution on  $TiO_2$  [152]. However, not much attention was given to the synthesis of colloidal perovskites until 2014 when the group of Pérez-Prieto presented a wet-chemical method for the first time [153]. Their approach relied on solvent engineering where precursors are dissolved in a good solvent (DMF) and rapidly injected into a bad solvent (toluene) containing long alkyl-chain ligands so that rapid crystallisation occurs, which is capped by the long

ligands. In this way, they were able to create colloidal solutions of  $\text{CH}_3\text{NH}_3\text{PbBr}_3$  particles with sizes of about 6 nm and bright fluorescence with FWHM of 20-25 nm. In a following paper, the same group reported PLQYs as high as 83% using capping molecules with different lengths [154]. Shortly after, Zhang *et al.* showed that this method can be used to synthesise colour-tunable mixed perovskites with emission wavelengths over the whole visible range [155]. At the same time, the group of Kovalenko prepared cubic  $\text{CsPbX}_3$  perovskite nanoparticles using oleates and the hot-injection method entirely based on organic solvents [156]. Besides using mixed halide precursors directly in the synthesis, Kovalenko *et al.* and Manna *et al.* reported independently that lead halide perovskite crystals can be post-synthetically altered via anion exchange [157, 158]. All the nanoparticles are only stable in organic solvents with moderate polarity because they dissolve in polar media. However, current research focusses on the encapsulation of the perovskite nanoparticles with a shell, which could allow them to be dispersed in aqueous media.

The crystal structure of the  $\text{APbX}_3$  unit cell is depicted in **Figure 2.8**. The lead anions are surrounded and connected with each other by six halide ions forming octahedral blocks. These octahedral blocks are aligned in a cubic arrangement creating a void, which is filled by a monovalent cation. Theoretical and experimental studies revealed that these materials have a direct band gap resulting in strong fluorescence [159]. The size of the band gap is mainly altered by the various halides resulting in band gaps of 1.5 eV and 2.3 eV for  $\text{CH}_3\text{NH}_3\text{PbI}_3$  and  $\text{CH}_3\text{NH}_3\text{PbBr}_3$ , respectively [160]. However, Filip *et al.* reported that the change of the band gap energy can also be induced geometrically with a steric distortion of the lattice due different sizes of the cations filling the voids [159]. Quantum size effects have been shown to be significant in the case of perovskite nanoparticles [156, 161]. Altogether, lead halide perovskite have become a promising alternative to semiconductor quantum dots due to their facile processability and optical properties [162].

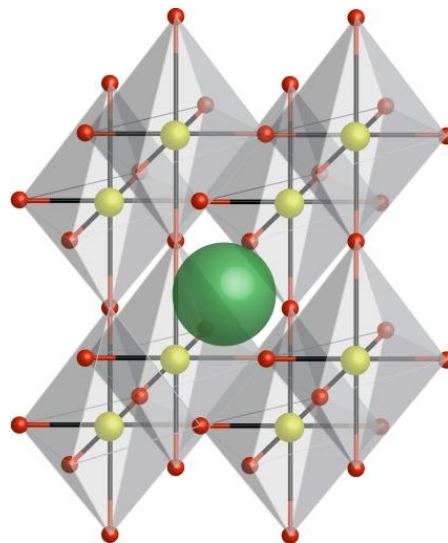


Figure 2.8: Visualisation of the  $\text{APbX}_3$  (A: monovalent cation, X: halide) perovskite crystal structure.

## 2.2 Functionalisation of nanoparticles

In the previous sections the synthesis of different types of nanoparticles was discussed. Independent from the synthesis method or the chemical composition of nanoparticles, surface ligands play a major role during and after nanoparticle formation. The functionalisation of nanoparticles is of utmost importance for almost every application because the ligands on the nanoparticle surface determine colloidal properties such as solubility, stability and targeted function [163]. Examples of different polar ligands used as coating for water-soluble nanoparticles are polyelectrolytes (e.g. polystyrene sulfonate, polyacrylic acid) or polyethylene glycol (PEG) derivatives. Aliphatic amines, aliphatic acids and certain non-ionic polymers (e.g. PVP) belong to the group of organic ligands. Surface ligands are grafted onto nanoparticles by different functional groups as shown in Figure 2.9 [163].

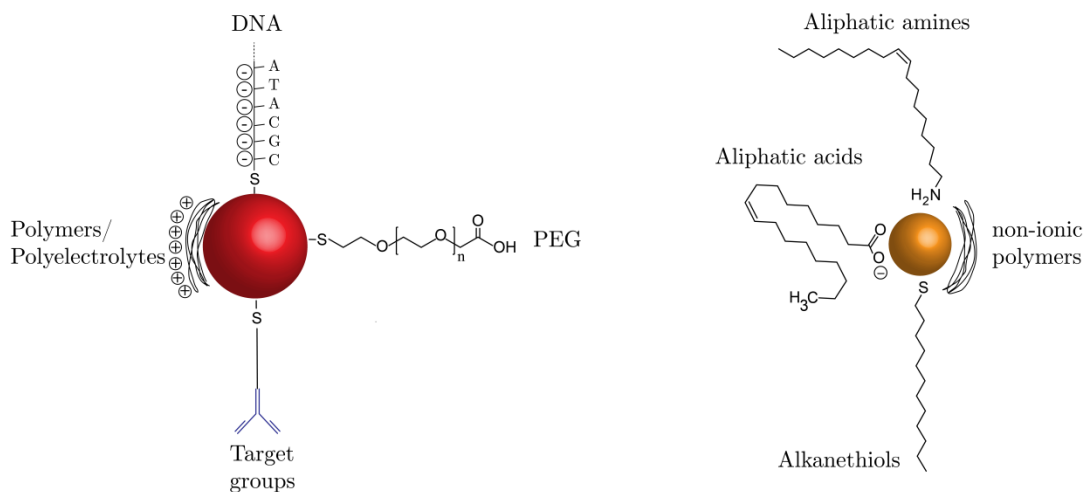


Figure 2.9: Functionalisation of nanoparticles by attachment of molecules such as PEG or DNA on the surface via functional groups.

A very important chemical group for the attachment of molecules to gold is the thiol (-SH) group. The affinity of thiols to gold surfaces is very high with binding energies close to Au-Au bonds [164]. Brust *et al.* used alkanethiols to synthesise small gold nanoparticles (2-4 nm) in organic media for the first time showing the strong interaction between thiols and gold in a colloidal system [64]. Later, the first DNA-AuNP assemblies were presented by Mirkin *et al.* and Alivisatos *et al.* using thiol-modified oligonucleotides [13, 14]. Even though thiol chemistry has been the most used routine for the functionalization of nanoparticles with (bio-)molecules for more than two decades, the nature of the interaction between thiols with gold surfaces was only recently determined [164].

Organophosphorus compounds ( $R_3P$ , R = organic derivative) have first been utilised by Schmid *et al.* to synthesise ultra-small gold nanoclusters with diameters of only 1.4 nm with the chemical formula  $Au_{55}(PPh_3)_{12}Cl_6$  [165]. Schmid and Alivisatos *et al.* established the water-soluble phosphine compound bis(*p*-sulfonatophenyl)phenyl phosphine (BSPP) as stabiliser for gold nanoparticles with diameters of 5-10 nm [166, 167]. This compound allowed them to highly concentrate the nanoparticles by centrifugation, which led to aggregation beforehand. In addition, this ligand can readily be replaced by thiol-containing molecules (see **section 2.3**).

Apart from thiols and phosphines, many other functional groups are used to graft molecules on the nanoparticle surface. Examples are amines (-NH<sub>2</sub>), carboxylic groups (-COOH) or phosphonates (R-PO(OH)<sub>2</sub>) [163]. The affinity of a certain functional group depends on nanoparticle composition. For instance, amines have

been used for silver surfaces and carboxylic acids are used to coat upconversion nanoparticles [68, 168].

The rich library of affine groups allows one to tailor molecules according to the task to be performed. For example, directed peptide linkage on gold nanoparticles can be achieved by including one cysteine, which is an amino acid containing a thiol moiety [169]. The specific peptide sequences on the nanoparticles may then stimulate a certain cell response in biological systems [170]. Another example is L-lipoic acid, which contains a thiol group to be linked to a nanoparticle and a terminal carboxyl group for performing further reactions (e.g. EDC coupling) [171].

Certain chemical groups have higher affinities towards nanoparticle surfaces than others. Generally, groups with a higher bond energy spontaneously displace previously attached molecules [172]. For example, citrate molecules coating gold nanoparticles are displaced by BSPP, which can further be exchanged with thiol groups (**Figure 2.10(1)**). Nevertheless, ligands bearing the same binding group can also be exchanged leading to mixed layers (**Figure 2.10(2)**).

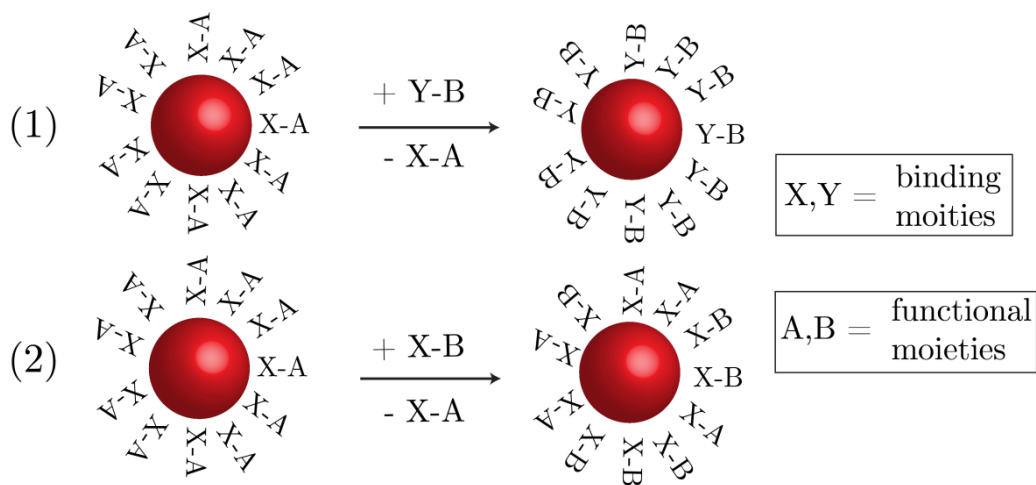


**Figure 2.10:** Post-functionalisation of nanoparticles via ligand exchange. (1) Complete ligand exchange by a binding group with higher affinity towards the surface and (2) partial exchange by molecules with the same binding group.

This method of post-functionalisation is the most popular and named ligand exchange. It is a convenient and efficient method to change the functionality of nanoparticles after synthesis. In particular, phase-transfers from the organic to the aqueous or vice versa can be achieved by ligand exchange [163, 173]. Examples are quantum dots post-functionalised with lipoic acid or upconversion nanoparticles

transferred from the organic to the aqueous phase with polyacrylic acid (PAA) (see chapter 4).

In order to maintain colloidal stability, it is necessary to consider the size and the charge of the molecules to be attached. If there is not enough charge and/or the ligand is not large enough, nanoparticles undergo irreversible aggregation and eventually precipitate. This aspect will be discussed in **section 2.3**.

## 2.3 Nanoparticle growth models and DLVO theory

### 2.3.1 LaMer model

The first conclusive model for nanoparticle nucleation and growth that was supported with a series of experiments was published by LaMer *et al.* in 1950 and is nowadays referred to as LaMer model [50]. In this work, sulfur hydrogels were prepared by titrating hydrochloric acid (HCl) into an aqueous solution containing sodium thiosulfate ( $\text{Na}_2\text{S}_2\text{O}_3$ ) producing elementary sulfur as  $\text{S}_2$ . Since sulfur has only a low solubility in water, at a certain concentration the solution becomes turbid indicating for formation of sulfur particles. A systematic approach of several conditions allowed the group to describe nanoparticle formation and growth according to the graph depicted in **Figure 2.11**.

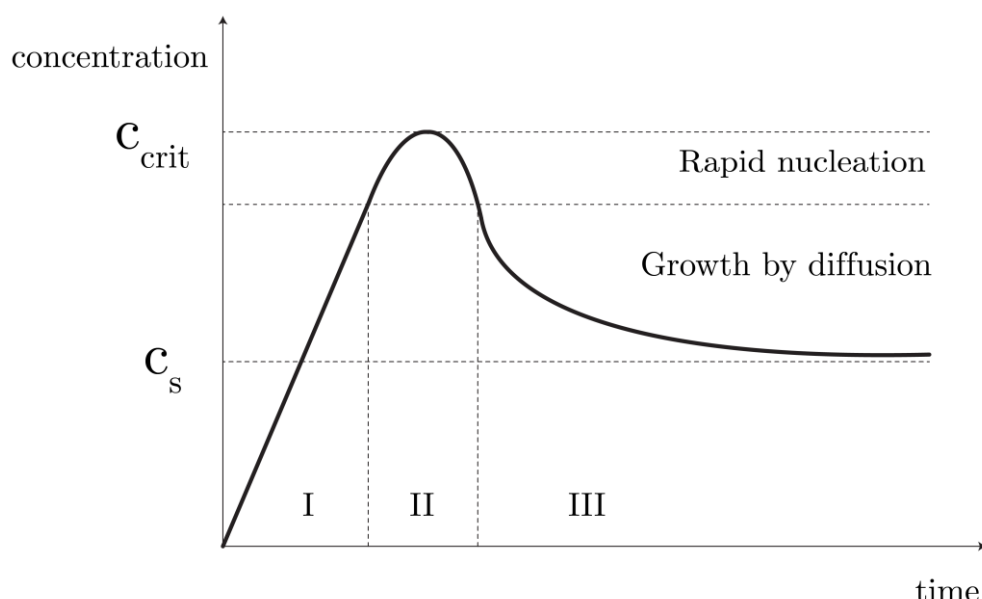


Figure 2.11: Illustration of the precursor concentration changing with time according to the LaMer model. At stage I, there is an increase in monomer concentration until a critical supersaturation  $c_{\text{crit}}$  is reached. At this point rapid nucleation occurs, which relieves the saturation (stage II). In stage III, the nuclei grow by a diffusion-limited process until the saturation concentration  $c_s$  is reached. Adapted from ref. [50].

The graph describes the change of the concentration of elementary sulfur in the solution with time. In the beginning, the concentration linearly increases with successive addition of hydrochloride acid into the precursor solution. The concentration rises even after reaching the saturation concentration,  $c_s$ , of sulfur leading to supersaturation (Stage I). Once a critical concentration  $c_{crit}$  is reached, the sulfur starts nucleating. The degree of supersaturation decreases rapidly so that the nucleation can be considered as a single event in time (nucleation, stage II). After nucleation, the nuclei grow by diffusion-limited addition of free sulfur from the solution onto the nuclei (growth, stage III).

The authors discussed that controlling the initial concentrations of the precursors is very important for the synthesis of monodisperse colloids. If the concentration is too high, several nucleation events can be induced by exceeding the critical concentration more than once when further reducing agent is added. In addition to the qualitative description of the nucleation, a mathematical model for the growth was developed. The thorough investigation of LaMer *et al.* allowed researchers to systematically tune the appropriate reaction conditions for the synthesis of different types of colloids [174].

### 2.3.2 Size-focussing and broadening regime

The findings from LaMer *et al.* are related to the free enthalpy and the surface tension of clusters in solutions [175]. For a cluster consisting of  $n$  atoms the change of the total free energy is given by

$$\Delta G = n \cdot (\mu_c - \mu_s) + 4\pi r^2 \sigma.$$

Equation 2.5: The change in the free energy  $G$  for  $n$  atoms forming a cluster in solution.

The chemical potentials  $\mu_c$  of the crystalline phase and  $\mu_s$  of the solution phase determine if a phase transition is favourable. In order for nanoparticle formation to occur, the  $\mu_c$  must be smaller than  $\mu_s$ . The first term plays the main role in bulk crystals but the second term with the surface tension  $\sigma$  is not negligible for nano-sized particles due to the high surface-to-volume ratio. For spherical particles with density  $\rho$  and molar mass  $M$ , the equation for the free energy becomes

$$\Delta G = \frac{\rho \cdot N_A}{M} \frac{4\pi}{3} r^3 (\mu_c - \mu_s) + 4\pi r^2 \sigma.$$

Equation 2.6: The change in the free energy  $G$  considering spherical particles.

From this equation a critical radius  $r_c$  can be calculated, which determines the minimal radius for stable nuclei. At this radius, the volume term overcomes the surface term and the total free enthalpy becomes negative meaning that nuclei dissociation becomes non-spontaneous. The change of the free energy depending on the radius for a spherical particle according to equation 2.6 is shown in Figure 2.12.

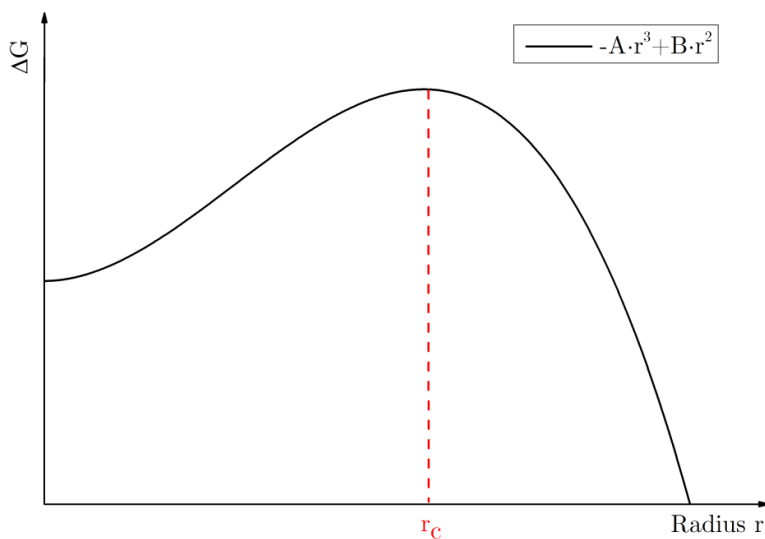


Figure 2.12: The change of the free energy depending on the radius of nanoparticles formed from monomers in solution according to equation 2.6. The surface tension imposes an energy barrier, which is overcome once the particle reaches the critical radius  $r_c$  and spontaneous growth commences.

After nucleation there are two stages of growth, the size-focussing regime and the broadening regime [174]. The former regime appears typically at the beginning of the reaction after the nucleation step. In this case, a vast excess of monomers is present in solution so that on any free site of a nanocrystal further monomers will attach. Importantly, the relative width  $\Delta r/\bar{r}$  of the size distribution decreases with time, i.e. smaller crystals reach the mean radius of the ensemble quicker than the larger nanocrystals grow bigger. However, once the pool of monomers starts depleting the critical radius changes to larger radii and small clusters may dissolve again completely. This phenomenon called Ostwald ripening has been described by Wilhelm Ostwald in 1900 and can be explained with the Gibbs-Thompson effect, which states that smaller droplets have a higher vapour pressure than larger ones due to higher curvature [174, 176]. When this stage is reached, size broadening

occurs because the dissolving smaller particles are incorporated into the larger nanoparticles. Therefore, the nucleation stage should be well separated from the growth stage for monodisperse nanoparticles in order to avoid the size broadening regime [62].

### 2.3.3 DLVO model

In this section the factors influencing the colloidal stability of a solution will be discussed. The colloidal stability of a nanoparticle solution is determined by mainly two forces as depicted in **Figure 2.13**. The DLVO model, named after Derjaguin, Landau, Verwey and Overbeek, explains the aggregation behaviour of a colloidal solution based on these two forces [177].

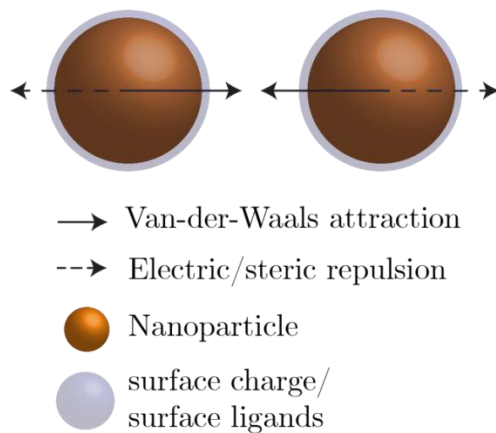


**Figure 2.13:** The interaction between two particles in solution. Attractive Van-der-Waals forces and repulsive electrostatic forces determine the colloidal stability according to the DLVO theory.

On the one hand, there are repulsive electrostatic forces from charged molecules adsorbed on the nanoparticle surface. Since counter-ions are attracted to the surface, an electrical double layer is forming. Depending on the ionic species and the concentration of the electrolytes, a certain ion-concentration profile from the surface into the solution is created governing the electrostatic interaction between particles. The electrical double layer consists of a layer with tightly bound ions (Stern layer) and layer with less strongly attached ions (diffuse layer).

On the other hand, there are attractive Van-der-Waals forces between nanoparticles. Van-der-Waals forces stem from spontaneous fluctuations in charge density of a molecule, which in turn polarise surrounding molecules. This leads to an electrostatic interaction between the molecules where the dielectric properties determine the strength and direction of the resulting force. The Hamaker constant,

derived from the analytical work of Hamaker, is a measure for the strength of the interaction [178]. While the Van-der-Waals interaction is attractive in most cases (in particular between the same materials), repulsive forces can also occur [179].

The interaction energies from Van-der-Waals and double layer interaction for two equal spheres can be expressed as [179, 180]:

$$W(D) = -\frac{A}{12D} \text{ (Van-der-Waals interaction)}$$

$$W(D) = \frac{Q^2}{4\pi\epsilon_0\epsilon(1+\kappa r)^2} \cdot \frac{e^{-\kappa(D-2r)}}{D} \text{ (Double layer interaction)}$$

**Equation 2.7: Attractive Van-der-Waals interaction (top) and repulsive double layer interaction (bottom) between two spheres in solution resulting from DLVO theory.**

$A$  denotes the Hamaker constant,  $R$  the radius of the spheres,  $\kappa$  the Debye screening length,  $Q$  the total charge of each sphere and  $D$  the distance between the two spheres. It should be noted that the Van-der-Waals interaction in Equation 2.7 is a limiting case ( $D \ll R_1, R_2$ ) resulting from the more general Hamaker formalism [180].

**Figure 2.14** depicts the attraction and repulsion as well as the net energy depending on distance between two spheres according to above equations. It can be seen that the double layer contribution is dominant except for very small distances where the Van-der-Waals term overcomes the other term. An energy barrier is therefore created by repulsive electrostatic forces that need to be overcome by the colloids in order to aggregate [181]. Larger particles sizes and less surface charge as well as larger amounts of counter ions present in solution lower the energy barrier. It is possible that under certain conditions a local minimum in the net energy occurs, which typically corresponds to reversible agglomeration or flocculation of the nanoparticles. In particular, steric effects from ligands are responsible for such a behaviour and will be discussed below.

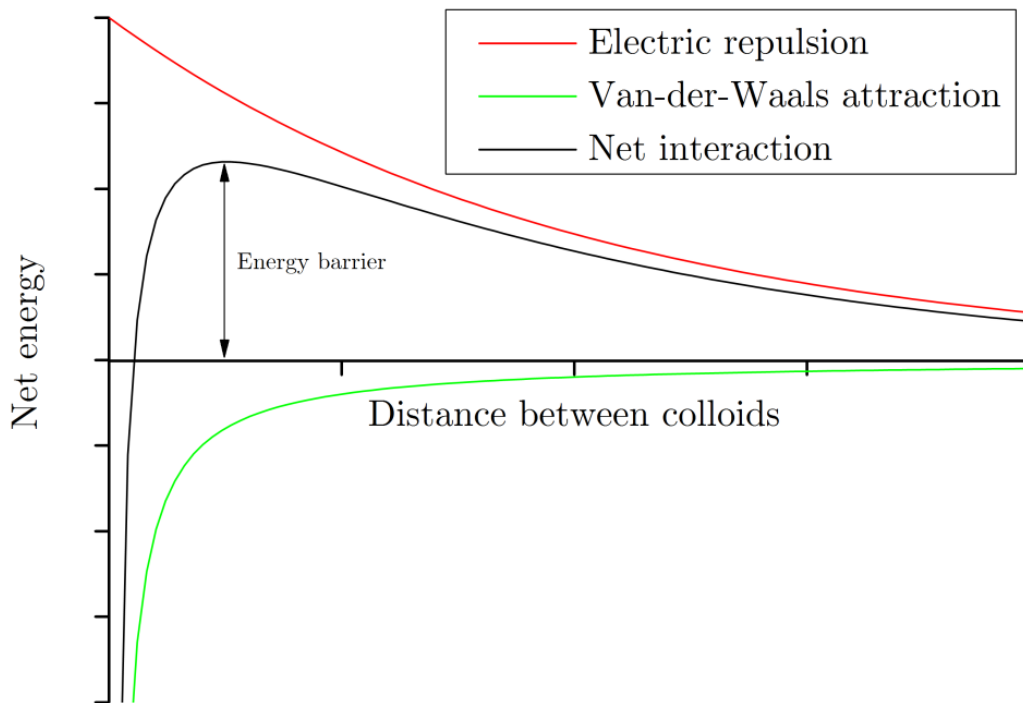


Figure 2.14: The interaction between Van-der-Waals attraction and electric repulsion as described by the DLVO theory for two spheres. An energy barrier is imposed by the electric force.

A measure for the surface charge and therefore the energy barrier is the  $\zeta$ -potential (zeta potential), which gives an indication about the stability of a colloidal system [182]. It is defined as the electric potential at so-called slipping plane, which is located in the diffuse layer. It marks the boundary between which ions are following a moving particle or not. Therefore, the  $\zeta$ -potential is not the surface potential of the particle. It is experimentally determined by applying an electric field and measuring the velocity, which is then correlated with the nanoparticle charge.  $\zeta$ -potential values of at least  $\pm 25$  mV are accepted threshold values for long term colloidal stability. Lower values indicate that colloids might aggregate over time. However, the actual behaviour of the colloidal system varies depending on multiple parameters such as particle size, solvent and temperature. Furthermore, the pH can strongly influence the  $\zeta$ -potential as adsorbed molecules might protonate or de-protonate and therefore change the surface potential of the particle. All these variables make it very important to choose appropriate ligands for nanoparticle functionalisation without impeding the colloidal stability of the system [183].

One important factor, which is not included in the DLVO theory, is steric stabilisation [184, 185]. Bulky ligands on the surface have an additional effect on a colloidal

solution. Steric hindrance can prevent nanoparticles to irreversibly aggregate if the shell does not allow the nanoparticles surfaces to touch each other. There are several different interactions that belong to the group of steric interactions [179]. First, there is the so-called osmotic interaction. It describes the exclusion of solvent molecules in between nanoparticles when they are in close proximity. This creates a region of high pressure towards the gap of nanoparticles, which can effectively be described as an additional repulsive term. Secondly, related to the osmotic interaction, there is the solvophobic or hydrophobic interaction if a bad solvent is added to a nanoparticle dispersion. This can lead an attraction between nanoparticles because the interaction between similar ligands and solvents is energetically favourable. Lastly, there is a repulsive elastic interaction stemming from the loss of configurational entropy when ligands on the nanoparticles are at very close proximity.

Therefore, even uncharged molecules such as non-ionic polymers can be used for nanoparticle capping without colloidal destabilisation [186]. In this case, reversible agglomeration may occur where Van-der-Waals forces bring particles into close proximity but due to steric hindrance, the nanoparticles do not aggregate irreversibly as discussed earlier. This behaviour is very important for processes that involve nanoparticles powders or the formation of nanoparticle clusters [183]. An example is semiconductor quantum dot powder, which can be obtained by evaporating the solvent of the dispersion. Long alkane chains are creating a steric barrier so that the nanoparticles do not aggregate. This allows to re-disperse the particles in an appropriate solvent. Examples for ligands exhibiting additional steric hindrance are dodecanethiol in organic solvents or polyvinylpyrrolidone (PVP) and polyethylene glycol (PEG) in aqueous solvents [187, 188].

## 2.4 DNA as a tool in nanotechnology

This section will give an introduction to DNA as a molecule and its use for programmed assembly of nanoparticles in ordered structures.

### 2.4.1 Structure and properties of DNA

Desoxyribonucleic acid (DNA) is a remarkable molecule encoding biological information in living organisms [189]. It consists of two major components, the phosphate-deoxyribose backbone and the information encoding nucleobases (see **Figure 2.15**). The backbone carries one negative charge per phosphate group

basically over the whole pH range due to a  $pK_a$  value of only about 2. Single stranded DNA (ssDNA) consists of arbitrary sequences of the four nucleobases adenine (A), cytosine (C), guanine (G) and thymine (T). As discovered by Crick and Watson in the 1950s, two complementary DNA strands form a pair because the four nucleobases couple by forming hydrogen bonds between A and T and C and G [190]. The double-stranded DNA (dsDNA) has a helical conformation as depicted in **Figure 2.15**. It should be noted that the bonding is directional, i.e. two single-stranded DNAs (ssDNA) need to be in reversed order. DNA sequences are synthesised from the 5'-end to the 3'-end and therefore the sequence 5'-ATCG-3' is complementary to the sequence 5'-CGAT-3'.

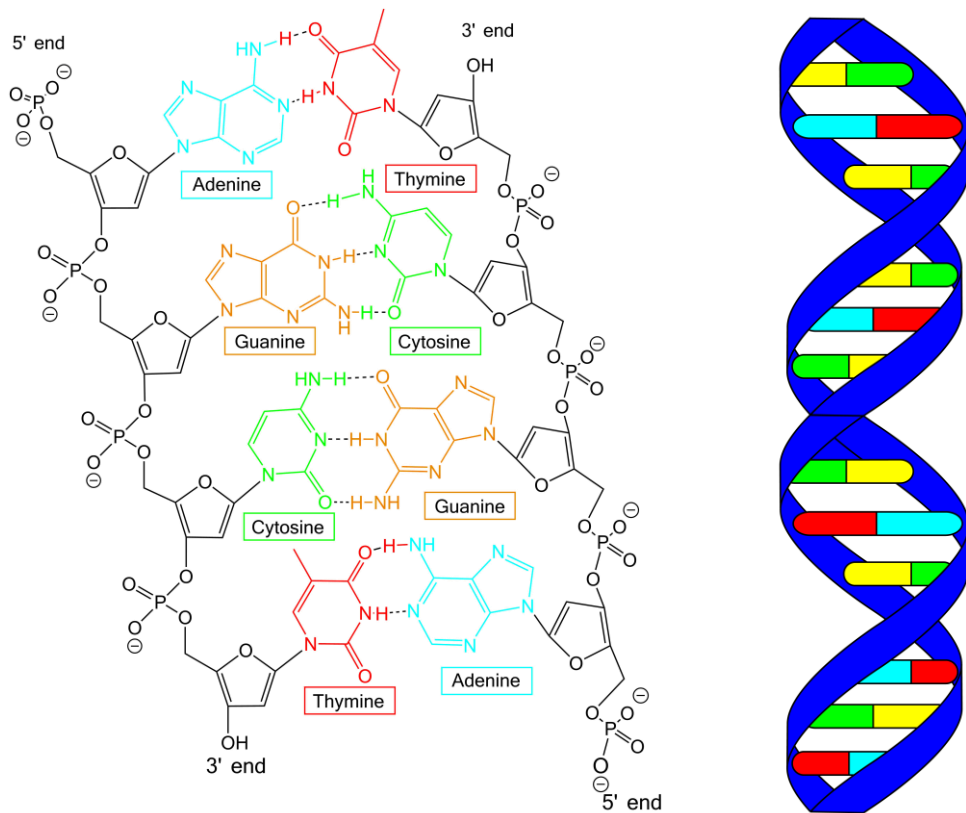


**Figure 2.15:** Structure of double stranded DNA. The specific complementarity of the two base pairs adenine-thymine and guanine-cytosine leads to hybridisation with a double helical conformation.

The forces present in dsDNA are: a) attractive hydrogen bonding and  $\pi$ -stacking between the nucleobases and b) electrostatic repulsion from the negatively charged backbone [191]. The  $\pi$ -stacking interactions results from the hydrophobic effect and London dispersion forces [192]. The former considers that non-polar molecules break hydrogen bonding in the polar solvent (water). The formation of bonds

between the bases and the folding into an ordered structure results in exclusion of water from non-polar parts of the helix and an overall favourable change in the free energy is achieved [193]. The latter force arises from instantaneous induced dipoles due to electron density fluctuations between two or more molecules and becomes stronger with increasing polarizability of the electron cloud. In the case of DNA, the interaction between the delocalised  $\pi$ -electron clouds of the nucleobases make stacking favourable [191]. Even though hydrogen bonding and stacking forces are weak, they become significant in larger numbers, e.g. in long oligonucleotides. In 2006, Yakovchuk *et al.* reported that base stacking is responsible for the stability of dsDNA rather than hydrogen bonding, which was found to have a destabilising effect [194]. This behaviour has been verified using artificial DNA analogues [195].

Because of the electrostatic repulsion, DNA hybridisation is sensitive to the ionic strength, the temperature and the pH of the solution [196]. A certain amount of cations is needed to screen the negatively charged phosphate groups and allow the DNA strands to overcome the electrostatic barrier. Larger amounts of cations and especially multivalent cations greatly enhance the stability of dsDNA. The temperature is crucial due to the relatively weak non-covalent bonds holding the DNA together. Heating will break the bonds between the nucleobases and cause dehybridisation to single stranded DNA. The pH is affecting the stability of dsDNA negatively at acidic ( $\text{pH} < 5$ ) or basic ( $\text{pH} > 10$ ) pH values due to protonation or deprotonation of the oligonucleotide bases.

An important measure for practical purposes is the melting temperature  $T_m$  of dsDNA which is defined as the temperature at which 50% of the dsDNA are dehybridised. This value can be determined experimentally by performing so-called melting curves [197]. In this method, an oligonucleotide solution is slowly heated and cooled while measuring the UV absorption of the DNA. The aromatic purine and pyrimidine rings in the DNA bases absorb UV light with a maximum around 260 nm (**Figure 2.16**). The melting curve analysis relies on the hyperchromic effect of DNA, which is responsible for a significant decrease of the extinction coefficient of about 37% when two strands are hybridised. The effect can be explained with the stacking interactions between the nucleobases, which reduces the resonance of the aromatic rings leading to decrease absorption [198]. A typical sigmoidal melting curve profile of complementary oligonucleotides is shown in **Figure 2.17**. The shape can be

explained with the collaborative effects of the hybridisation process, i.e. already formed base pairs influence hybridisation of neighbouring bases [199]. The melting temperature  $T_m$  is determined at the point of inflection of the curve. Melting temperatures can also be calculated theoretically with different models. The most common model is the nearest neighbour method where the enthalpy for the formation of a base pair as well as stacking effects of neighbouring bases are taken into consideration yielding very useful approximations of the melting temperature [200]. There are publicly available online platforms, which implement different theoretical models for the calculation of the melting temperature, e.g. Oligocalc [201].

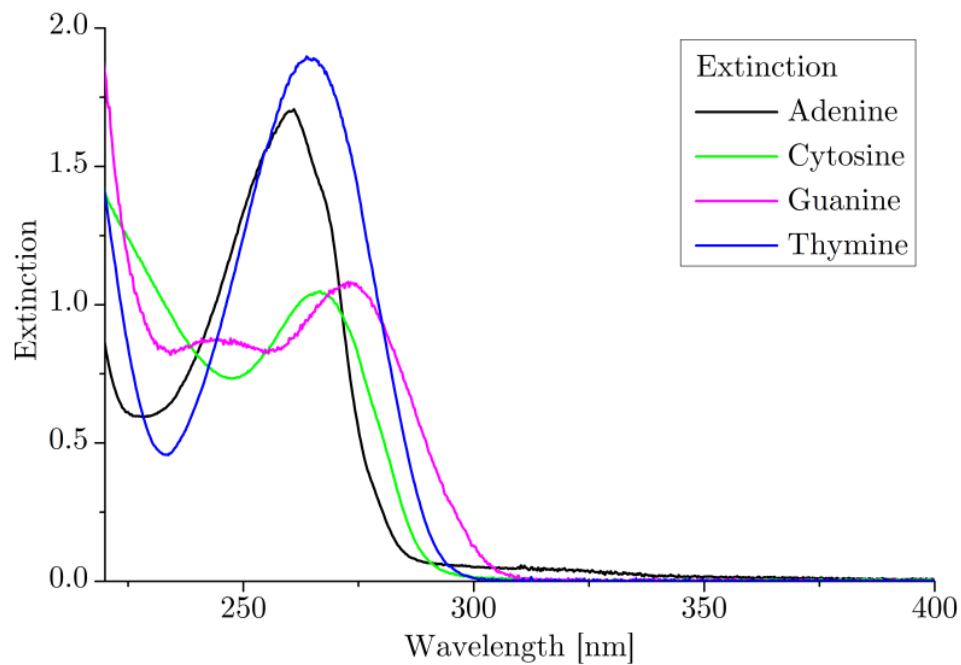


Figure 2.16: Extinction spectra of the four DNA nucleobases [202].

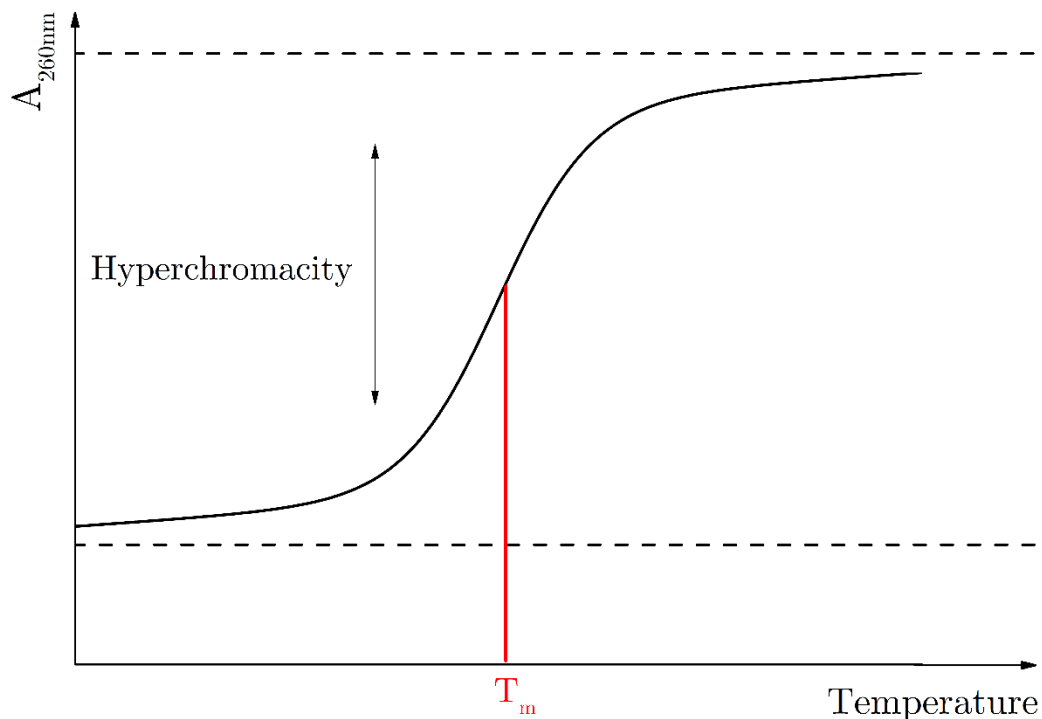


Figure 2.17: Illustration of the absorption at 260 nm during DNA melting experiments. An increase of the absorption indicates the dehybridisation of dsDNA due to the hyperchromic effect. The melting temperature is defined at the point of inflection of the sigmoidal curve.

Double stranded DNA is susceptible to intercalation by molecules with planar aromatic rings [203]. These molecules are called intercalators. Energetically, intercalating molecules usually stabilise the double helix by additional  $\pi$ -stacking interactions. Intercalators are interesting because they can be used to detect dsDNA (e.g. SYBR green I or ethidium bromide), used for sensing applications such as SERS (e.g. acridine orange) or applied for DNA crosslinking (e.g. 5-methoxypsoralen) [203-205].

#### 2.4.2 DNA crosslinking

As described earlier, two hybridised DNA strands that form dsDNA are not coupled permanently but can dehybridise readily under certain conditions. Especially when nanoparticles are involved, the ionic strength needs to be carefully tuned in order to avoid nanoparticle aggregation ([section 2.3.3](#)).

In order to overcome this problem, crosslinking techniques have been developed. This means that covalent interstrand bonds are created, which permanently connect

dsDNA even in low ionic strength media or at elevated temperatures. There are different ways to crosslink DNA, which involve either external molecules (intercalators) or internal modifications of the oligonucleotide sequences. Some examples will be discussed in the following.

Firstly, enzymatically driven reactions have been reported. For instance, the group of Schuster used oligonucleotides functionalised with 2,5-bis(2-thienyl)pyrrole (SNS) molecules, which act as monomers for a polymerisation reaction [206]. This reaction is started by combining horseradish peroxidase and hydrogen peroxide ( $H_2O_2$ ) (Figure 2.18) with the SNS-modified DNA. The group applied this method for the assembly of gold nanoparticles in various structures by careful design of the oligonucleotides [207]. However, a drawback of enzymatic reactions is their sensitivity to the environmental conditions (pH, temperature, ions), which often prevent *in situ* cross-linking with nanoparticles.

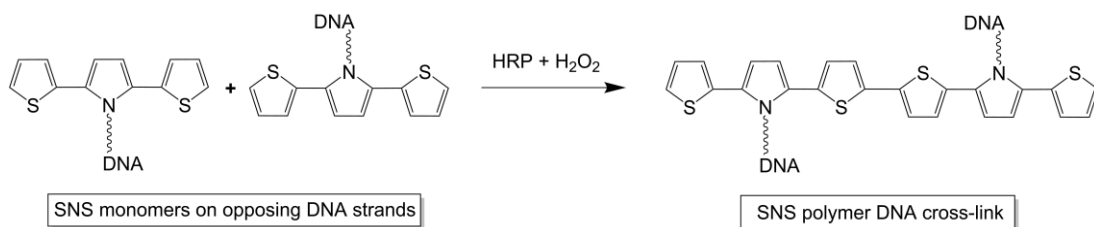


Figure 2.18: Scheme of the structure of SNS monomers and the polymerisation reaction yielding crosslinked DNA strands by enzymatic ligation.

Secondly, intercalating molecules like 5-Methoxysoralen have been used to crosslink DNA (Figure 2.19) [208, 209]. This molecule in particular has specificity towards 3'-AT-5' combinations requiring careful design of the DNA. Furthermore, a crosslink can only be facilitated if there are two opposite thymine bases between the psoralen. Once intercalated, a [2+2]-photocycloaddition between the double bond of the thymine and the intercalator can occur under irradiation with UV-A light ( $\sim 365$  nm) as shown in Figure 2.19. However, low crosslinking reaction yields of only around 20% for psoralen derivatives was reported by Smith *et al.* [208].

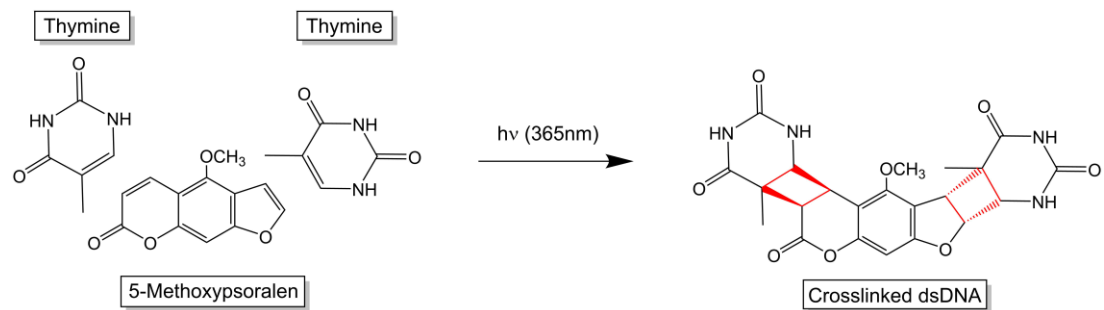


Figure 2.19: Structure of 5-Methoxysoralen and its UV-mediated reaction with thymine bases.

Thirdly, a similar approach utilising UV irradiation was followed in this work but rather than using intercalators, oligonucleotides were modified directly with 3-cyanovinyl carbazole (Figure 2.20). This molecule was developed by Yoshimura *et al.* as efficient light-induced crosslinker for DNA [24]. The reaction is identical to that of the psoralen derivatives where the molecule forms a covalent bond with an opposite thymine base. However, quantitative crosslink formation in a few seconds was reported with 3-cyanovinyl carbazole. Another novel feature is the possibility to efficiently de-crosslink the dsDNA by irradiation with UV-B light ( $\sim 312$  nm). The group showed that the reverse reaction is completed after 60 seconds of UV irradiation. In a more recent modification of the carbazole molecule the efficiency was increased so that the de-crosslink reaction also could be performed in few seconds [210]. The reaction [2+2]-photocycloaddition is depicted in Figure 2.21. The highly energetic UV light excites an electron from the highest occupied molecular orbital (HOMO) to the lowest unoccupied molecular orbital (LUMO), which is then able to form a new bond with the double bond of the cyanovinyl group. This happens through the formation of an exciplex and a diradical intermediate between the excited thymine and the alkene. The intermediates are in a triplet state so that the spin inversion to the singlet state needs to occur before the cyclobutane is finally produced [211]. It should be noted that several different stereoisomers are produced [212, 213]. The reaction can be reversed with light of higher energy (UV-B).

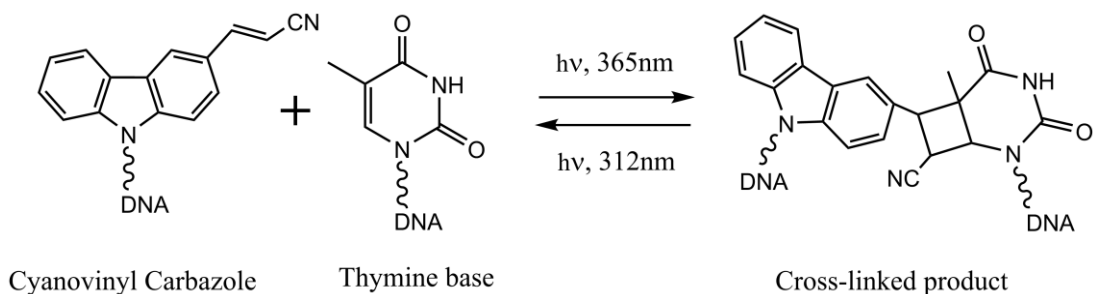


Figure 2.20: Reaction of 3-cyanovinyl carbazole with a thymine base under UV-A irradiation forming a cyclobutane bridge via a [2+2]-photocycloaddition.

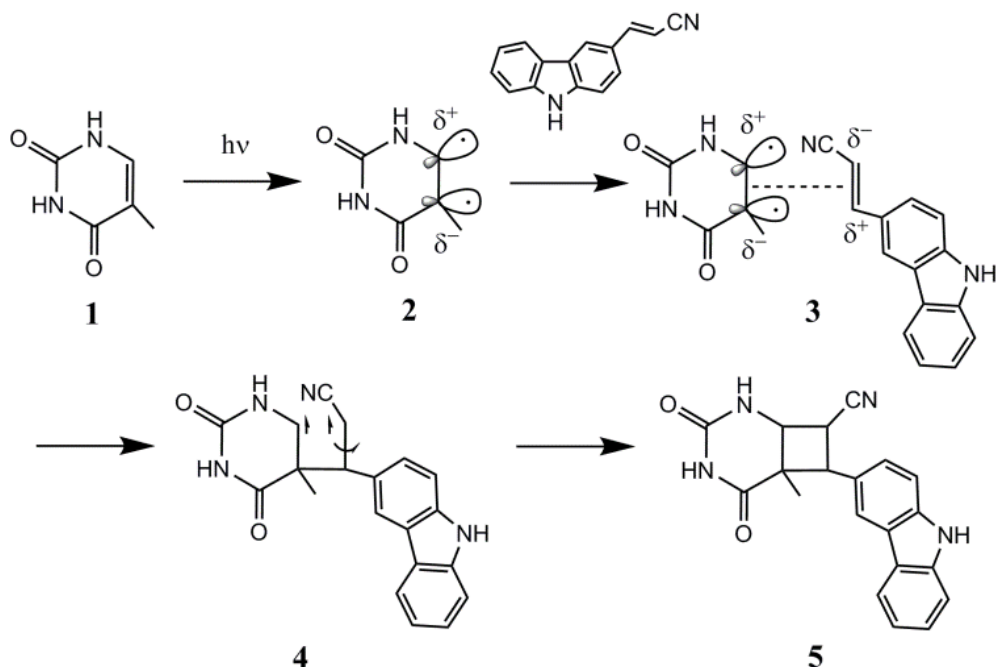


Figure 2.21: Reaction mechanism of the [2+2]-photocycloaddition between thymine and 3-cyanovinyl carbazole.

Lastly, the well-known azide-alkyne click (AAC) reaction is nowadays an established tool for DNA crosslinking [23]. In 2001, the click chemistry paradigm was described by Sharpless, Kolb and Finn for the first time [214]. They defined classes of reactions with several properties such as modularity, which allows building molecules similarly to DNA or proteins. The AAC reaction belongs to the class of [3+2]-cycloadditions and in particular to the Huisgen 1,3-dipolar cycloaddition, which was independently discovered as a model click reaction by Sharpless *et al.* and Meldal *et al.* in 2002 [215, 216]. In their work, they found that using Cu(I) as a catalyst leads to selective formation of a triazole from azide and alkyne moieties. Therefore, specific covalent linkage between two molecules bearing the respective functional groups can readily be facilitated. Since then, the copper-catalysed AAC (CuAAC) was further explored

and has been extensively used for the functionalization of molecules and nanoparticles in the recent past [217]. Several years later, a copper-free variation termed strain-promoted AAC (SPAAC) was developed by Bertozzi *et al.* in 2004 based on work conducted by Wittig and Krebs in the 1960s [218, 219]. The SPAAC relies on strained alkynes like cyclooctynes, which become by far more reactive due to the energetically unfavoured bond deformation [220]. In the recent years, several cyclooctyne derivatives such as dibenzocyclooctyne (DIBO) and bicyclo[6.1.0]nonyn (BCN) were developed [221, 222]. The reaction between BCN and an azide is shown in **Figure 2.22**. The strain-promoted coupling is not limited to alkynes and azides but has also successfully been performed with alkynes and nitrones (SPANC) making the reaction even more versatile [223].

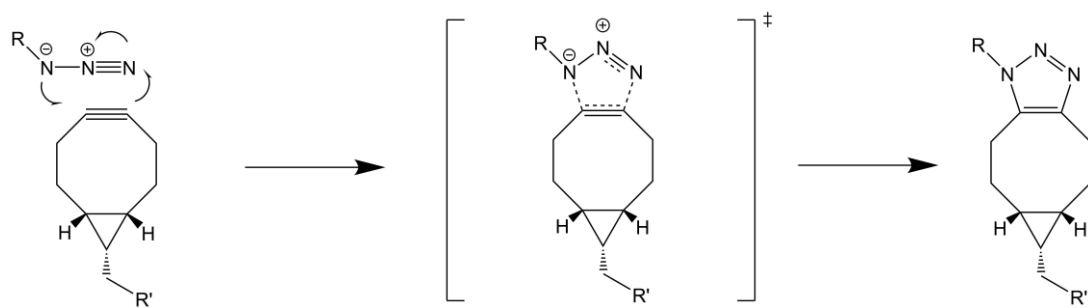


Figure 2.22: Reaction mechanism for the strain-promoted 1,3-dipolar cycloaddition between BCN and an azide.

Both the CuAAC and the SPAAC reactions have their advantages and disadvantages. The main disadvantage of the former reaction is the need for Cu(I) as a catalyst, which is readily oxidised to Cu(II) [224]. For this reason, the copper precursor is typically prepared *in situ* with reducing agents such as sodium ascorbate. The stability of Cu(I) can further be increased by utilisation of complexation ligands. Additionally, the amount of copper needs to be chosen carefully when oligonucleotides are involved because it can induce DNA degradation [225]. Another disadvantage is the toxicity of reactive oxygen species towards life cells created during copper reduction [226]. These disadvantages led to the development of the SPAAC reaction [227].

In this work, the SPAAC between BCN and azide containing oligonucleotides as well as light-induced coupling of 3-cyanovinylcarbazole were investigated in conjunction with gold nanoparticles to form stable and programmable nanoparticle assemblies (**Chapter 5**). These will be described in the next section.

## 2.5 Self-assembly of nanoparticles

Self-assembly of different materials has been of interest for a long time [228]. The concept of self-assembly is that single entities called building blocks arrange themselves in larger, ordered structures spontaneously. Even before colloid chemistry has become popular, the directed assembly of molecules in solution and on surfaces has been explored [229, 230]. One famous example is the formation of self-assembled monolayers (SAMs) of aliphatic molecules on gold surfaces [231, 232]. The importance of these assemblies is that chemical and physical properties like wettability, adhesion or biocompatibility can be altered to an unprecedented degree because of the molecular nature of the functionalization. For instance, artificial superhydroobic surfaces mimicking the lotus leaf have been produced by changing the surface at the nanoscale [233]. Even more interestingly, surfaces that can be switched reversibly by an external stimulus from superhydrophobic to superhydrophilic have been presented in the recent past [234]. Such examples clearly show how novel properties can be derived from self-assembly [235].

As the science of colloidal systems became more elaborated and reliable protocols for the synthesis of nanoparticles were developed, the concepts of self-assembly have quickly been adopted for these systems. **Figure 2.23** shows various parameters with which self-assembly of nanoparticles can be achieved [8].

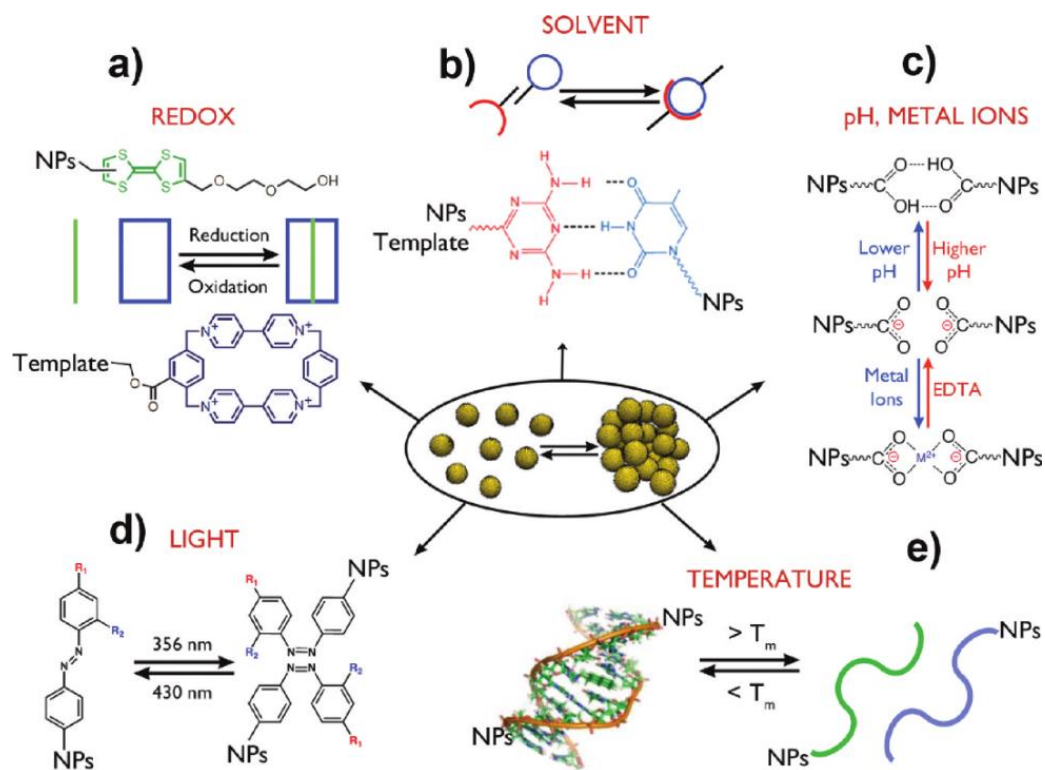


Figure 2.23: An overview about different parameters that can be used to trigger self-assembly of molecules and nanoparticles in ordered structures. Reprinted with permission from ref. [8]. Copyright 2010, American Chemical Society.

As described in the previous section, the properties of DNA make it a perfect tool for the directed assembly of nano-sized building blocks into larger discrete crystals [17]. A pioneer and inventor of the field of DNA nanotechnology was Seeman who predicted and realised three-dimensional nanoscale objects by carefully designed DNA strands [15, 236]. Several years later, Mirkin and Alivisatos showed that DNA can be used to organise gold nanoparticles in larger structures [13, 14]. In their work, Mirkin and co-workers modified gold nanoparticles with a dense shell of oligonucleotides and showed that two batches of nanoparticles with complementary DNA are reversibly forming aggregates depending on the temperature. A different route was pursued by Alivisatos and co-workers who used nanoparticles with few oligonucleotides and with different complementarities to achieve a directed, templated organisation of nanoparticles via a third oligonucleotide.

Mirkin's approach was initially used for simple aggregation of a large number of nanoparticles in order to study physical and chemical properties such as influence on the melting temperature by the nanoparticles [237, 238]. In recent years, this technique has proven to be extremely useful for the formation of superlattices [239]. By careful design, large artificial crystals with lattice structures like body-centered

cubic (bcc) or face-centered cubic (fcc) were synthesised via self-assembly [240, 241]. Superlattices are interesting for a basic understanding of self-assembly and could provide a platform for materials with new properties that are even not found in nature, e.g. metamaterials [242, 243]. Recently, a gold nanoparticle superlattice has been shown to act as a photonic crystal for the first time [244].

On the other hand, Alivisatos' approach is closer to the ideas of Seeman. DNA sequences, which fold into pre-defined objects are the driving force for the assembly of discrete structures [245]. Furthermore, the group discovered that gel electrophoresis is a suitable tool for the purification and separation of nanoparticles functionalised with different numbers of DNA [246, 247]. This allows extraction of the desired building blocks for the controlled construction of complex objects and motifs [248]. Gel electrophoresis can also be applied another time to purify the assemblies from unreacted and unwanted species with high effectivity [249, 250].

Novel properties of plasmonic assemblies originate from plasmon coupling, which can be compared to the hybridisation of orbitals in molecules [251, 252]. If two plasmonic nanoparticles are in close proximity the plasmon resonance splits into four different modes, which can be assigned to bonding and anti-bonding levels (**Figure 2.24**) [253, 254]. As a result, a shift in absorption and scattering is observed. In addition, large enhancements of the electric field in between the nanoparticles as a result of plasmon coupling are possible. An example is the so-called plasmon ruler, which relies on the sensitivity of the LSPR to the distance of the nanoparticles [255, 256]. They have been applied in living cells to monitor biological processes as an alternative to dye-based energy transfer sensors with superior photostability and brightness [257]. Theoretical calculations suggested that chiral plasmonic structures show circular dichroism at the plasmon resonance, i.e. left- and right-circular polarised light is absorbed in different amounts [12, 258]. This optical activity was found in tetrahedral structures with four different nanoparticle sizes and compositions as well as in helical arrangements showing that new optical properties can be imposed by controlled self-assembly [259, 260]. Another application, which utilises the plasmonic enhancement of the electric field is surface enhance Raman spectroscopy (SERS) [261] (see **section 5.3**).

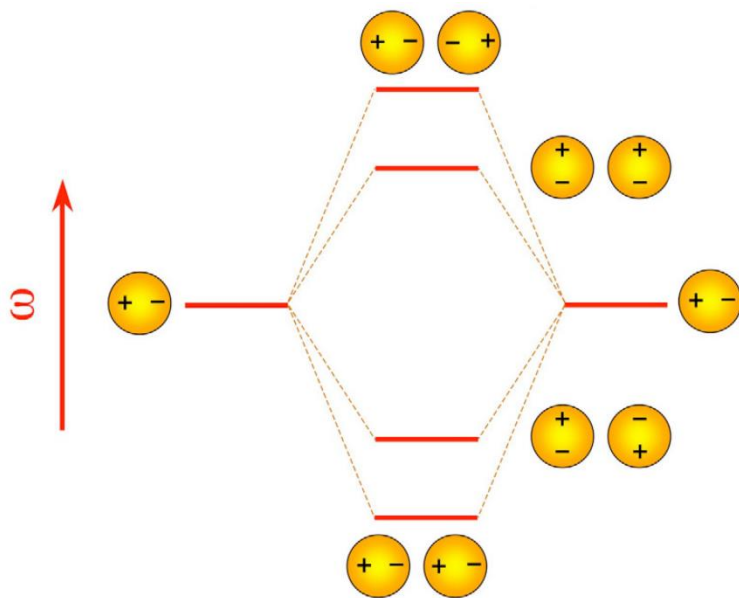


Figure 2.24: Energy splitting due to plasmon coupling of two spherical nanoparticles. Re-printed with permission from ref. [253], Copyright 2013, Elsevier.

Due to the success of the DNA self-assembly of nanoparticles, a new paradigm was presented recently introducing a “new periodic” table where nanoparticles of different shape, size and composition are considered as the atomic entities analogous to the periodic table of the elements [262] (**Figure 2.25 (left)**). DNA plays the role of the electrons that connect the single atoms by bonding so that artificial molecules are formed (**Figure 2.25 (right)**). In conjunction with a set of DNA design rules for the self-assembly, a systematic investigation of novel materials is facilitated and may help to predict properties of certain nanoparticle combinations in the future [239].

Altogether, there has been a tremendous development in the field of self-assembling nanostructures in the last decade, which led to interesting and promising new materials. In this work, DNA-directed assembly of plasmonic and fluorescent nanoparticles is investigated and a novel tool for the reversible cross-linking with 3-cyanovinyl carbazole is presented. Different from other pathways shown in **Figure 2.23**, the utilisation of DNA provides an unprecedented degree of specificity. The arbitrary combination of the four nucleobases can be used to create very complex designs, which is successfully implemented in so-called DNA origamis [263]. Therefore, DNA is still one of the most promising ways for the self-assembly of discrete building blocks into well-defined structures. However, as discussed earlier, the hybridisation process is not as robust as other interactions like electrostatic or solvent-mediated assembly [264]. On the one hand, the DNA is prone to

dehybridisation. On the other hand, the reaction yields through hybridisation are typically much lower than with other techniques. In order to try to overcome these disadvantages, the crosslinking approach is investigated.

In the following chapter, the experimental procedures consisting of nanoparticle synthesis and characterisation as well as the formation of nanoparticle assemblies are described.

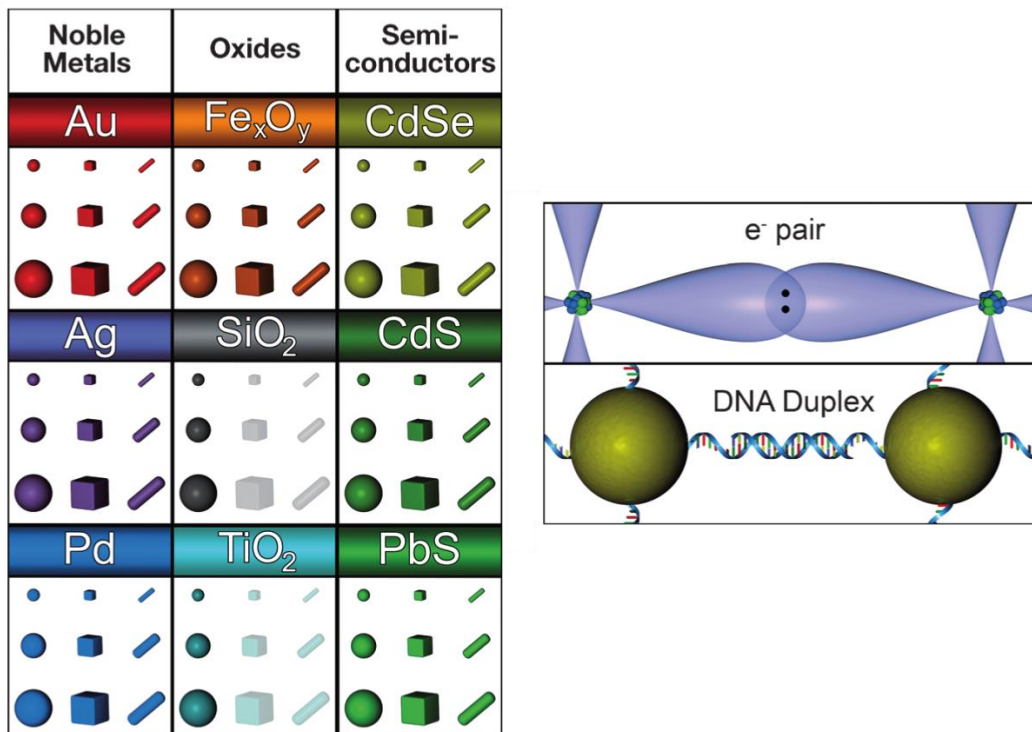


Figure 2.25: Concepts of a “new” periodic table. Nanoparticles act as atoms depending on the size, shape and composition and DNA plays the role of the bond forming electrons connecting the atoms to form “artificial” molecules. Re-printed with permission from ref. [262], Copyright 2013, John Wiley and Sons.



## Chapter 3. Experimental

This chapter includes the experimental routines for the synthesis and functionalisation of nanoparticles in **section 3.1** and **section 3.2** followed by characterisation techniques in **section 3.2**.

### 3.1 Nanoparticle synthesis and functionalisation

#### 3.1.1 Gold and silver nanoparticles

##### 3.1.1.1 Synthesis of $7 \pm 1.5$ nm gold nanoparticles

Gold nanoparticles were synthesised following the protocol from Zhang *et al.* using sodium borohydride as a strong reducing agent in aqueous solution [265] (**Section 2.1.1**). 100 mL of an ice-cold solution containing sodium tetrachloroaurate(III) (0.3 mM) and potassium carbonate (1 mM) was placed in an ice-bath. An ice-cold solution of sodium borohydride (0.5 mg/mL, 5 mL) was prepared freshly. The sodium borohydride solution was quickly added to the precursor solution under vigorous stirring in 5  $\times$  1 mL aliquots. The solution turned orange/red after completed addition and was further stirred for five minutes. Larger aggregates were removed by centrifugation. Then bis(*p*-sulfonatophenyl)phenyl phosphine (20 mg, 534.62 g/mol) was added to the gold nanoparticle solution and stirred for at least 16 hours in order to replace the loosely bound borohydride and carbonate ions [166]. In order to concentrate and wash the nanoparticles, sodium chloride was added until the colour changed to purple and subsequent centrifugation was performed. The nanoparticles were redispersed in Milli-Q water and filtered through a 0.2  $\mu$ m syringe filter to remove potential aggregates. Finally, the nanoparticle solution was stored at 4°C in the dark until further use.

##### 3.1.1.2 Synthesis of $15 \pm 1$ nm gold nanoparticles

Gold nanoparticles were synthesised according to the Turkevich/Frens method (see **section 2.1.1**). A solution containing sodium tetrachloroaurate(III) (100 mL, 1 mM) was brought to the boil while being vigorously stirred on a hot plate. At the same time, a solution of trisodium citrate (20 mg/mL, 5 mL) was heated to the boil in a separate vial. As soon as both solutions were boiling, 5 mL of the citrate solution was rapidly added to the gold solution. Immediately after addition, a colour change from yellow to colourless to purple occurred. After 30-60 seconds, the purple colour became wine red indicating the formation of gold nanoparticles. The solution was

further boiled for another 15 minutes to finish the reaction and finally left to cool to room temperature. Then, bis(*p*-sulfonatophenyl)phenyl phosphine dipotassium salt (BSPP) (15 mg) was added and the solution was moderately stirred overnight. The citrate ligands were exchanged by the phosphine compound due to higher affinity of the BSPP to the gold surface [166] (see **section 2.2**). The nanoparticles were filtered through a 0.2  $\mu\text{m}$  syringe filter to remove larger aggregates. In order to concentrate the gold nanoparticles, sodium chloride was added until the solution became blue and then the solution was centrifuged (5000 rpm, 10 minutes) yielding a precipitate. After completely removing the supernatant, the pellet was re-dispersed in Milli-Q water leading to gold nanoparticle solutions with concentrations of *ca.* 300 nM. The gold nanoparticles were stored at 4°C until further use.

### 3.1.1.3 Synthesis of larger gold nanoparticles up to $30 \pm 3$ nm

Nanoparticles with sizes up to  $30 \pm 3$  nm were prepared with the seeding-based growth method reported by the group of Puntes [62] (see **section 2.1.1**). First, gold nanoparticles were prepared by adding 0.5 mL NaAuCl<sub>4</sub> solution (25 mM) into a boiling solution containing trisodium citrate (75 mL, 2.2 mM) under vigorous stirring. The solution changed its colour from colourless to brilliant red and was boiled for another 10 minutes. Then the temperature was reduced to 90°C. The as-synthesised gold nanoparticles act as seeds for further growth by incremental addition of gold precursor and trisodium citrate. Once the temperature reached 90°C, 0.5 mL of NaAuCl<sub>4</sub> solution (25 mM) was added and the reaction left for 30 minutes after which it was completed. This step was repeated once more. The solution was then diluted by extraction of 27.5 mL and addition of 1 mL sodium citrate (60 mM) and 26.5 mL Milli-Q water. The extracted solution is called generation 0 (g0). In order to further grow the nanoparticles, the same procedure was repeated until the desired size was achieved and the solution was cooled to room temperature. 20 mg of BSPP were added and the solution gently stirred for at least 16 hours to replace the citrate ligands with phosphines. Finally, the nanoparticles were filtered through a 0.2  $\mu\text{m}$  syringe filter and concentrated by centrifugation. The solution was stored at 4°C in the dark until further use.

### 3.1.1.4 Synthesis of silver nanoparticles

Silver nanoparticles were synthesised according to the method of Bastús *et al.* using the citrate reduction route with tannic acid as an additive [68]. A solution (100 mL) containing trisodium citrate (5 mM) and tannic acid (0.025 mM) was brought to the

boil under vigorous stirring. Once boiling, 1 mL of a silver nitrate solution (25 mM) was quickly injected. An immediate colour change from colourless to yellow occurred. After one minute, the solution was removed from the hot plate and left to cool to room temperature on a second stirrer plate under vigorous stirring. The nanoparticles were filtered through a 0.2  $\mu\text{m}$  syringe filter and subsequently stored at 4°C in the dark until further use.

### 3.1.2 Synthesis of $\text{Cd}_{1-x}\text{Se}_x\text{Zn}_{1-y}\text{S}_y$ quantum dots

$\text{Cd}_{1-x}\text{Se}_x\text{Zn}_{1-y}\text{S}_y$  quantum dots were synthesised using a hot-injection solvothermal method reported by Bae *et al.* [118] (see section 2.1.3). CdO (0.4 mmol), zinc acetate ( $\text{Zn}(\text{ac})_2$ ) (4 mmol), oleic acid (5 mL), 1-octadecene (20 mL) and a magnetic stirrer bar were placed in a 100 mL three-neck flask. The flask was connected to a Schlenk line and a vacuum (1 mbar) was applied to remove water from the solution. Then the flask was filled with inert gas (argon) and the temperature was raised to 150°C while stirring until the solution turned clear and all the powder was dissolved. After this step, the temperature was raised to 310°C. A second precursor stock solution containing TOP-S and TOP-Se was prepared by placing selenium (see Table 3.1) and sulphur (4 mmol) in a vial together with trioctylphosphine (TOP, 3mL). Depending on the amount of selenium the emission wavelength was tuned. The solution was stirred and heated until the powder completely dissolved and a clear solution was obtained. Once the first solution reached 310°C, the second solution was injected rapidly. An immediate colour change indicated the formation of nanoparticles. The temperature was kept at 300°C for 10 minutes after which the heat source was removed and the reaction vessel was left to cool to room temperature. The nanoparticles were precipitated with 250 mL ethanol and centrifuged (6000 rpm, 10 minutes). The pellet was redispersed in 2 mL hexane and washed twice more with excess ethanol. Finally, the nanoparticles were redispersed in hexane and the concentration estimated as outlined in Appendix A.2. The QDs were stored at 4°C in the dark until further use.

Quantum dot (Emission maximum)	Amount Selenium precursor (mmol)
QD490	0.1
QD520	0.2
QD540	0.4
QD580	1.0

Table 3.1: Influence of the amount selenium on the emission of  $\text{Cd}_{1-x}\text{Se}_x\text{Zn}_{1-y}\text{S}_y$  quantum dots.

### 3.1.3 Synthesis of Upconversion nanoparticles

$\text{NaYF}_4:\text{Yb},\text{Er}$  and  $\text{NaYF}_4:\text{Yb},\text{Tm}$  upconversion nanoparticles were synthesised by solvothermal decomposition following the protocol of Li *et al.* [137]. Yttrium(III) chloride hexahydrate (0.79 mmol), ytterbium(III) chloride hexahydrate (0.20 mmol) and thulium(III) chloride hexahydrate (0.01 mmol) were placed in a 100 mL round-bottom three-neck flask together with 6 mL oleic acid and 15 mL 1-octadecene. The flask was heated to 150°C in order to facilitate the dissolution of the salts in the organic media. Once all the salts were dissolved, the clear solution was cooled to room temperature. Then, a solution containing sodium hydroxide (2.5 mmol) and ammonium fluoride (4 mmol) dissolved in 10 mL methanol was added dropwise to the previous solution under vigorous stirring. The turbid solution was then slowly heated to 100°C in order to evaporate the methanol. When the methanol was completely removed, the flask was sealed and quickly heated to 300°C for 1.5 hours, which led to nanoparticle formation. After the reaction finished, the solution was cooled to room temperature. Finally, three washing steps with excess ethanol and centrifugation (6000 rpm, 10 minutes) were performed. After the last washing step, the supernatant was removed and the particles dried at room temperature overnight. The nanoparticles were then weighed and re-dispersed in hexane or tetrahydrofuran to a concentration of 50 mg/mL and stored at 4°C in the dark until further use.

### 3.1.4 Synthesis of lead halide perovskite nanoparticles

*Methylammonium lead halide ( $\text{CH}_3\text{NH}_3\text{PbX}_3$ ):*

Methylammonium lead halide nanoparticles were synthesised according to ligand-assisted reprecipitation (LARP) the method by Zhang *et al.* [155]. First, methylammonium halide salts were made by mixing equimolar quantities of methylamine with the respective acid (HCl, HBr or HI) in an ice-bath. The solution was stirred for 2 hours and then dried using a freeze-dryer. The powders were stored

in a desiccator until further use. In the next step, a precursor solution containing the methylammonium halide (0.16 mmol) and the lead halide ( $\text{PbX}_2$ , 0.2 mmol) in DMF (10 mL) was prepared. To this solution, 20  $\mu\text{L}$  of n-octylamine and 0.5 mL of oleic acid were added. Finally, 1 mL of this precursor solution was then added dropwise to 10 mL of toluene under vigorous stirring leading to an immediate colour change. The nanoparticles were used as-synthesised and stored at 4°C in the dark.

In a different synthesis, the oleylamine ligand was replaced by cetyltrimethylammonium bromide (CTAB). A mixture of MABr (0.16 mmol),  $\text{PbBr}_2$  (0.2 mmol) and CTAB (0.04 mmol) in DMF (10 mL) was prepared and 0.5 mL OA added. Again, 1 mL of this solution was added into 10 mL of toluene yielding a yellow coloured solution with green fluorescence. The nanoparticles were washed by centrifugation and re-dispersed in toluene and stored at 4°C in the dark.

#### *Caesium lead halide ( $\text{CsPbBr}_3$ ):*

Lead halide perovskites containing caesium as a cation were synthesised according to a solvothermal method published by Protesescu *et al.* [156]. First, a caesium oleate precursor was synthesised by dissolving  $\text{Cs}_2\text{CO}_3$  (2.5 mmol) in a mixture of 40 mL 1-octadecene and 2.5 mL oleic acid with Schlenk line techniques. The mixture was first dried under vacuum at 100°C for 30 minutes and then the temperature was raised to 150°C for 1 hour until no residue of caesium carbonate was left. Another solution was prepared containing 0.2 mmol  $\text{PbX}_2$  in 5 mL 1-octadecene together with 0.5 mL oleylamine and 0.5 mL oleic acid. The solution was dried under vacuum as well for 30 minutes at 100°C and then raised to 180°C. The vacuum was replaced with inert gas and 0.4 mL of the caesium oleate solution was rapidly injected. After 5 seconds, the reaction vessel was quickly cooled down in an ice-bath. The resulting solution was washed twice by centrifugation (8500 rpm) and the pellet re-dispersed with toluene. The solution was then stored at 4°C in the dark.

## 3.2 Nanoparticle functionalisation

### 3.2.1 Gold and silver nanoparticles

#### 3.2.1.1 DNA attachment to 15 $\pm$ 1 nm gold nanoparticles

The preparation of AuNPs bearing a single strand of DNA (monoconjugates) was conducted according to modified literature procedures [246]. First, BSPP-coated 15

$\pm 1$  nm prepared as described in **section 3.1.1** were centrifuged (16400 rpm, 10 minutes), the supernatant removed and re-dispersed in phosphate buffer (20 mM, pH 7.4). The AuNPs (250  $\mu$ L, 300 nM) were mixed with thiol-modified oligonucleotides (15  $\mu$ L, 5  $\mu$ M) in a 1:1 ratio. Then, a freshly prepared BSPP solution (20  $\mu$ L, 50 mg/mL) was added in order to cleave the disulphide bond in the thiol linker (see **section 4.5.1**). The AuNPs were incubated for 1 hour in the dark at room temperature. The AuNPs were then separated by the number of attached strands via agarose gel electrophoresis in 0.5x TBE buffer (2.25% w/v, 10 V/cm, 60 minutes). The monoconjugate band was cut into small pieces and immersed in 0.5x TBE where the nanoparticles diffused from the gel into the solution overnight under moderate shaking. The solution with the monoconjugates was filtered through a 0.2  $\mu$ m filter in order to remove small pieces of agarose. The monoconjugates were finally concentrated by centrifugation and re-dispersed in phosphate buffer (20 mM, pH 7.4) and stored at 4°C until further use.

### 3.2.1.2 DNA attachment to 30 $\pm$ 3 nm gold nanoparticles

BSPP-coated AuNP with diameters of 30  $\pm$  3 nm were centrifuged (8000 rpm, 5 minutes) and the pellet re-dispersed in PBS (250  $\mu$ L, 20 mM, pH 7.4). Oligonucleotides were then added in a 3:1 DNA:AuNP ratio together with BSPP (20  $\mu$ L, 50 mg/mL). The solution was incubated for 1 hour under mild shaking to avoid precipitation of the gold nanoparticles. The AuNP-DNA conjugates were purified by three-fold centrifugation (8000 rpm, 5 minutes) to remove unbound DNA and finally re-dispersed in PBS (20 mM, pH 7.4). Separation by gel electrophoresis was not possible due to the insufficient DNA length [246].

### 3.2.1.3 Silver nanoparticle ligand exchange

As-synthesised AgNPs were capped with citrate and tannic acid. For ligand exchange with SH-mPEG ( $M_w = 356$  g/mol) or folic acid, stock solutions (100  $\mu$ M) in borate buffer (20 mM, pH 8) were freshly prepared. 5 mL of AgNPs were centrifuged (16400 rpm, 10 minutes) and redispersed in 1 mL borate buffer (20 mM, pH 8). The concentration of AgNP was estimated to 3 nM (see **Appendix A.1**). Then, 50  $\mu$ L from the stock solution of SH-mPEG or folic acid were added to the AgNPs and mildly stirred overnight. The nanoparticles were then washed three times and redispersed in phosphate buffer (20 mM, pH 7.4).

### 3.2.2 Semiconductor quantum dots

#### 3.2.2.1 Ligand exchange and phase transfer

As-synthesised  $\text{Cd}_{1-x}\text{Se}_x\text{Zn}_{1-y}\text{S}_y$  nanoparticles were coated with oleic acid and trioctylphosphine. The phase transfer from the organic to the aqueous phase was facilitated as published by Aldeek *et al.* using L-lipoic acid (LA) in a ligand exchange reaction [266]. First, a solution of LA in methanol (500  $\mu\text{L}$ , 100 mM) was irradiated with UV-A light (50 mW/cm<sup>2</sup>, 365 nm) for 30 minutes. A colour change from yellow to colourless indicated the reduction of the disulphide bond in the ring (see **section 4.5.3**). Then, a solution of QDs in hexane (750  $\mu\text{L}$ , 3  $\mu\text{M}$ ) was prepared. The irradiated LA solution was added to the QD solution under vigorous stirring and tetramethylammonium hydroxide (10  $\mu\text{L}$ , 100 mM) was added to increase the pH. On the one hand, this leads to a deprotonation of the carboxyl group of the lipoic acid. On the other hand, thiols are deprotonated to thiolates, which makes them more reactive. After 15 minutes, the nanoparticles were washed several times with ethanol and water and centrifuged (16400 rpm, 10 minutes). Finally, the quantum dots were re-dispersed in borate buffer (10 mM, pH 9). The nanoparticles were stored at 4°C in the dark until further use.

#### 3.2.2.2 Attachment of DNA to LA-coated quantum dots

The terminal carboxyl group on the LA-coated quantum dots allowed for the attachment of amine-modified DNA via EDC/NHS coupling (see **section 4.5.3**). Two solutions containing 0.3 M EDC in MES buffer (0.1 M, pH 6) and 0.3 M sulfo-NHS in MES buffer (0.1 M, pH 6) were freshly prepared and used immediately. LA-coated quantum dots (200  $\mu\text{L}$ , 10  $\mu\text{M}$ ) in borate buffer (10 mM, pH 9) were mixed with 20  $\mu\text{L}$  EDC, 40  $\mu\text{L}$  sulfo-NHS solution and a 5x excess of oligonucleotides (**Seq1(-Cy3)**). The nanoparticles were incubated overnight under moderate shaking. The DNA-conjugated nanoparticles were washed three times with Milli-Q water and centrifugation (16400 rpm, 10 minutes). After the last washing step, the nanoparticles were re-dispersed in phosphate buffer (20 mM, pH 7.4).

### 3.2.3 Upconversion nanoparticles

#### 3.2.3.1 Ligand exchange and phase transfer

Rare-earth doped  $\text{NaYF}_4$  upconversion nanoparticles were capped with oleic acid after synthesis. In order to transfer them to water, the multidentate ligand

polyacrylic acid (PAA) was used [267]. A PAA solution in THF (10 mL, 25 mg/mL) was freshly prepared and upconversion nanoparticles in THF (500  $\mu$ L, 50 mg/mL) were added. The solution was ultra-sonicated for 30 seconds and then moderately stirred with a magnetic stirrer bar overnight. The nanoparticles were then centrifuged (16400 rpm, 10 minutes) and washed twice with ethanol and once with Milli-Q water. The nanoparticles were finally re-dispersed in borate buffer (10 mM, pH 9) and stored at 4°C in the dark until further use.

### 3.2.3.2 DNA attachment on PAA-coated upconversion nanoparticles

Some carboxyl groups on the PAA-coated upconversion nanoparticles are not bound to the nanoparticles' surface and are therefore available for the attachment of amine-modified DNA via EDC/NHS coupling (see **section 4.5.3**). Two solutions containing EDC (0.3 M) in MES buffer (0.1 M, pH 6) and sulfo-NHS (0.3 M) in MES buffer (0.1 M, pH 6) were freshly prepared and used immediately. 200  $\mu$ L of PAA-coated UCNP (5 mg/mL) in borate buffer (10 mM, pH 9) were mixed with 20  $\mu$ L EDC and 40  $\mu$ L sulfo-NHS solution and 50x excess of oligonucleotides (**Seq2**). The nanoparticles were incubated overnight under moderate shaking. The DNA-conjugated nanoparticles were washed three times with Milli-Q water and centrifugation (16400 rpm, 10 minutes). After the last washing step, the nanoparticles were re-dispersed in phosphate buffer (20 mM, pH 7.4).

## 3.3 DNA hybridisation and assembly of DNA-NP conjugates

### 3.3.1 DNA hybridisation and crosslinking

The DNA experiments without nanoparticles were conducted as follows. Depending on the type of assembly, an equimolar mixture of the different strands was prepared (0.05  $\mu$ M, 100  $\mu$ L) in phosphate buffer (20 mM, pH 7.4). In order to increase the ionic strength, an appropriate amount of 2 M NaCl was added to reach the designated concentration (typically 200 mM NaCl). Hybridisation was performed by heating the mixture to 95°C and slow cooling to room temperature in 3 hours. Then, gel electrophoresis in a 6% PAGE gel was performed. After electrophoresis, the gel was stained with ethidium bromide and analysed.

In order to crosslink the carbazole-modified oligonucleotides, the same hybridisation procedure was followed. After hybridisation, the DNA solution was cooled in an ice-bath and irradiated with UV-A light (50 mW/cm<sup>2</sup>, 365 nm) in a crosslinker. In order

to test the crosslinking performance, the samples were dehybridised by heating to 95°C for 5 minutes and subsequent rapid cooling to 0°C in an ice-bath in order to prevent hybridisation. Then, formamide was added to a final concentration of 20% v/v and the samples were run in a 6% denaturing PAGE gel. After electrophoresis, the gel was stained with ethidium bromide and analysed.

### 3.3.1 Gold nanoparticle assemblies

Different assemblies of gold nanoparticles were made using three different sets of oligonucleotides, which were either unmodified or modified with alkyne and azide groups or with 3-cyanovinyl carbazole moieties (see **section 5.1**). The procedure for the preparation of gold nanoparticle assemblies is the same for all different oligonucleotides.

#### 3.3.1.1 Gold nanoparticle dimers

Gold nanoparticle dimers were made by mixing equimolar amounts of two batches of AuNP-DNA monoconjugates with two different DNA strands. Typical reaction volumes consisted of 200  $\mu$ L per reaction with concentrations of 5 nM. The ionic strength was raised to 50 mM by addition of 1 M NaCl solution in phosphate buffer (20 mM, pH 7.4). The solution was then heated to 65°C in a water bath, incubated for 5 minutes and then slowly left to cool to room temperature in the water bath. The solution was shaken briefly every 20 minutes. The water bath reached room temperature (<30°C) after 2.5 hours. After hybridisation, the nanoparticle assemblies were separated and purified by agarose gel electrophoresis (1.75% w/v, 0.5xTBE, 10 V/cm, 45 minutes). The dimer band was cut in small pieces and immersed in 0.5x TBE buffer overnight with moderate shaking. The solution was filtered through a 0.2  $\mu$ m syringe filter in order to remove small pieces of agarose. Finally, the dimers were centrifuged and re-dispersed in phosphate buffer (20 mM, pH 7.4, 50 mM NaCl).

#### 3.3.1.2 Gold nanoparticle trimers

For the synthesis of gold nanoparticle trimers, equimolar amounts of three different AuNP-DNA monoconjugates were mixed together. Then the procedure as described in **section 3.3.1.1** was applied. In order to gather the trimers, the trimer band was cut and treated as outlined before.

### 3.3.1.3 Gold nanoparticle tetrahedra

The synthesis of 15 nm gold nanoparticle tetrahedral was carried out either in a one step or in a two-step procedure. In the former, all four AuNP-DNA conjugates were mixed in equimolar ratios. In the latter, two different dimers were first synthesised as described in **section 3.3.1.1**. Typically, the two different dimer pairs **SC1+SC2** and **SC3+SC4** were used for the synthesis of tetrahedra structures (see **Appendix A.3**). The dimers containing 3-cyanovinyl carbazole were crosslinked before further hybridisation (see **section 3.3.1.4**). Then, equimolar amounts of the two crosslinked dimer pairs were mixed (500  $\mu$ L, 10 nM). The solution was then heated to 65°C for 5 minutes and slowly cooled down to room temperature as described before. Agarose gel electrophoresis (0.5xTBE, 1.75% w/v, 10 V/cm, 45 minutes) was performed for the separation of the tetrahedral structures. The tetrahedra band was cut out and immersed in 0.5x TBE buffer overnight with moderate shaking.

### 3.3.1.4 Crosslinking and de-crosslinking of 3-cyanovinyl carbazole modified assemblies

Gold nanoparticle assemblies containing 3-cyanovinyl carbazole modified DNA were UV irradiated in a UVP CX-2000 photo-crosslinker (50 mW/cm<sup>2</sup>) with light centered either at 365 nm (UV-A) or 312 nm (UV-B). The samples were placed in an ice-bath and irradiated for 15 minutes.

## 3.3.2 Assemblies of upconversion nanoparticle and quantum dots

The DNA-functionalised QDs and upconversion nanoparticles were mixed in three different molar ratios, i.e. UCNP:QD ratios of 1:10, 1:25 and 1:100. The samples were topped up with phosphate buffer (20 mM, pH 7.4) and sodium chloride was added to a final concentration of 80 mM. The total volume was 400  $\mu$ L. The final concentration of UCNP was 1 nM. Hybridisation was performed by heating to 60°C for 5 minutes and subsequent cooling to room temperature over 2 hours. In order to avoid precipitation, the samples were shaken every 10 minutes.

## 3.4 Characterisation techniques

### 3.4.1 Ultraviolet-Visible spectroscopy

This spectroscopy method is widely employed for the analysis of absorbing materials. A sample is scanned over the ultraviolet and visible range of the light with monochromatic light of a given intensity and the change in the intensity is detected. For dilute samples and negligible scattering, Beer-Lambert's law holds:

$$A = -\log_{10} \left( \frac{I}{I_0} \right) = \varepsilon \cdot c \cdot d,$$

Equation 3.1: Beer-Lambert's law for dilute solutions.

where A is the absorbance defined as the negative decadic logarithm of the transmitted intensity (I) divided by the incident intensity ( $I_0$ ),  $\varepsilon$  the molar extinction coefficient, c the concentration of the analyte and d the path length of the light through the sample. It should be noted that absorption and scattering cannot be distinguished with this method.

UV-Visible measurements were performed with a Shimadzu UV-2700 UV-Vis spectrometer using a quartz cuvette with a path length of 10 mm. A blank spectrum was taken with the same solvent as used in the sample and was automatically subtracted from the sample spectra by the software. The concentration of a molecule in solution can be calculated if the molar extinction coefficient is known. A table of molar extinction coefficients for gold nanoparticles between 5-100 nm was published by Haiss *et al.* and is used to calculate the concentrations of gold nanoparticle solutions [60]. The concentration of CdSe quantum dots can also be estimated by UV-Vis spectroscopy as published by Yu *et al.* [268]. Examples will be given in **Appendix A.2**.

### 3.4.2 Fluorescence spectroscopy

Fluorescence spectroscopy is a rather sensitive method for light emitting specimen and is applied in a wide range of scientific research. It relies on radiative electronic relaxation of a molecule from an excited state to a lower state. Usually, the sample is excited at a certain wavelength and the emitted light at higher wavelengths is measured (the fluorescence is typically red shifted due to energy dissipation by vibrational or rotational modes). Fluorescence spectra were acquired using a Cary Eclipse Fluorimeter with step widths of 1 nm or lower and using a quartz cuvette with a path length of 1 cm.

Fluorescence spectroscopy was used to analyse semiconductor quantum dots, upconversion nanoparticles as well as lead halide perovskite nanoparticles. Photoluminescence quantum yields were determined using a standard protocol (see **Appendix A.4**). Absorption and fluorescence spectra of two reference dyes

(rhodamine 6G and fluorescein), for which the PLQYs are known, were measured in order to estimate the PLQY.

For the detection of upconversion emission, a home-built setup was employed (Figure 3.1). A 500 mW laser diode with an emission at 980 nm (Laserbtb, PL-980) was used as an excitation source. The sample was placed in a transparent quartz cuvette and the light focussed into the cuvette with a lens. A second lens was used to focus the emitted light from a 90° angle into an optical fiber connected with a spectrometer (Ocean Optics, USB4000). A shortpass filter was placed in front of the fiber to filter out scattered light from the laser diode. The setup was assembled by Prof. Muskens from the Integrated Nanophotonics group.

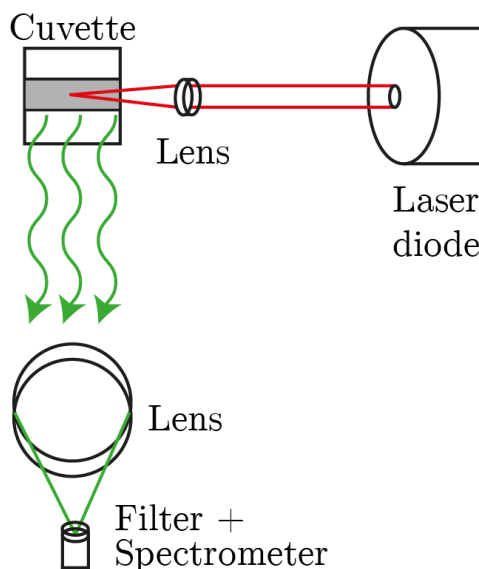


Figure 3.1: Set-up for upconversion detection. The light of a laser diode (980 nm, 500 mW) is focussed by a lens into the sample in a transparent cuvette. The emitted light is collected with a spectrometer using a second lens. Scattered light from the laser diode is removed by a filter in front of the detector.

### 3.4.3 Surface enhance Raman spectroscopy

The Raman spectra presented in section 5.3 were obtained using a home-built setup (Figure 3.2). The light of a 532 nm laser source with 50 mW power output was first filtered with a bandpass filter and then focussed with an objective (NA = 0.5) into the sample. The back-scattered light was then first filtered using an angle-tuned edge filter to reduce the Rayleigh scattering intensity and filtered again with another longpass filter before entering the spectrometer (Andor Shamrock 193i). The setup was assembled by Prof. Muskens from the Integrated Nanophotonics group.

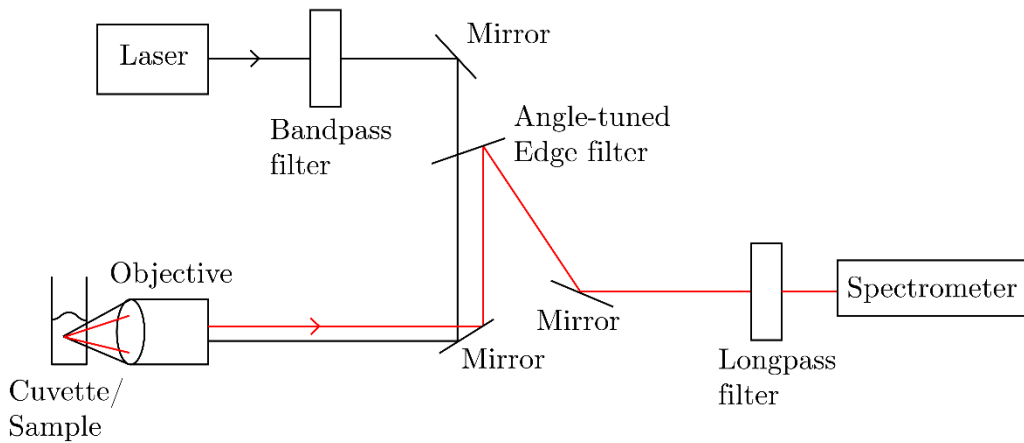


Figure 3.2: Home-built setup for Raman scattering measurements. Laser light (532 nm, 50 mW) is first filtered with a bandpass filter and focussed using an objective (NA = 0.5). The backscattered light is filtered twice before entering the spectrometer.

### 3.4.4 Transmission Electron Microscopy (TEM)

Microscopy techniques allow for the visualisation of objects, which are not visible by the eye. Light microscopes are limited by their resolution to about  $\frac{\lambda}{2}$ , i.e. in the range several hundred of nanometres. In order to visualise objects at the nanoscale, electron microscopes are utilised. Electrons increase the resolution by a factor of about 100 due to their wave nature with a de Broglie wavelength of about 1 nm. Therefore, it is possible to visualise much smaller objects than with a light microscope. The principle is similar to that of a light microscope except that a high vacuum is needed so that the electron beam is not scattered and the lens system consists of coils, which electromagnetically direct the electron beam.

TEM images were acquired using a Hitachi H7000 transmission electron microscope with a bias voltage of 80 kV. Samples for TEM were prepared by placing a small droplet (10  $\mu$ L) of the sample solution onto 400 mesh copper grids coated with a Formvar and a carbon film making the grids hydrophobic. While solutions with organic solvents dried within seconds, aqueous solutions were left for 10 minutes after which most of the solution was removed with a filter paper so that only a thin water film remained. This film then dried within 30 minutes and the specimen was ready for analysis.

### 3.4.5 Energy dispersive X-ray spectroscopy (EDX)

A possibility to find out the composition of a material is by analysing the specific X-ray emissions of the sample. If an atom is excited either with photons or electrons of

high enough energy ( $E \geq 1\text{-}20 \text{ keV}$ ), electrons in the shell of the atom can be scattered out leaving a void. Electrons from higher shells are then filling the void under emission of a photon with typical energies of several keV (see Figure 3.3). The transitions are named  $X_y$  where  $X$  is the name of the shell, which contains the void (i.e. K, L, M,...) and  $y$  describes the distance of the filling shell from the void with greek letters (i.e.  $\alpha$ ,  $\beta$ ,  $\gamma$ ,...). For example, the transitions from L->K and from M->K are denoted with  $K_\alpha$  and  $K_\beta$ , respectively.

Since the energies of electronic transitions between the shells are characteristic for each element, the emitted photons are called characteristic X-rays. This concept is used in energy dispersive X-ray spectroscopy where a sample is bombarded with highly energetic electrons and the X-ray emission is detected. The limitation of this method is that many elements have overlapping characteristic X-rays making it difficult or sometimes even impossible to determine the presence of certain elements in unsuitable mixtures.

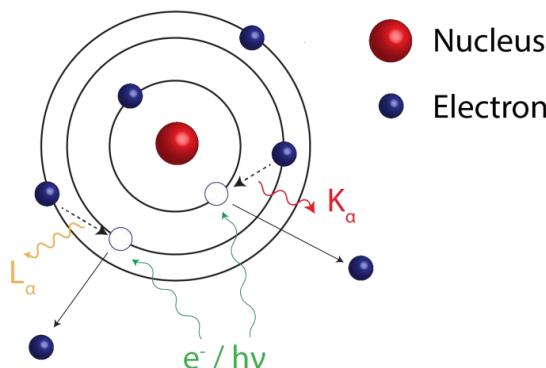


Figure 3.3: Illustration of the principle of the generation of characteristic X-ray radiation used in EDX analysis. Electrons are removed from the atom by excitation with light or energetic electrons leaving a gap behind. These are filled by other electrons under emission of a photon. The transitions are named according to the shell with the gap (K, L, M,...) and the electron filling the gap ( $\alpha, \beta, \gamma$ ).

It is possible to analyse the elemental composition using TEM, which has the advantage that the sample can directly be selected. Furthermore, the source for the excitation of the sample (accelerated electrons) is the same that is used to visualise the sample, i.e. the X-ray spectrum naturally occurs when TEM is used. In a typical spectrum, there are the aforementioned characteristic X-rays from the elements in the sample but also a background which stems from the continuous Bremsstrahlung of electrons being decelerated by the targets as well as from the TEM grids and the grid holder inside of the microscope.

In this work, EDX was used to verify the presence of the different metals in semiconductor quantum dots and upconversion nanoparticles. The measurements were performed on a FEI Tecnai T12 transmission electron microscope with an integrated EDX system from EDAX.

### 3.4.6 Gel electrophoresis

Gel electrophoresis has become an important tool for the separation of differently sized or charged objects like DNA sequences or nanoparticles. Electrophoresis describes the movement of colloidal particles or molecules in an electric field. The velocity of the objects mainly depends on the charge and the size under given conditions. In order to increase the separation, gel matrices such as agarose or polyacrylamide are typically employed because they alter the electrophoretic mobility significantly. While originally utilised for DNA fragments and proteins, gel electrophoresis is now also widely used in nanoscience for the separation and purification of nanoparticles. In practice, two different types of gel matrices are used: Polyacrylamide and agarose gels.

#### 3.4.6.1 Polyacrylamide gel electrophoresis (PAGE)

Polyacrylamide gels are made by polymerisation of a mixture of acrylamide and *N,N*-Methylenebisacrylamide using an initiator such as ammonium persulfate (APS) and a catalyser like tetramethylethylenediamine (TEMED) (see **Figure 3.4**). The resulting network has pore sizes from few tens of nanometres to several hundred nanometres depending on the mixture and the total concentration of the monomers. This makes it suitable for the separation of small objects like oligonucleotides.

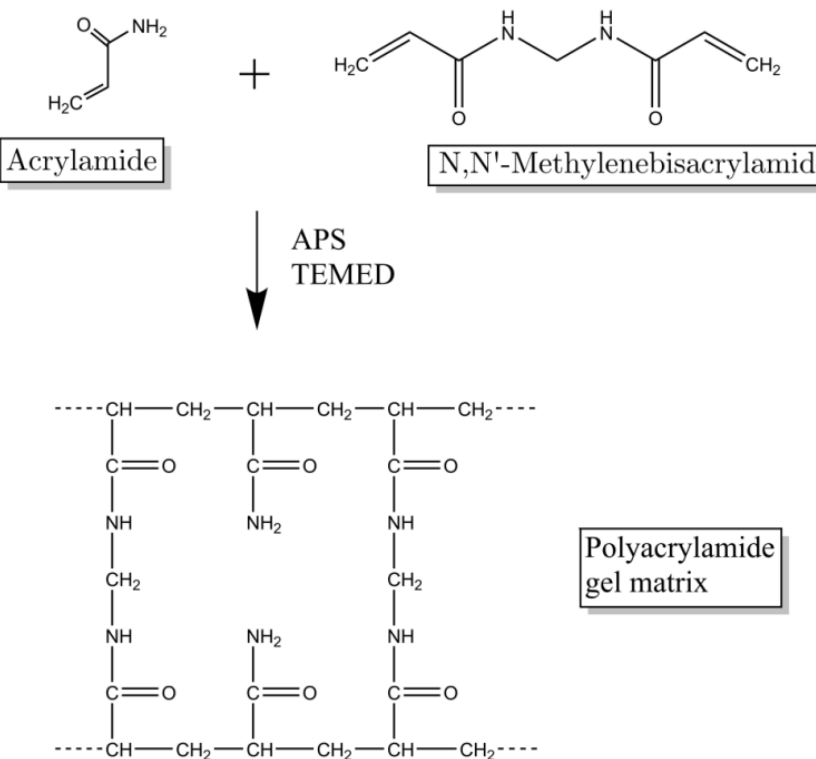


**Figure 3.4: Formation of a polyacrylamide gel matrix from the two precursors acrylamide and *N,N'*-Methylenebisacrylamide.**

Polyacrylamide gels were prepared using a Bio-Rad Protean II xi cell. Gels were prepared in volumes of 70 mL. For a 6% w/v native polyacrylamide gel, 10.5 mL 40% 19:1 acrylamide:bis-acrylamide solution, 14 mL 5x TBE buffer and 45.5 mL Milli-Q water were mixed in a beaker. 56  $\mu$ L of TEMED were added and the solution was thoroughly stirred. In order to start the polymerisation, 560  $\mu$ L of an APS solution (10% w/v) was rapidly injected and the solution stirred again. The solution was then quickly transferred into the casting tray and left for one hour to polymerise completely. Denaturing polyacrylamide gels were prepared accordingly except for additional dissolution of urea to a final concentration of 7 M. Before loading the samples, the gel was equilibrated by pre-running for 1 h at 10 W. In all electrophoresis runs, the running buffer was 1x TBE. After pre-running, samples were mixed with a Ficoll® PM400 solution (15% w/v, 3x TBE) to a final Ficoll® concentration of 5% w/v and to a final volume of 50  $\mu$ L when native PAGE was performed. Ficoll® is a neutral polymer increasing the density of the solution in order to facilitate the loading of the sample into the gel and to ensure that it remains at the bottom of the well. For denaturing gels, 50% v/v formamide was added. As an indicator, a mixture of bromophenol blue (0.1% w/v) and xylene cyanol (0.1% w/v) in formamide were used. These dyes migrate through the gel at different speeds and

are used as indicators for the electrophoresis progress. Gel electrophoresis was undertaken at 10 W for 2 h. After electrophoresis, the gels were stained with ethidium bromide (5 µg/mL) in Milli-Q water for 15 min and finally analysed using a Bio-Rad Gel Doc EZ system.

#### 3.4.6.2 Agarose gel electrophoresis

Agarose gels are made from a polysaccharide, which gels in aqueous solution when it is boiled and left to cool down (Figure 3.5). The pore sizes are larger compared to polyacrylamide gels starting with several hundred nanometres for a 1% w/v gel, which makes it suitable to separate larger objects like proteins or nanoparticles [269].

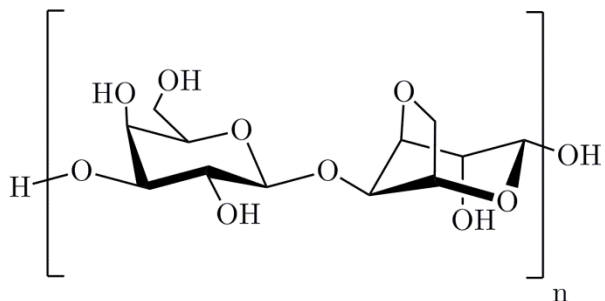


Figure 3.5: Chemical structure of agarose.

Agarose gels were prepared by placing agarose powder in a flask and adding an appropriate amount of 0.5x TBE buffer. For example, a 2% w/v agarose gel consisted of 1.6 g agarose powder in 80 mL 0.5x TBE buffer. The mixture was then heated with a microwave and was boiled until the solution became clear. In order to minimise evaporation, the flask was covered with a petri-dish. The hot solution was left to cool for 30 seconds at room temperature and cast in a Bio-Rad GT cell. Before loading the samples, they were mixed with a Ficoll®-400 solution (15% w/v, 3xTBE) to a final concentration of 2.5% w/v when they were run natively. For denaturing conditions, formamide was added to a final concentration of 30% v/v. The samples were run with 0.5x TBE running buffer and an electric field of 10 V/cm. For recovering the desired products, appropriate parts of the gel were cut with a scalpel into small pieces and immersed in 0.5x TBE buffer with overnight shaking.

#### 3.4.7 Dynamic light scattering (DLS)

The size of colloidal nanoparticles or macromolecules suspended in a liquid can be analysed by dynamic light scattering, which relies on Brownian motion and Rayleigh

scattering. Light from a monochromatic and coherent light source like a laser is used to illuminate the solution where the dispersed molecules scatter the light in all directions. The scattered light from different molecules create an interference pattern, which fluctuates due the constant movement of the molecules caused by Brownian motion. Finally, the time scale of these fluctuations is analysed and correlated with the diffusion coefficient, which allows the calculation of the hydrodynamic diameter with the Stokes-Einstein relation.

The measurements were performed on a Malvern Zetasizer Nano ZS. The light source was a He-Ne-Laser with a wavelength of 633 nm. The measurements were performed with a 173° backscattering arrangement. Samples were made up to 1 mL with Milli-Q water and placed in disposable cuvettes. Each measurement consisted of 10 sub-runs of 15 seconds and was repeated three times.

### 3.4.8 Zeta-potential

The  $\zeta$ -potential is a measure of net the surface charge on dispersed particles and is an important factor for determining the colloidal stability of nanoparticle suspensions (see [section 2.3.3](#)). It can be measured similar to the hydrodynamic radius by illuminating the sample with a laser and by applying an electric field to the solution of interest. The velocity of the particles is determined by analysing the mixture of scattered light from the particles with a reference beam. This yields a Doppler shift caused by the particle motion which can be correlated to the zeta-potential using the Smoluchowski model.

The measurements were performed as the DLS measurements on a Malvern Zetasizer Nano ZS with a He-Ne-Laser source at 633 nm. Samples were made up to 1 mL with Milli-Q water and placed in a disposable cuvette. Each measurement consisted of at least 10 sub-runs and was repeated three times.

## Chapter 4. Results on nanoparticle synthesis and characterisation

In this chapter, the characterisation of the nanomaterials described in **chapter 3** will be discussed.

### 4.1 Plasmonic nanoparticles

#### 4.1.1 Gold nanoparticles

The gold nanoparticles synthesised according to the protocol of Turkevich *et al.* are formed by reduction of sodium tetrachloroaurate with trisodium citrate [40] (see **section 2.1**). **Figure 4.1** shows a representative TEM image and size distribution of  $15 \pm 1$  nm gold nanoparticles. It can be clearly seen that the nanoparticles are well separated and no larger aggregates are present. Furthermore, the size distribution is fairly narrow with a mean size of 15.7 nm and a standard deviation of 1.0 nm. The nanoparticle sizes were determined with the free software ImageJ [270]. The resulting histograms were then fitted with a normal distribution. Even though nanoparticle size distributions are typically fitted with log-normal distributions, the normal distributions gave better results (in terms of  $R^2$ ) in this work.

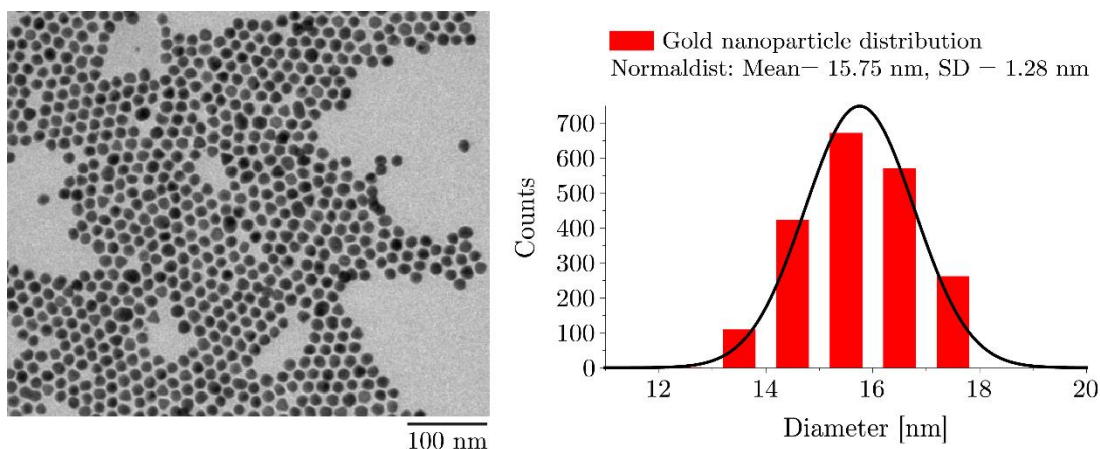


**Figure 4.1:** (A) TEM image of  $15 \pm 1$  nm gold nanoparticles synthesised with the citrate reduction method. (B) Statistical analysis of the gold nanoparticle diameters.

After synthesis, citrate molecules are electrostatically adsorbed on the surface of the nanoparticles. Citrate has three  $pK_a$  values of 3.13, 4.76 and 6.40 meaning that the molecule is partially deprotonated except under very acidic conditions [271]. The resulting charges lead to a stabilisation of the colloid according to the DLVO theory (see **section 2.3.3**). However, if the ionic strength is increased above

approximately 30 mM or if ions of higher valence (e.g.  $Mg^{2+}$ ) are added, the nanoparticles will undergo irreversible aggregation [272]. Therefore, the AuNP are functionalised with BSPP via a ligand exchange reaction presented by Loweth *et al.*, which is depicted in **Figure 4.2** [166]. Phosphine readily displaces the loosely bound citrate molecules due to a higher affinity towards the gold surface.

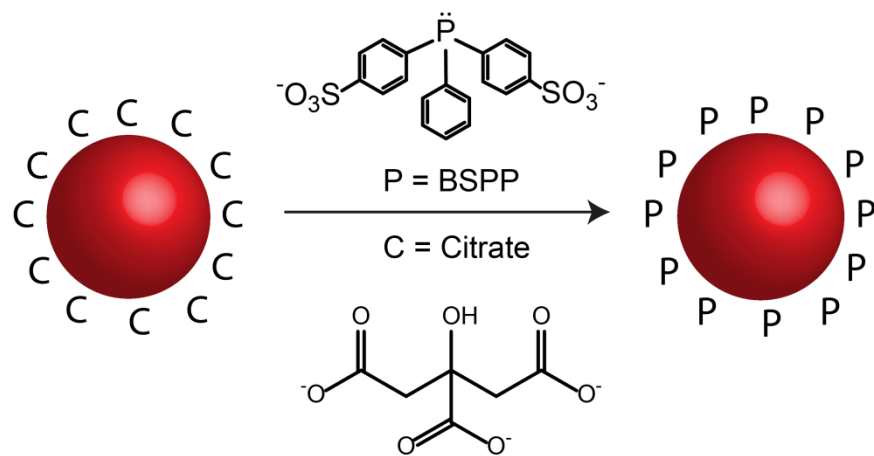


Figure 4.2: Functionalisation of citrate-coated gold nanoparticles with BSPP via a ligand exchange reaction.

Besides the negative charges from the sulfonate groups ( $R-SO_3^-$ ), BSPP molecules are much bulkier than citrate molecules. This increases the particles' stability against aggregation due to steric hindrance. In addition, the functionalisation allows the concentration of the nanoparticles by centrifugation, which else causes aggregation.

The extinction spectra of as-synthesised citrate-stabilised and BSPP-functionalised gold nanoparticles are presented in **Figure 4.3**. The nanoparticles have an absorption peak at around 520 nm, which stems from the LSPR as described in **section 2.1.2**. It can be seen that a small shift of the LSPR of 3 nm occurs after the functionalisation with BSPP, which can be explained by the change of the local refractive index on the nanoparticle surface. This demonstrates that the LSPR can be used to monitor interaction between molecules and the nanoparticle [273].

The  $\zeta$ -potentials of citrate- and BSPP-coated gold nanoparticles are depicted in **Figure 4.4**. Initially, the nanoparticles have a potential of  $-28.4 \pm 4.6$  mV from the citrate molecules attached to the nanoparticle surface. Such a value suggests good colloidal stability without considering steric effects (see **section 2.3.3**). After functionalization with BSPP, the zeta potential becomes even more negative with

$-44.4 \pm 3.36$  mV. This indicates the successful functionalization and the increased colloidal stability of the nanoparticles.

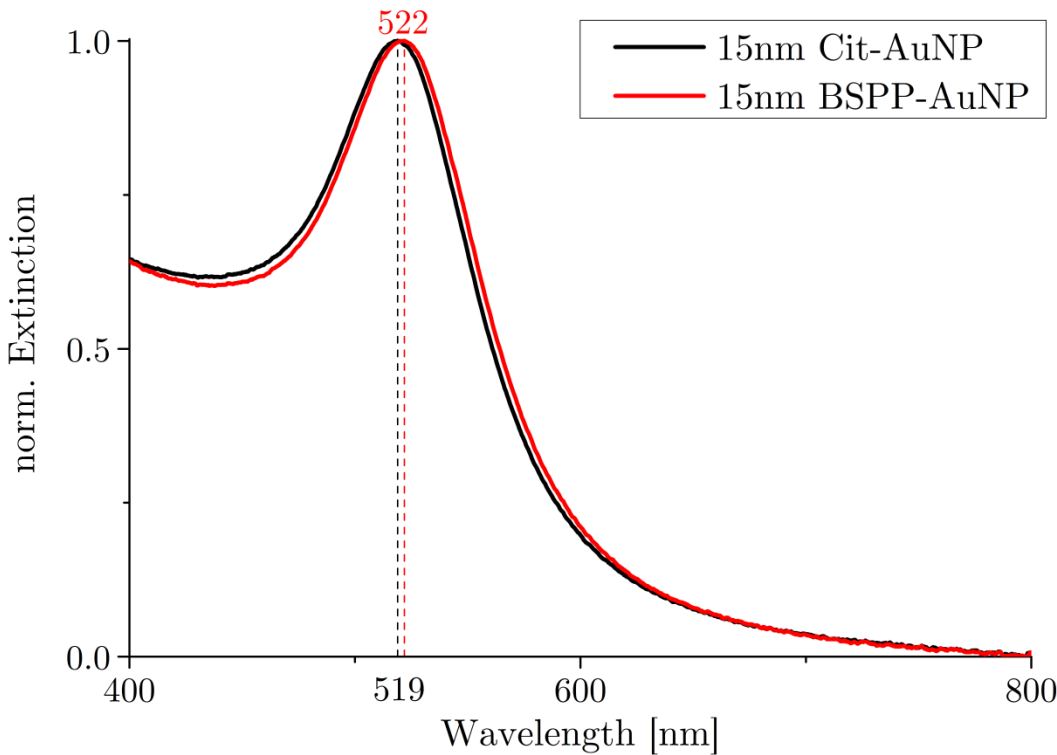


Figure 4.3: Extinction spectra of citrate- and BSPP-functionalised  $15 \pm 1$  nm gold nanoparticles. The peak of the LSPR is shifted from 519 nm to 522 nm after ligand exchange.

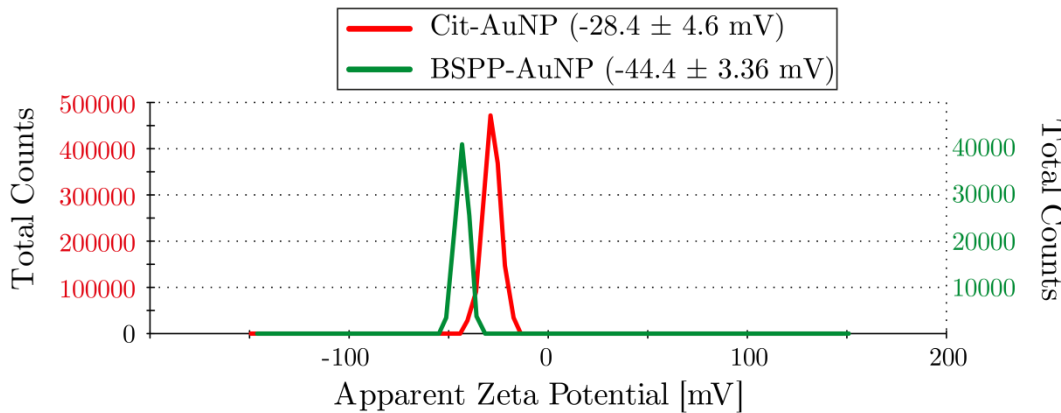


Figure 4.4: Zeta-potential of citrate- and BSPP-coated gold nanoparticles. After functionalisation with BSPP the increased value from  $-28.4$  mV to  $-44.4$  mV indicates the successful capping and enhanced colloidal stability.

Figure 4.5 illustrates the lack of colloidal stability against ionic strength for as-synthesised citrate-capped gold nanoparticles. As an example, the nanoparticles were dispersed in 0.5x TBE. There is an immediate change in the extinction spectra where the LSPR peak shifts to the red and a shoulder at around 600 nm appears, which

turns the colour of the solution purple/blue. The shoulder indicates nanoparticle agglomeration or aggregation and is explained by plasmon coupling of many nanoparticles. Similar results are obtained if the nanoparticles are centrifuged and redispersed. This example shows the necessity of a suitable surface coating depending on the experimental procedures. It should be noted that a lack of colloidal stability does not necessarily need to be evident from UV-Vis, e.g. when the aggregation is very slow. In this case, DLS is a better method to determine if a colloid is stable because it is much more sensitive to the presence of clusters than UV-Vis.

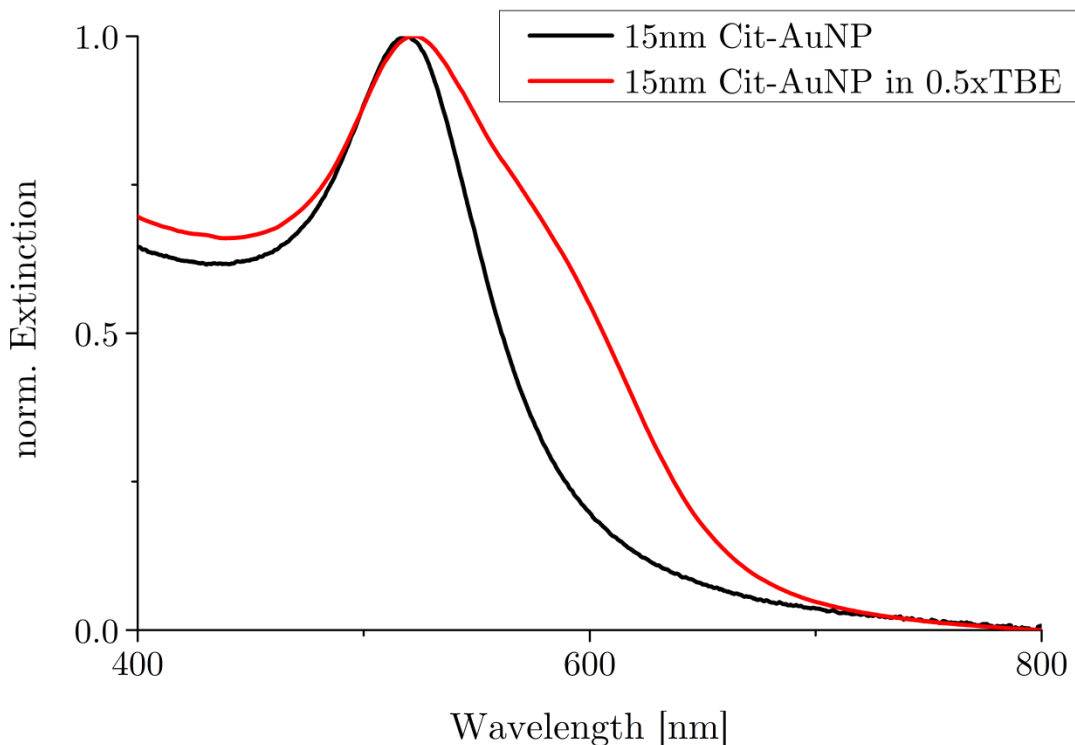
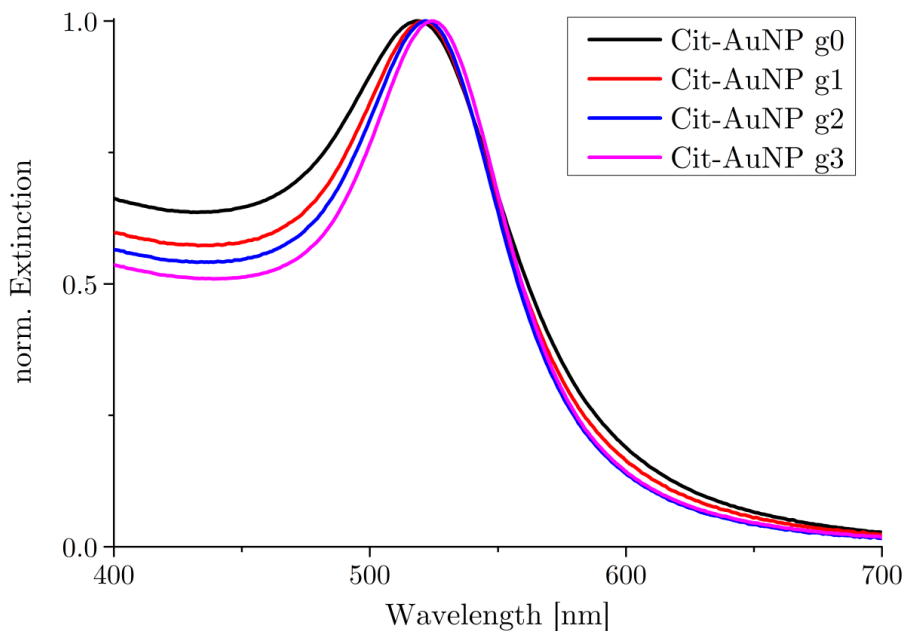


Figure 4.5: Extinction spectra of citrate-coated gold nanoparticles as-synthesised and in 0.5xTBE buffer. The aggregation of the gold nanoparticles leads to a shoulder in the spectrum caused by plasmon coupling.

Larger gold nanoparticles were synthesised using the protocol developed by the group of Puntes [62] (see [section 2.1.1](#)). In this method, as-synthesised gold nanoparticles used as seeds, which are subsequently grown by further addition of gold precursor ( $\text{NaAuCl}_4$ ) and citrate. After every three additions about half of the solution was extracted and termed generation  $n$ . The other half was further grown until the desired nanoparticle size is reached. The increase in nanoparticle size can be followed by UV-Vis spectroscopy as shown in [Figure 4.6](#). On the one hand, the peak of the LSPR shifted with increasing nanoparticle size due to the excitation of higher order modes as expected from the Mie theory considering a size-dependent

dielectric function [72] (see **section 2.1.2**). On the other hand, the absorbance at the LSPR peak increases with size, which can be explained by the larger volume and decreasing damping effects. The plasmon resonance shifted from 519 nm (g0, 12 nm) to 522 nm (g1, 18 nm), 523 nm (g2, 23 nm) and 525 nm (g3). The values for the plasmon shift as well as the size of the gold nanoparticles of g3 ( $30 \pm 3$  nm) determined with TEM were in good agreement with the results from Puntes *et al.* [62].

After functionalisation with BSPP, the respective UV-Vis spectra shifted by 3 nm. The gold nanoparticles were then stable enough to be concentrated by centrifugation. However, the larger gold nanoparticles are much more susceptible to aggregation even at relatively low sodium chloride concentrations of about 30 mM (**Figure 4.7**). It has been reported by several groups that the functionalization with short polyethylene glycol leads to a better stabilisation of gold nanoparticles [274, 275].



**Figure 4.6:** UV-Vis spectra of citrate-coated gold nanoparticles synthesised with the growth method from Bastús *et al.* Both, the shift of the plasmon peak and the changing ratio  $A_{400}/A_{\max}$  indicate the growth of the nanoparticles.

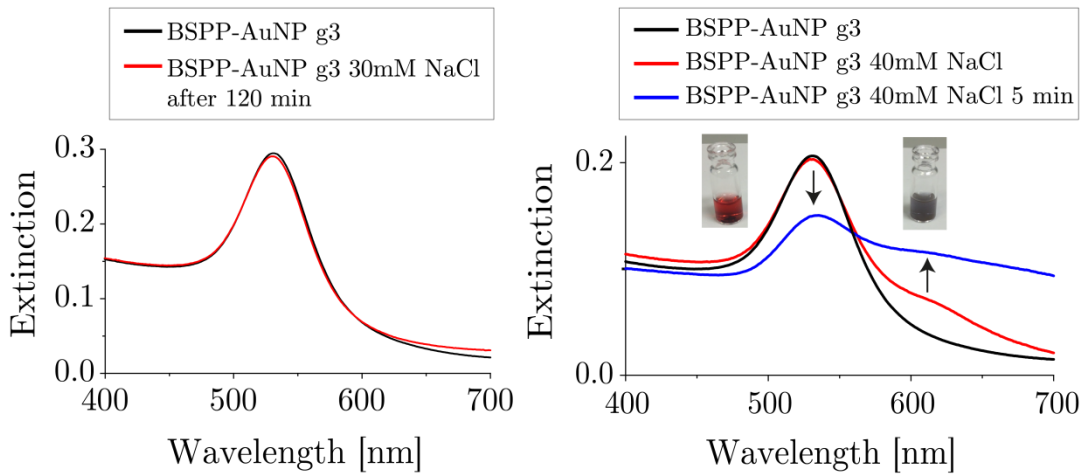


Figure 4.7: Stability of  $30 \pm 3$  nm BSPP-functionalised gold nanoparticles (g3) against NaCl. While there is no significant change in the UV-Vis spectra at 30 mM NaCl after 2 hours (left), aggregation is indicated by a shoulder at 620 nm and a decrease of the main peak after 5 minutes at 40 mM NaCl (right). The photographs show the colour change from red to blue due to agglomeration/aggregation of the gold nanoparticles.

Small gold nanoparticles with diameters of  $7.5 \pm 1.5$  nm were synthesised with sodium borohydride as a strong reducing agent [265]. Different from the Turkevich method, tiny gold nanoclusters are forming immediately after addition of NaBH<sub>4</sub>, which is indicated by an immediate colour change from yellow to brown. This brown solution contains gold nanoparticles of small diameters ( $d < 3$  nm), which do not have a plasmon resonance [64]. By adding several aliquots of the reducing agent these nanoclusters are grown successively leading to an orange/red solution due to the development of a LSPR.

Figure 4.8 shows a representative TEM image and the size distribution of the small gold nanoparticles. The mean diameter of the nanoparticles is 7.6 nm with a standard deviation of 1.3 nm. The extinction spectrum of the  $7 \pm 1.5$  nm gold nanoparticles has a significantly damped LSPR as expected (Figure 4.9). Additionally, the plasmon resonance is slightly blue-shifted at 519 nm. This behaviour is in accordance with the intrinsic size effects explained in section 2.1.2.

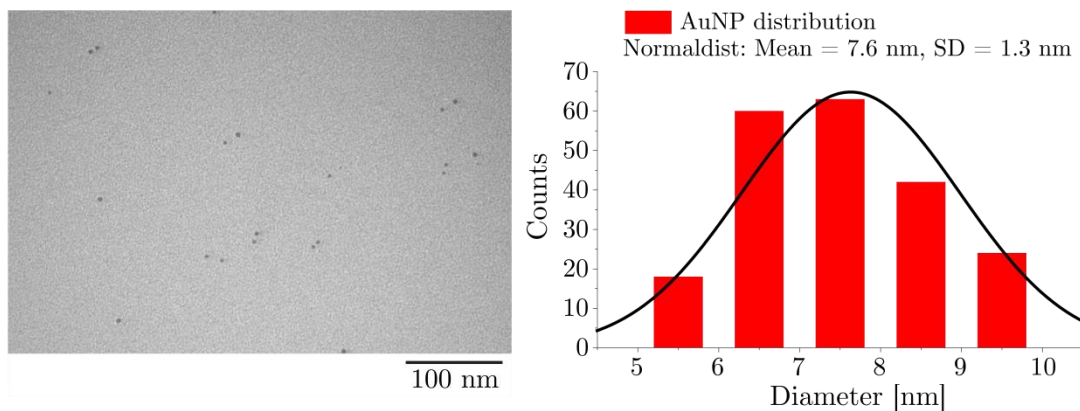


Figure 4.8: A representative TEM image and the size distribution of  $7 \pm 1.5$  nm AuNPs.

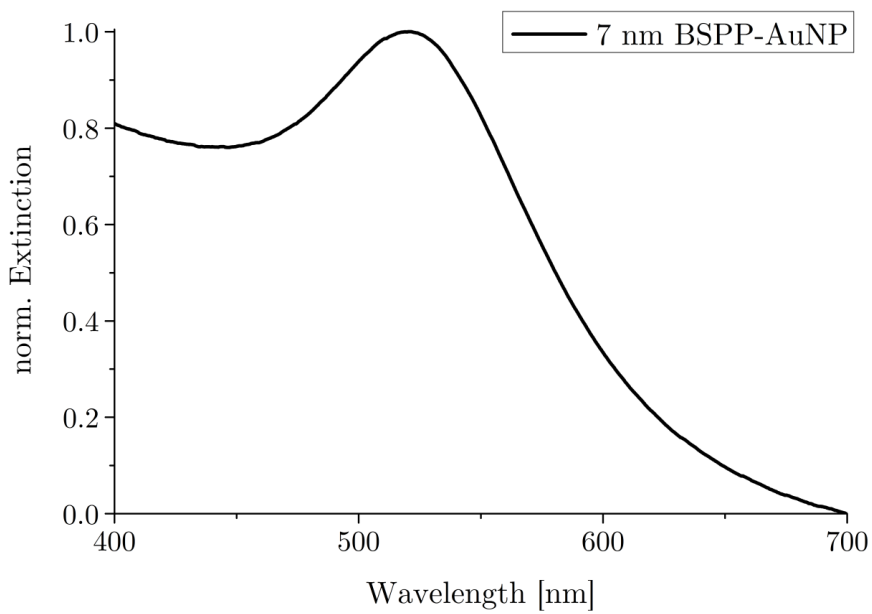
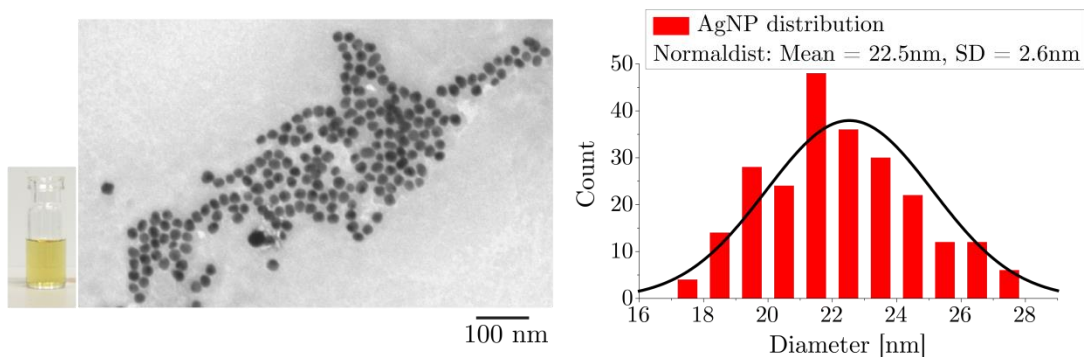


Figure 4.9: Extinction spectrum of BSPP-coated  $7 \pm 1.5$  nm gold nanoparticles.

#### 4.1.2 Silver nanoparticles

Silver nanoparticles were also synthesised by citrate reduction together with a small amount of tannic acid, which leads to faster nucleation according to Bastús *et al.* and therefore a narrower size distribution because of a longer size-focussing and shorter Ostwald ripening phase (see section 2.1.1) [68]. A representative TEM image of the as-synthesised AgNPs is shown in Figure 4.10. Similar to the gold nanoparticles, it can be seen that the nanoparticles are well separated due to the electrostatic stabilisation via adsorbed citrate ions and tannic acid. The size distribution of the silver nanoparticles has a mean value of 22.5 nm with a standard deviation of 2.6 nm.



The UV-Vis spectrum of as-synthesised silver nanoparticles consists of a strong absorption at 404 nm (Figure 4.11), which stems from the LSPR of the AgNP. The silver nanoparticles, similar to gold nanoparticles, are prone to aggregation if the ionic strength is raised. At a concentration of 50 mM NaCl a shoulder appears in the absorption spectrum. This is accompanied by a colour change from yellow to grey indicating the aggregation of the silver nanoparticles because of plasmon coupling between the particles in the clusters.

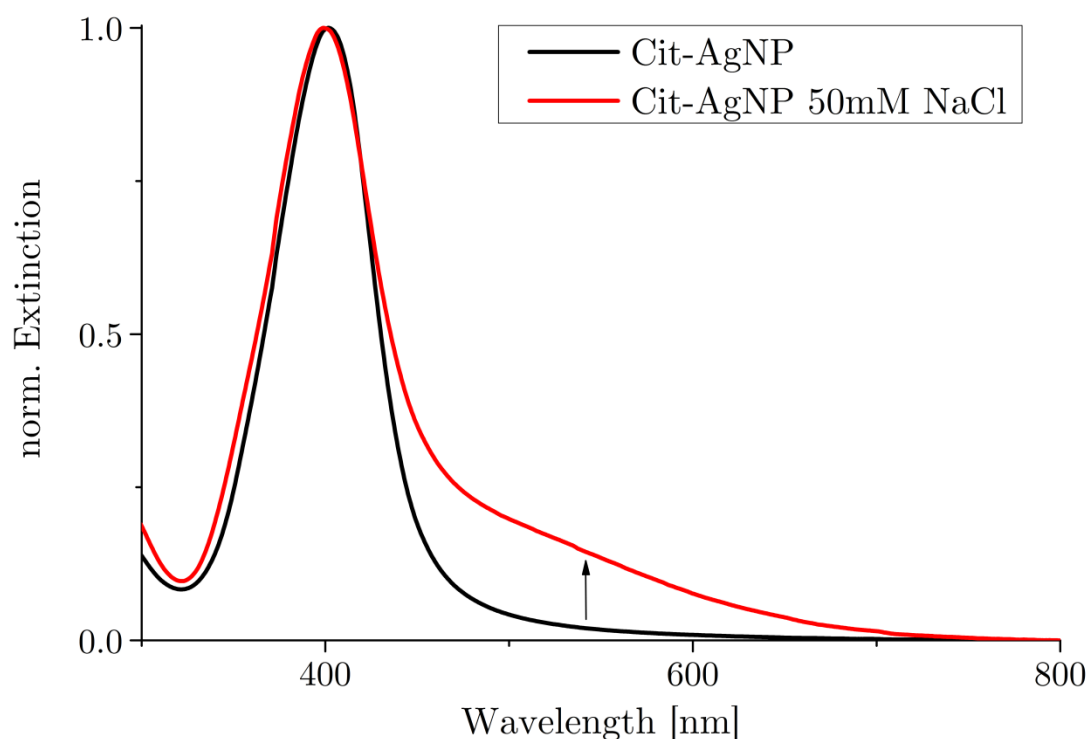


Figure 4.11: UV-Vis spectra of  $22.5 \pm 2.5$  nm citrate-coated AgNP without (black) and with 50 mM NaCl (red). The arrow indicates the development of a shoulder due to aggregation.

An attempt was made to increase the colloidal stability of the silver nanoparticles against ionic strength with thiolated methoxy polyethylene glycol (SH-mPEG) and folic acid. In several reports, thiols and primary amines were employed to post-functionalise silver nanoparticles [68, 276, 277]. However, it seems not to be clear, which functional groups forms a stronger bond with AgNP [278, 279]. Short PEGs are typically used to functionalise nanoparticles because they form dense monolayers on the surface. Folic acid has a terminal primary amine as an anchoring group and is a rather large molecule, which adds steric hindrance to the nanoparticle surface. In addition, this molecule has two terminal carboxyl groups, which provide electrostatic repulsion as well as the possibility to apply EDC/NHS coupling chemistry for further functionalisation [280].

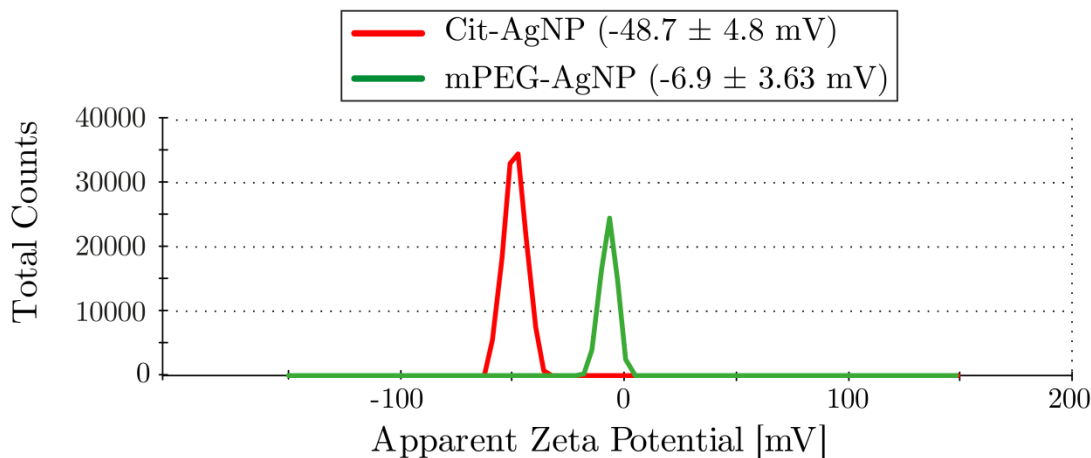


Figure 4.12: Zeta potentials of citrate- and SH-mPEG-coated silver nanoparticles. The significant reduction of the zeta potential from  $-48.7$  mV to  $-6.9$  mV indicates the ligand exchange with SH-mPEG.

$\zeta$ -potentials of as-synthesised citrate-coated and mPEG-functionalised silver nanoparticles are depicted in Figure 4.12. The citrate-stabilised AgNPs have a negative value of  $-48.7 \pm 4.8$  mV. On the other hand, there is a large decrease of the surface charge to  $-6.9 \pm 3.63$  mV after functionalisation with SH-mPEG. A decrease of the surface charge was expected after ligand exchange because the mPEG ligand is nearly neutral [281]. Even though the surface charge is now close to neutral, the colloidal stability is increased due to steric effects stemming from the dense mPEG layer on the surface.

Unexpectedly, silver nanoparticles mixed with SH-mPEG showed a small blue shift of 2-3 nm compared with the citrate-coated AgNP (Figure 4.13). Typically, the LSPR of

AgNPs blue-shifts when their size decreases. It is known that silver nanoparticles are prone to dissolution, which might have happened during the functionalisation process. However, when the ionic strength is increased to a final concentration of 100 mM NaCl, only a small rise in the 500 nm region is visible. Thus, it can be concluded that the SH-mPEG molecules attached to the AgNPs making them more stable against ionic strength. Similar results were obtained using folic acid as a ligand (Figure 4.14). Again, there was a small blue-shift in the absorption maximum, which was not expected. Similar to the SH-mPEG functionalised AgNP, the nanoparticles are stable to a sodium chloride concentration of at least 100 mM.

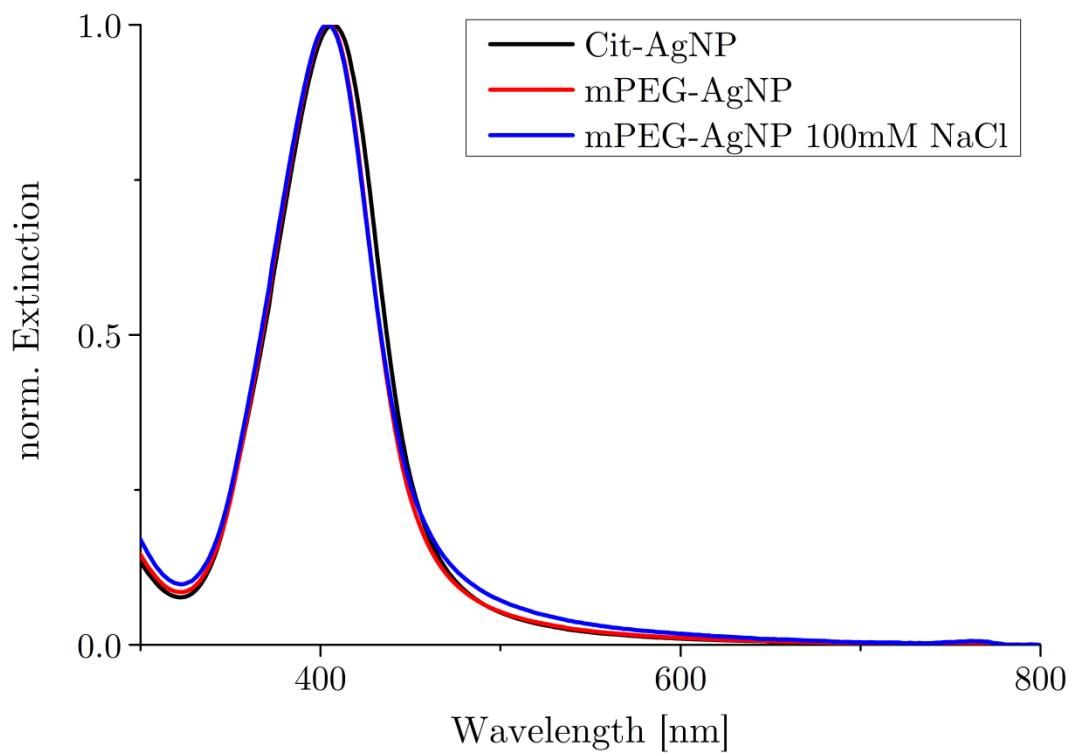


Figure 4.13: UV-Vis spectra of  $22.5 \pm 2.5$  nm SH-mPEG and citrate functionalised silver nanoparticles.

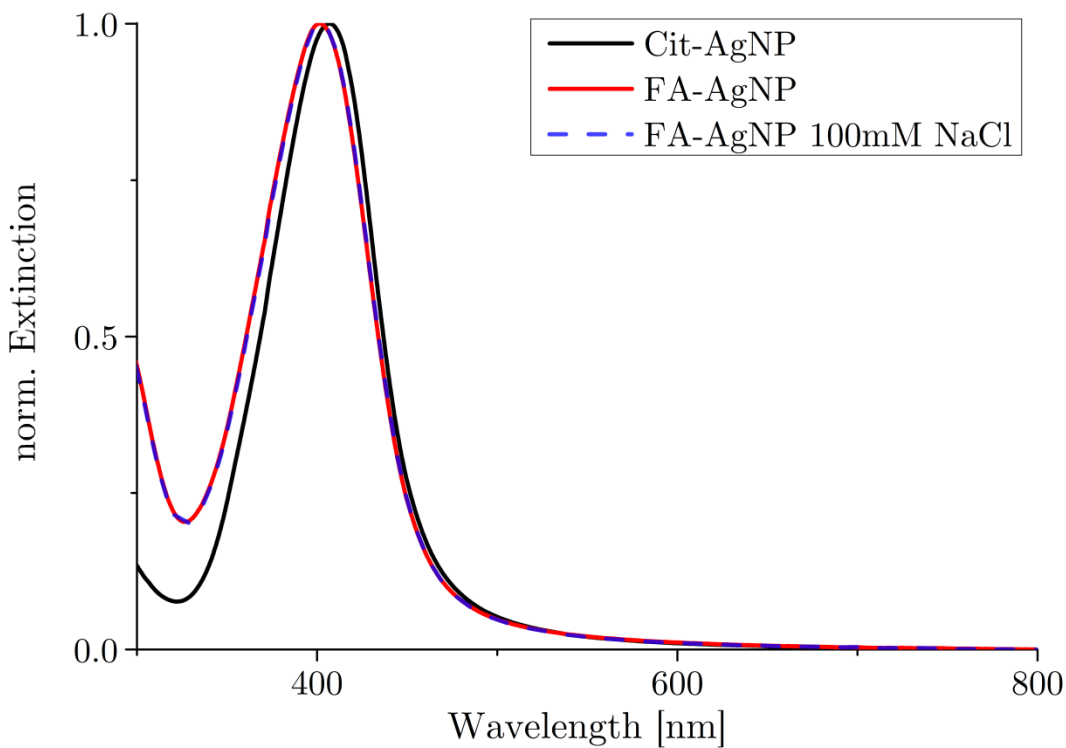


Figure 4.14: UV-Vis spectra of  $22.5 \pm 2.5$  nm folic acid-functionalised and citrate-capped silver nanoparticles.

## 4.2 Semiconductor quantum dots

Semiconductor quantum dots were synthesised via the hot-injection method as outlined in **section 2.1.3**. The synthetic protocol published by Bae *et al.* is carried out by first dissolving zinc acetate and cadmium oxide in a mixture of oleic acid and 1-octadecene at  $150^\circ\text{C}$  yielding the complexed precursors  $\text{Zn}(\text{OA})_2$  and  $\text{Cd}(\text{OA})_2$ , respectively [118]. The reaction temperature is then raised to  $310^\circ\text{C}$  before a mixture of TOP-S and TOP-Se is injected in order to create nucleation burst leading to a single species of quantum dots (see **section 2.3.1**). The protocol differs from typical synthesis methods because the CdSe core and the ZnS shell are grown at the same time giving rise to alloyed nanoparticles with a continuous transition from core to shell, which is denoted as  $\text{Cd}_{1-x}\text{Se}_x\text{Zn}_{1-y}\text{S}_y$  (**Figure 4.15**).

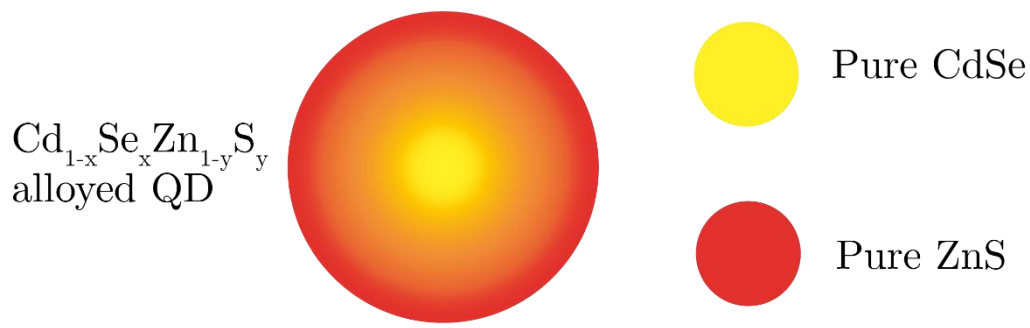


Figure 4.15: Illustration of the composition gradient in  $\text{Cd}_{1-x}\text{Se}_x\text{Zn}_{1-y}\text{S}_y$  quantum dots. The core (yellow) consists of CdSe and the outer shell layers of ZnS.

A representative TEM image of as-synthesised quantum dots with an emission maximum at  $\lambda_{\text{max}} = 520$  nm (QD520) and their size distribution are presented in **Figure 4.16**. From the same sample an EDX spectrum was acquired in order to verify that all the four elements are present. The peaks were assigned to certain elements by comparison with EDX tables containing information about the energies of the characteristic X-rays. All four elements (Cd,Zn,Se,S) were clearly observed as expected (**Figure 4.17**). In addition, several other elements (C,O,Si,P,Cu) were also detected. While carbon, oxygen, silicon and copper are background signals from the TEM grid and grid holder, the phosphorus signal can be explained with the TOP bound on the nanoparticle surface. The EDX measurements only give a qualitative elemental composition of the ensemble of nanoparticles. In order to verify that the nanoparticles consist of alloys, different techniques such as EELS would be needed, which allows determining the elemental distribution spatially within the particles.

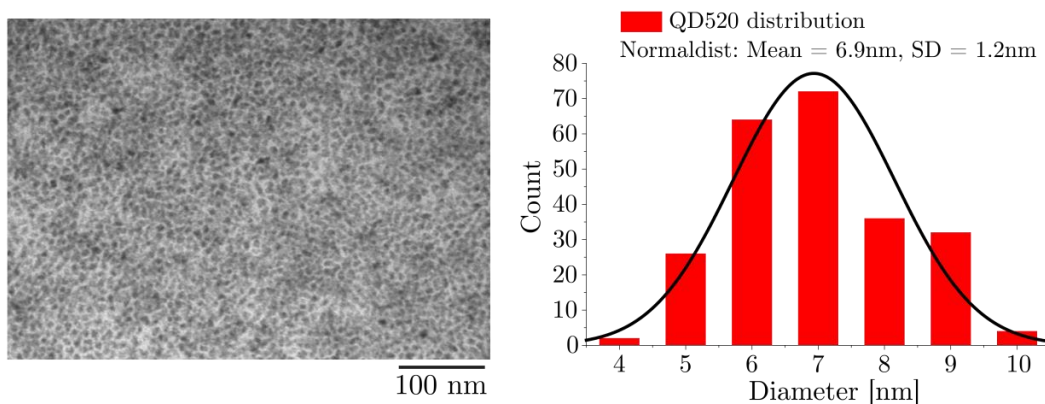


Figure 4.16: Representative transmission electron micrograph of  $\text{Cd}_{1-x}\text{Se}_x\text{Zn}_{1-y}\text{S}_y$  quantum dots (QD520) and their size distribution.

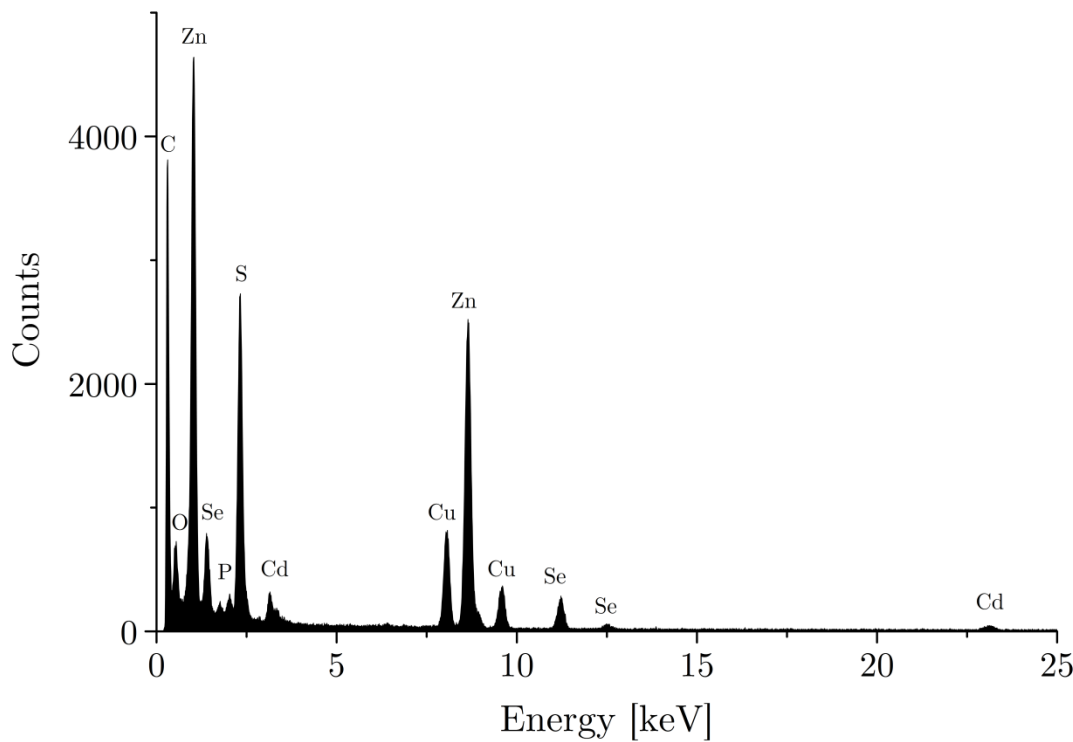


Figure 4.17: EDX spectrum of semiconductor quantum dots (QD520).

In many procedures, the CdSe core and the ZnS shell are grown with a two-step method increasing the control of the nanoparticle size as well as the thickness of the shell for optimised emission wavelengths and quantum yields [104]. A capping shell reduces the surface defects and non-radiative trap states, which improves the quantum yield of the nanoparticles (see [section 2.1.3](#)). However, this procedure is by far more time consuming. Bae *et al.* investigated the consumption of the reactants and found that the cadmium and selenium precursors are by far more reactive than the other two [118, 119]. Therefore, a CdSe core is formed very rapidly until almost all of one precursor is depleted followed by growth of the shell. The emission spectrum of the quantum dots can accordingly be tuned by changing the amounts of selenium because larger cores are synthesised with a higher amount of selenium precursor causing a red-shift of the emission maximum (see [section 2.1.4](#)).

The absorption and emission spectra of four different quantum dots that were synthesised with varying amounts of selenium are presented in [Figure 4.18](#). The emission maximum of the quantum dots was tuned from 480 nm (QD480) to 580 nm (QD580) with increasing amounts of selenium as expected. Furthermore, the quantum dots showed a Gaussian emission profile with a FWHM of about 40 nm. The shift of the emission wavelength can be explained with the quantum

confinement, which states that smaller nanoparticles emit at shorter wavelengths (see **section 2.1.3**). While the emission changes with the amount of selenium precursor, the actual sizes of the CdSe cores could not be determined due to the low resolution of the TEM. The quantum yield of these quantum dots varied depending on their size. Since the amount of shell precursors (Zn, S) was kept constant, it might be that the shell was growing too large, which negatively influenced the quantum yield [104]. In particular, the sample QD480 had a significantly lower PLQY than the other samples, which can be seen directly in **Figure 4.19**. While the samples QD520, QD540 and QD580 fluoresce very strongly, the blue quantum dots are shining much weaker.

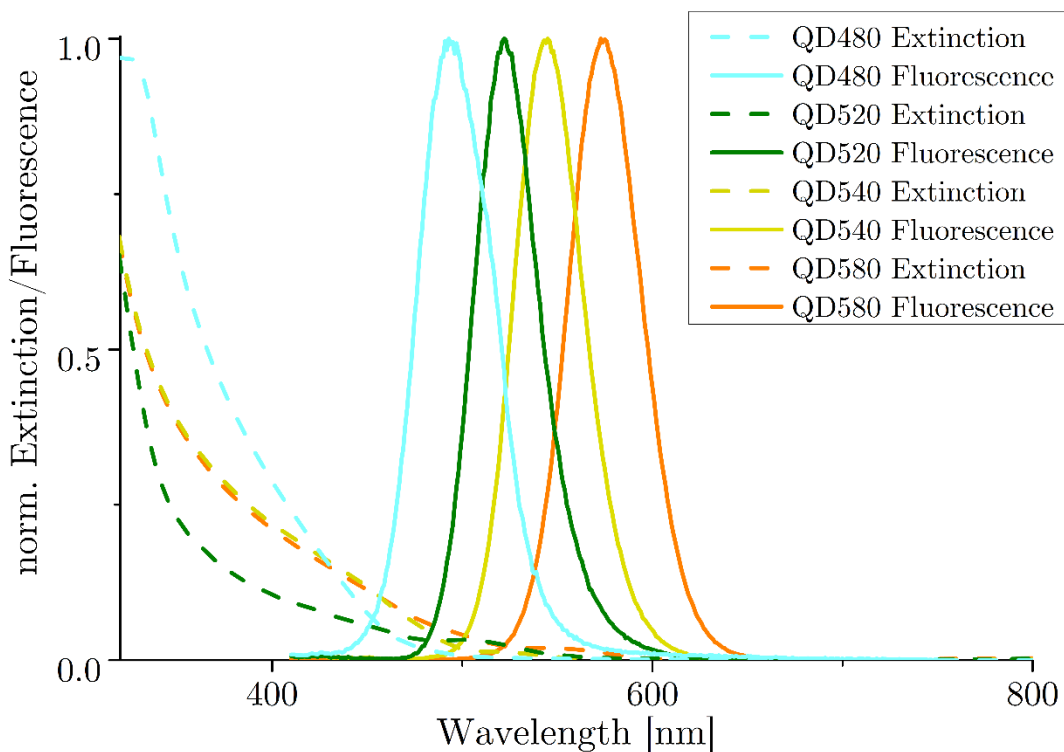


Figure 4.18: Extinction and fluorescence spectra of different  $\text{Cd}_{1-x}\text{Se}_x\text{Zn}_{1-y}\text{S}_y$  quantum dots. The excitation was at 400 nm.

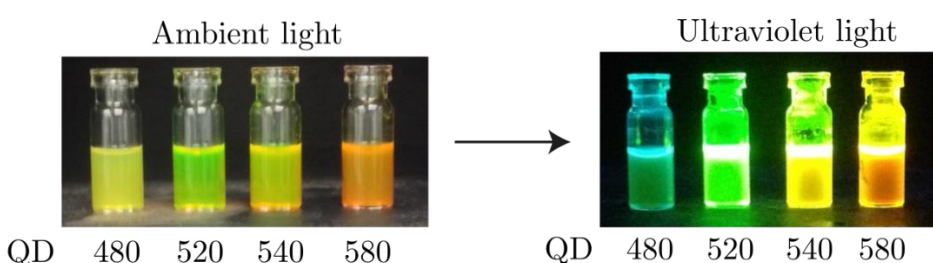


Figure 4.19: Photographs of quantum dots (QD480-QD580) under ambient light and under UV irradiation.

The as-synthesised quantum dots were highly soluble in many organic solvents due to the surface capping with oleic acid and trioctylphosphine. In order to be able to attach DNA on these particles they had to be transferred to aqueous solution. This was done by exchanging the organic ligands with L-lipoic acid, which had a higher affinity towards the zinc sulphide shell through the two thiol groups [171, 282]. The group of Matoussi have developed a rapid exchange of the ligands by activation with UV light [266] (Figure 4.20). The dithiolane ring in the lipoic acid was opened by irradiation with UV-A light and two sulfanyl radicals are formed, which readily react with the quantum dot surface. The reaction was performed in methanol in order to minimise side reactions with oxygen and hydrogen. The reaction can be monitored by measuring the absorption at 333 nm stemming from the dithiolane ring (Figure 4.20). After irradiation for 30 minutes, the absorption peak has completely vanished indicating the opening of the ring. Additionally, the inset images show that the former yellow lipoic acid solution turned colourless after irradiation.

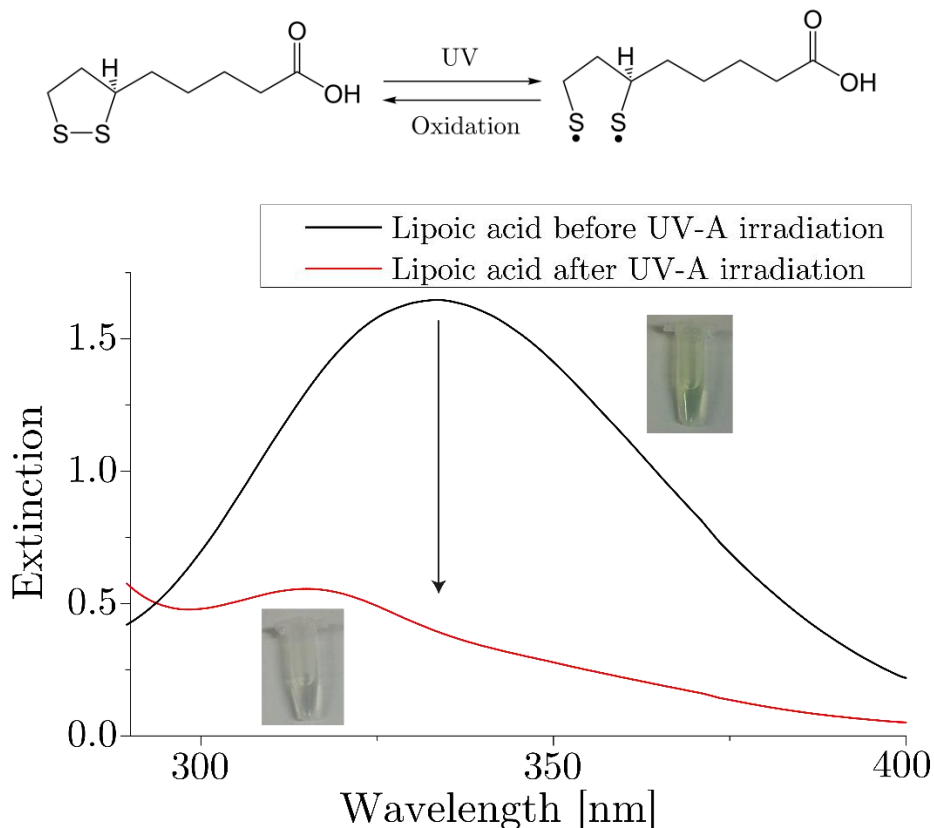


Figure 4.20: Top: Activation of L-lipoic acid by cleaving the dithiolane bond with UV-A irradiation. Bottom: In the course of the reaction the absorption peak at 333 nm drops indicating the opening of the ring structure. The photographs show the colour change from yellow to colourless due to the opening of the ring.

The activated lipoic acid was then added to the quantum dots under vigorous stirring, which led to an immediate transfer from the organic phase to the methanol phase indicating the successful ligand exchange. The quantum dots exhibit a small broadening in the emission after functionalization (Figure 4.21). The carboxylic group of the lipoic acid serves two purposes. Firstly, it protects the quantum dots from aggregation through electrostatic repulsion in near-neutral and alkaline media. Secondly, it is used as an anchor for the attachment of amine-modified DNA via EDC/Sulfo-NHS coupling (see section 4.5.3).  $\zeta$ -potential measurements presented in Figure 4.22 reveal a negatively charged surface with a potential of  $-35 \pm 4.58$  mV. Therefore, the charge is large enough to provide a good colloidal stability. This can be further seen in a TEM micrograph of the water-soluble quantum dots (Figure 4.23) showing that the quantum dots are well-dispersed after functionalisation with lipoic acid. It should be noted that it cannot be ruled out that a certain number of ligands are bent over with the carboxyl group facing towards the surface. This could be analysed by IR spectroscopy because the carboxyl group is sensitive to its different states (protonated/unprotonated, bound/unbound).

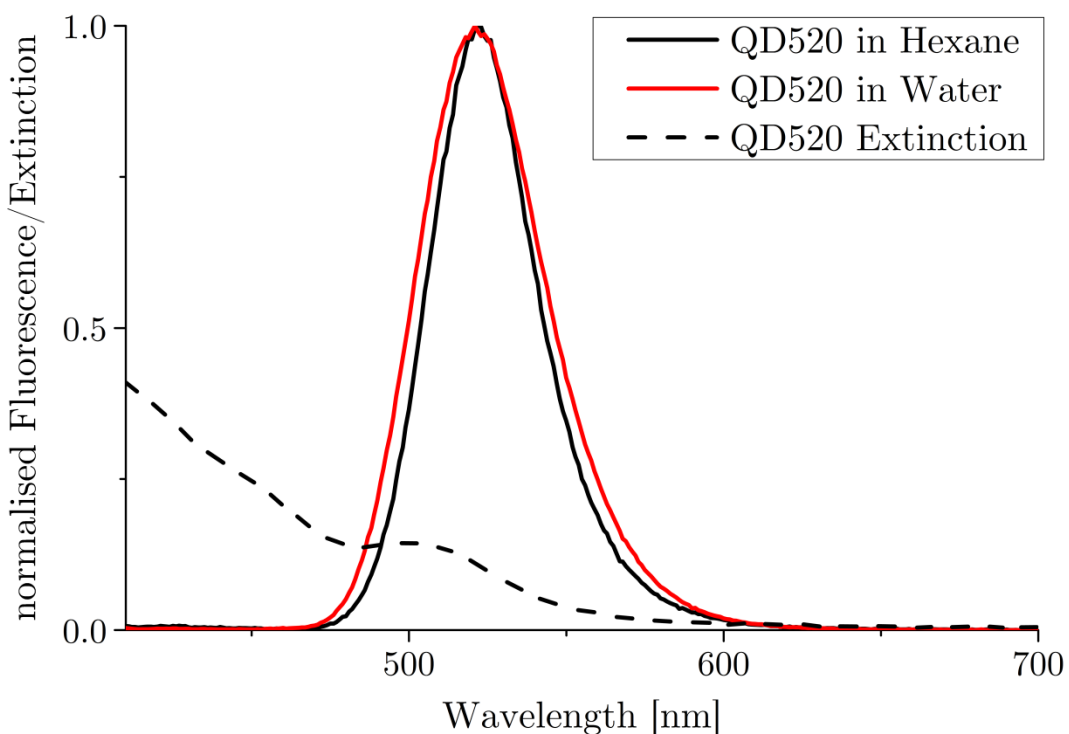


Figure 4.21: Fluorescence spectra of QD520 in hexane and after transfer to water. The extinction spectrum was acquired in water. The excitation was at 400 nm.

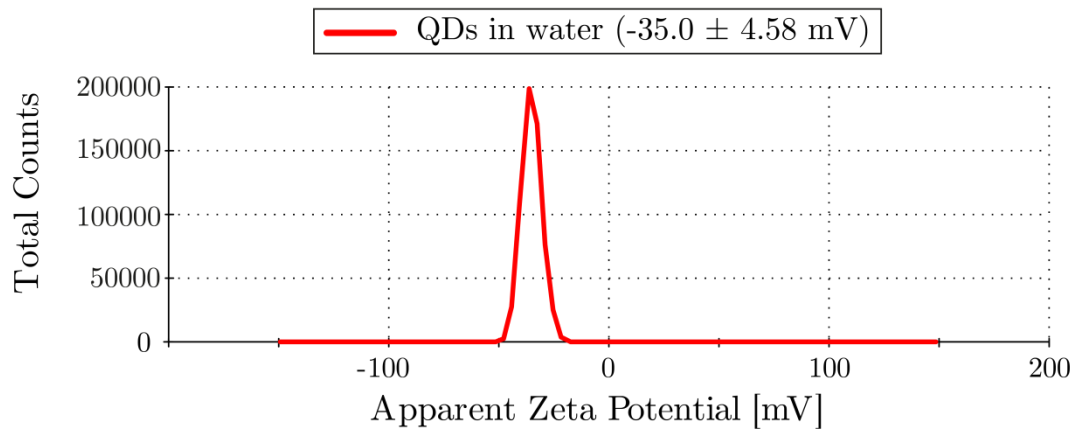


Figure 4.22: Zeta potential of L-lipoic acid-functionalised quantum dots in water.

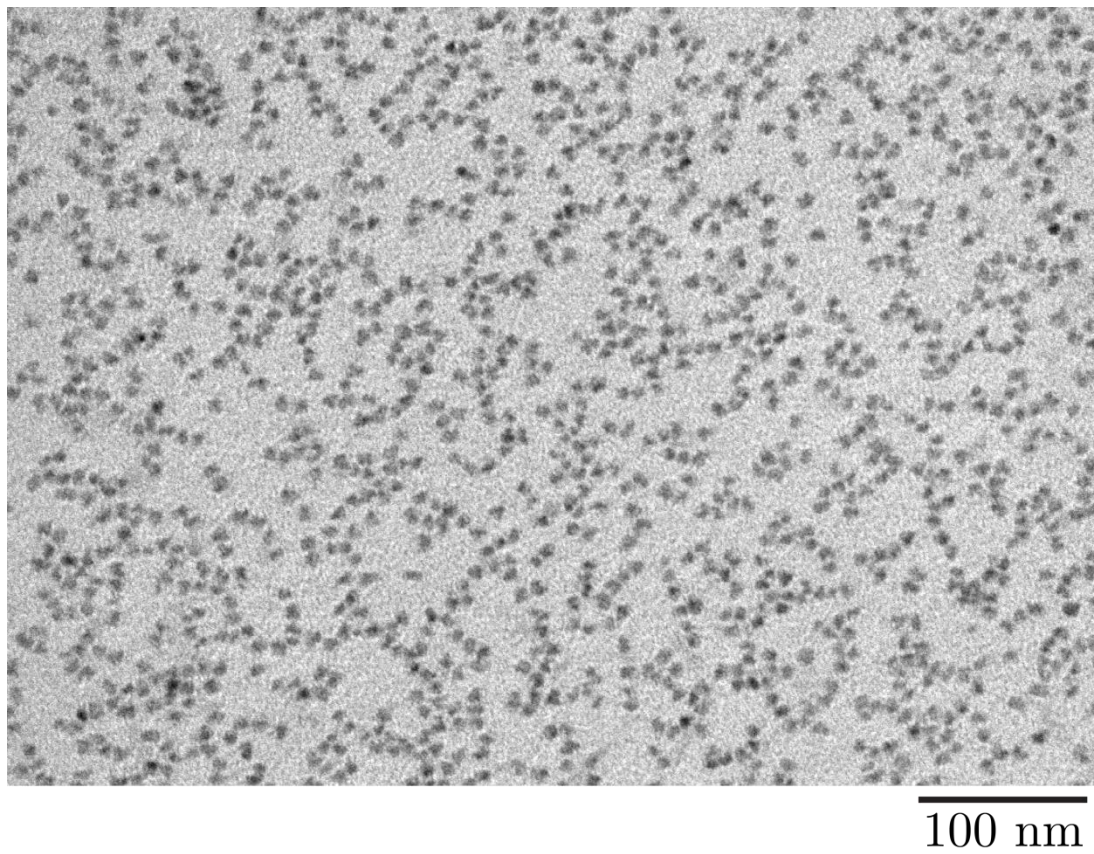


Figure 4.23: TEM micrograph of quantum dots (QD520) functionalised with lipoic acid.

### 4.3 Upconversion nanoparticles

Upconversion nanoparticles were synthesised by solvothermal decomposition according to the protocol of Li *et al.* [137]. Chloride salts of yttrium, ytterbium and erbium or thulium were first dissolved in oleic acid at 150°C to form  $\text{Y(OA)}_3$ ,  $\text{Yb(OA)}_3$  and  $\text{Er(OA)}_3$  or  $\text{Tm(OA)}_3$  precursors. Then, sodium fluoride and sodium

hydroxide in methanol are slowly added to the solution at room temperature. After evaporation of the non-organic solvents methanol and water, the temperature is quickly increased to 300°C, which led to nucleation and growth of the upconversion nanoparticles. The resulting nanoparticles were made of a NaYF<sub>4</sub> template in which a certain percentage of Y<sup>3+</sup> ions were replaced by Yb<sup>3+</sup> and Er<sup>3+</sup> (NaYF<sub>4</sub>:Yb,Er) or Tm<sup>3+</sup> (NaYF<sub>4</sub>:Yb,Tm). The doping concentration was controlled by the amounts of rare earth metal precursor. The resulting nanoparticles were protected with oleic acid ligands making them soluble in many organic solvents.

A TEM image of thulium doped upconversion nanoparticles is shown in **Figure 4.24**. For both, erbium and thulium-doped upconversion nanoparticles, EDX spectra were acquired to check the chemical composition of the nanoparticles (**Figures 4.25 and 4.26**). As discussed before, the elements not belonging to the nanoparticles were associated with the TEM grid and the TEM grid holder. It should be noted that the first ytterbium line (1.521 keV) and thulium line (1.462 keV) are too close to each other to be spectrally resolved. Furthermore, the thulium line at higher energy (7.179 keV) is hidden in the strong copper peak. This is an example of the limitation of this technique. Nevertheless, the EDX analysis was only used as a complementary characterisation technique and the presence of thulium was evident from the photoluminescence spectrum.

The EDX spectrum of erbium doped upconversion nanoparticles is shown in **Figure 4.26**. Here, the same peaks stemming from the elements of the nanoparticle are clearly visible again. In addition, a small peak from the erbium (6.949 keV) can be seen. The low intensity can be explained with the low doping (2%) of erbium. There is another small peak visible at about 10 keV, which is only explainable as an impurity from the apparatus (grid, grid holder). Nevertheless, this peak does not influence the conclusion of the measurements.

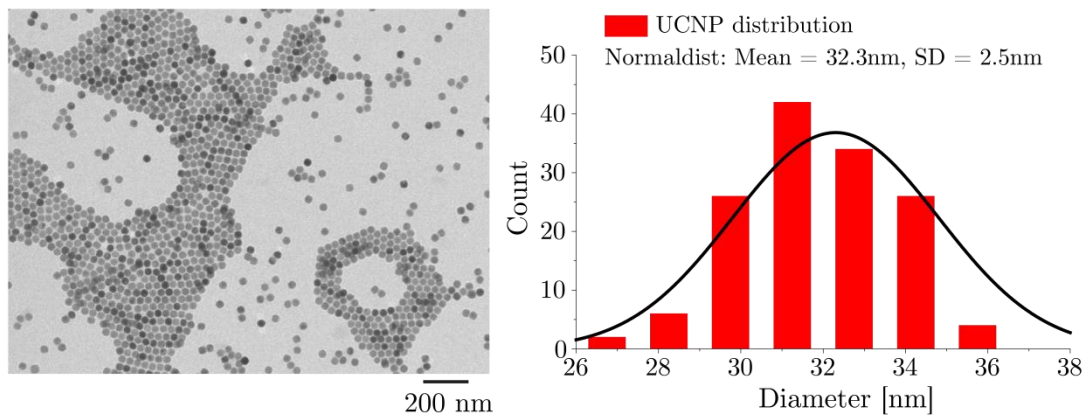


Figure 4.24: TEM micrograph and size distribution of  $\text{NaYF}_4:\text{Yb,Tm}$  upconversion nanoparticles.

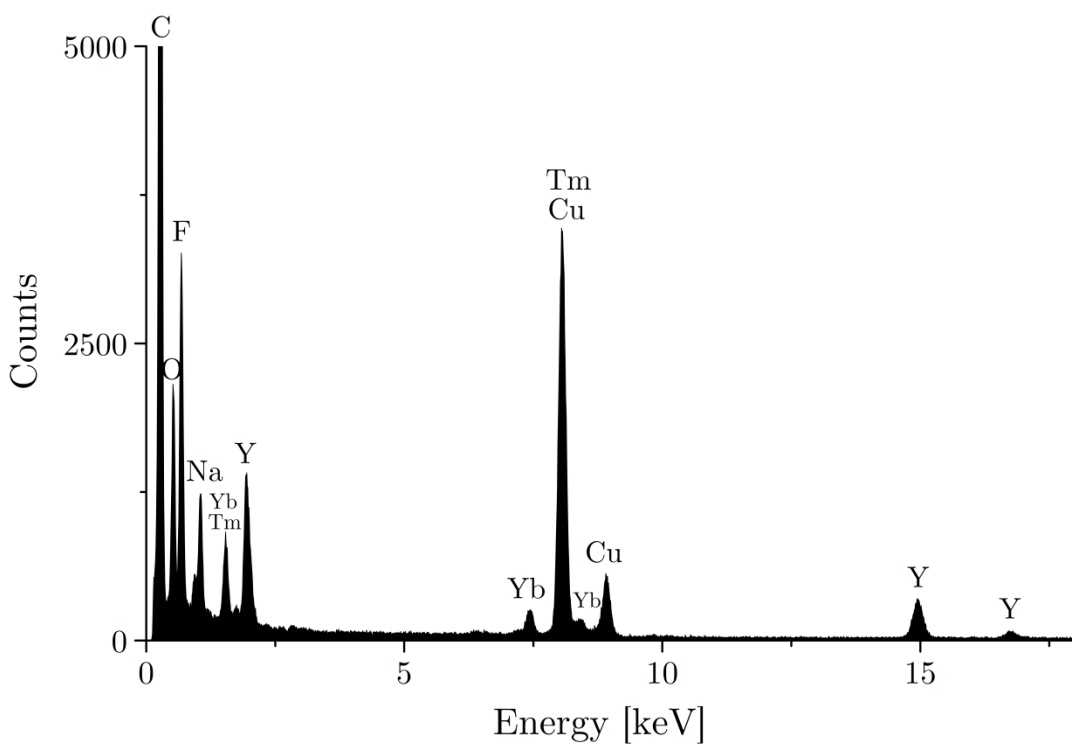


Figure 4.25: EDX spectrum of  $\text{NaYF}_4:\text{Yb,Tm}$  upconversion nanoparticles.

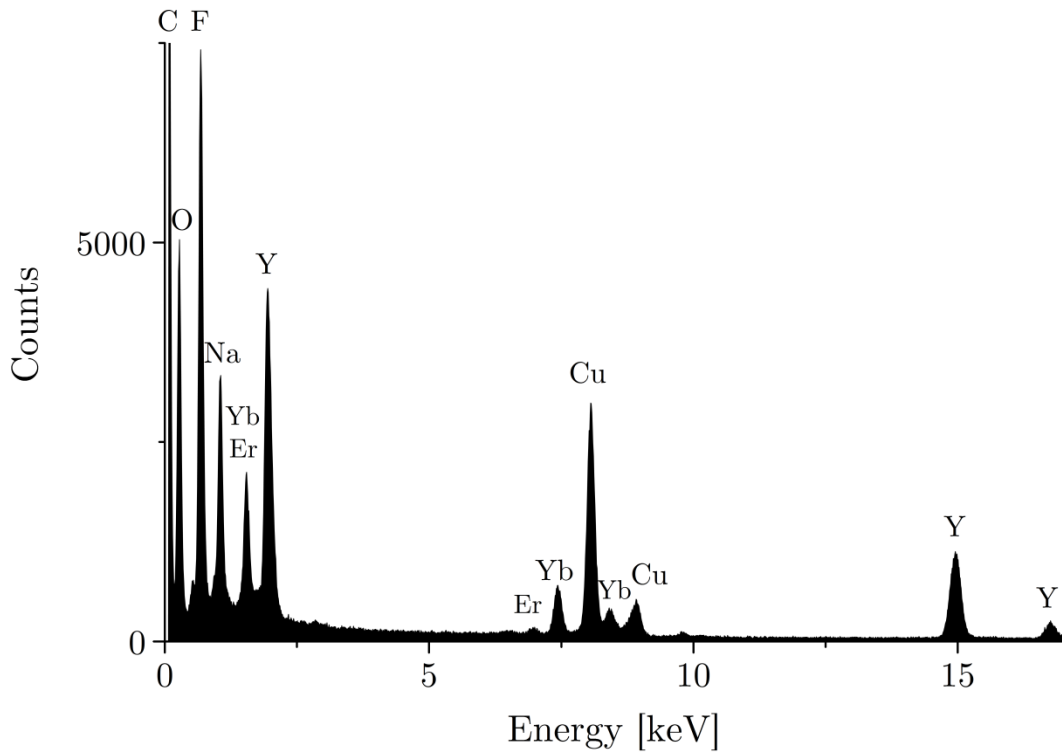


Figure 4.26: EDX spectrum of  $\text{NaYF}_4:\text{Yb,Er}$  upconversion nanoparticles.

The emission of the rare-earth doped nanoparticles is very peculiar due to its large anti-stokes shift [28]. Even though this is a multi-photon process, rather efficient upconversion can already be achieved with photodiodes instead of ultrafast lasers (section 2.1.6). Energy transfer from the ytterbium atoms to the co-doped thulium and erbium atoms leads to their dopant-specific emission spectra [144]. In the case of erbium doped nanoparticles, emissions in the green at 522 nm and 541 nm and in the red at 658 nm are present, which belong to the transitions of  $^2\text{H}_{11/2}$ ,  $^4\text{S}_{3/2} \rightarrow ^4\text{I}_{15/2}$  and  $^4\text{F}_{9/2} \rightarrow ^4\text{I}_{15/2}$ , respectively (Figure 4.27). Thulium-doped nanoparticles have a different emission spectrum consisting of two lines in the blue at 450 nm and 474 nm, one in the red at 650 nm and one in the NIR at 798 nm. The transitions for these lines are  $^1\text{D}_2 \rightarrow ^3\text{F}_4$ ,  $^1\text{G}_4 \rightarrow ^3\text{H}_6$ ,  $^1\text{G}_4 \rightarrow ^3\text{F}_4$  from blue to red and  $^1\text{G}_4 \rightarrow ^3\text{H}_5$  and  $^3\text{H}_4 \rightarrow ^3\text{H}_6$  for the infrared line [144]. The different emission channels can to a certain degree be influenced by different concentration of rare-earth dopants [145, 283]. A comparison between thulium doped nanoparticles with different thulium concentrations evidently shows that the ratio between the blue and the infrared line is biased towards the blue for a lower thulium doping (Figure 4.28).

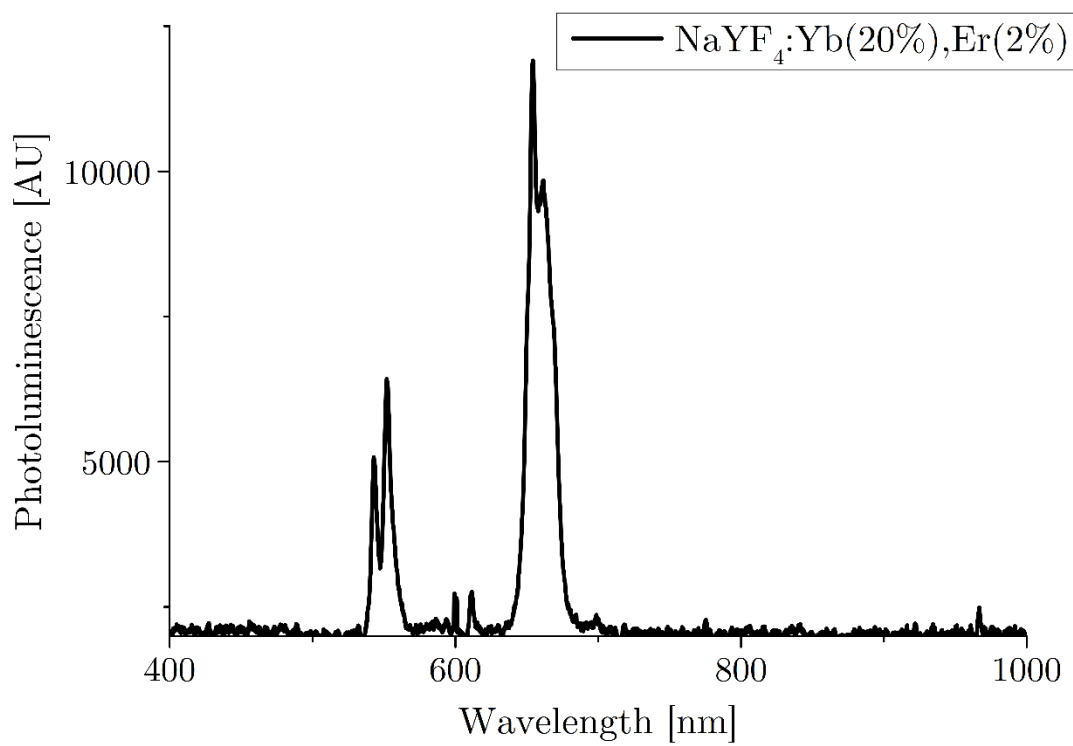


Figure 4.27: Emission spectrum of  $\text{NaYF}_4$ :Yb,Er upconversion nanoparticles. The excitation wavelength was 980 nm.

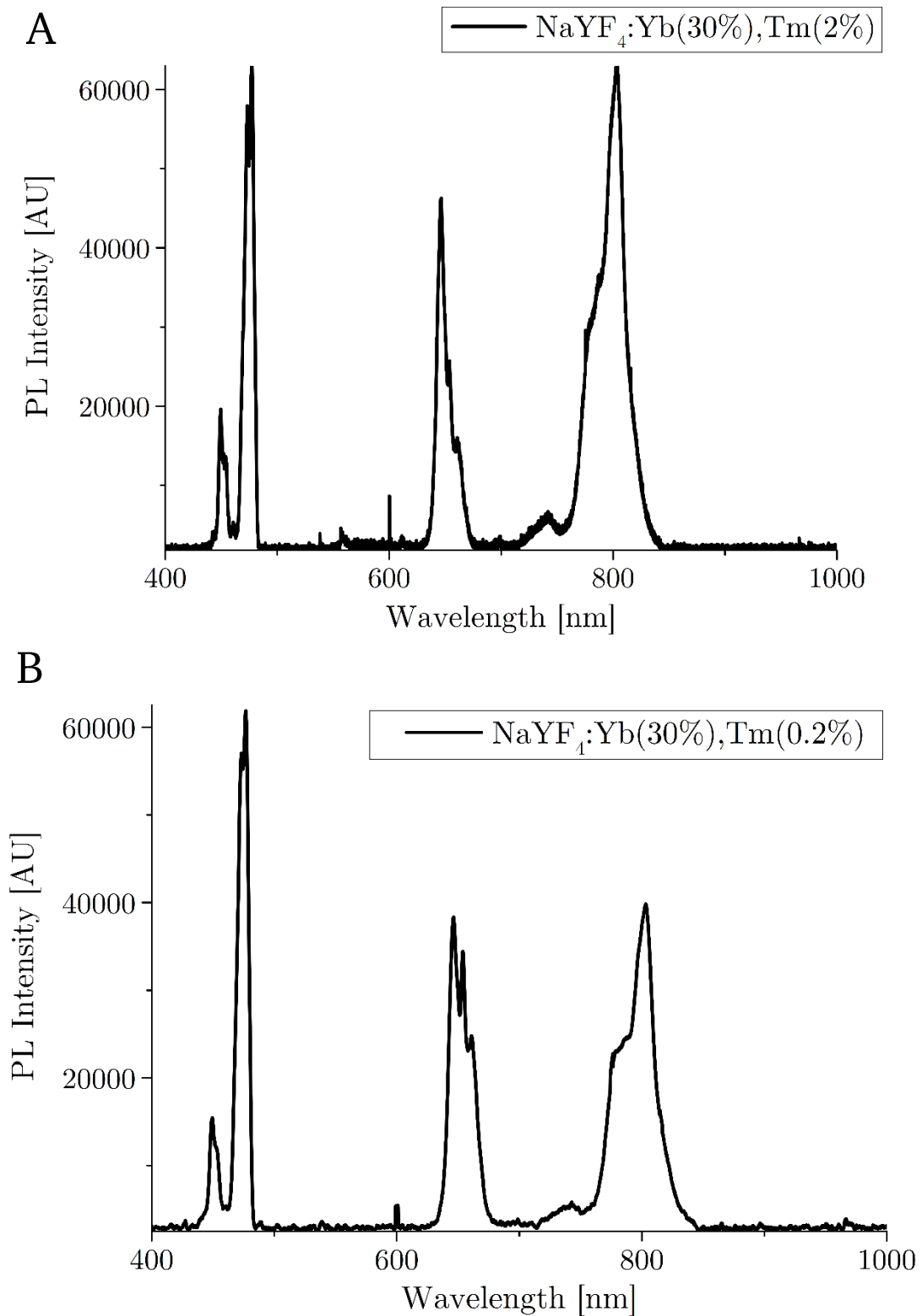


Figure 4.28: Emission spectrum of NaYF<sub>4</sub>:Yb,Tm upconversion nanoparticles doped with 20% Yb,2% Tm (spectrum A) and 30% Yb,0.2% Tm (spectrum B). The excitation wavelength was 980 nm.

The oleic acid capped upconversion nanoparticles were rendered water-soluble by performing a ligand exchange reaction with polyacrylic acid (PAA) [267]. Different from the other nanoparticles, upconversion nanoparticles have no affinity towards amines or thiols [284]. Instead, it has been reported that negatively charged groups such as carboxyl groups are coordinated to the nanoparticle surface via electrostatic interaction with the yttrium and rare-earth cations. The replacement of the bound oleic acid was facilitated using multi-dentate ligands such as the polymer PAA. Both, the nanoparticles and the PAA were soluble in tetrahydrofuran (THF) so that the two components could be mixed together directly. Then, the ligand exchange slowly proceeded and after 24 hours the nanoparticles were readily soluble in aqueous solutions. The carboxyl groups of PAA served similar to the lipoic acid two purposes: Electrostatic stabilisation and coupling capabilities via EDC/sulfo-NHS chemistry. The degree of ligand replacement could not be determined. However, the solubility in aqueous media suggests that a major part of the OA was replaced with PAA.

$\zeta$ -potential measurements and TEM imaging was performed on the PAA-coated upconversion nanoparticle to provide additional characterisation. The  $\zeta$ -potential of  $-28.6 \pm 4.66$  mV indicated a high negative surface charge from the PAA (Figure 4.29). The TEM image in Figure 4.30 depicts the water-dispersed UCNPs showing that the ligand exchange was performed successfully.

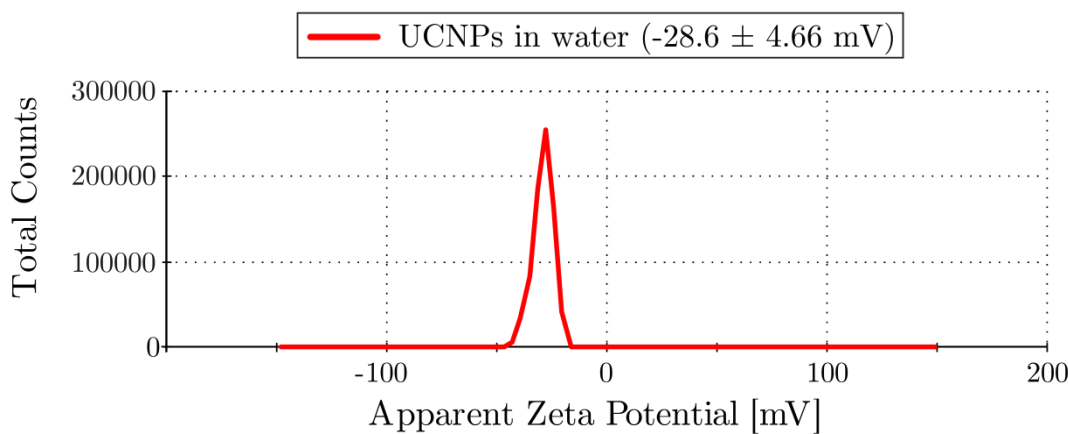


Figure 4.29: Zeta potential of PAA-coated upconversion nanoparticles in water.

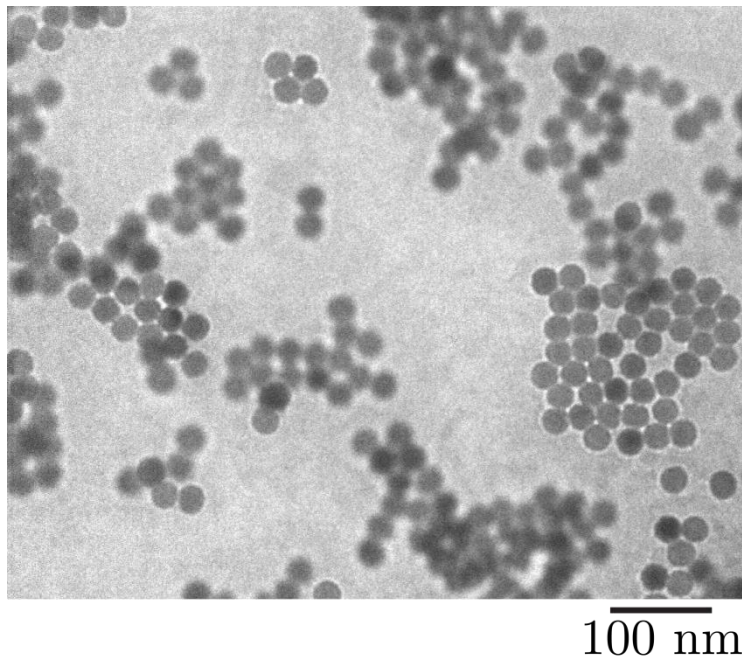


Figure 4.30: TEM micrograph of PAA-coated upconversion nanoparticles in water.

#### 4.4 Lead halide perovskite nanoparticles

In the last couple of years, lead halide perovskites became a very promising material for manufacturing efficient solar cells [33]. Very recently, methods for synthesising lead halide perovskite nanoparticles were developed and are rapidly evolving right [153, 155, 156]. In this work, two different methods were employed. First, a re-precipitation method will be discussed leading to small nanoparticles with diameters of around 5-7 nm. Then, a hot-injection method yielding larger particles will be described.

In the first method, a precursor solution containing the relevant constituents of the final nanoparticles was prepared. Typically, DMF was used because this solvent is suitable for dissolution of lead halide salts as well as methylammonium halide precursor. Furthermore, DMF is miscible with other organic solvents, which was essential for the re-precipitation method. The solution was dropped in an organic solvent (toluene) with a low solubility for the precursors inducing precipitation [285]. Due to the long aliphatic ligands present in solution, the growth was limited and small  $\text{CH}_3\text{NH}_3\text{PbX}_3$  ( $\text{X} = \text{I}, \text{Br}, \text{Cl}$ ) nanoparticles were formed. The composition of the nanoparticles depended on the mixture of halides in the precursor solution. A representative TEM image of as-synthesised  $\text{CH}_3\text{NH}_3\text{PbBr}_3$  nanoparticles together with their size distribution is shown in Figure 4.31. It can be seen that the

nanoparticles are very small with a mean diameter of only 3.4 nm with a standard deviation of 0.6 nm.

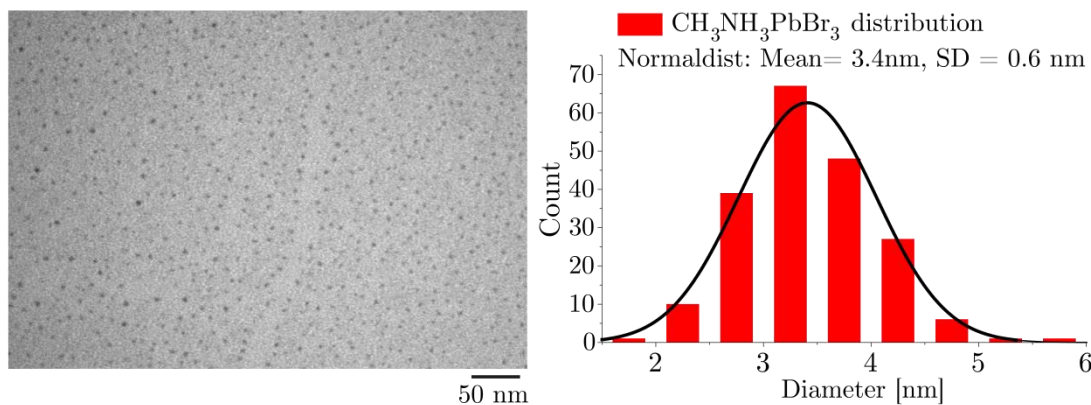


Figure 4.31: TEM micrograph and size distribution of  $\text{CH}_3\text{NH}_3\text{PbBr}_3$  nanoparticles synthesised with a re-precipitation method.

Similar to the semiconductor quantum dots, the fluorescence of the perovskite nanoparticles was visible by the naked eye under ambient light indicating high quantum yields. Spectroscopic analysis consisting of extinction, fluorescence and photoluminescence excitation (PLE) spectra of these perovskites nanoparticles is presented in Figure 4.32. All spectra were taken with nanoparticles in suspension. The fluorescence of the perovskite nanoparticles had its peak at 522 nm and a FWHM of only 25 nm. This emission matched the band gap, which can be seen in the extinction spectrum at 520 nm. In addition to the band gap onset, there was an intense peak in the extinction spectrum. In order to examine if this peak also contributed to the emission at 522 nm a PLE spectrum was taken. The PLE graph follows the extinction spectrum showing that the excitation at the peak wavelength also contributed to the fluorescence at 522 nm. The explanation might be that there was a higher energy state, which was resonantly excited similar to the higher exciton peaks visible in quantum dot spectra [286]. However, it remains unclear why the peak is as intense.

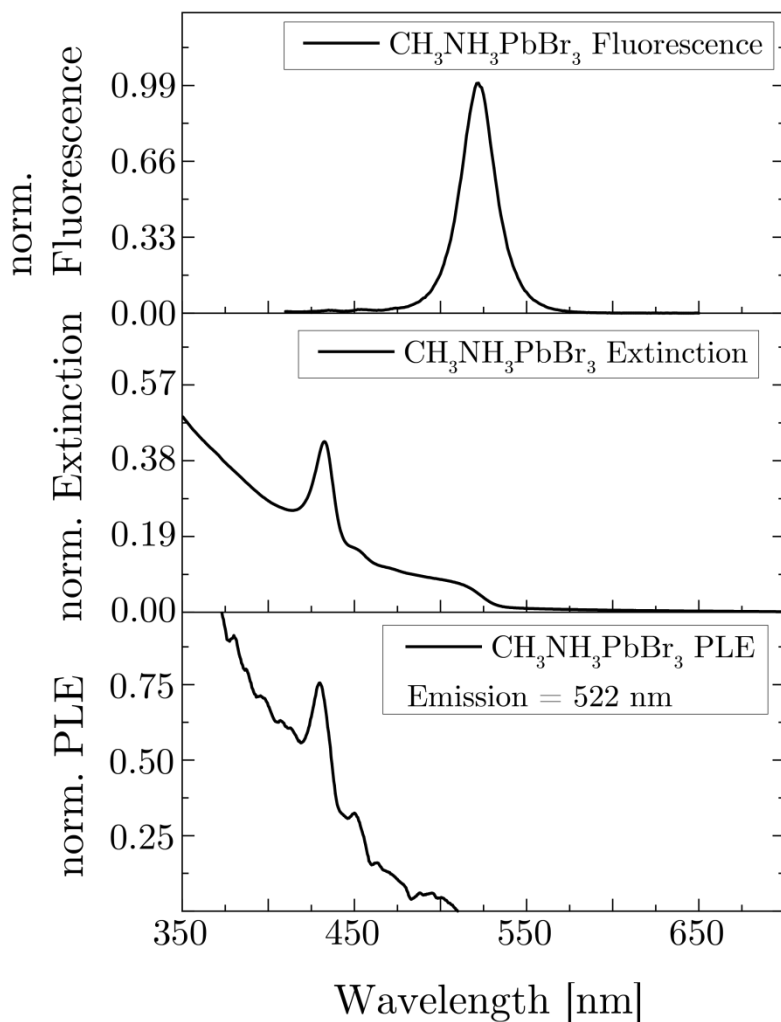
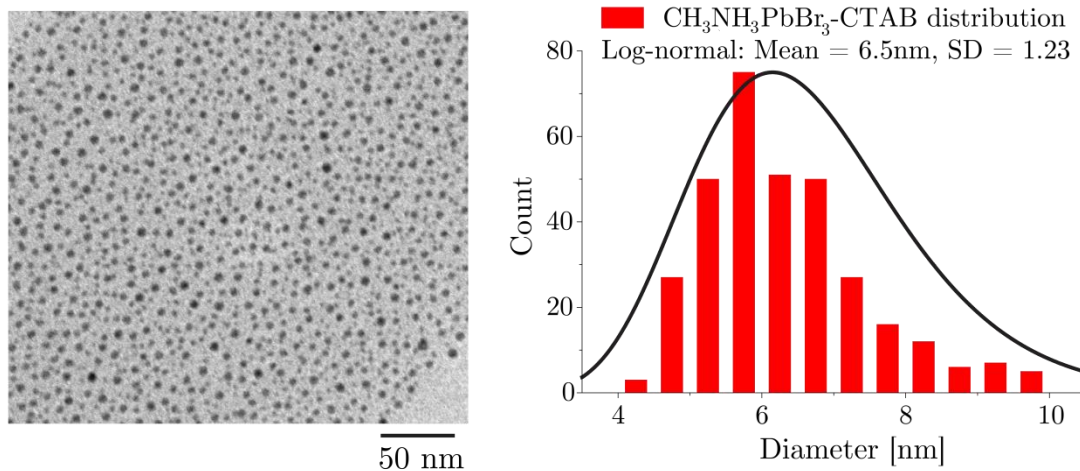


Figure 4.32: Fluorescence spectrum (top), extinction spectrum (middle) and photoluminescence excitation spectrum (bottom) of  $\text{CH}_3\text{NH}_3\text{PbBr}_3$  nanoparticles synthesised with a re-precipitation method.

The major drawback of these nanoparticles is their unsatisfying stability. Perovskite nanoparticles disintegrate when they get in contact with a polar solvent. Due to their small size it was not possible to centrifuge the particles down in order to remove the residual DMF from the precursor solution. The residual DMF caused uneven films when spin-coating techniques were applied because it dried much slower than the toluene causing dissolution of the precursors and interface effects due to different surface tensions [287]. Vacuum drying or evaporation of the solvent by heating was not possible without destroying the nanoparticles [288].

A solution for these problems was discovered in this work by replacing one of the capping ligands (octylamine) with the cationic quaternary amine cetrimonium bromide (CTAB). The idea was that this molecule with its longer tail and the charged head might increase the stabilisation of the nanoparticles. The CTAB was dissolved

together with the other precursors in DMF yielding a colourless solution. When this solution was then dropped in toluene, again a coloured and fluorescent solution was obtained. Furthermore, it was now possible to centrifuge and clean the particles allowing the removal of all the residual DMF. The nanoparticles' integrity was not altered by the washing steps. A TEM image and a size distribution of the CTAB-modified nanoparticles are shown in **Figure 4.33**.



**Figure 4.33:** TEM micrograph and size distribution of  $\text{CH}_3\text{NH}_3\text{PbBr}_3$  nanoparticles synthesised with CTAB.

The nanoparticle size is a few nanometres larger compared to the particles synthesised without CTAB. As a surfactant, CTAB readily forms micelles in solution [289]. An explanation for the ability to centrifuge these nanoparticles might be their bigger size as well as an agglomeration of the CTAB micelles by Van-der-Waals interactions between the aliphatic tails. Nevertheless, the steric hindrance of the long tails also prevented the nanoparticles from irreversible aggregation.

The perovskite nanoparticles synthesised with CTAB had similar spectroscopic properties as the others, which is shown in **Figure 4.34**. The fluorescence spectrum had its maximum at 523 nm with a FWHM of 27 nm. The peak matched the band gap wavelength measured by UV-Vis spectroscopy. In the extinction spectrum there was a strong resonance in the UV at 357 nm. However, this peak was found to belong to an energy state, which probably relaxed in a non-radiative way. This can be seen from the PLE spectrum where at the same wavelength a depression appeared meaning that at this wavelength the fluorescence at 523 nm is suppressed. The origin of this behaviour could not be resolved.

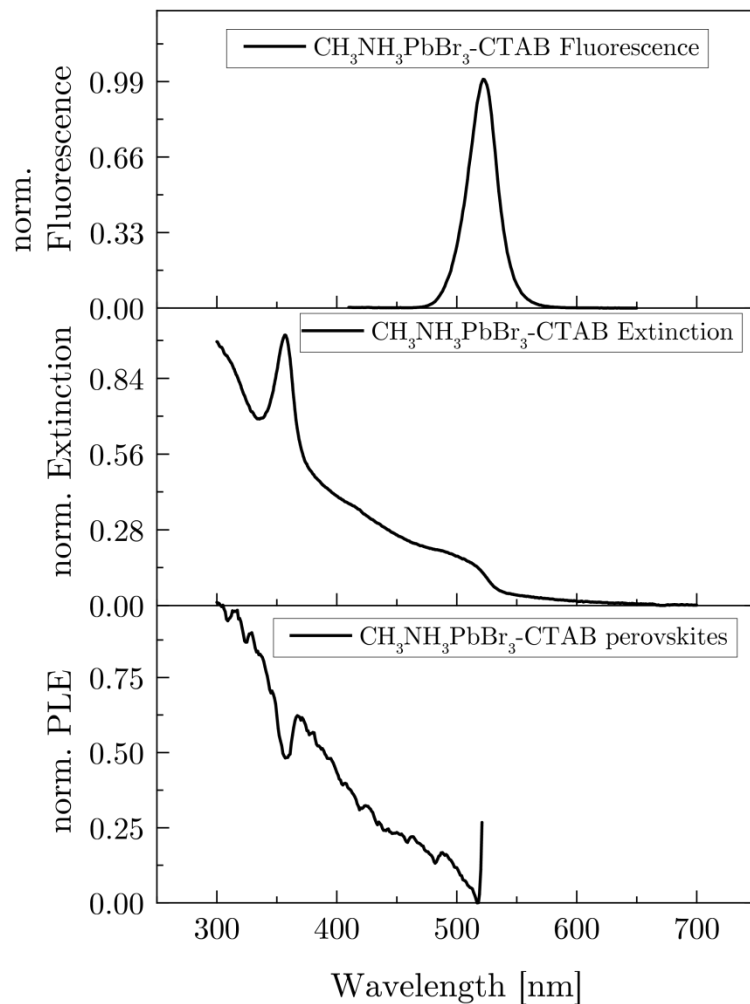


Figure 4.34: Fluorescence spectrum (top), extinction spectrum (middle) and photoluminescence excitation spectrum (bottom) of  $\text{CH}_3\text{NH}_3\text{PbBr}_3$  nanoparticles synthesised via re-precipitation with CTAB.

Cubic  $\text{CsPbX}_3$  perovskite nanoparticles were synthesised with a hot-injection method according to the protocol of Protesescu *et al.* [156]. Caesium oleate precursor was rapidly injected in a mixture of the lead halide salt dissolved in oleic acid and oleylamine. Nanoparticle formation was completed within seconds. A TEM image and the size distribution of these nanoparticles is shown in Figure 4.35. The size was measured in terms of the diagonal of the cubes and with a mean value of 11.7 nm and a standard deviation of 1.5 nm the nanoparticles were rather monodisperse. Furthermore, the sizes did not vary for perovskites with different halide ions. This shows that the quantum size effect only plays a minor role for the nanoparticle emission wavelength as discussed in section 2.1.7.

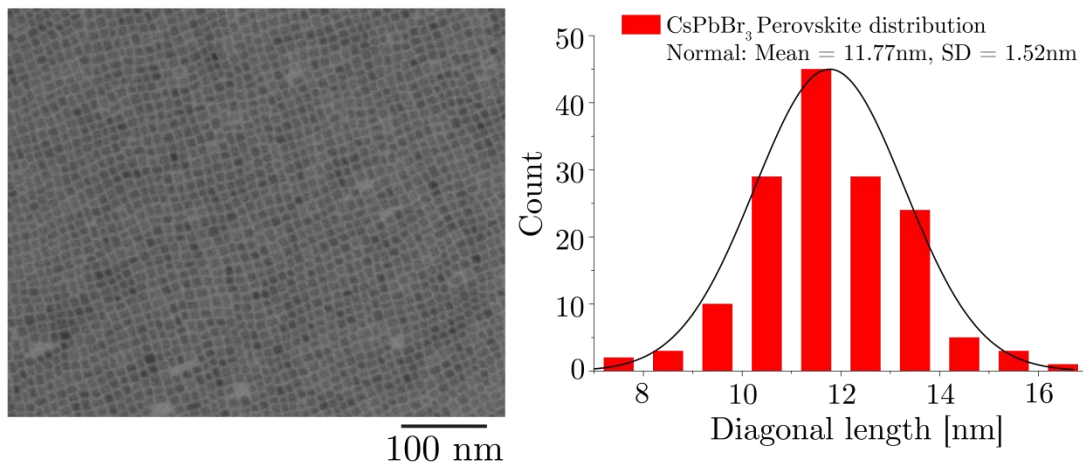


Figure 4.35: TEM micrograph of  $\text{CsPbBr}_3$  nanoparticles synthesised via a hot-injection method. The nanoparticle sizes were measured in terms of the diagonal.

The emission wavelength could be tuned by employing different ratios of halide precursors. In **Figure 4.36** photographs of the caesium lead halide perovskite nanoparticles with different amounts of bromide and iodide are shown under ambient light as well as under UV-A illumination. The peak wavelength clearly red-shifted with increasing iodine content due to a decreasing band gap (see **section 2.1.7**) [160]. By employing Br/Cl mixtures the wavelength could be blue-shifted.

The extinction and emission spectra of nanoparticles with different halide mixtures are shown in **Figure 4.37**. Besides the onset at the band gap energy, there were no other peaks at higher energies. The nanoparticles had emission maxima from 520 nm ( $\text{CsPbBr}_3$ ) to 690 nm ( $\text{CsPbI}_3$ ) with FWHM values between 20-50 nm. This demonstrates the good control of the nanoparticle emission similar to quantum dots.

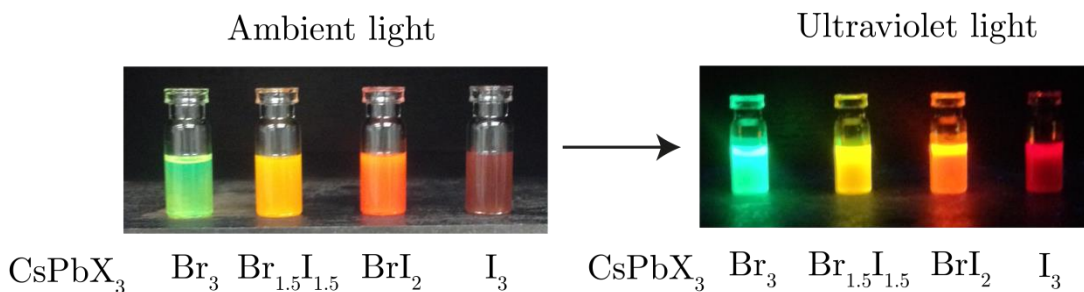


Figure 4.36: Photographs of  $\text{CsPbX}_3$  nanoparticles under ambient light and under illumination with UV-A light.

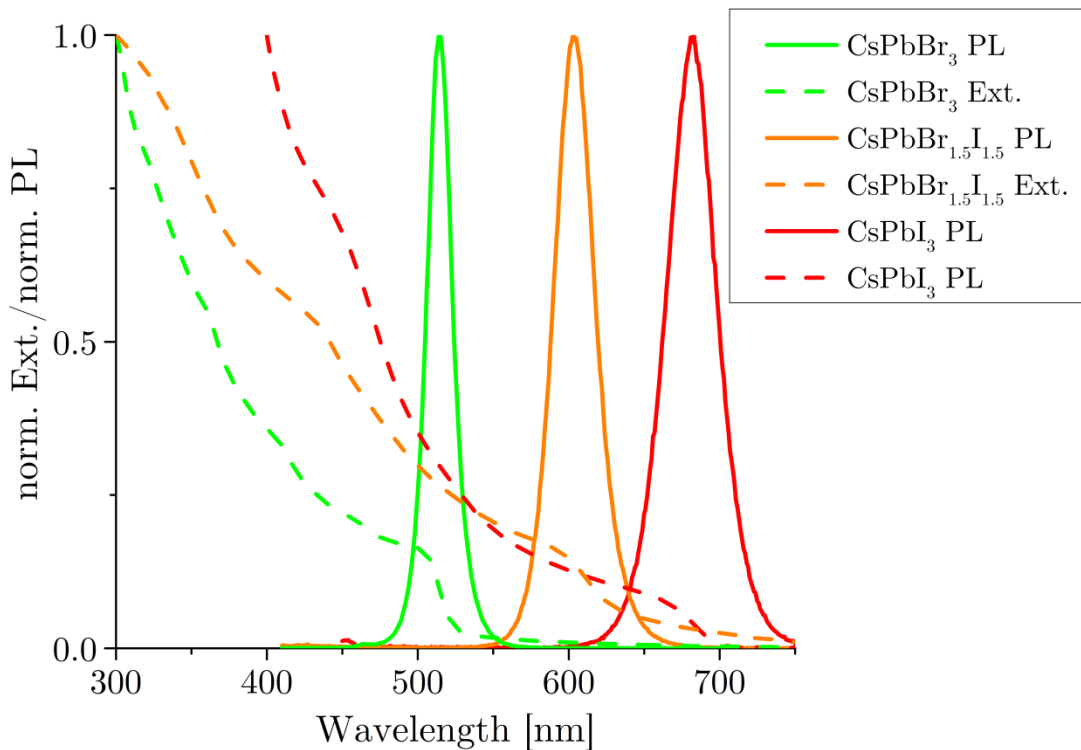


Figure 4.37: Extinction and fluorescence spectra of  $\text{CsPbX}_3$  nanoparticles with different halide mixtures.

Since perovskite nanoparticles have emerged only in 2014, there is a lot of potential for further research. Promising results for the application in photovoltaics, display technology and lasing have been reported recently [162]. Another example is a sensing platform for the explosive material 2,4,6-trinitrophenol, which has been reported by Muthu *et al.* showing the versatility of these novel materials [290].

The above-mentioned synthesised perovskite nanoparticles are currently further analysed in collaboration with the Hybrid Photonics group at the same faculty. In particular, exciton dynamics as well as lasing properties in nano-cavities and with distributed Bragg reflectors (DBR) are investigated. Furthermore, research on the phase-transfer to the aqueous phase by employing amphiphilic polymers and growth of an inorganic shell around the perovskites is currently conducted.

## 4.5 DNA-functionalisation of nanoparticles

In the previous part, the synthesis and characterisation of the nanoparticles used in this work were described. Since the aim of this work was to utilise DNA for controlled self-assembly of nanoparticles, the DNA attachment to the various nanoparticles will be described in the following.

#### 4.5.1 Gold nanoparticles

BSPP-functionalised gold nanoparticles are a perfect platform for the attachment of DNA [166]. The oligonucleotides employed in this work have been functionalised with a linker containing a disulphide group (Figure 4.38).

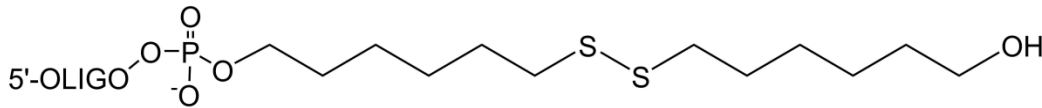


Figure 4.38: Structure of the thiol-linker used as oligonucleotide modification for the attachment of DNA to nanoparticles.

For effective anchoring onto the gold nanoparticle surface via the strong gold-thiol bond, the disulphide was cleaved by reduction of the S-S bond. The formation of SAMs on gold surfaces with disulphides and thiols showed that thiols bind more readily and faster than disulphides [291]. A similar behaviour was observed with gold nanoparticles where SH-DNA attached to the AuNPs within an hour and uncleaved DNA needed much more time. There are several thiol-containing reagents like mercaptoethanol or dithiothreitol (DTT), which are often used to cleave disulphide bonds [292]. However, thorough washing is needed to remove the reducing agents after cleavage. Instead, several phosphine-based reagents like *tris*(2-carboxyethyl)phosphine (TCEP) or BSPP have been used as mild reducing agents for this purpose [293, 294]. As the gold nanoparticles are already coated with BSPP, further addition does not influence the surface capping. The reaction of BSPP with a disulphide is shown in Figure 4.39 [295].

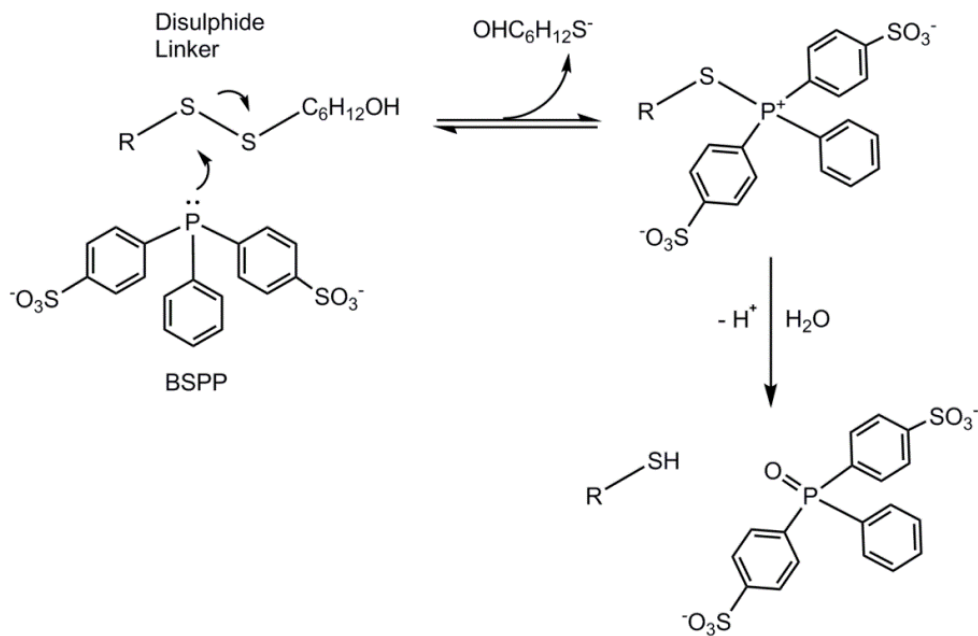
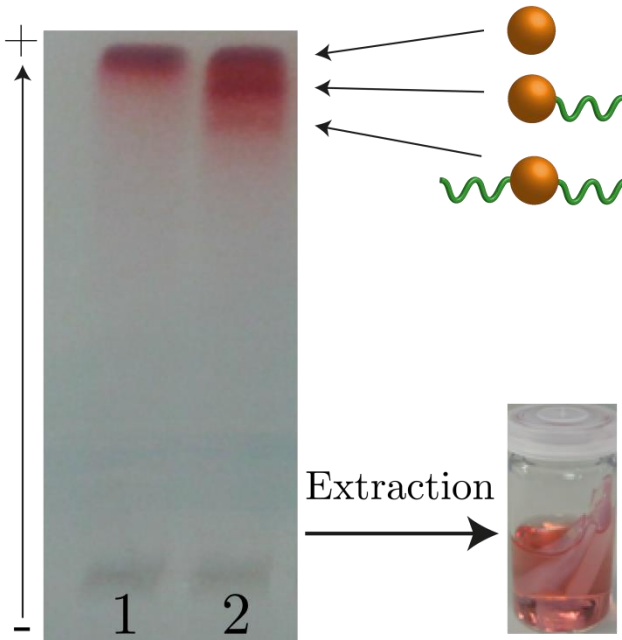


Figure 4.39: Illustration of the disulphide cleavage with BSPP.

Mixing BSPP-stabilised gold nanoparticles with thiolated DNA and BSPP leads to an efficient attachment in one hour due to the stronger thiol-gold bond, which readily displaces BSPP. However, the exact number of DNA strands on each nanoparticle cannot be controlled and nanoparticles with different numbers of oligonucleotides are obtained. In order to optimize control over nanoparticle assembly, the nanoparticles with a single DNA strand were separated [249]. A fast and efficient method to achieve separation was agarose gel electrophoresis. It was shown by Zanchet *et al.* that if the number of oligonucleotide bases is at least 5-10 times the nanoparticle diameter in nanometres, a separation of gold nanoparticle-DNA conjugates depending on the number of attached oligonucleotides is possible by gel electrophoresis [246]. Long DNA strands change the overall electrophoretic mobility to such an extent that different AuNP-DNA conjugates run in different bands.

The oligonucleotides employed in the first part of the work consisted of 87 bases (see **Appendix A.2**) and allowed the separation of 15 nm gold nanoparticles by the number of attached strands. **Figure 4.40** shows a sample agarose gel (2.25% w/v) of AuNP-DNA conjugates after electrophoresis. In lane 1, a reference containing only 15 nm gold nanoparticles was run next to gold nanoparticles incubated with DNA (lane 2). Three distinct bands were obtained corresponding to unconjugated, monoconjugated and diconjugated nanoparticles. The monoconjugate band was then extracted from the gel by soaking it in 0.5x TBE buffer and letting the gold

nanoparticles diffuse out of the gel overnight. The imperfection of the band separation as well as the cutting with the scalpel made it possible that a small fraction of unwanted species was present after extraction.



**Figure 4.40: Separation of  $15 \pm 1$  nm AuNP-DNA conjugates (SA1) by the number of attached oligonucleotides with agarose gel electrophoresis (2.25% w/v). Lane 1: AuNP reference, Lane 2: AuNP mixed with DNA. The necessary band is then extracted from the gel by soaking the gel in buffer.**

In order to give a comparison with smaller nanoparticles,  $7 \pm 1.5$  nm gold nanoparticles were functionalised with the 87 mer DNA and run in an agarose gel (Figure 4.41). It is evident that a much better separation was achieved compared to the 15 nm gold nanoparticles. As discussed earlier, this is because the relative increase in size is much larger for the smaller nanoparticles. Again, lane 1 contained a reference and lane 2 the gold nanoparticle-DNA mixture.

The need for long oligonucleotides to enable sufficient separation is the drawback of this method [246]. In order to tackle this problem, Busson *et al.* introduced a method to separate larger gold nanoparticles with diameters of 36 nm [296]. First, the nanoparticles were incubated with the functional DNA, which is later used to form assemblies. Then, an excess of a partially complementary lengthening strand was added. In this way, the DNA length is increased so that separation by gel electrophoresis was possible. By this method, a better control of the nanoparticle functionalisation can be achieved if it is needed, e.g. when DNA templates for gold nanoparticle assembly are used [248]. Since the oligonucleotides were long enough

to separate the 15 nm gold nanoparticles, lengthening strands were not employed in this work. The extraction of DNA-AuNP conjugates with 30 nm particles could not be performed with the oligonucleotides in this work. Nevertheless, this was not necessary for the SERS experiments conducted with these particles (see **section 5.3**).

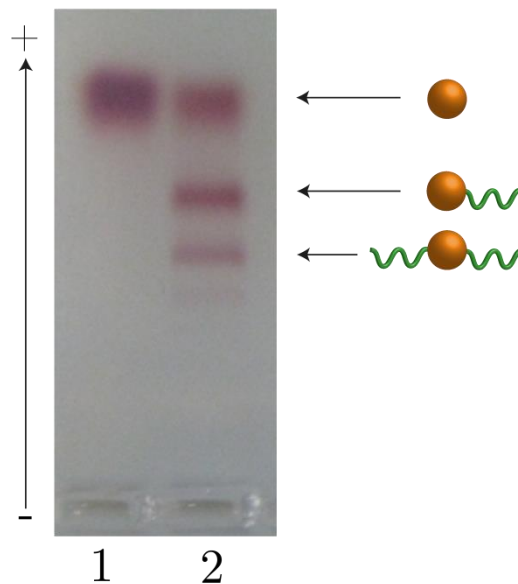


Figure 4.41:  $7 \pm 1.5$  nm AuNP-DNA conjugate (SA1) separation in an agarose gel (3% w/v).

#### 4.5.2 Silver nanoparticles

The attachment of DNA to silver nanoparticles has been described in several reports [278, 279]. However, in this work the preparation of silver nanoparticle-DNA conjugates did not succeed. A problem was that the *in situ* cleavage of the disulphide linker was not possible in the case of silver nanoparticles. Phosphine-containing molecules readily dissolve silver nanoparticles even in little amounts by complex-formation with the silver ions [297]. This has been tested by mixing silver nanoparticles with BSPP-coated gold nanoparticles (**Figure 4.42**). The plasmon peak of the former decreased while the peak of the latter increased and slightly shifted to the blue. This indicates that the concentration of the silver nanoparticles decreased and that there was some interaction with the gold nanoparticles. It might be possible that some of the silver deposited on the gold nanoparticles, which would explain the blue-shift of the LSPR [298]. This experiment shows that the application of silver nanoparticles is not as straight-forward as for the gold nanoparticles. In order to overcome this problem, it would be necessary to use amine-terminated DNA or to cleave the disulphide group beforehand.

Another problem besides the sensitivity towards BSPP was a lack of stability at sodium chloride concentrations higher than 50 mM (Figure 4.43). While the stability was increased by functionalisation with folic acid as well as short thiolated polyethylene glycol, the attachment of DNA without cleaving the disulphide group was not successful or could not be sufficiently controlled by gel electrophoresis. As an example, citrate-coated silver nanoparticles were incubated for different times (1-24 h) with DNA that was not de-protected and run in an agarose gel (Figure 4.43). Lane 1 contained a reference and the other lanes contained AgNP with increasing incubation times of 1 h, 6 h and 24 h. No band separation was observed, which suggests that there was no DNA attachment onto the silver nanoparticles. Similar results were obtained for silver nanoparticles with different surface ligands. Since the focus of this project lied on the assembly of nanoparticles further use of silver nanoparticles was not pursued.

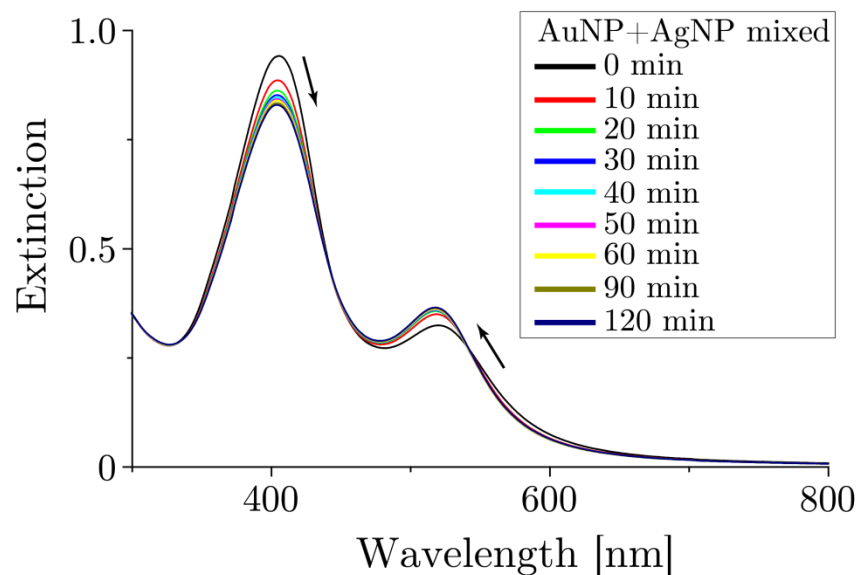


Figure 4.42: Extinction spectra of  $15 \pm 1$  nm BSPP-AuNPs mixed with  $22.5 \pm 2.5$  nm AgNPs monitored at different times. The arrows indicate that the AgNP plasmon peak is decreasing and the AuNP plasmon peak is increasing with time.

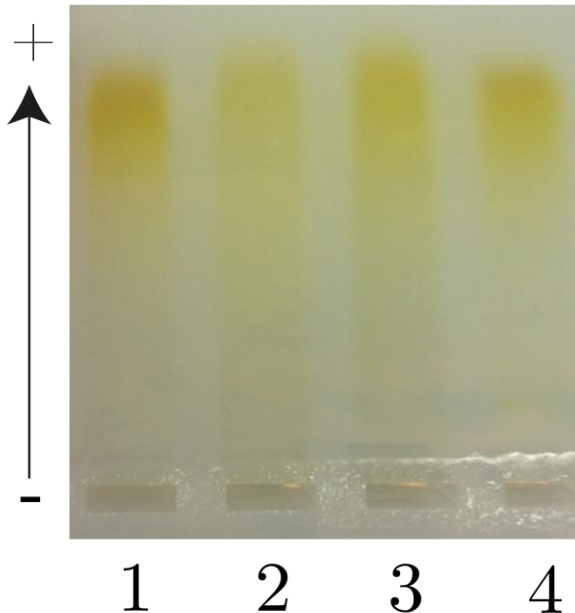


Figure 4.43: 2% Agarose gel containing  $22.5 \pm 2.5$  nm silver nanoparticles incubated with oligonucleotides (SC1) without de-protection. Lane 1: AgNP reference; Lane 2: AgNP 1 hour incubation; Lane 3: AgNP 6 hours incubation; Lane 4: AuNP 24 hours incubation.

#### 4.5.3 Quantum dots and upconversion nanoparticles

The functionalisation of the fluorescent nanoparticles (Quantum dots and upconversion nanoparticles) was conducted via a coupling reaction of carboxylic acids with primary amines activated by 1-Ethyl-3-(3-dimethylaminopropyl)carbodiimide (EDC) and *N*-hydroxysulfosuccinimide (Sulfo-NHS) [299, 300]. The reaction is illustrated in Figure 4.44 [301]. In the first step, the carboxylic acid is activated with EDC forming an *o*-acylisourea intermediate. Subsequently, primary amines can react with the activated molecule and form an amide bond. However, the intermediate is very unstable and very prone to hydrolysis in aqueous solution. In order to increase the yield of the reaction, Sulfo-NHS can be utilised forming an active ester, which subsequently reacts with primary amines. This EDC-based coupling reaction is widely used to attach biomolecules such as peptides or biotin/streptavidin to surfaces or particles [163].

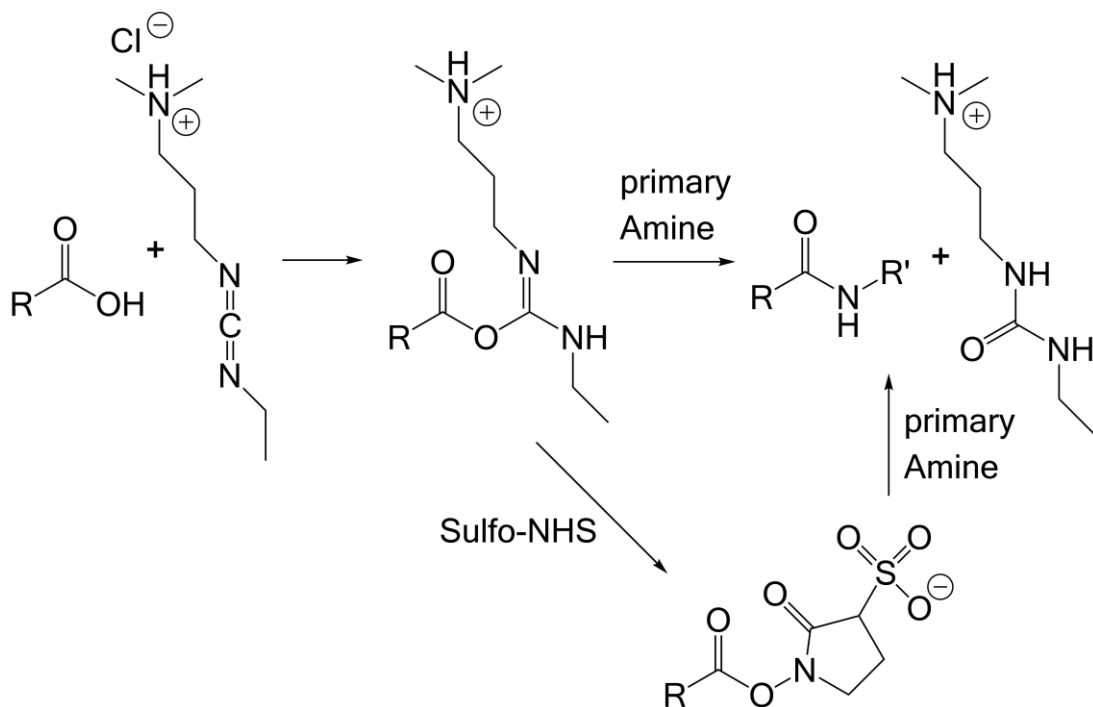


Figure 4.44: Illustration of a coupling reaction between a carboxylic acid and a primary amine with EDC and Sulfo-NHS. First, the carboxylic acid is activated with EDC formation an unstable o-Acylisourea intermediate. This intermediate then readily reacts with a primary amine coupling it to the carboxylic acid via an amide bond. The stability can be improved by addition of Sulfo-NHS, which forms a semi-stable ester with the carboxylic acid. Adapted from ref. [301].

In this work, amine-modified oligonucleotides were coupled to the fluorescent nanoparticles (QDs and UCNPs). As outlined above, the nanoparticles were functionalised with molecules containing terminal carboxyl groups (PAA and lipoic acid) enabling the coupling with EDC/Sulfo-NHS chemistry. The purpose for the functionalisation of these nanoparticles with oligonucleotides was to investigate if a resonance energy transfer from the upconversion nanoparticles to the quantum dots by nanoparticle assembly could be facilitated. Short oligonucleotides with only 15 bases were used to bring the particles as close as 5 nm to each other. The details of this study will be discussed in **Chapter 6**.

## 4.6 Summary

In this chapter, the nanoparticle characterisation and functionalisation with different ligands as well as oligonucleotides was presented.

Spherical gold and silver nanoparticles synthesised with the Turkevich method were functionalised with various ligands. The plasmonic properties of these nanoparticles were analysed with UV-Vis spectroscopy. Shifts and broadening of the LSPR peak referred to the colloidal stability of the nanoparticles and were used to determine

successful ligand exchange reactions. As a complementary analysis technique,  $\zeta$ -potential measurements were discussed. Gold nanoparticles were modified with thiol-modified oligonucleotides and gel electrophoresis was introduced as a tool for the separation of gold nanoparticles according to the number of attached DNA strands. The functionalisation of silver nanoparticles with oligonucleotides was not successful and the reasons were discussed.

On the other hand, fluorescent CdSe/ZnS and rare-earth doped upconversion nanoparticles were synthesised and characterised. The extinction and fluorescence spectra of the semiconductor quantum dots were recorded. Phase-transfer from organic solvents to aqueous solutions was facilitated with L-lipoic acid via a ligand exchange reaction.  $\zeta$ -potential measurements indicated that the particles had a highly negatively charged surface maintaining colloidal stability. The rare-earth doped upconversion nanoparticles had a tuneable emission in the visible upon irradiation with a NIR laser diode, depending on the co-doped lanthanides. A phase-transfer was performed by replacing oleic acid ligands with the polymer PAA, rendering the particles water-soluble. Both types of fluorescent nanoparticles were functionalised with amine-modified DNA via EDC/Sulfo-NHS coupling chemistry.

Lead halide perovskite nanoparticles were synthesised and characterised by UV-Visible and fluorescence spectroscopy. While the fluorescence spectra showed a narrow single peak emission, a second peak appeared in the absorption spectrum. The origin could not be determined. The processability of the nanoparticles was improved by exchanging octylamine with CTAB in the synthesis, which allowed for the complete removal of DMF.

In the upcoming chapters, the described nanoparticles will be used in two different ways. Gold nanoparticles were used as model particles for the ligation of oligonucleotides in three-dimensional nanoparticle assemblies in **Chapter 5**. For the first time, a reversible crosslink reaction is presented utilising 3-cyanovinyl carbazole as a UV-sensitive DNA cross-linker. Furthermore, the potential limitation of spontaneous crosslink reactions such as the well-known alkyne-azide click reaction will be discussed. In **chapter 6**, a resonance energy transfer system consisting of upconversion nanoparticles and semiconductor quantum dots will be presented. Short oligonucleotides were used to bring them in close proximity to each other, which is needed to detect energy transfer. This system has not been reported yet in

the literature and demonstrates the feasibility of using short oligonucleotides for the assembly of different types of nanoparticles.



## Chapter 5. Formation and Ligation of AuNP-DNA assemblies

In the previous chapter, the synthesis, functionalization and characterisation of several different nanoparticles were discussed. In this chapter, the self-assembly of AuNP-DNA conjugates will be described. While DNA has proven to be a versatile platform for directed assembly, the need for increased stability in conditions like low ionic strength and high temperatures is of importance [21, 302, 303]. In order to tackle this issue,  $15 \pm 1$  nm gold nanoparticles have been employed in conjunction with 3-cyanovinyl carbazole modified DNA to create fortified structures. For the first time, a simple and efficient method for reversible ligation of AuNP-DNA assemblies is presented.

At the beginning, the oligonucleotide sequences and their hybridisation behaviour without nanoparticles will be briefly discussed in **Section 5.1**. Thereafter, the self-assembly of gold nanoparticles and the crosslinking of the assemblies will be presented in **Section 5.2**. Finally, an application for Surface enhanced Raman spectroscopy is shown in **Section 5.3**.

Parts of this chapter were published in: Harimech, P. K.; Gerrard, S. R.; El-Sagheer, A. H.; Brown, T.; Kanaras, A. G. "Reversible Ligation of Programmed DNA-Gold Nanoparticle Assemblies", *Journal of the American Chemistry Society*, 2015, 137, 9242-9245.

### 5.1 Characteristics of employed oligonucleotides

#### 5.1.1 Design, modification and melting temperature

In this work, three sets of oligonucleotides were used to investigate the crosslinking reaction between oligonucleotides coated gold nanoparticles. Each set contained four oligonucleotides allowing the formation of dimers, trimers and a tetrahedral structure. Each DNA strand had a total length of 87 bases and consisted of three sections of 26 base pairs. One section was fully complementary to exactly one section in one of the other three strands. The direction of the respective complementary section was designed as such that 5' and 3' were reversed and the strands were able to hybridise. In this way, each strand was able to bind only in one way with each of the other strands (see **Table 5.1**). Every oligonucleotide was chemically modified

with a disulphide linker to facilitate the attachment to gold nanoparticles (see **section 4.5.1**). While one set of oligonucleotides was not further modified (**SA1-SA4**), one set was modified with azide (**SB1, SB2**) and BCN (**SB3, SB4**) moieties (see **Appendix A.3**) and one set with 3-cyanovinyl carbazole moieties (**SC1-SC4**) (see **Table 5.1**).

SC1	5'-HSC <sub>6</sub> H <sub>12</sub> -TTT <b>GCC TGG AGA TAC AXA CAC ATT ACG GC</b> TTT <b>CCC TAT TAG AAG AXA TCA GGT GCG CG</b> TTT <b>CGG TAA GTA GAC GGT GTC AGT TCG CC</b>
SC2	5'-HSC <sub>6</sub> H <sub>12</sub> -TTT <b>CGC GCA CCT GAT GTC TTC TAA TAG GG</b> TTT <b>GCG ACA GTC GTT CAX ATA GAA TGC CC</b> TTT <b>GGG CTG TTC CGG GTG TGG CTC GTC GG</b>
SC3	5'-HSC <sub>6</sub> H <sub>12</sub> -TTT <b>GGC CGA GGA CTC TGT CTC CGC TGC GG</b> TTT <b>GGC GAA CTG AXA CCG TCT ACT TAC CG</b> TTT <b>CCG ACG AGC CAX ACC CGG AAC AGC CC</b>
SC4	5'-HSC <sub>6</sub> H <sub>12</sub> -TTT <b>GCC GTA ATG TGT CTG TAT CTC CAG GC</b> TTT <b>CCG CAG CGG AGA XAG AGT CCT CGG CC</b> TTT <b>GGG CATT CTA TGT GAA CGA CTG TCG</b>

Table 5.1: Oligonucleotide sequences modified with 3-cyanovinyl carbazole. The colours indicate the complementarity between the DNA strands. The X denotes the 3-cyanovinyl carbazole modification within the DNA strands.

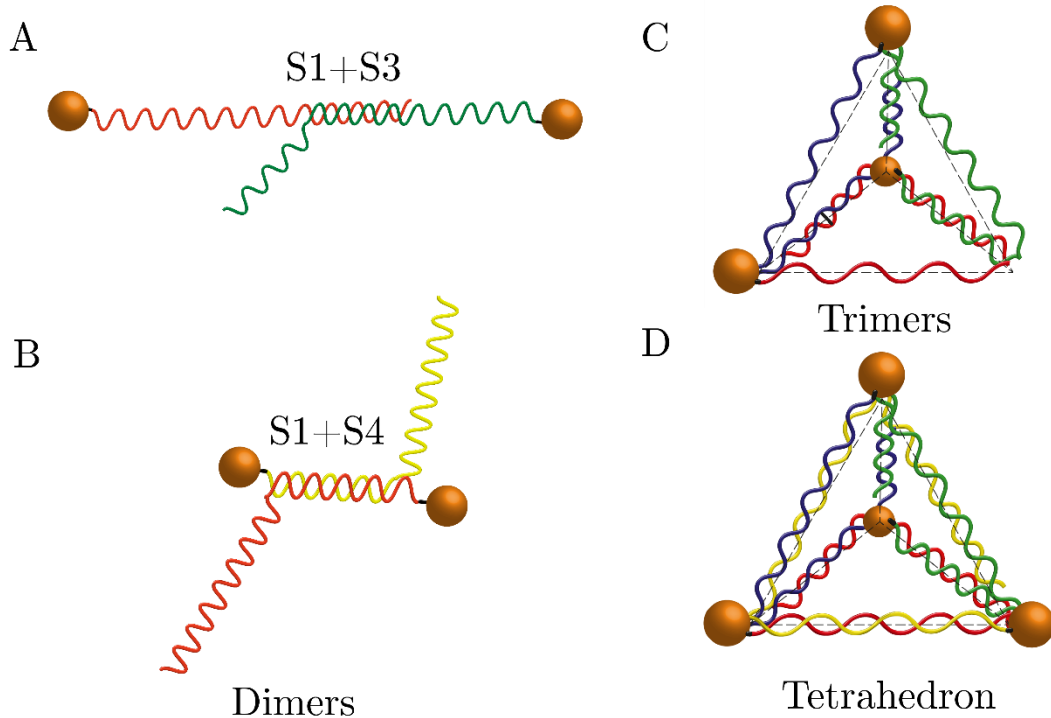
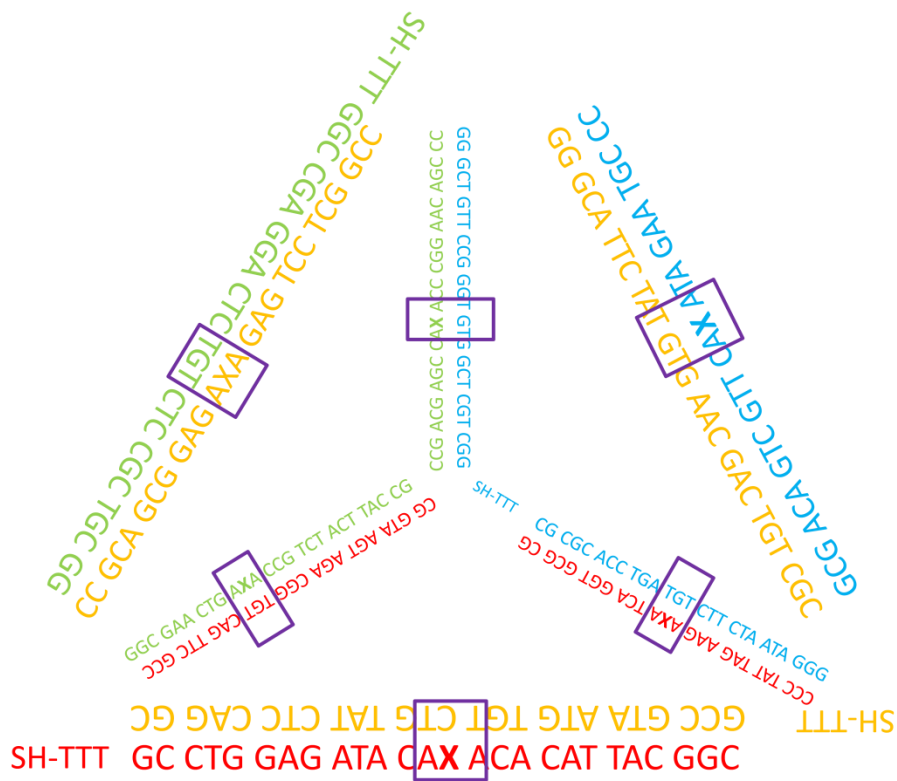


Figure 5.1: Illustration of different assemblies from different combinations of oligonucleotides are mixed. A: S1+S3, B: S1+S4, C: S1-S3, D: S1-S4. The spheres indicate the positions of the nanoparticles in NP-DNA assemblies.



**Figure 5.2:** Illustration of the tetrahedron formed by directed folding of all four oligonucleotides from Table 5.1. The 5'-end is at the thiol-modification. The three thymine bases (TTT) in between the different sections were omitted. Each oligonucleotide is coloured with a single colour (SC1: red, SC2: blue, SC3: green, SC4: yellow). The boxes indicate the 3-cyanovinyl carbazole crosslinking sites.

Illustrations of the resulting assemblies obtained with different oligonucleotide combinations are depicted in **Figure 5.1** and **Figure 5.2**. The complementarity of each strand to each other led to an intertwining of the strands in such a way that they folded into an equilateral pyramid. The thiol linkers were located at the vertices of the structure and were pointing outwards for facilitation of nanoparticle assembly. Additionally, the oligonucleotides had TTT-spacers after the thiol linker and in between the 26 base pair sequences. These have been fitted in order to reduce strain from the structure as the oligonucleotides were bending along the corners [249]. Depending on the crosslinker modification, the boxes in **Figure 5.2** indicate the positions of 3-cyanovinyl carbazole or azide/BCN pairs. Since the design of such a structure is not trivial, oligonucleotide sequences from the literature were used with slight modifications [249]. Potential problems are self-complementarity and partial complementarity of different strands. While the former might lead to hairpin loop formation, the latter might cause unwanted hybridisation on certain parts of the strand and therefore wrong products, e.g. long DNA chains. As the number of

oligonucleotides increases and the strands become longer, the difficulty in avoiding these problems rises.

A melting analysis was conducted by measuring the absorbance at 260 nm for three cycles from 20°C to 85°C (see **Section 2.4**). In this experiment, 0.5 nmol of oligonucleotide was dissolved in 1 mL phosphate buffer (20 mM, pH = 7.4) containing 200 mM NaCl. The melting curve of a dimer mixture is plotted in **Figure 5.3**. The graph contains the typical hyperchromicity around the melting temperature caused by dehybridisation of the DNA (see **section 2.4.1**). The melting temperature was determined at the point of inflection. For the dimer made from **SA1+SA2**, a melting temperature of 74°C was determined.

The theoretical melting temperature was calculated with the nearest-neighbour method using the free online tool OligoCalc [201]. For the fully complementary 26 base pair part of the DNA at a concentration of 500  $\mu$ M and 200 mM NaCl, a melting temperature of 74.2°C was calculated. This comparison indicates that the theoretical model could be used determine the melting temperatures in very good approximation. Therefore, OligoCalc was utilised for further melting temperature approximations.

Besides the hyperchromicity, a rise in the absorption was visible. Due to the length of the oligonucleotides, there was a certain small self-complementarity in each strand with itself as well as partial complementarity between different strands other than the full complementarity. Therefore, as the temperature increased these unstable and only loosely bound duplexes dehybridised at much lower temperature than the fully complementary 26 bases leading to a steady increase in the absorption spectrum. It should be noted that oligonucleotides bound to nanoparticles were spatially restricted and therefore the self-complementarity did not play a role in nanoparticle assembly. After the melting temperature of the oligonucleotides was established, further hybridisation experiments were conducted using gel electrophoresis for analysis.

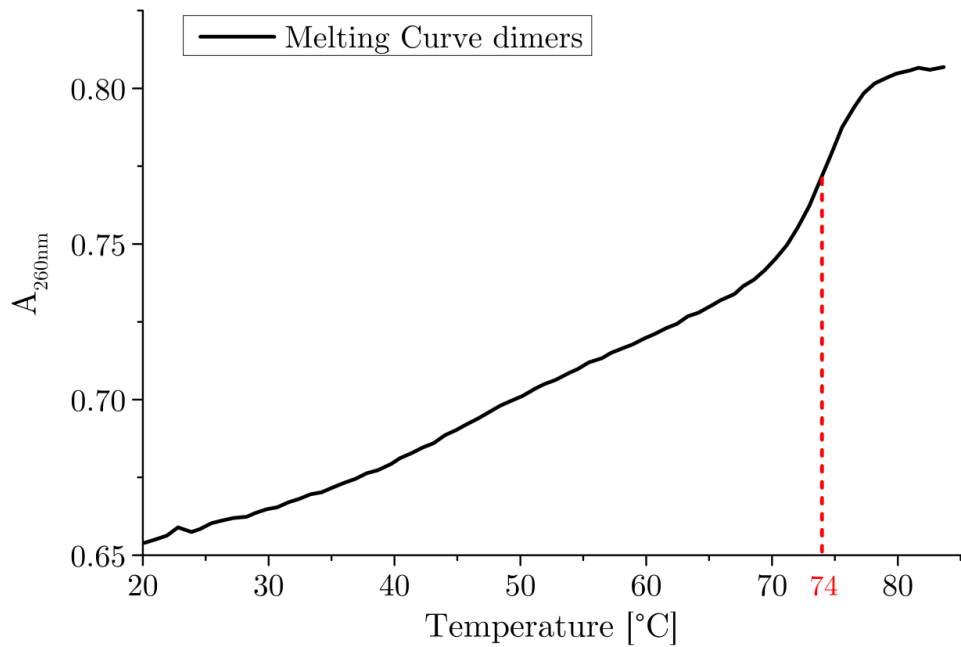


Figure 5.3: Melting curve of oligonucleotide dimers (SA1+SA2). The curve was determined as an average from 3 complete cycles. The melting temperature was determined at the point of inflection as 74°C.

### 5.1.2 Polyacrylamide gel electrophoresis

The hybridisation of different combinations of the oligonucleotides was validated by native polyacrylamide gel electrophoresis. As explained in section 3.4.6, gel electrophoresis is used to separate molecules by size and charge. Since the charge of all the strands was the same, the size dictated the differences in electrophoretic mobility [246].

#### 5.1.2.1 Unmodified oligonucleotides

First, the hybridisation of oligonucleotides without crosslinking modifications will be discussed. Different mixtures of the oligonucleotides led to different bands during gel electrophoresis indicating the formation of different assemblies. A representative gel is shown in Figure 5.4.

Lane 1 contained single oligonucleotide strands as a reference. Lanes 2 and 3 contained two different combinations of a mixture of two DNA strands (**SA1+SA4** and **SA1+SA3**). Both the oligonucleotides were running slower with respect to the reference. Furthermore, there was retardation between the two combinations because the complementarity was either at the beginning or in the middle of the DNA causing a difference in length (see Figure 5.1). Likewise, in lanes 4-7 the four combinations of three oligonucleotides were further retarded than the previous

assemblies. The four different combinations showed different retardations, which can be explained by different GC contents in the different structures. It has been reported that different oligonucleotide compositions migrate at different speeds in gel electrophoresis [304]. Finally, in lane 8 all four oligonucleotides were mixed leading to the formation of the potential tetrahedral structure, which was even further delayed. The single band shows that there is only one configuration on how the four strands form the structure, which indicates that the band corresponds to a tetrahedron. However, other techniques like AFM and mass spectrometry would be needed to determine the three-dimensionality of the product. A DNA ladder would not be appropriate because it corresponds only to linear DNA and was therefore omitted in this work. Clearly, the different structures (dimers, trimers, tetramers) ran very differently from each other showing their increasing complexity. Furthermore, the hybridisation yields were high. However, there was an agglomeration visible in the wells for the trimers and tetramers. The residue in the wells may have been caused by too high loading or due to formation of higher ordered structures. For example, possible that several intertwined structures could have formed, which were too large to pass into the gel [236].

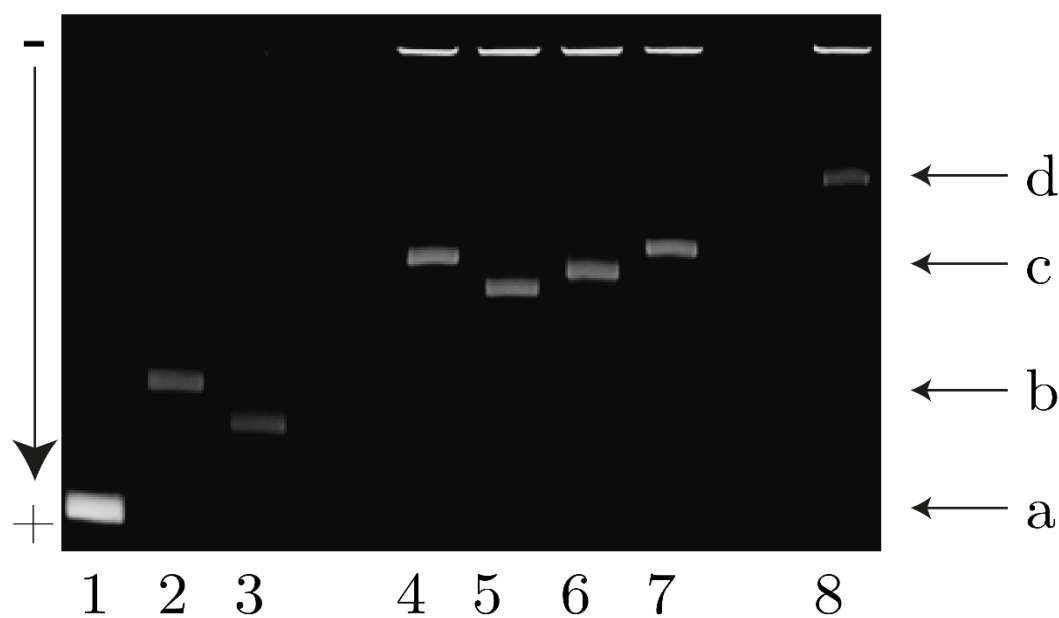


Figure 5.4: 6% native polyacrylamide gel of different DNA mixtures without crosslinking groups (SA1-SA4). The gel was stained with ethidium bromide. Lane 1: Single strand; Lanes 2-3: DNA dimers (SA1+SA3 and SA1+SA4); Lanes 4-7: DNA trimers; Lane 8: DNA tetramers. The different bands were labelled as single strands (a), DNA dimers (b), DNA trimers (c) and DNA tetrahedra (d).

### 5.1.2.2 Oligonucleotides modified with azide- and alkyne-modification

Next, the oligonucleotides functionalised with azide and BCN groups (**SB1-SB4**) were analysed by PAGE and compared with the unmodified DNA. A representative gel is shown in **Figure 5.5**. It should be noted that the gels in this section were visualised using a transilluminator with a 254 nm UV source and not stained with ethidium bromide and that the black speckles are artefacts.

In Lane 1, a reference strand (**SA1**) was used. Lanes 2 and 3 show dimer oligonucleotide mixtures of unmodified DNA (**SA1+SA4**, **SA1+SA3**). As before, the different dimers have different electrophoretic mobilities. However, the hybridisation was not completely finished so that unreacted strands appeared at the bottom of the gel. Lanes 4 and 5 contained oligonucleotides with azide and BCN groups (**SB1+SB3**, **SB1+SB4**).

There was no difference between the retardation of the modified DNA and the unmodified DNA (bands *a-c*). This indicated that the same assemblies have formed. However, several bands appeared above the dimer band (area *d*, arrows) in lanes 4 and 5. The appearance of these extra bands was investigated in further experiments. The results helped to explain the problems faced with nanoparticle hybridisation, which will be discussed later (see **section 5.2.2**).

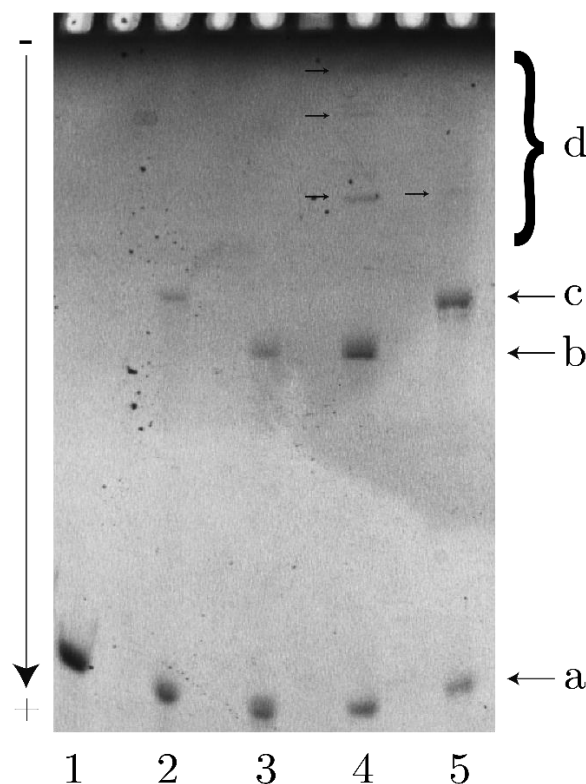


Figure 5.5: 6% native polyacrylamide gel containing different DNA dimer mixtures with unmodified and azide/BCN-modified oligonucleotides. Lane 1: Single strand reference; Lane 2: SA1+SA4; Lane 3: SA1+SA3; Lane 4: SB1+SB3; Lane 5: SB1+SB4. The different bands were labelled as single strands (a), dimers (b+c), and higher order complexes (d, indicated with arrows).

Several gels were run with different conditions including varying sodium chloride concentrations as well as temperature in order to verify that these extra bands were a result of the azide/BCN modifications. In all experiments, phosphate buffer (20 mM, pH 7.4) was used. Indeed, it was found that these additional bands occurred whenever two or more oligonucleotides with both BCN and azide groups were hybridised. In **Figure 5.6**, a gel containing two DNA dimer mixtures with different NaCl concentrations as well as a mixture of all four strands is presented. Lane D shows the dye xylene cyanol as a reference. Lane 1 contained a dimer mixture (**SB1+SB3**) hybridised with 100 mM NaCl. In lane 2, the same dimer mixture was used but with 200 mM NaCl. Lane 3 contained a mixture of all DNA strands (**SB1-SB4**) with 200 mM NaCl. In each case, equimolar amounts were used. In lanes 1 and 2 there is a ladder-like structure (c) visible above the dimer band (b) and the unreacted single strands (a). Furthermore, in lane 3 where all four DNA strands were mixed no dimer band appeared and only a very weak band of unreacted oligonucleotides was present.

This finding showed that there was no influence caused by the different NaCl concentrations, i.e. the formation of larger complexes due too high ionic strength could be ruled out. An evident spot at the bottom of the loading well could be seen in lane 3 (red arrow). An explanation could be that the click reaction resulted in the formation of large DNA fragments that were not able to pass through the gel. It might be that these large fragments complete block the lane so that the other oligonucleotides were not able to pass into the gel.

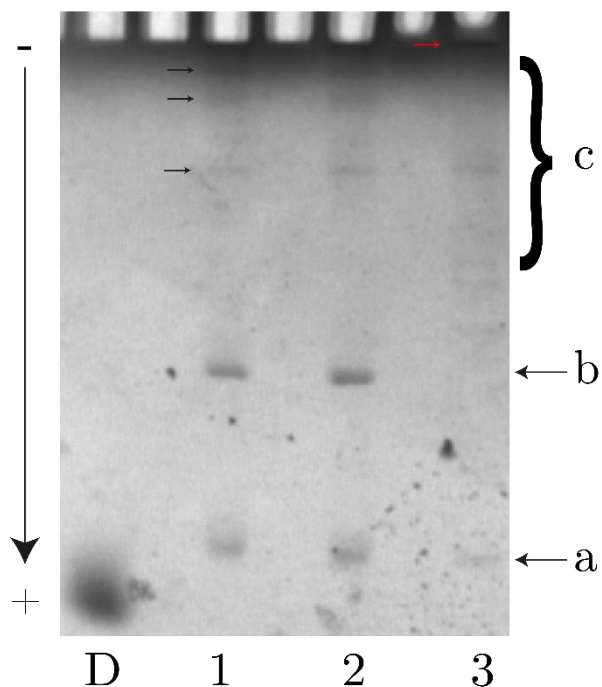


Figure 5.6: 6% native polyacrylamide gel of different DNA mixtures. Lane D: Cyanol xylene reference; Lane 1: DNA dimers (SB1+SB3) with 100 mM NaCl; Lane 2: DNA dimers (SB1+SB3) with 200mM NaCl; Lane 3: DNA tetrahedra (SB1-SB4) with 200 mM NaCl. The different bands were labelled as single strands (a), DNA dimers (b), and higher order complexes (c, black arrows). The red arrow indicates DNA residue, which did not pass into the gel.

Another gel is shown in Figure 5.7 where oligonucleotide dimer mixtures (SB1+SB3) were hybridised at different temperatures. This parameter influences the reactivity of the click reaction as well as the hybridisation behaviour (see section 2.4). In all cases, the phosphate buffer (20 mM, pH 7.4) containing 200 mM NaCl was employed. The hybridisation temperature of the different samples was varied from 55°C to 70°C in 5°C steps. Lane D contained the xylene cyanol dye for tracking the migration. From lane 1 to lane 4 the temperature was increased. It can be seen that all four samples showed similar hybridisation behaviour with the same bands (unreacted (a), dimers (b) and larger structures (c)) appearing as in the previous

samples. Nevertheless, the material not passing through the gel increased with higher temperatures.

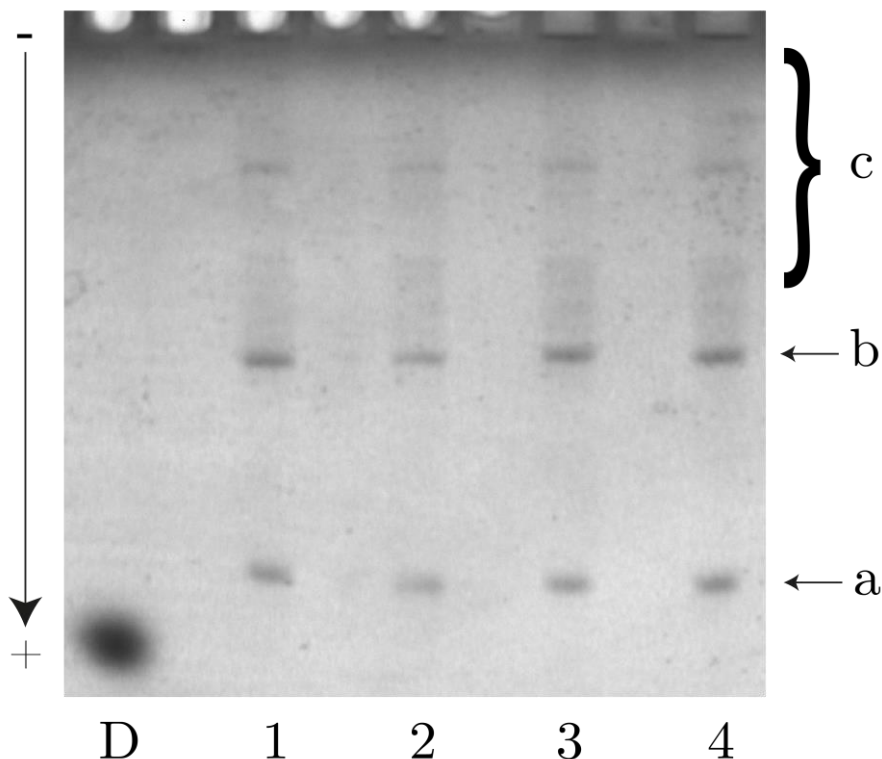


Figure 5.7: 6% native polyacrylamide gel of DNA dimers (SB1+SB3) hybridised at different temperatures. Lane D: Cyanol xylene reference; Lane 1: 55°C; Lane 2: 60°C; Lane 3: 65°C; Lane 4: 70°C. The different bands were labelled as single strands (a), DNA dimers (b), and higher order complexes (c).

All these findings suggest that the oligonucleotides with the different click groups participated in uncontrolled click reactions between several strands leading to clusters of DNA. The increased reactivity of the clicking groups with increasing temperature would explain the larger amount of DNA stuck in the well. Even though there were residues present in the wells when the unmodified oligonucleotides were used, no ladder-like band structure appeared in the gel. Furthermore, the higher order bands only occurred when the DNA strands with both clicking groups were mixed. It might be that if the BCN group is replaced by a less reactive group like DIBO the uncontrolled click reaction could be avoided [305, 306]. However, it was not possible in the scope of this work to further test other cyclooctynes.

As an alternative crosslinking technique, the molecule 3-cyanovinyl carbazole was chosen [24, 213]. Besides having control over the crosslink reaction with an external

stimulus, the reaction can be reversed, which is not possible with the SPAAC reaction and therefore introduces a new type of functionality.

#### 5.1.2.3 Oligonucleotides modified with 3-cyanovinyl carbazole

Oligonucleotides functionalised with 3-cyanovinyl carbazole (**SC1-SC4**) were compared with the non-functionalised DNA strands (**SA1-SA4**) using PAGE. In all experiments, phosphate buffer (20 mM, pH 7.4, 200 mM NaCl) was used. The results are shown in **Figure 5.8**. In the odd lanes the carbazole modified DNA was run next to the unmodified DNA in the even lanes. Single oligonucleotide strands (lanes 1+2), DNA dimers (lanes 3+4), DNA trimers (lanes 5+6) and DNA tetrahedral structures (lanes 7+8) were run for comparison.

Besides the distinct electrophoretic mobilities, it is evident from the PAGE gel that the two different sets hybridised in exactly the same way. Furthermore, the ladder-like bands present in the azide/BCN-modified DNA were not observed any longer with the 3-cyanovinyl carbazole groups. On the one hand, this indicated once more that the azide/BCN modification influenced the hybridisation result. On the other hand, the result shows that the hybridisation worked as expected.

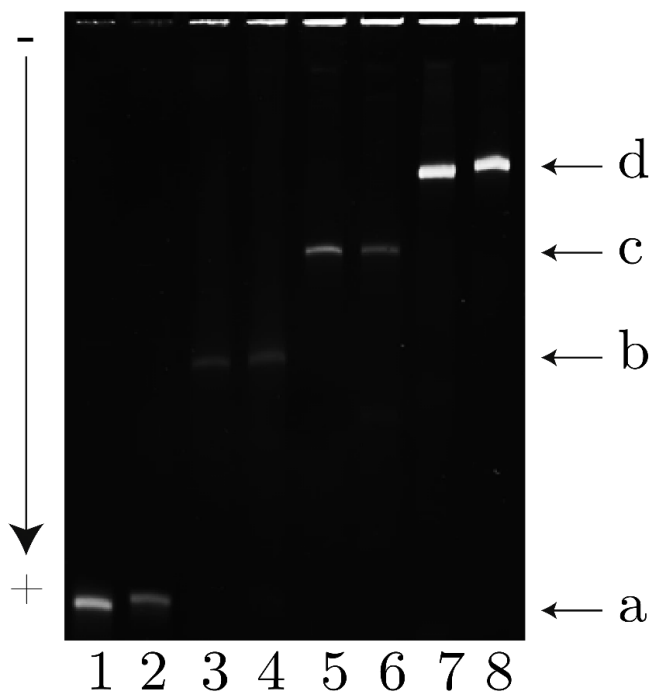


**Figure 5.8:** 6% native polyacrylamide gel of carbazole-modified and unmodified oligonucleotides. The odd lanes contain the carbazole strands and the even lanes the unmodified strands. The gel was stained with ethidium bromide. Lanes 1+2: single strand (SA1,SC1); Lanes 3+4: two strands (SA1+SA2,SC1+SC2); Lanes 5+6: three strands (SA1-3,SC1-3); lanes 7+8: all four strands (SA1-4,SC1-4). The bands are labelled as single strands (a), dimers (b), trimers (c) and tetrahedra (d).

After the proper hybridisation of the oligonucleotides was verified, the next step was to test the crosslinking reaction between the 3-cyanovinyl carbazole modification and thymine base on the opposite strand (see **section 2.4.2**). Two different oligonucleotides were hybridised as before and then irradiated with UV-A light centered at 365 nm, which promoted a [2+2]-photocycloaddition reaction [24]. The samples were placed in an ice bath in order to ensure that there was no thermal effect from the UV light that might have led to denaturation of the dsDNA. Several illumination durations were performed to check if there is an influence on the dsDNA.

The results of this experiment are presented in the polyacrylamide gel in **Figure 5.9**. In each lane the same type of oligonucleotide dimer (**SC1+SC2**) was used. The illumination times were decreased from 300 s (lane 1) to 240 s (lane 2), 120 s (lane 3), 60 s (lane 4) and finally 30 s (lane 5). It can be seen that in the last lane with the shortest irradiation time only two bands were present (*b* and *d*), which were related to unreacted single strands and oligonucleotide dimers, respectively. As the irradiation time was increased, two additional bands (*a* and *c*) appeared and became more pronounced with longer illumination. Since the bands *a* and *c* run faster than the bands *b* and *d*, degradation of the oligonucleotides due to prolonged irradiation is most likely the reason of this observation [307].

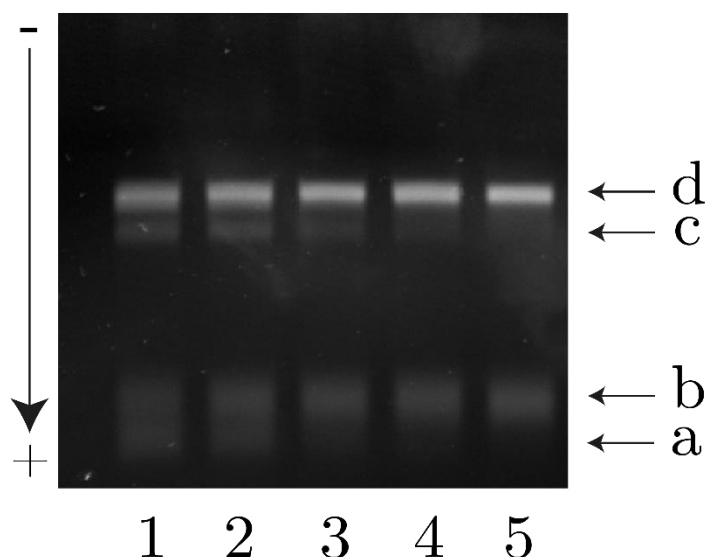


**Figure 5.9:** 6% native polyacrylamide gel with carbazole-modified oligonucleotide dimers (**SC1+SC2**) after different times of UV-A irradiation. The gel was stained with ethidium bromide. Lane 1: 300 s; Lane 2: 240 s; Lane 3: 120 s; Lane 4: 60 s; Lane 5: 30 s. The bands are labelled as degraded single strand (*a*), single strand (*b*), degraded dimer (*c*) and dimer (*d*).

The crosslinking of the oligonucleotides was verified by denaturing polyacrylamide gel electrophoresis. Denaturing of dsDNA was achieved using several methods [308]. Firstly, urea embedded in the polyacrylamide matrix helped breaking the hydrogen bonds of the dsDNA as it migrated through the gel. Secondly, the samples were mixed with formamide, which is known to lower the melting temperature of the dsDNA due to disruptive interaction with the helix [309]. Finally, heating above the melting temperature and rapid cooling to room temperature (typically with an ice-bath) provided effective denaturation. Denaturing gel electrophoresis was therefore a suitable tool to investigate crosslinked DNA because the covalent bond formed after irradiation prevented the dsDNA to completely dehybridise.

**Figure 5.10** shows a denaturing polyacrylamide gel with samples (SC1-SC4) that were crosslinked for 30 seconds. For denaturation, urea and formamide were employed and the sample heated to 95°C for 30 seconds with subsequent rapid cooling to 0°C in an ice-bath. This procedure broke the oligonucleotide assemblies into single strands if no covalent bond was formed. DNA dimers (lane 2), DNA trimers (lane 3) and DNA tetrahedral structures (lane 4) were well retarded in comparison to the single strands (lane 1). This shows that the DNA crosslinking reaction was performed very efficiently and that the oligonucleotide assemblies were highly stable even under the highly unfavourable conditions used in this experiment. On the other hand, non-crosslinked DNA assemblies completely disintegrated as it was expected.

The conclusions of the experiments are the following: 1) The unmodified and carbazole-modified oligonucleotides formed distinct assemblies depending on the number of strands mixed (dimers, trimers, tetramers). 2) The DNA modified with BCN/azide groups reacted in an uncontrolled way, probably due to the high reactivity of the BCN molecule. 3) The 3-cyanovinyl carbazole modification yielded successful crosslinks, which was verified by denaturing PAGE.

In the next part, the assembly of gold nanoparticles with these oligonucleotides will be discussed and the successful crosslinking with the 3-cyanovinyl carbazole modification in this hybrid system will be shown.

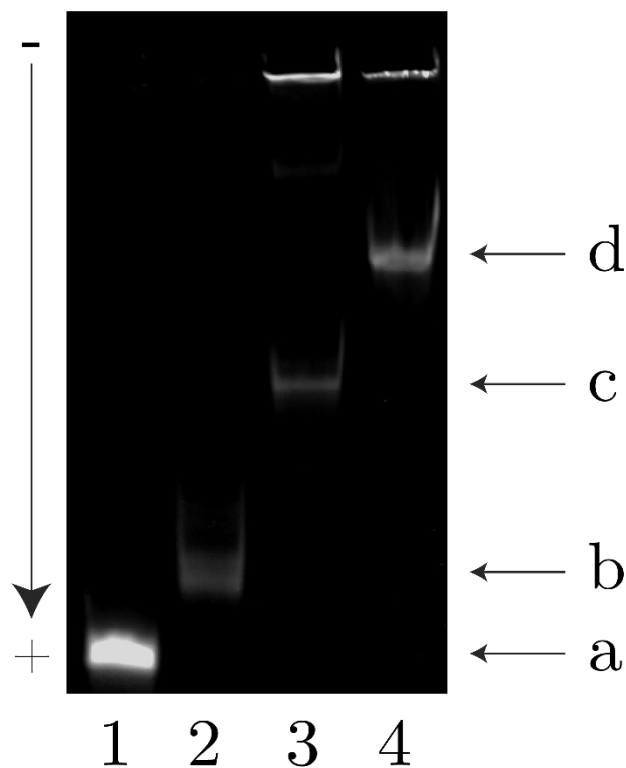


Figure 5.10: 6% denaturing polyacrylamide gel with 3-cyanovinyl carbazole-modified and cross-linked oligonucleotides. The gel was stained with ethidium bromide Lane 1: Single strand (SC1); Lane 2: two oligonucleotides (SC1+SC2); Lane 3: three oligonucleotides (SC1-3); Lane 4: All four oligonucleotides (SC1-4). The bands were labelled as single strands (a), dimers (b), trimers (c) and tetrahedra (d).

## 5.2 Directed gold nanoparticle assembly

After the characterisation of the oligonucleotide hybridisation, the DNA strands were utilised for the formation of self-assembled nanostructures. It should be noted that one drawback of nanoparticle assembly is that typically the overall yield of the reaction is rather low [310, 311]. While this is commonly encountered in the literature, there is rarely a discussion about this issue [312]. Furthermore, the hybridisation conditions for nanoparticle assembly are clear and vary significantly in different reports. For a similar system, sodium chloride concentrations between 50-100 mM and annealing temperatures from 50°C-95°C as well as different buffers for hybridisation have been reported [249, 250, 259, 311]. Therefore, several experiments were conducted trying to optimise the system. It will be shown that for some unknown reason the assembly yield is limited under the conditions tested. In the following experiments, AuNP dimers and AuNP trimers were made from AuNP-**S1**+AuNP-**S2** and AuNP-(**S1-S3**), respectively.

### 5.2.1 Unmodified oligonucleotides

AuNP-DNA monoconjugates were the starting point for the formation of nanoparticle dimers, trimers and tetramers (see section 4.5.1). The AuNP-DNA monoconjugates were mixed in equimolar amounts and different hybridisation conditions were then tested to optimise the system.

The annealing temperature was varied as the largest effect on hybridisation performance was expected when the temperature is varied by around 5-10°C above and below the melting temperature (see section 2.4.1). The ionic strength was varied with the limitation that BSPP-functionalised gold nanoparticles were only stable in sodium chloride concentrations less than 80 mM. In all experiments phosphate buffer with a pH of 7.4 was used because only minor hybridisation changes were expected in the pH range of 7-8. The samples were heated at the desired temperature for 5 minutes and then slowly cooled down to room temperature (<30°C) in about 3 hours.

Figure 5.11 shows a typical agarose gel in which unreacted gold nanoparticle monoconjugates were separated from gold nanoparticle dimers [250]. The salt concentration was 60 mM and the hybridisation temperature was changed in 5°C steps from 75°C (lane 1) to 60°C (lane 4). Firstly, it can be seen that there are only two bands present, which were assigned to unreacted AuNPs (band *a*) and AuNP dimers (band *b*). Secondly, the intensity of the second band slightly increases with decreasing annealing temperature. It has been reported previously that oligonucleotides might detach from gold nanoparticles when the temperature of the solution becomes too high [313]. This could explain the decreased hybridisation yield at higher temperatures. Thirdly, it is evident that after hybridisation a lot of nanoparticles remain unreacted, which shows the aforementioned problem of assembly yield. It should be noted that under similar conditions the free oligonucleotides hybridise in high yields (see section 5.1.2).

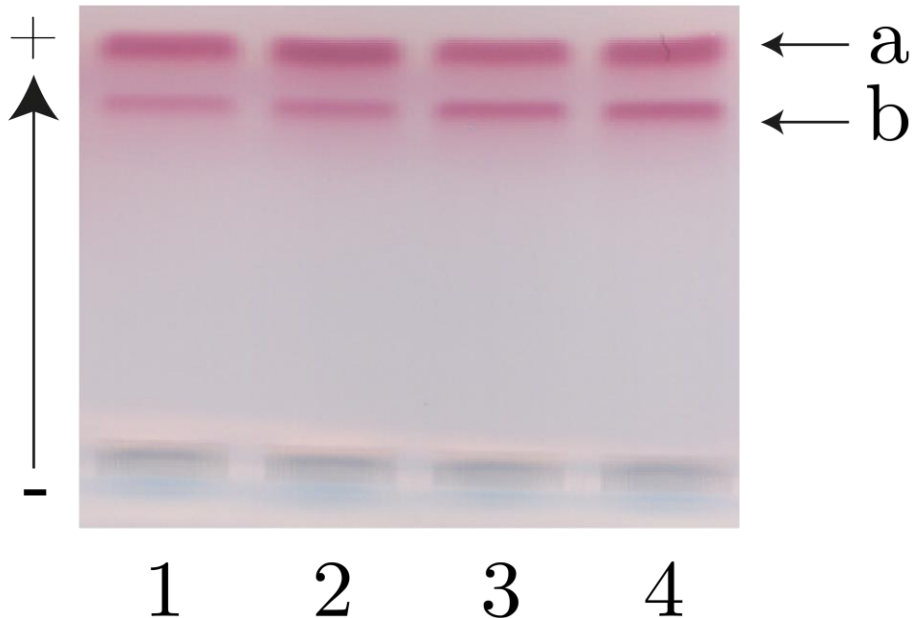
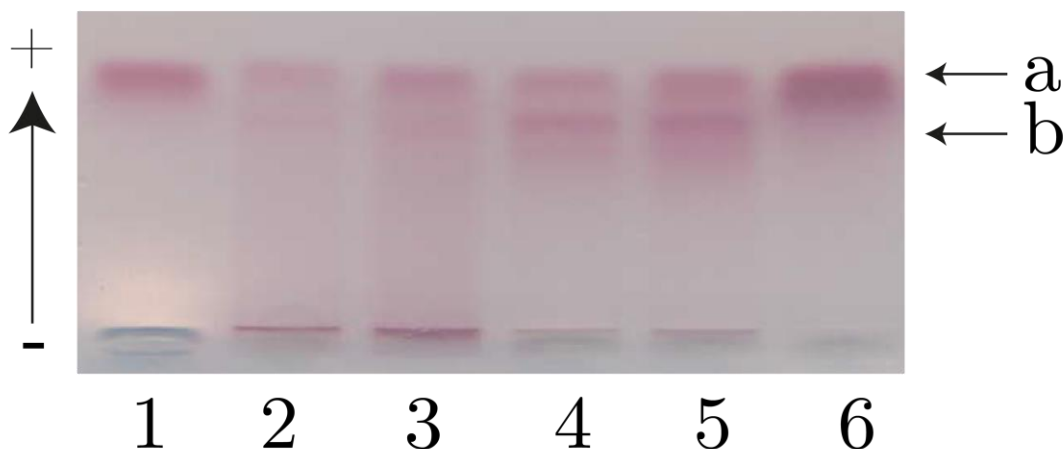


Figure 5.11: 2% agarose gel of 15nm gold nanoparticle dimers (SA1+SA2) hybridised at different temperatures. The buffer used was phosphate buffer (20 mM, pH 7.4) and the final NaCl concentration was 60 mM. Lane 1: 75°C, Lane 2: 70°C, Lane 3: 65°C, Lane 4: 60°C. The lanes are labelled as single AuNPs (a) and AuNP dimers (b).

Similar results as above were obtained when the ionic strength was varied. The outcome is shown in **Figure 5.12**. The hybridisation temperature was set to 65°C and the sodium chloride concentration was varied between 10 mM and 100 mM. In lane 1, a monoconjugate reference was run. The NaCl concentration in the different lanes was 100 mM (lane 2), 80 mM (lane 3), 60 mM (lane 4), 40 mM (lane 5) and 10 mM (lane 6).

In the samples with sodium chloride concentrations of 40 mM and higher dimer bands appeared. However, the degree of hybridisation performance differed between the samples. It can be seen that the best results in terms of dimer band intensity were at NaCl concentrations between 40 mM and 60 mM (lanes 4 and 5). At higher concentrations aggregation of the nanoparticles started to occur. The large clusters of the gold nanoparticles were not entering the pores of the agarose gel and therefore remained in the well (lanes 2 and 3). Due to aggregation, the hybridisation yield of dimers is significantly reduced and only a faint dimer band is visible. If the salt concentration was very low no hybridisation could be detected, which was expected because of the electrostatic repulsion between both, the gold nanoparticles and the oligonucleotides. Furthermore, the intensity ratio the monomer and dimer band was still below 50% under varying conditions.



**Figure 5.12:** 2% agarose gel of 15nm gold nanoparticle dimers (SA1+SA2) hybridised with different sodium chloride concentrations. The hybridisation temperature was 65°C and the buffer was phosphate buffer (20 mM, pH 7.4) with varying NaCl contents. Lane 1: Monoconj. reference; Lane 2: 100 mM NaCl; Lane 3: 80 mM NaCl; Lane 4: 60 mM NaCl; Lane 5: 40 mM NaCl; Lane 6: 10 mM NaCl. The lanes are labelled as single AuNPs (a) and AuNP dimers (b).

So far the nanoparticles were in all the experiments heated in a water bath at the designated hybridisation temperature for 5 minutes and then left to cool to room temperature. It took 20-30 minutes to reach 50°C and another 2.5 hours to reach a temperature of 30°C or less. Next, the annealing time was increased and the influence of agitation investigated. The idea was to overcome potential kinetic limitations by increasing the reaction time and the diffusion of the nanoparticles in solution.

**Figure 5.13** depicts the agarose gel at three different conditions. In all experiments, the NaCl concentration was 50 mM. Lane 1 contained AuNP-DNA monoconjugates as a reference. In lane 2, the sample was incubated at 65°C for 5 minutes and left to cool to 50°C at which the sample was shaken for two additional hours at 50°C. Lane 3 shows a sample that was heated to 65°C for one hour and subsequently left to cool to room temperature. Lane 4 contained a sample that was heated to 50°C and shaken for 2 hours before left to cool to room temperature.

The total hybridisation yield of gold nanoparticle dimers was not improved by any of the conditions chosen in these experiments. The prolonged incubation at 10-15°C below the melting temperature (lane 2) did not improve the nanoparticle dimer formation compared to the experiments conducted before. The extended heating period at 65°C (lane 3) as well as the lack of incubation at higher temperatures (lane 4) led to very poor nanoparticle assembly yields. There was only a very faint dimer

band visible in those two lanes indicating unsuccessful dimer formation. In the case of the longer incubation at 65°C, there the oligonucleotides probably detached from the gold nanoparticles, which was observed in other experiments before. On the other hand, if the hybridisation was not performed at a temperature high enough it might be that the kinetics of the nanoparticle assembly was too slow to be observed. This would also explain why there was no improvement under the condition in lane 2.

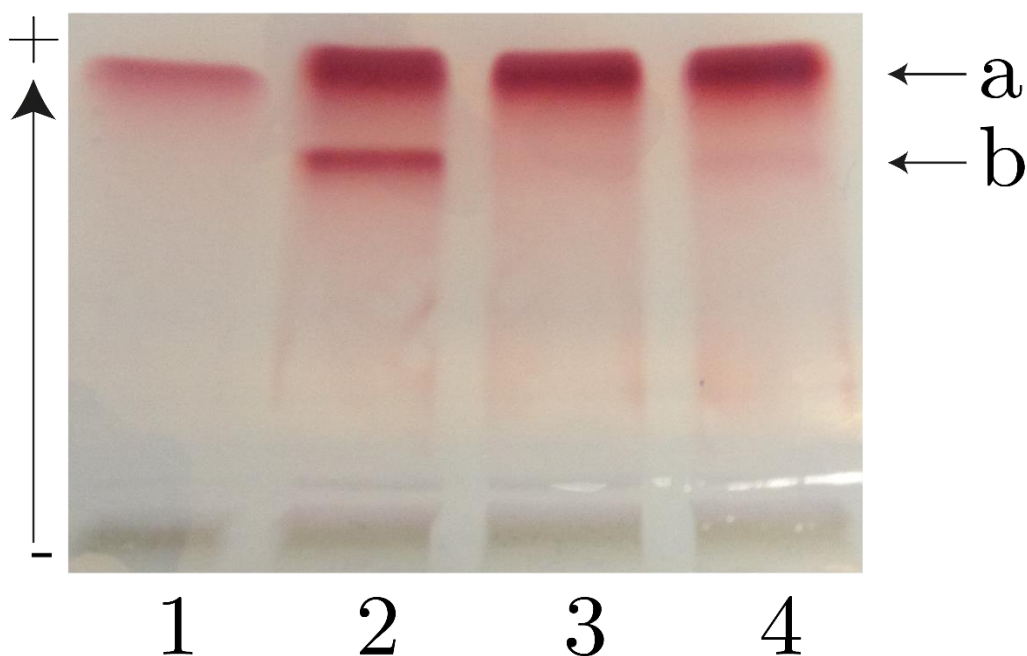


Figure 5.13: 2% agarose gel of 15 nm gold nanoparticle dimers (SA1+SA2) hybridised with different conditions. The buffer was phosphate buffer (20 mM, pH 7.4) with 50 mM NaCl. Lane 1: Monoconj. reference; Lane 2: Hybr. Temp = 65°C, shaken for 2 h at 50°C; Lane 3: Hybr. Temp = 65°C for 1 h; Lane 4: Hybr. Temp = 50°C, shaken for 2 h at 50°C. The lanes are labelled as single AuNPs (a) and AuNP dimers (b).

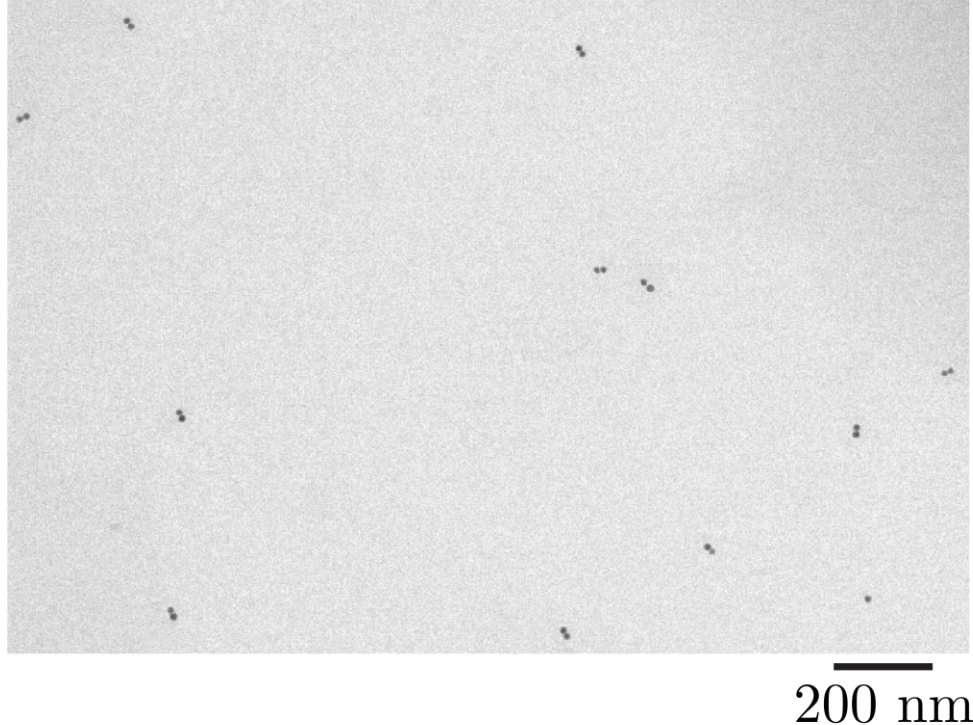
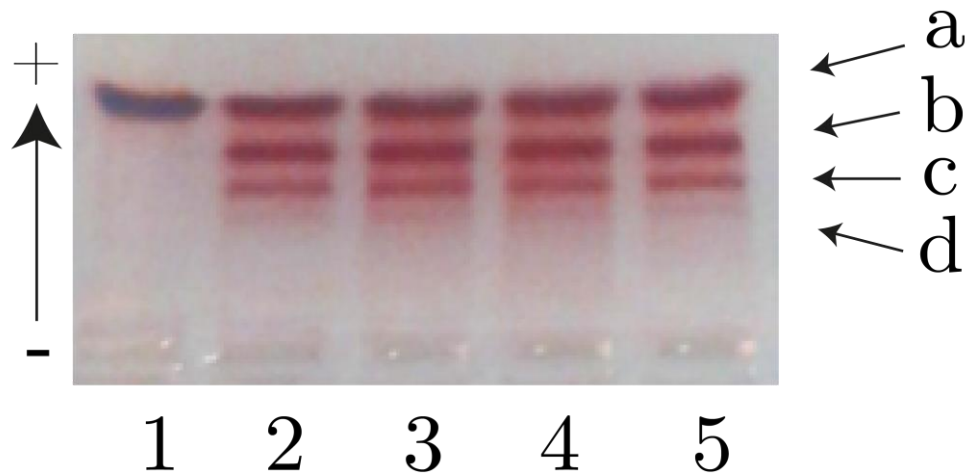
Agitation of the samples was assumed to increase the diffusion of the gold nanoparticles in the solution and therefore to facilitate hybridisation. While prolonged shaking was found not to increase the hybridisation yield, few short inversions of the solution every 5-10 minutes at the beginning of the reaction did accelerate the reaction. With this method hybridisation consistent yields between 40-50% were obtained in three hours of hybridisation. It remains unclear what the reason for this behaviour was but most probably the hybridisation process was diffusion-limited and therefore shaking increased the kinetics. In order to gain a better understanding, it would be useful to take theoretical models into account, which consider the diffusion of the gold nanoparticles and hybridisation probabilities

as parameters. Such modelling could give indications on how long the hybridisation process takes to be completed as well as what final results could be expected.

In the last part of this subsection, the hybridisation of all four AuNP-DNA monoconjugates will be discussed. The result is shown in **Figure 5.14** where four different hybridisation parameters (NaCl concentration and temperature) were chosen. All monoconjugates were mixed in equimolar ratios. Lane 1 contains AuNP-DNA monoconjugates as a reference. In lanes 2 and 3 the sodium chloride concentration was 50 mM and 65 mM, respectively. The samples were hybridised at 60°C for 5 minutes and slowly left to cool down to room temperature in three hours. The sample in lane 4 was also hybridised at 60°C with 50 mM NaCl but prepared beforehand so that the total reaction time at room temperature was 18 hours. Lane 5 shows a sample, which was hybridised with 50 mM NaCl at 55°C for 5 minutes and left to cool to room temperature. In addition, this sample was shaken every 10 minutes in the first 30 minutes.

After the hybridisation of all four different AuNP-DNA monoconjugates there were four bands after gel electrophoresis. This indicated that dimers, trimers as well as tetramers formed during the hybridisation process. The different assemblies were well separated and could be extracted individually so that assembly purities of up to 85% were obtained. Representative TEM images of the respective bands are shown in **Figures 5.15-5.17**. There was always a certain percentage of other nanoparticle assemblies present after extraction as gel electrophoresis is not a perfect purification method. Another important observation was that there is no significant difference in the hybridisation yields for the different conditions. It was at least expected to shift the intensities towards the higher ordered structures by changing the reaction time. However, it remains unknown why the assembly yield was limited and further work needs to be conducted to optimise the hybridisation of nanoparticles with oligonucleotides.

To conclude this section, it has been shown that oligonucleotides present a versatile platform for the self-assembly of gold nanoparticles. Gold nanoparticle dimers, trimers and tetramers were separated by gel electrophoresis and extracted from the gel yielding nanoparticle assemblies with high purity. In the next section, oligonucleotides chemically modified with azide and BCN groups will be considered.



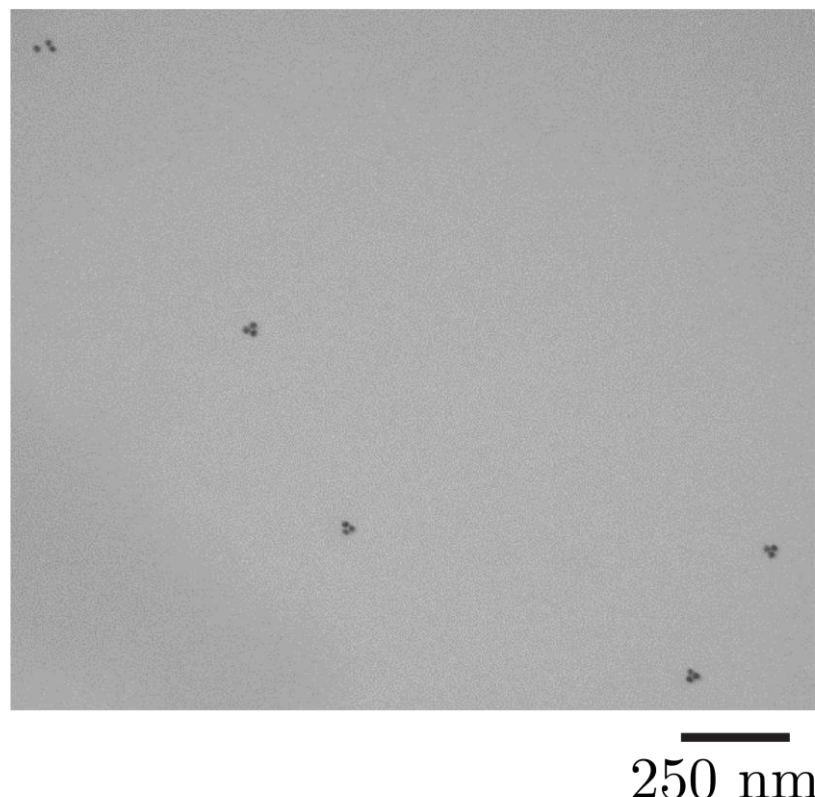


Figure 5.16: Representative TEM micrograph of gold nanoparticle trimers purified by agarose gel electrophoresis.

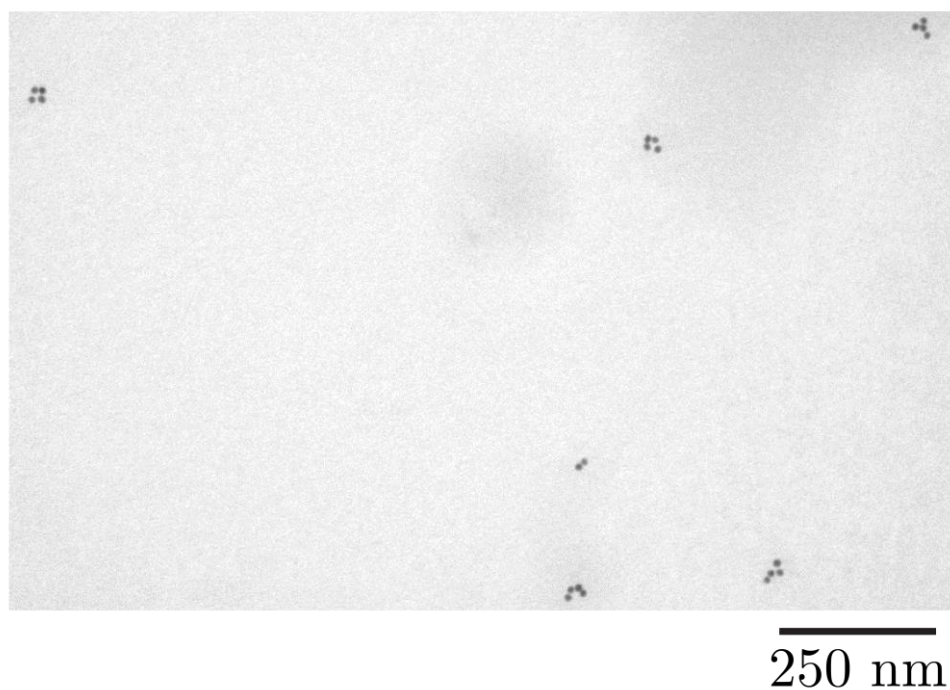


Figure 5.17: Representative TEM micrograph of gold nanoparticle tetramers purified by agarose gel electrophoresis.

### 5.2.2 Azide/BCN-modified oligonucleotides

In this part the assembly of gold nanoparticles using oligonucleotides with clicking groups will be discussed. The SPAAC reaction (see **section 2.4.2**) was performed with BNC and azide groups to promote copper-free click chemistry [221]. Two groups were placed in each oligonucleotide allowing covalent crosslinks to be formed in the middle of each edge of the tetrahedron (see **Appendix A.3**). The expected results were higher stability of the nanoparticle assemblies as well as a potential increase in hybridisation yield because once two strands hybridise they would not dehybridise again, even above the melting temperature.

In **Figure 5.18**, a representative gel is shown for a mixture containing all four different AuNP-monoconjugates. The nanoparticles were hybridised at 60°C for 5 minutes, shaken 3 times in 30 minutes and then left to cool to room temperature. The sodium chloride concentration was 50 mM (lane 1) and 65 mM (lane 2), respectively. The nanoparticles formed various assemblies, which were separated during gel electrophoresis. The intensity of band *d*, which was the tetramer band, increased with higher salt concentration. Additionally, the ratio between the unreacted monoconjugates (band *a*) and the assemblies was smaller in lane 2 compared to the sample in lane 1. However, a fifth band appeared (band *e*) indicating that larger assemblies have formed during hybridisation.

The nanoparticle self-assembly with the azide/BCN-modified oligonucleotides was clear from the bands that were obtained after gel electrophoresis. An increase of the salt concentration led to more intense bands especially for the larger assemblies. The hybridisation was increasingly favoured when more counter-ions were in the media. In addition, the irreversible bond from the SPAAC reaction should increase the product yield. However, a significant amount of unreacted strands was still present. Even though the fifth band was an unexpected, it was consistent with the previous results from DNA assemblies of BCN/azide-modified oligonucleotides (**section 5.1.2.2**).

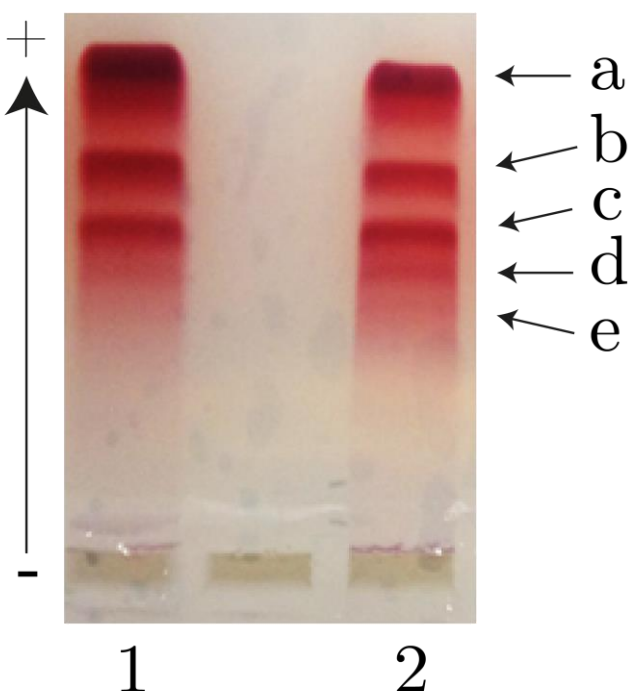


Figure 5.18: Agarose gel of hybridised AuNP-monoconjugates with azide/BCN-modified oligonucleotides (SB1-SB4). The hybridisation temperature was 65°C. Phosphate buffer (20 mM, pH 7.4) and two different salt concentrations were used. Lane 1: 50 mM NaCl; Lane 2: 65 mM NaCl. The bands correspond to monoconjugates (a), dimers (b), trimers (c), tetramers (d) and higher ordered structures (e).

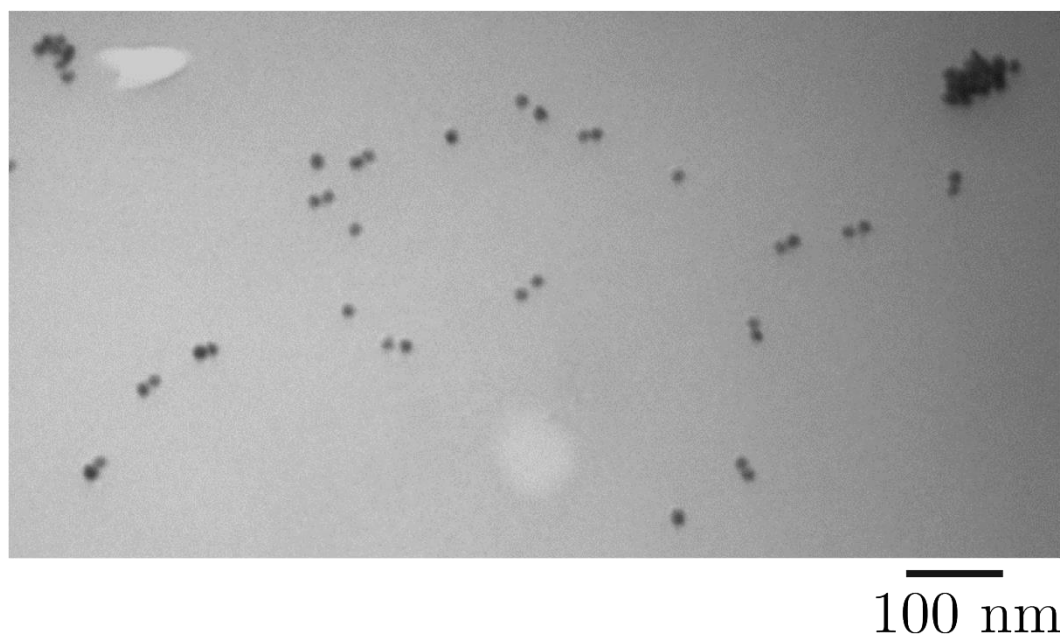


Figure 5.19: Representative TEM micrograph of the AuNP dimer band made with azide/BCN-modified DNA (SB1-SB4) after gel electrophoresis (see Figure 81, lane 2, band b).

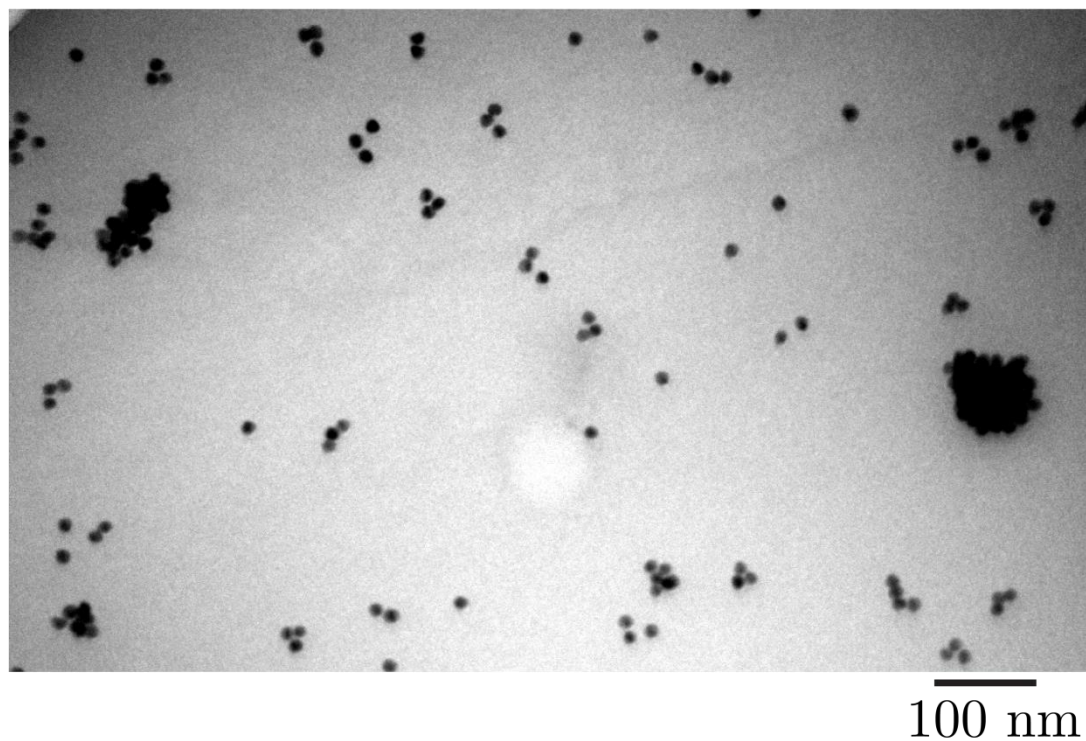


Figure 5.20: Representative TEM micrograph of the AuNP trimer band made with azide/BCN-modified DNA (SB1-SB4) after gel electrophoresis (see Figure 81, lane 2, band c).

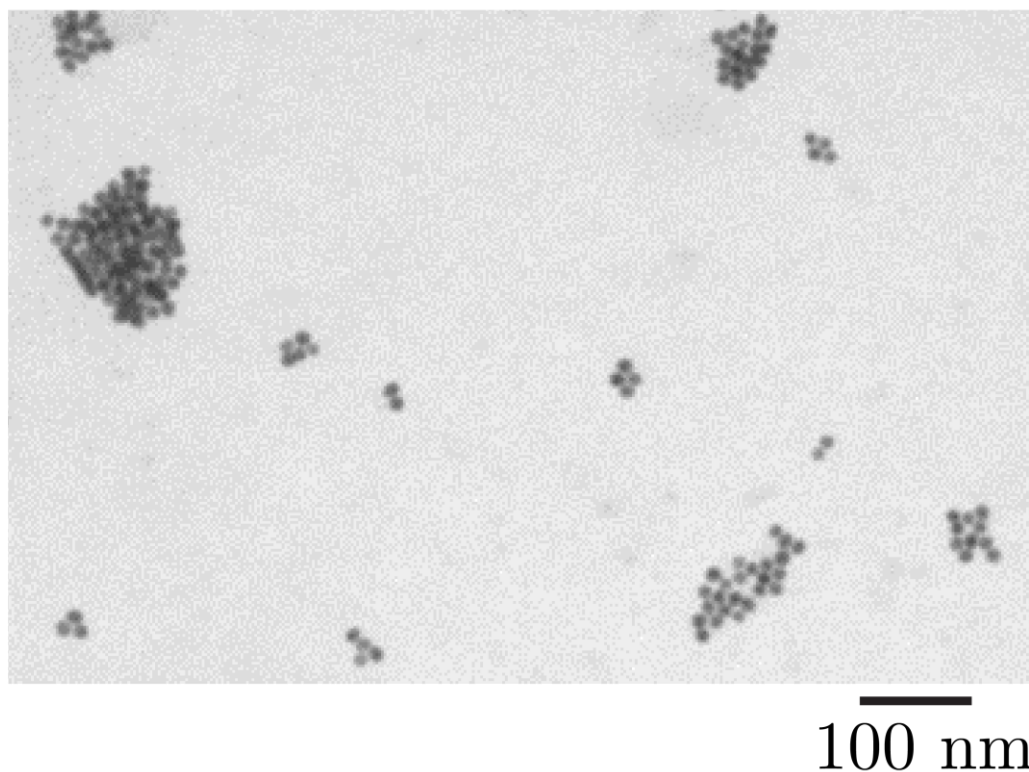


Figure 5.21: Representative TEM micrograph of the AuNP tetramer band made with azide/BCN-modified DNA (SB1-SB4) after gel electrophoresis (see Figure 81, lane 2, band d).

The TEM images shown in **Figure 5.19-5.21** depict the contents of the bands *b-d* from the sample in lane 2 (**Figure 5.18**). As expected, the main contents of band *b* and *c* were dimers and trimers, respectively. Nevertheless, in all TEM images large aggregates of gold nanoparticles were found. These clusters might form over time, which would explain the presence of the bands. The number of aggregates increased from the top bands to the bottom bands. The tetrahedron band *d* contained almost only aggregates. This behaviour was encountered in all experiments where AuNP-DNA monoconjugates with the two different clicking groups were employed.

In **section 5.1.2**, the polyacrylamide gel analysis of the azide/BCN-modified DNA revealed a ladder-like structure that could be explained with spontaneous multiple reactions of the clicking groups. This explanation is supported by the behaviour of the gold nanoparticle assemblies during hybridisation. Most probably, the click reaction between the BCN and the azide modification happened quicker than the hybridisation process so that the oligonucleotides were not crosslinked at the designed positions. The oligonucleotides on the gold nanoparticles were also relatively flexible due to their length and this may have led to uncontrolled clicking when nanoparticles were in close proximity to each other.

On the other hand, there were no additional bands found in the oligonucleotide mixtures with the same clicking group (azide or BCN). This outcome was verified by hybridising the two AuNP-DNA monoconjugate pairs (**SB1+SB2,SB3+SB4**) with the same modification (azide+azide and BCN+BCN). The resulting agarose gel is depicted in **Figure 5.22**. Different from the previous gel, only two bands appeared indicating that there were only dimers and larger structures present. TEM analysis of the respective dimer bands (band *b*) showed the expected result with highly enriched dimers ( $\geq 80\%$ ) without any clusters (**Figure 5.23**).

In conclusion, the SPAAC reaction between oligonucleotides with two BCN and azide groups was investigated in order to promote crosslinking of oligonucleotides. When oligonucleotides with different clicking groups were mixed and hybridised, several unexpected bands appear in the PAGE gel (**section 5.1.2**). A similar behaviour was found when AuNP-DNA conjugates were hybridised to form nanoparticle assemblies. TEM micrographs showed large clusters of nanoparticles after hybridisation, consistent with the previous results. However, if AuNP-DNA conjugates with the same clicking group were mixed no such clusters appeared. Therefore, it became

clear that if more than one clicking group per oligonucleotide is involved, unwanted crosslinking cannot be excluded. Further experiments could be conducted with less reactive cyclooctynes to check if the problem of uncontrolled crosslinking could be avoided. In order to overcome these issues, an alternative chemistry has been employed, which involves the utilisation of 3-cyanovinyl carbazole – a photo-reactive molecule [24, 213].

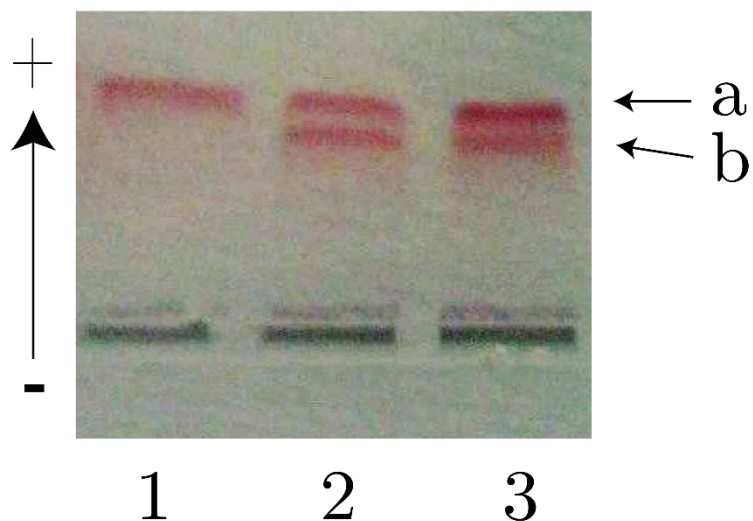


Figure 5.22: Agarose gel of gold nanoparticle dimers. The DNA pairs containing the same clicking groups were utilised. Lane 1: Monoconjugate; Lane 2: SB1+SB2 (azide); Lane 3: SB3+SB4 (BCN). The bands are labelled as monoconjugates (a) and dimers (b).

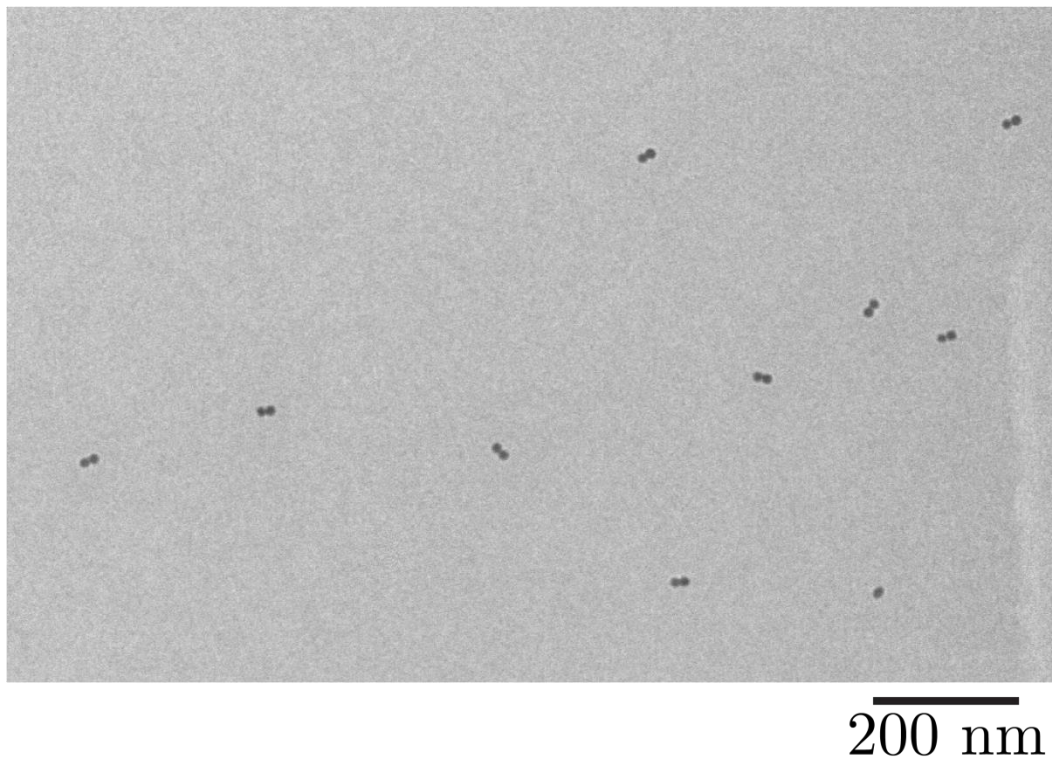


Figure 5.23: TEM image of AuNP dimers. The contents are from the agarose gel in Figure 5.22 (Lane 2, band b).

### 5.2.3 3-cyanovinyl carbazole-modified oligonucleotides

As outlined earlier, 3-cyanovinyl carbazole is a molecule that forms a cyclobutane ring with a thymine base upon irradiation with UV-A light [24] (see **section 2.4.2**). While there have been few reports on 3-cyanovinyl carbazole for oligonucleotide crosslinking, there are no reports to date where this molecule was used to crosslink nanoparticle assemblies [213, 314, 315]. The main advantage of this photo-responsive molecule is that it promotes a reversible photo-reaction, which is of particular interest if one wants to control the crosslinking and de-crosslinking of nanoparticle assemblies [316, 317].

Figure 5.24 illustrates the experimental route for gold nanoparticle dimers. As described before, AuNP-DNA monoconjugates were hybridised to form gold nanoparticle dimers. After hybridisation, the dimers were illuminated with UV-A light in order to crosslink the oligonucleotides at the position of the 3-cyanovinyl carbazole. The crosslinked dimers were then stable under denaturing conditions. The reaction was reversed by illumination with UV-B light leading to single nanoparticles when the sample was denatured. The reversibility of the covalent link provides a new feature, which is not available in the SPAAC reaction or with psoralen [209].

This scheme is also valid for other types of assemblies like trimers and tetramers, which have been synthesised in this work as well.

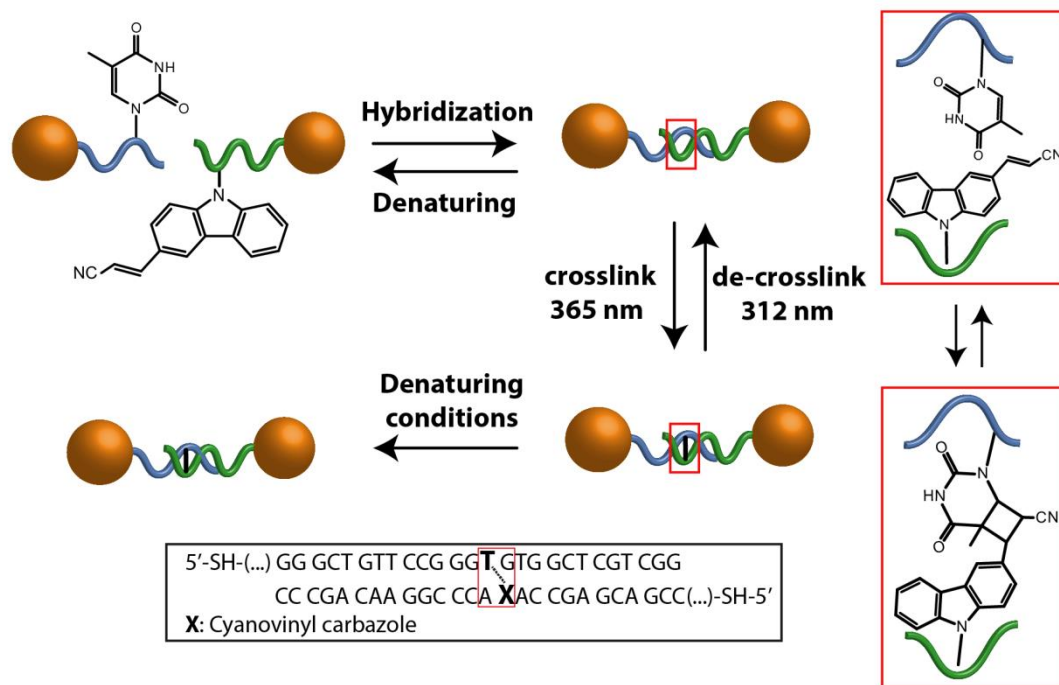
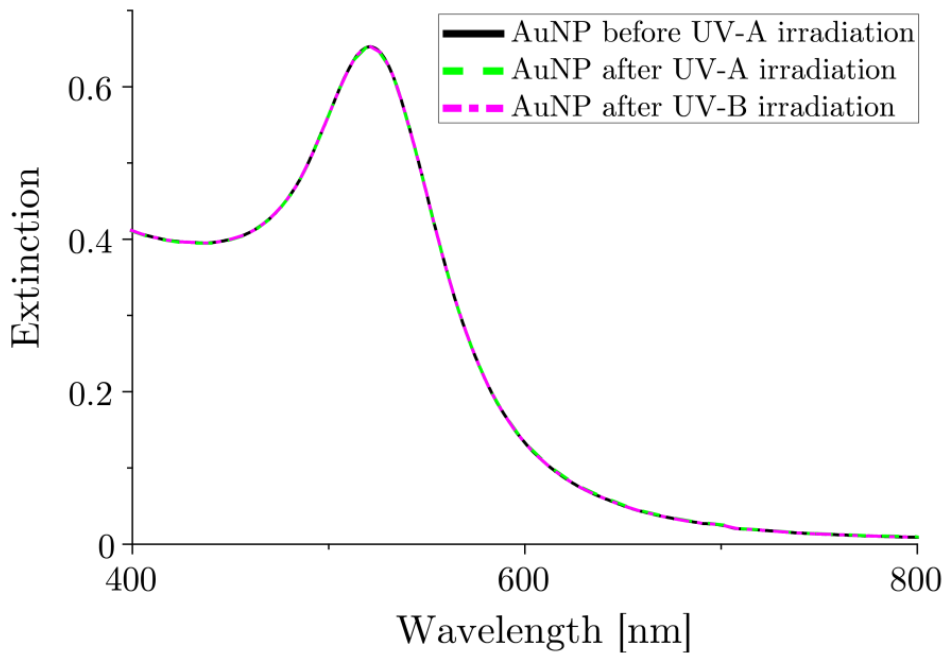


Figure 5.24: Illustration of DNA cross-linking and de-crosslinking on gold nanoparticle dimers. Gold nanoparticles conjugated with complementary oligonucleotides are hybridized to form dimers. One of the oligonucleotides contains a 3-cyanovinyl carbazole group, which can react with an adjacent thymine, in the opposite strand, upon light irradiation. Irradiation with UV-A light allows the formation of a cyclobutane bridge between the opposite thymine base as indicated by the red box. After cross-linking, the dimers remain intact even under denaturing conditions. The crosslinked DNA strands can be reversibly de-crosslinked with UV-B light irradiation.



**Figure 5.25:** UV-Vis spectra of  $15 \pm 1$  nm gold nanoparticles before and after irradiation with UV-A (365 nm) and UV-B light (312 nm) for 15 minutes. The perfect overlap of the spectra indicates that there is no change of the gold nanoparticles during UV irradiation.

In a first experiment, gold nanoparticles were irradiated with UV-A and UV-B light in order to account for a potential change in morphology or size. The reason is that ultraviolet light is used for the synthesis of nanoparticles with different shapes [318, 319]. The nanoparticles were irradiated under the conditions used for the carbazole crosslink reaction, i.e. in phosphate buffer (20 mM, pH 7.4, 50 mM NaCl) and cooled in an ice bath. A UV-Visible spectrum was taken before and after the irradiation (Figure 5.25). It can be seen that each of the two spectra before and after UV-A and UV-B illumination overlap. This indicated that the nanoparticles were not altered by the UV illumination, which was verified by TEM imaging.

The hybridisation of the different monoconjugates and separation of the nanoparticle assemblies were performed as explained earlier. The nanoparticle assemblies were then irradiated for 15 minutes with the respective UV light for crosslinking and de-crosslinking and subsequently analysed by agarose gel electrophoresis as well as TEM.

In order to test the successful crosslinking of gold nanoparticle dimers, denaturing conditions were applied. This was done by addition of formamide to the nanoparticles and incubation at 70°C for 5 minutes. Subsequently, the solution was quickly cooled to room temperature in an ice-bath. Similar as for the DNA the

crosslinked nanoparticle assemblies were expected to be stable under these conditions. For comparison, the assemblies were run under native conditions with Ficoll-400 instead of formamide. Two different final volume percentages of formamide were used to check if the denaturing conditions were appropriate for this system. It should be noted that the density of formamide was high enough to replace Ficoll-400 completely. The agarose gel showing the results of the denaturing experiment is presented in **Figure 5.26**.

In lanes 1 and 2, gold nanoparticle monoconjugates and dimers were run under native conditions as a reference. Lanes 3-5 contained monoconjugates, non-crosslinked dimers and crosslinked dimers with 30% v/v formamide under denaturing conditions. Lanes 6-8 contained the same set of samples but with 50% v/v formamide. Clearly, all monoconjugate as well as dimer bands ran on the same level showing that formamide did not influence the electrophoretic mobility of the nanoparticles. This includes the colloidal stability of the gold nanoparticles against formamide. More importantly, the non-crosslinked dimers (lanes 4 and 7) were completely denatured whereas the crosslinked dimers (lanes 5 and 8) were retarded as the control in lane 2.

On the one hand, it can be concluded that the denaturing conditions applied in this experiment were sufficient to destroy the nanoparticle assemblies. From the two different conditions tested in this experiment, it is clear that a formamide content of 30% v/v was high enough for complete denaturation of the nanoparticle assemblies. On the other hand, it was shown that the crosslink reaction worked effectively even in nanoparticle assemblies. Different from the azide/BCN-modified oligonucleotides no clustering of nanoparticles occurred.

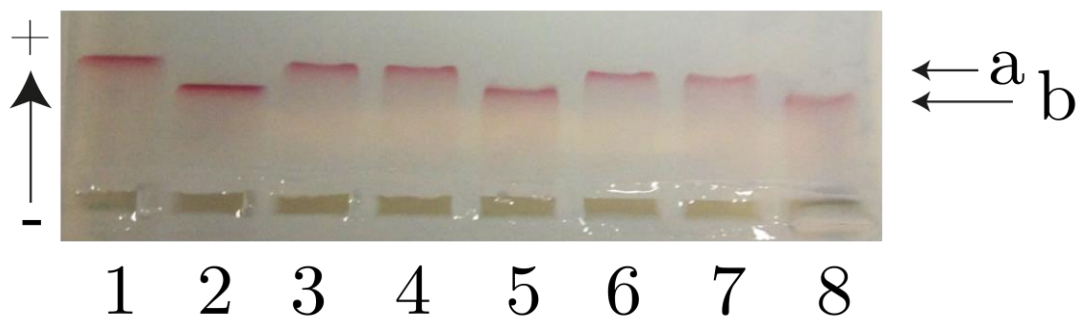


Figure 5.26: 2% agarose gel of non-crosslinked (nc) and crosslinked (c) gold nanoparticle dimers (SC1+SC2). Lane 1: monoconjugates native; Lane 2: dimers native; Lane 3: monoconjugates formamide (30%); Lane 4: dimers (nc) formamide (30%); Lane 5: dimers (c) formamide (30%); Lane 6: monoconjugates formamide (50%); Lane 7: dimers (nc) formamide (50%); Lane 8: dimers (c) formamide (50%). The percentages are given as final v/v %. The bands are labelled as monoconjugates (a) and dimers (b).

The experiment shows how crosslinking oligonucleotides can stabilise gold nanoparticle assemblies even under very unfavourable conditions. While similar stabilisation can also be achieved by other means, for example utilising the SPAAC reaction or polymeric crosslinkers as discussed in **section 2.4.2**, the carbazole chemistry allows reversing the crosslinking reaction. This novel functionality will be shown in the following experiments with gold nanoparticle assemblies. The model assemblies of gold nanoparticle dimers, trimers and tetramers have been studied in the following ligation experiments.

In addition to UV-A irradiation, the samples were irradiated with UV-B and another time with UV-A light to complete an oligonucleotide crosslinking and de-crosslinking cycle. Following this, all samples were denatured with formamide and heat as described above and run against native control sample. **Figure 5.27** shows an agarose gel containing gold nanoparticle dimers. The monoconjugate reference in lane 1 ran on the same level as the de-crosslinked sample in lane 3. On the other hand, the two crosslinked and re-crosslinked samples ran slower indicating that the dimers were still intact even after denaturation. The gel demonstrates that the oligonucleotide crosslinking reaction worked very effectively in both directions [24, 314]. There was no sign of degradation after the full irradiation cycle. The respective bands were extracted from the gel and analysed with TEM (**Figure 5.28**). The images supported the findings from the agarose gel. The percentage of dimers present in the crosslinked sample was with an average of 85% as high as in the non-denatured sample. On the contrary, the amount of single nanoparticles after de-crosslinking was 90% on average. After re-crosslinking the dimer content dropped by

a few per cent with an average of 80% compared with the non-denatured sample. The loss could be explained with a small number of assemblies that might have denatured during irradiation or with incomplete crosslinking. Nevertheless, these numbers demonstrate that 3-cyanovinyl carbazole is a very effective crosslinker that can be used for *in situ* crosslinking of nanoparticle assemblies.

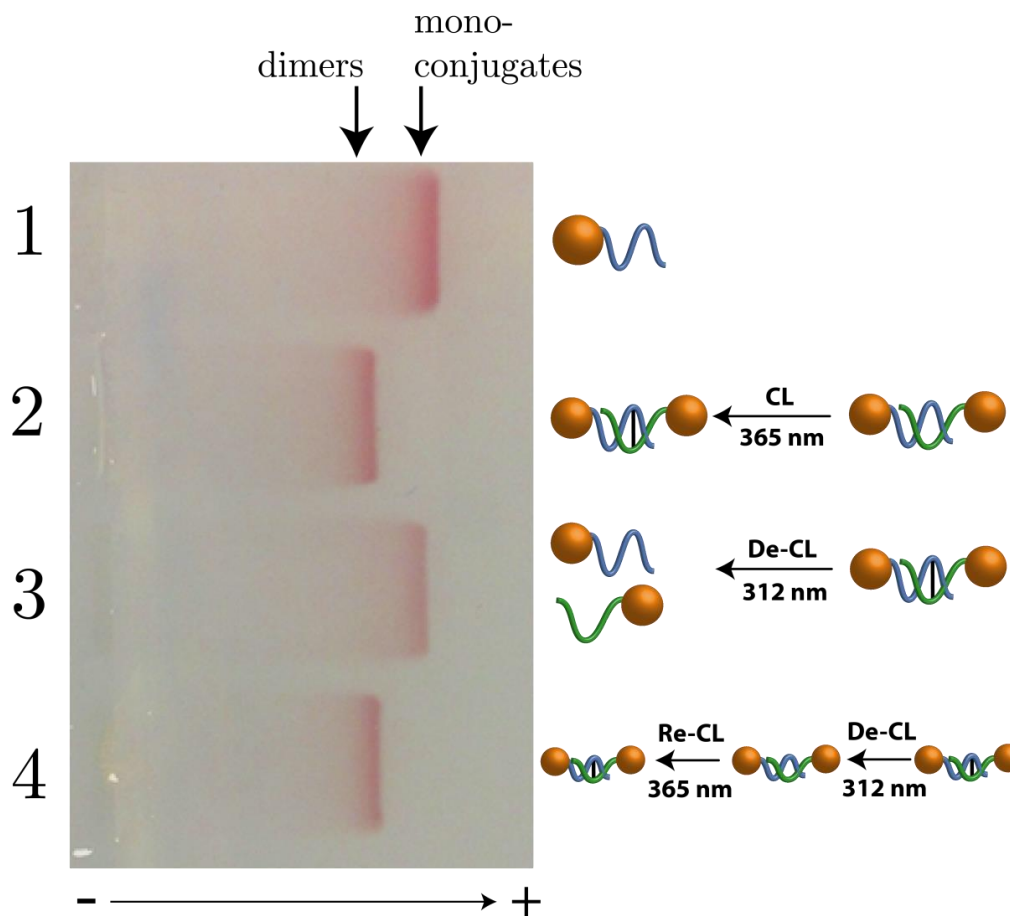


Figure 5.27: Agarose gel electrophoresis of gold nanoparticle dimers (SC1+SC2) under denaturing conditions showing the reversibility of the photo-crosslinking reaction. Lane 1: Mono-conjugates as reference; Lane 2: Cross-linked dimers; Lane 3: De-crosslinked dimers running as mono-conjugate band; Lane 4: Re-crosslinked dimers.

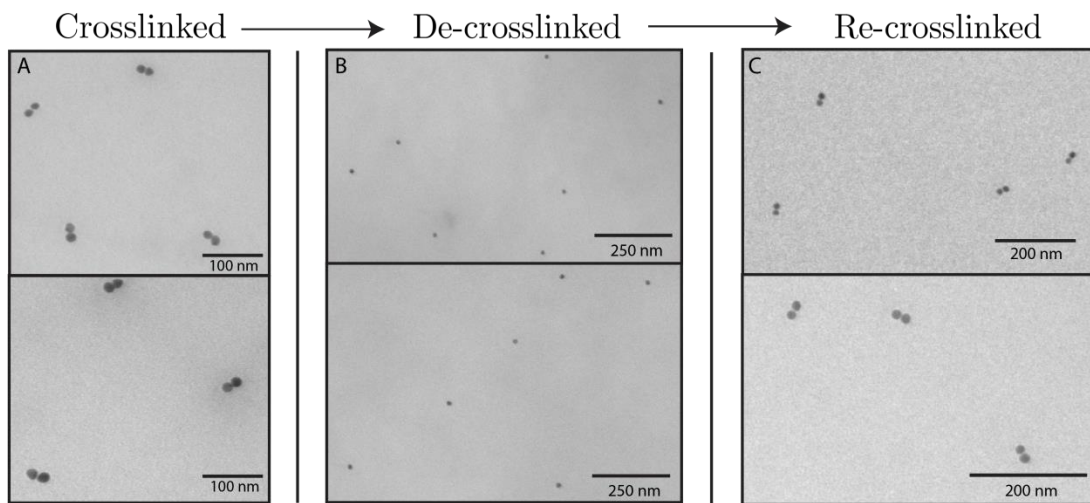


Figure 5.28: Representative TEM images of crosslinked and de-crosslinked 13 nm gold nanoparticle assemblies. The samples were deposited on the grids under DNA denaturing conditions. Photo-crosslinked gold nanoparticle dimers (A), de-crosslinked nanoparticle dimers, which disassemble to mono-conjugates (B), and re-crosslinked dimers (C).

Similar experiments were conducted with gold nanoparticle trimers and gold nanoparticle tetramers. In order for these nanoparticle structures to remain stable during denaturation, several crosslinks needed to be formed in one structure. While the gold nanoparticle trimers needed at least two of the three 3-cyanovinyl carbazole molecules to form interstrand bonds, the tetrahedral structures needed at least four of the six groups to react (Figure 5.29).

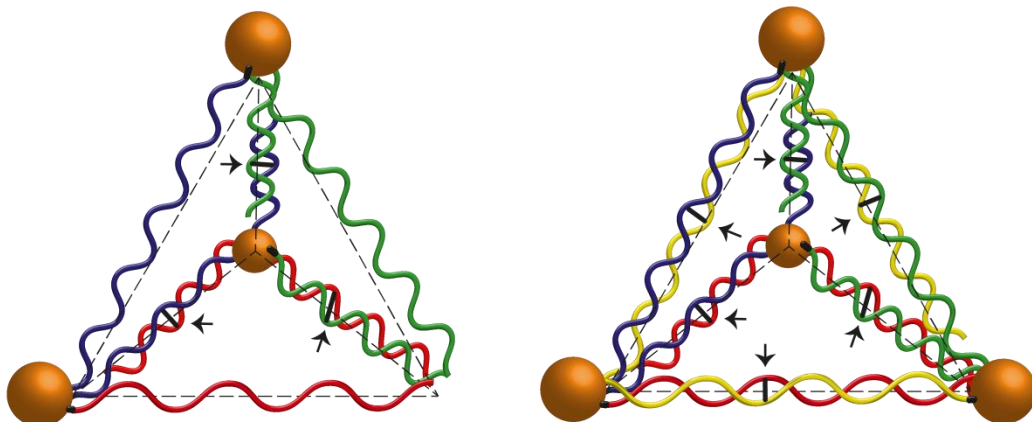


Figure 5.29: Illustration of the trimer and tetrahedron formation with three and four oligonucleotides. The arrows and black lines indicate the position of the 3-cyanovinyl carbazole groups.

The results of these experiments are shown in Figures 5.30 and 5.31 for the nanoparticle trimers and in Figures 5.32 and 5.33 for the nanoparticle tetramers, respectively. For comparison, monoconjugates and dimers were run as an additional

reference in the trimer sample and dimers as well as trimers in the tetrahedra sample. From the agarose gels it is evident that the carbazole reaction is working very well even in the more complex structures. Whereas the crosslinked and re-crosslinked trimer bands (lanes 3 and 5) were well behind the dimer (lane 2) and monoconjugate bands (lane 1), the de-crosslinked trimers (lane 4) were completely dehybridised and ran as a single band. TEM analysis of the bands verified that there was a high purity of the assemblies after the crosslinking steps and that almost no structures remained after de-crosslinking (Figure 5.31). The same result was achieved with the tetramer assemblies. The band of the gold nanoparticle pyramids (lanes 4 and 6) ran slower than the gold nanoparticle trimer reference (lane 3) after denaturing. On the other hand, when the assemblies are de-crosslinked and denatured the band runs on the level of the gold nanoparticle monoconjugates. This means that two aspects were demonstrated in these experiments. Firstly, several reactions could be triggered simultaneously in the same oligonucleotide in high yields. Secondly, complex nanoparticle assemblies could be stabilised and remained intact in very high numbers even in denaturing conditions.

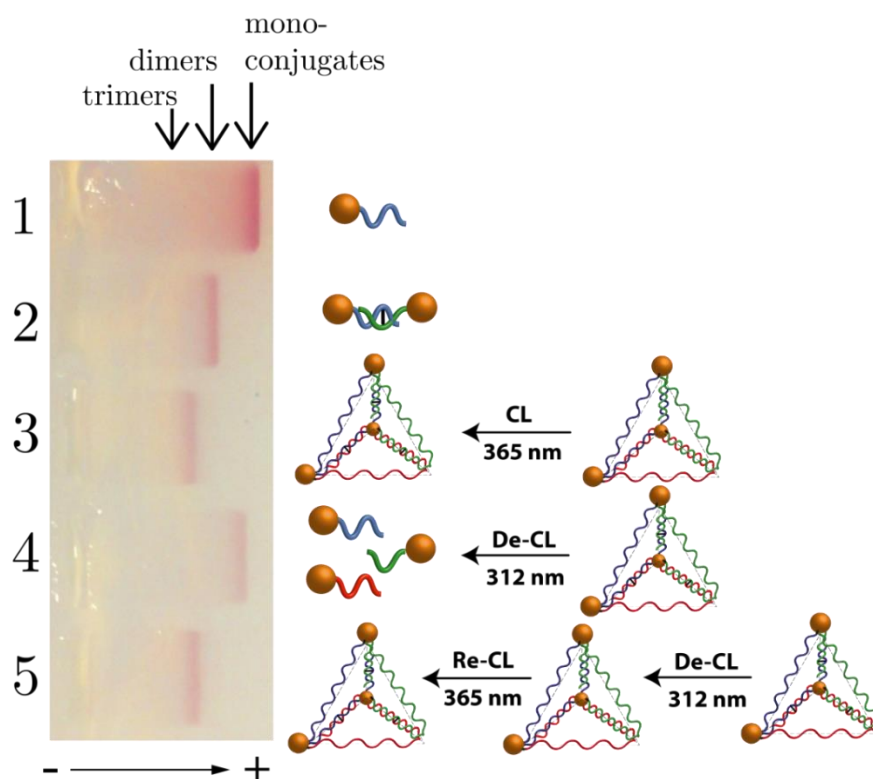


Figure 5.30: An agarose gel comparing crosslinked and de-crosslinked trimers (SC1-3) with mono-conjugates and dimers in denaturing conditions. Lane 1: reference mono-conjugates; Lane 2: reference dimers; Lane 3: crosslinked trimers; Lane 4: de-crosslinked trimers; Lane 5: re-crosslinked trimers.

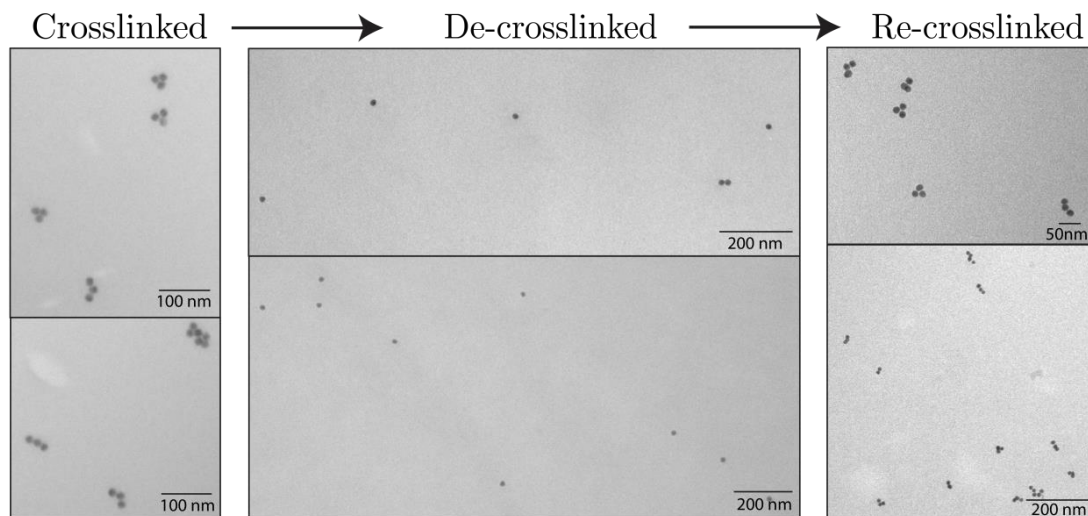


Figure 5.31: TEM images of crosslinked trimers, de-crosslinked trimers and re-crosslinked trimers.

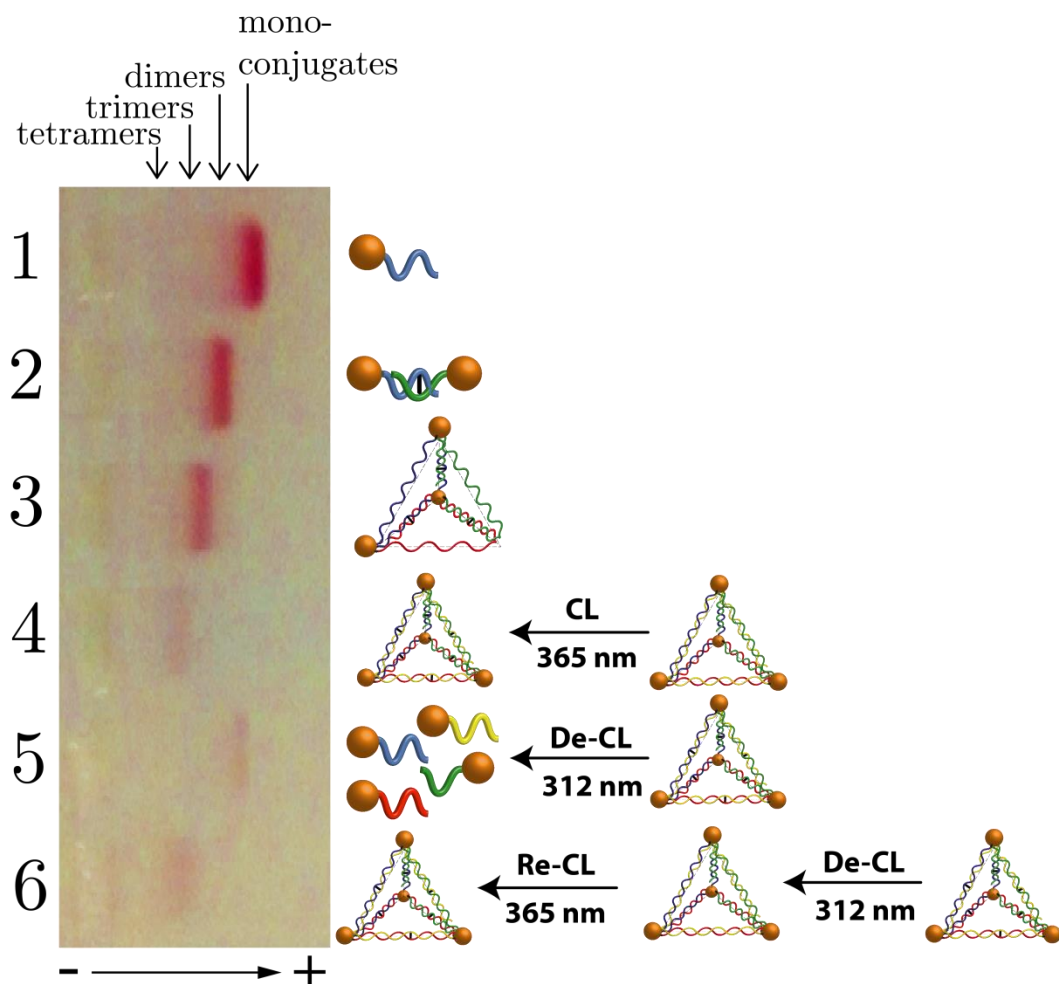


Figure 5.32: An agarose gel comparing crosslinked and de-crosslinked tetramers (SC1-4) with mono-conjugates, dimers and trimers in denaturing conditions. Lane 1: reference mono-conjugates; Lane 2: reference dimers; Lane 3: reference trimers; Lane 4: crosslinked tetramers; Lane 5: de-crosslinked tetramers; Lane 6: re-crosslinked Tetramers.

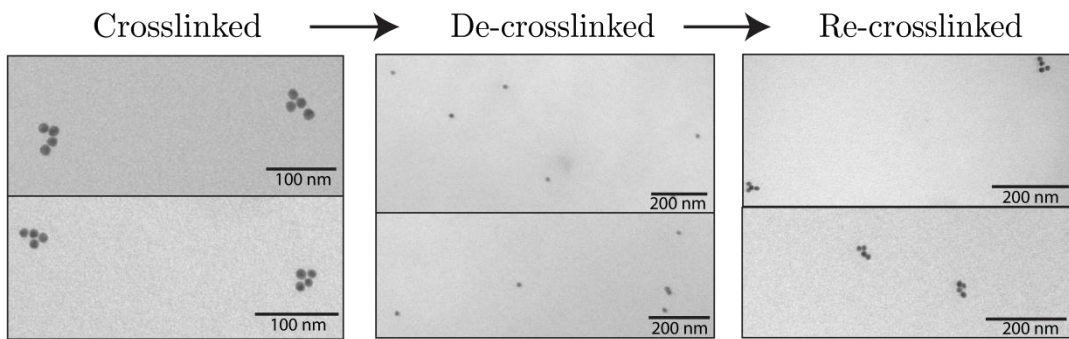


Figure 5.33: TEM images of crosslinked tetrahedra, de-crosslinked tetrahedra and re-crosslinked tetrahedra.

As a complementary method DLS was used to analyse the nanoparticle assemblies qualitatively [259] (see [section 3.4.7](#)). When the nanoparticles were bound in assemblies, their Brownian motion was reduced and a larger hydrodynamic radius was obtained. The results are shown in [Figure 5.34](#). The different nanoparticle assemblies were measured by DLS after extraction from the agarose gel. The hydrodynamic radius increased with the complexity of the assembly as expected.

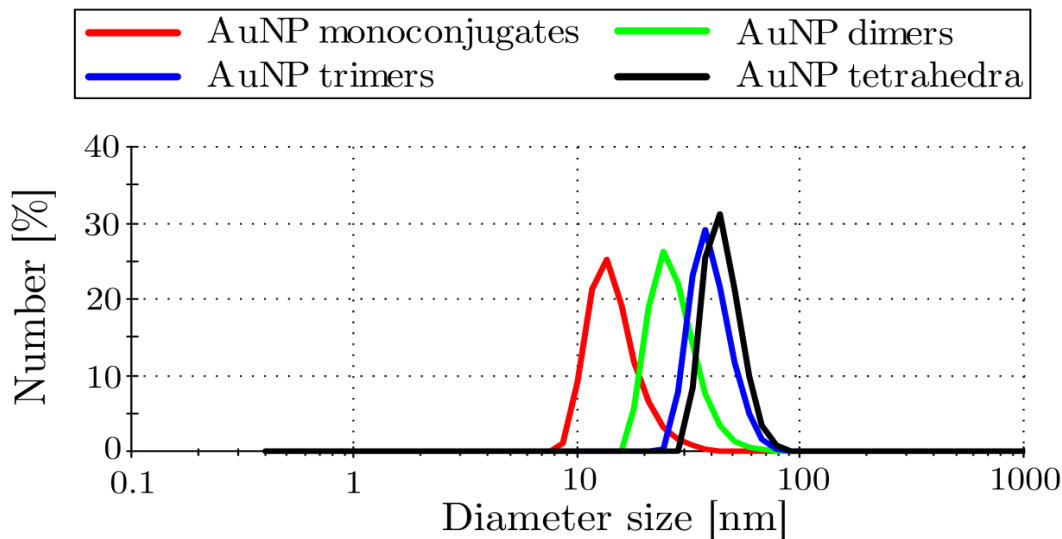


Figure 5.34: Dynamic light scattering spectra of gold nanoparticle monomers (red), dimers (green), trimers (blue), tetrahedra (black). The peaks of the hydrodynamic diameters are at 16.06 nm (single NP), 27.74 nm (dimers), 40.31 nm (trimers) and 45.41 nm (tetrahedra).

Further analysis was conducted by means of UV-Vis spectroscopy in order to check if plasmon coupling could be observed from gold nanoparticle assemblies (see [section 2.5](#)). The extinction spectra depicted in [Figure 5.35](#) showed only a small LPSR redshift of a few nanometres between the nanoparticle assemblies and the monoconjugates. The tetrahedral assemblies had a small broadening at around 600

nm. These findings are in accordance with previously published data from Lan *et al.* [320]. They investigated the influence of particle size and distance on the LSPR of gold nanoparticle dimers. The particles had diameters up to 40 nm and gaps down to 5 nm were realised. The experimental results were compared with theoretical simulations. They found that the experimental results deviate significantly from simulated spectra [251, 320]. While the theoretical models suggest a significant redshift of the LSPR at gaps of only 5 nm, only a small shift was measured experimentally. However, a broadening of the LSPR was detected instead, which the authors attributed to enhanced scattering of nanoparticle dimers at a higher resonance wavelength compared to single AuNPs. A similar broadening was found for the tetrahedral structures. The theoretical gap of the nanoparticles in the tetrahedron was 11 nm (32 bases with a distance of 3.4 Å). The small broadening is only present in the tetrahedral structures, which might be due to the collaborative plasmon coupling of all the nanoparticles in the structure.

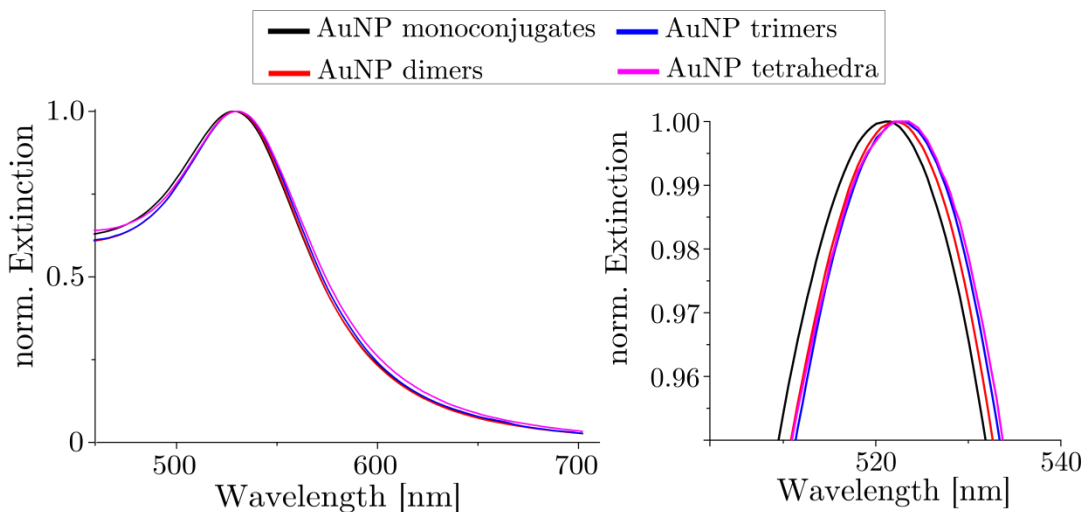


Figure 5.35: UV-Visible spectrum of gold nanoparticle mono-conjugates, dimers, trimers and tetrahedral structures.

In conclusion, it was shown that 3-cyanovinyl carbazole can be employed as an effective crosslinker molecule for *in situ* crosslinking of gold nanoparticle assemblies. Even complex assemblies using oligonucleotides with multiple crosslinking sites react in high yields and are stable under denaturing conditions. The reversibility of the reaction was demonstrated. In the last part of this chapter, larger gold nanoparticle dimers were used in surface enhanced Raman (resonance) spectroscopy (SER(R)S) experiments.

### 5.3 Nanoparticle assemblies for SER(R)S

Raman scattering was first discovered in 1928 after the effect had been predicted by Smekal in 1923 [321-323]. Raman spectroscopy has become an important and widely used tool in which vibrational and rotational modes of molecules and crystals are detected by measuring inelastically scattered light from the sample [324]. Several properties of crystals such as crystallinity, composition or doping can be deduced using this method. Even biological systems have already been analysed using Raman spectroscopy, showing the versatility of this method [325].

The principle of Raman spectroscopy is depicted in **Figure 5.36**. Monochromatic light (typically a laser source) is irradiated on a sample. The incident photons have a small probability to interact with molecules exciting them into a virtual state (VS). If there is no coupling with a vibrational or rotational mode of the molecule, the photon is re-emitted with the same energy, which is known as Rayleigh scattering [326]. However, if there is coupling the re-emitted photon can be lower in energy (Stokes scattering) or higher in energy (anti-Stokes scattering). Typically, Stokes scattering is used for analysis in Raman spectroscopy. Because only a small fraction of photons is scattered with an energy transfer ( $\sim 10^{-5}$  of the incident intensity), high concentrations of molecules and high laser powers are needed to obtain a measurable Raman signal [327].

One way to increase the sensitivity of Raman measurements is to rely on molecules with an electronic transition close to the excitation wavelength. This type of set-up is termed resonance Raman (RR) spectroscopy. When molecules are excited at an electronic transition, certain modes, which are associated with the transition, will show greatly increased Raman scattering [328]. However, if chromophores or other fluorescent molecules are involved in the measurements, the fluorescence needs to be excluded from the signal as its intensity is  $10^3$ - $10^{11}$  times larger than the Raman signal [329]. In order to avoid fluorescence, the sample can be irradiated at the absorption tail of the fluorophore while still maintaining resonant Raman enhancement. This is referred to as pre-resonance condition [330, 331].

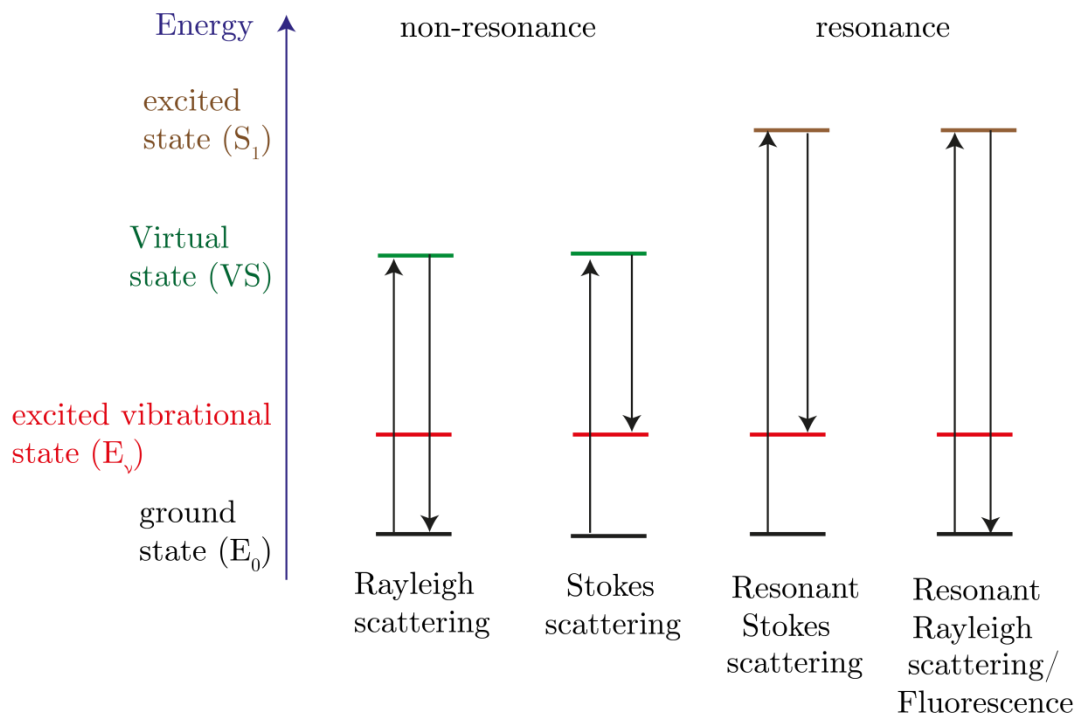


**Figure 5.36: Principle of (non-)resonant Raman scattering.** An incident photon has a small probability of interacting with molecules so that they are excited to a virtual excited state (VS). The molecule then either re-emits a photon of the same energy (Rayleigh scattering), of lower energy (Stokes scattering) or of higher energy (anti-Stokes scattering, not shown). If the molecule has an electronic transition at the wavelength of the incident light ( $E_0 \rightarrow S_1$ ), the excitation is in resonance leading to larger scattering probabilities.

A new type of Raman scattering enhancement was discovered by Fleischmann *et al.* in 1973 [332]. This effect is termed surface enhanced Raman scattering (SERS) and is associated with electromagnetic enhancements from the LSPR of nano-sized gold and silver [333-335]. A major milestone was the detection of single molecules based on large enhancement factors of up to  $\sim 10^{15}$  compared to conventional Raman spectroscopy [336, 337]. Such high enhancement factors are possible when the principle of resonance Raman scattering is combined with the plasmonic enhancement in SERS. This combination is therefore termed surface enhanced resonance Raman spectroscopy (SERRS). The technique has become a very active field of research as plasmonic nanoparticles with different shapes and tuneable LSPR became available [338, 339].

To date most of SER(R)S studies have been conducted on substrates prepared with lithographic and wet chemistry methods [340-342]. A major challenge is the reproducibility of such substrates with consistently high enhancement factors [343, 344]. Typically, there is a spot to spot variation of the SER(R)S signal on a single

prepared surface. The reason is that this spectroscopy technique is very sensitive to the distance of the nanoparticles either from each other or from an active Au/Ag surface ( $I_{SERS} \sim R^{-12}$ ) [345].

An alternative to substrate-based SER(R)S detection is a solution-based experimental setup [346]. As a proof of concept experiment acridine orange (AO) was used in conjunction with  $30 \pm 3$  nm gold nanoparticle dimers (**SC1+SC4**). The idea was to investigate if the hot-spot in between these gold nanoparticles can be utilised for SER(R)S experiments (see **section 2.5**). Acridine derivatives are known Raman reporter molecule for excitations in the visible [347]. Furthermore, it is used as a DNA/RNA marker with the ability of intercalating oligonucleotides [348]. The DNA-AO complex has an absorption maximum at 502 nm and an emission maximum at 526 nm [349]. The gold nanoparticle dimers had a LSPR at 528 nm (**Figure 5.37**). It should be noted that the broadening of the LSPR was much more pronounced than in the case of the assemblies with the smaller nanoparticles (see **section 5.2.3**). As excitation source a 532 nm laser was used because it is both, pre-resonant with absorption of AO as well as resonant with the LSPR of the gold nanoparticles. Therefore, the conditions for SER(R)S were met. The set-up is described in **section 3.4.3**. Such a solution-based Raman system might be of interest for analytical purposes because it is rather cost-efficient using only wet-chemistry methods.

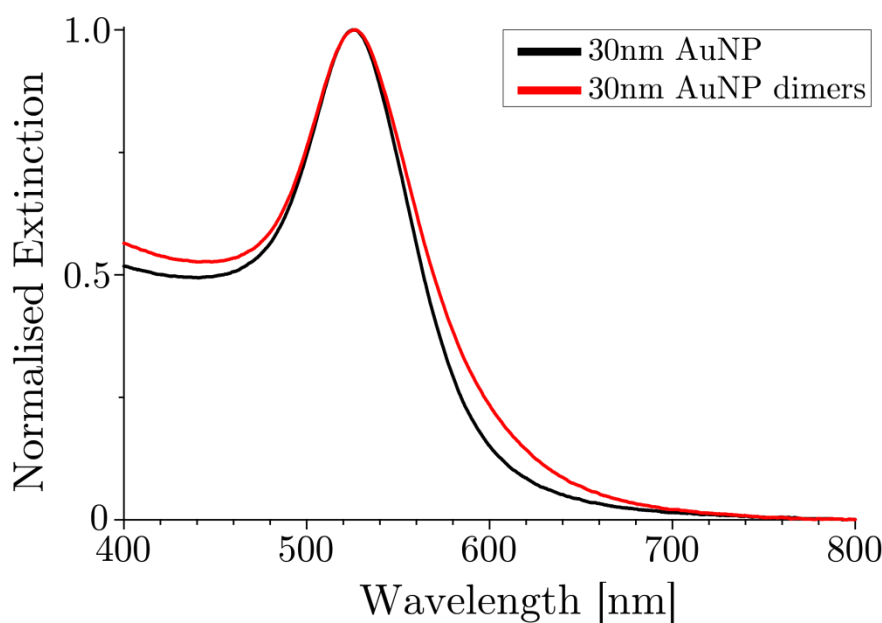
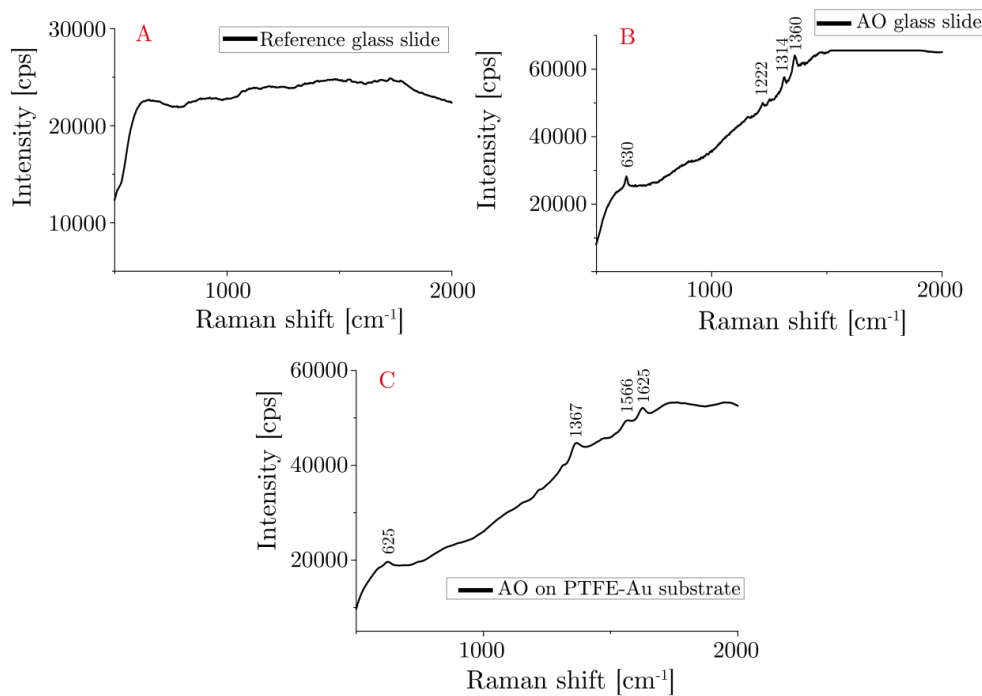


Figure 5.37: Extinction spectra of  $30 \pm 3$  nm AuNPs and dimers purified after gel electrophoresis. The broadening of the plasmon bands indicates a plasmonic interaction between the two nanoparticles in the dimer.

Reference experiments were conducted with concentrated AO solution (5 mg/mL) on both, a microscope glass slide and Sterlitech silver filters with a 300 nm gold film (provided by the group of Prof. Muskens). A drop 200  $\mu$ L was placed on the glass slide and left to dry. The filter was immersed in the concentrated solution and subsequently blow dried with nitrogen. The results are shown in **Figure 5.38**. While on the reference glass slide without any AO solution there are no Raman peaks visible (**Figure 5.38(A)**), Raman peaks are obtained from both the glass slide with AO (**Figure 5.38(B)**) as well as from the substrate (**Figure 5.38(C)**). These Raman peaks corresponded to certain stretches and deformations of parts of the AO molecule. Zimmermann *et al.* conducted a very thorough investigation of SERRS on AO and assigned the Raman peaks to the different vibrations [204]. For example, the peaks at 630  $\text{cm}^{-1}$ , 1360  $\text{cm}^{-1}$  and 1625  $\text{cm}^{-1}$  were assigned to ring+ $\text{CH}_3$  deformations,  $\text{CH}+\text{CH}_3$  deformations and ring stretches, respectively. Both samples had several peaks in common but there were also different peaks as well as varying intensities. It is common that the different peaks are shifted slightly depending on the substrate because of changing vibrations for different molecule orientations [350]. These control experiments verified that Raman scattering could be detected on a substrate at high concentrations.



**Figure 5.38:** Raman spectra of an empty reference glass slide (A) and an acridine orange solution (5mg/mL) deposited on a glass slide (B) and on a PTFE-Au substrate (C). Raman peaks appear in the acridine orange sample at 630, 1222, 1314 and 1360  $\text{cm}^{-1}$ .

As described earlier, it was expected that gold nanoparticle dimers enhance the Raman signal significantly due to plasmonic enhancement. **Figure 5.39** depicts Raman spectra of unhybridised  $30 \pm 3$  nm gold nanoparticles as well as hybridised  $30$  nm gold nanoparticle dimers with AO. The final concentration of AO was  $1 \cdot 10^{-8}$  M and the samples were incubated for 30 minutes. The ratio between AO molecules to the number of dimers was 50:1. The unhybridised gold nanoparticles showed no detectable Raman peaks (**Figure 5.39(A)**), which was in accordance with recent findings that spherical gold nanoparticles on their own do not provide sufficient field enhancement for SERS [351]. On the other hand, AO with gold nanoparticle dimers exhibited clear Raman peaks, which were at similar positions as in the substrate-based samples. It should be noted that an increase of the analyte did not significantly change the spectra. This could be explained by saturation of the dsDNA intercalation. Recently, a study with gold nanoparticle dimers concluded that only molecules in between the nanoparticle gap contribute significantly to SER(R)S [352]. The contribution of molecules close to the nanoparticle surface should therefore be negligible. The experiments showed that detection of a Raman reporter employing nanoparticle dimers with DNA interaction is possible at low concentrations. Unfortunately, it was not possible to directly compare this system to other systems because the enhancement factor could not be determined. In addition, it is difficult to compare the Raman performance of different molecules. Considering the dimensions of the laser spot and the concentration of the Raman reporter, acridine orange was detected in the fmol range, which is comparable to many reports. While there have been reports of detection down to zmol, the measurements are usually performed on a substrate with a nanoparticle ensemble [103, 353, 354]. An interesting approach is the formation of gold nanoparticle clusters, which leads to large enhancement factors allowing Raman spectroscopy on a single cluster level [355, 356]. There is still a lot of research conducted on the geometries and composition of SERS materials [357]. The initial results suggest that further analysis of this system might be of interest for the development of a solution-based SER(R)S device [358, 359].

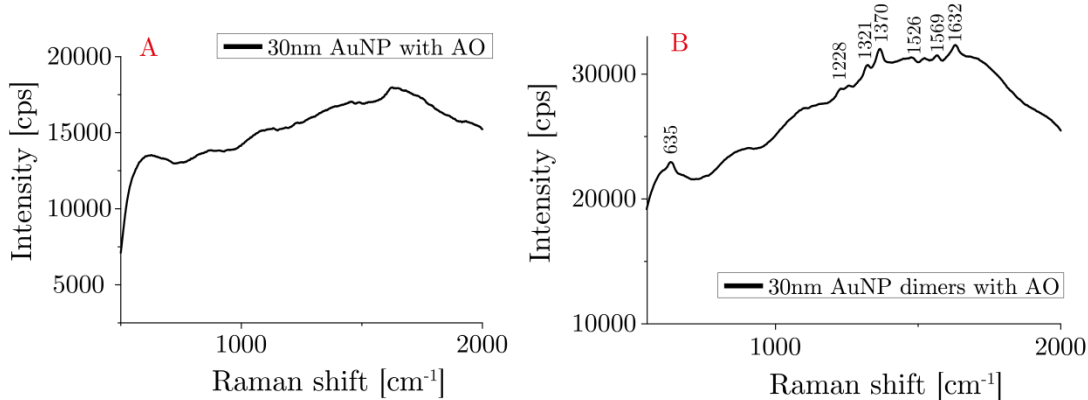


Figure 5.39: Raman spectra of 30nm gold nanoparticles (A) and 30nm gold nanoparticle dimers (B) with acridine orange at a concentration of  $10^{-8}$  M. While the single nanoparticles show no Raman peaks, several peaks at 635, 1228, 1321, 1370, 1526, 1569 and 1632  $\text{cm}^{-1}$  are present in the dimer sample.

## 5.4 Summary

Four different oligonucleotides were designed in such a way that a symmetric tetrahedron is formed when all strands are hybridised [249]. The oligonucleotides were analysed with polyacrylamide gel electrophoresis. One set of oligonucleotides was modified with azide and BCN groups in order to covalently crosslink the dsDNA via SPAAC. PAGE analysis revealed that unexpected bands appeared when oligonucleotides with the two different modifications were hybridised. This observation was contrary to earlier reports where DIBO was successfully applied for nanoparticle ligation [22]. Several different conditions such as different ionic strength or hybridisation temperature had no effect on the appearance of the extra bands. 15 nm gold nanoparticles were functionalised with these modified oligonucleotides and hybridised to form DNA-directed assemblies. Likewise, gel electrophoresis as well as TEM showed large clusters of gold nanoparticles. Since larger clusters were obtained in both PAGE and with AuNPs, it was concluded that the SPAAC reaction caused uncontrolled crosslinking between the DNA strands. Such a result has not been reported before. An explanation could be the high reactivity of the BCN molecule and that the reaction proceeded faster than the hybridisation. However, this explanation could not be verified in this work. In order to check this, other cyclooctynes with a lower reactivity like DIBO could be employed in future experiments.

As an alternative, a novel reversible and light-mediated crosslinking reaction employing the molecule 3-cyanovinyl carbazole was applied in conjunction with gold nanoparticle assemblies for the first time [24]. The four oligonucleotides were modified with this molecule and analysed by PAGE, which showed the same bands after hybridisation as the unmodified oligonucleotides. Denaturing PAGE indicated the successful crosslinking of the dsDNA with high yields. These findings are in agreement with the reports of Fujimoto *et al.* who invented this molecule [24]. Various gold nanoparticle assemblies consisting of dimers, trimers and tetramers were successfully synthesised. A full cycle of crosslinking and de-crosslinking was performed and high reactions yields were obtained. These experiments proved that 3-cyanovinyl carbazole could be employed as an alternative to the alkyne-azide click reaction. The additional reversibility is a novel feature, which is not found in other crosslinking techniques.

In the last part, gold nanoparticle dimers consisting of 30 nm AuNPs were assembled and crosslinked. A broadening in the UV-Visible spectrum indicated plasmon coupling between the larger nanoparticles due to their short distance from each other [320]. These nanoparticles were then employed in SERRS experiments utilising acridine orange as a Raman label, which intercalated dsDNA and was therefore located in the hot-spot of the gold nanoparticle dimers. Concentrations of acridine orange as low as  $10^{-8}$  M were detected in solution showing the promising capabilities of this system. The advantage of solution-based Raman spectroscopy is the reproducibility and the facile calibration [359]. Furthermore, wet-chemical methods are cost-efficient compared to top-down methods. The drawback is that the best sensitivities have been achieved with substrate-based SERS samples [360].

# Chapter 6. Upconversion nanoparticle-Quantum dot hetero-assemblies

## 6.1 Introduction

In **Chapter 5**, DNA was utilised to create self-assembled three-dimensional nanoparticle structures by design. Long oligonucleotides facilitated the purification of nanoparticles with a defined number of strands and acted as a template for organisation of nanoparticles on pre-set positions inside the assembly.

Another approach of assembling nanoparticles consists of the functionalisation with many oligonucleotides [14, 361]. These assemblies are particularly interesting as colorimetric sensors or for the creation of super-lattices [362, 363]. In this chapter, this approach will be used to investigate if a FRET system between upconversion nanoparticles (UCNPs) and semiconductor quantum dots (QDs) based on directed assembly with DNA can be realised.

Förster resonance energy transfer (FRET) is a well-known energy transfer mechanism between an excited donor molecule and an acceptor molecule [364, 365]. The energy is transferred radiationless via dipole-dipole interactions and can be described by Coulomb's law. Thus, the FRET efficiency depends on the distance between the FRET pair as  $1/r^6$ . Another factor influencing the FRET efficiency is the mutual orientation between the donor and the acceptor. Lastly, there needs to be an overlap of the donor emission and the acceptor absorption in order for FRET to occur.

Upconversion nanoparticles have attracted interest due to their capability of generating visible light upon near-infrared irradiation (see **Section 2.1.6**) [28, 366]. On the one hand, there are manifold reports on UCNPs as potential probes for biological applications including *in vivo* studies or as probes for molecule sensing [25, 367-369]. On the other hand, potential applications in solar cells as light harvesters are considered because there is not yet an efficient way of using the infrared spectrum of the sun for photovoltaics [148, 370-372].

Semiconductor quantum dots have been thoroughly studied in the last 20 years [134]. These particles are a model system for zero-dimensional materials with efficient and tuneable photoluminescence properties (see **section 2.1.4**). The

advantages of QDs compared with other dyes are high photostability and as well as a wide range of applicability through versatile surface chemistry. Quantum dots have been applied in many different fields from optoelectronics to biology.

In the recent past nanoparticle hybrid systems, which contain several types of different nanoparticles, have been actively researched on [373, 374]. The paradigm from Mirkin *et al.* demonstrates the ambition of creating versatile and multi-functional tools by employing nanoparticle assembly [239] (see **section 2.5**). However, to date there is still a comparably little number reports on such heterogeneous nanoparticle systems published.

While some reports on energy transfer between nanoparticles and organic dyes have been published [375-378], there have been only few reports utilising quantum dots and upconversion nanoparticles as a hybrid system [378, 379]. For example, Mattsson *et al.* used avidin-strepavidin recognition in order to synthesise UCNP-QD assemblies. They analysed the system with respect to FRET and developed an assay for the detection of biotin based on competitive binding between the biotin-functionalised QDs and free biotin. By time-resolved analysis of the luminescence decay, they found a FRET efficiency of 7% for nanoparticles with a distance of 6 nm. To date, there has been no report about a system where both particles are linked using oligonucleotides [380].

## 6.2 Assembly of UCNP and QDs with short DNA

The aim was to investigate hetero-assemblies between upconversion nanoparticles ( $\text{NaYF}_4:\text{Yb,Tm}$ ) and quantum dots ( $\text{CdSe/ZnS}$ ) using short oligonucleotides. **Figure 6.1** illustrates a FRET system with the two particles where they are coupled with DNA. Upconversion nanoparticles were transferred from organic solvents to water and then functionalised with oligonucleotides containing 15 bases (see **chapter 4**). Likewise, quantum dots were modified with completely complementary oligonucleotides. By mixing the two nanoparticles together, the quantum dots and the upconversion nanoparticles were forming assemblies via DNA hybridisation. The theoretical distance between the different particles was 5 nm. The system was analysed by fluorescence spectroscopy using a home-built setup (see **section 3.4.2**). Energy transfer from the upconversion nanoparticles to the quantum dots was expected after successful hybridisation (see **Appendix A.5**).

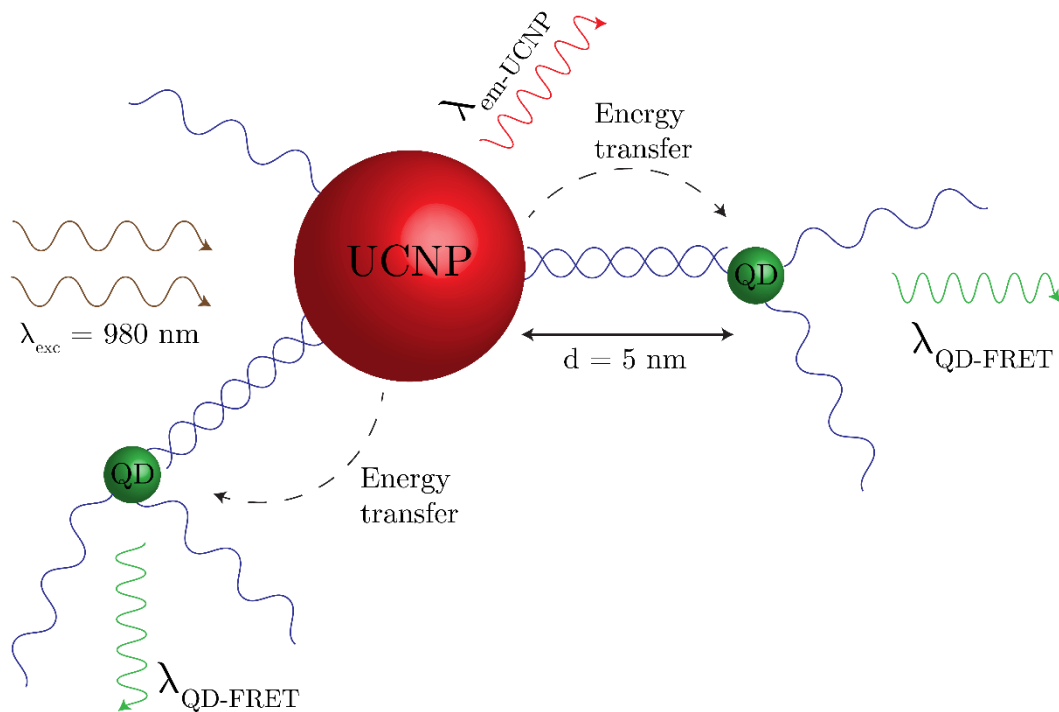


Figure 6.1: Illustration of an upconversion nanoparticle-quantum dot FRET system. The rare-earth doped upconversion nanoparticles (UCNP) absorb light in the infrared (980 nm) and emit light  $\lambda_{em-UCNP}$ . Some of the energy is transferred to quantum dots in close proximity via FRET, which leads to emission at a different wavelength  $\lambda_{QD-FRET}$ . This system utilises DNA as linker between the nanoparticles and enables control of the distance between the donor (UCNP) and the acceptor (QD).

The DNA sequences that were used in the experiments are listed in **Table 6.1**. All oligonucleotides were modified with an amine-linker at the 5'-end in order to attach them to the nanoparticles via EDC/Sulfo-NHS coupling chemistry (see **section 4.5.3**). The sequences consisted of 15 bases so that the length of the dsDNA was 5.1 nm (considering an interbase distance of 3.4 Å). The sequences **Seq1** and **Seq2** were completely complementary with a calculated melting temperature of 55°C (50 mM NaCl). A third oligonucleotide **Seq1-Cy3** with the same sequence as Seq1 but modified with the organic dye Cy3 at the 3'-end was synthesised and was used for control experiments.

<b>Seq1</b>	5'-NH <sub>2</sub> -C <sub>6</sub> H <sub>12</sub> -CGA GGA CAC GGA CCT
<b>Seq2</b>	5'-NH <sub>2</sub> -C <sub>6</sub> H <sub>12</sub> -AGG TCC GTG TCC TCG
<b>Seq1-Cy3</b>	5'-NH <sub>2</sub> -C <sub>6</sub> H <sub>12</sub> -CGA GGA CAC GGA CCT-Cy3

Table 6.1: Oligonucleotide sequences employed for the assembly of upconversion nanoparticles and quantum dots. The sequences Seq1 and Seq2 are completely complementary. The sequence Seq1-Cy3 is equal to Seq1 but contains a Cy3 label at the 3'-end.

In a first step, the nanoparticles were functionalised with L-lipoic acid (QDs) and PAA (UCNPs) in order to transfer them from organic to aqueous media and to have carboxyl groups available at the surface (see **section 3.2.2/3.2.3**). Then, the water-soluble nanoparticles were incubated with the amine-modified oligonucleotides together with the coupling agents EDC and Sulfo-NHS. Even though the EDC/Sulfo-NHS chemistry is well-established and is commonly used for coupling molecules to nanoparticles, there are a variety of protocols using different EDC/Sulfo-NHS concentrations as well as buffers [381, 382]. For each system the optimal parameters may differ because of different  $pK_a$  values for different molecules. The resulting coupling performance was unsatisfying when near-neutral phosphate buffer (0.1 M, pH = 7.4) was used. Here, the coupling yield was a lot better if the pH was reduced to slightly acidic conditions using MES buffer (pH = 6-6.5).

As control experiment for the attachment of the DNA, the oligonucleotide **Seq1-Cy3** was coupled to quantum dots with an emission wavelength of 540 nm (QD540). There were three measures for the successful attachment of oligonucleotides on the nanoparticle surface. Firstly, since the oligonucleotide has a Cy3 label, it has a bright pink colour. After the coupling reaction, the colour of the precipitate indicated the presence of **Seq1-Cy3** on the nanoparticles (**Figure 6.2**). The colour change is more intense after coupling with MES buffer indicating a higher DNA loading. In addition, the fluorescence emission of the DNA-functionalised nanoparticles under UV illumination was red-shifted with respect to the unmodified nanoparticles (**Figure 6.3**). This could be explained by FRET from the QDs to the Cy3 dye, which was located in close vicinity to the nanoparticles. The absorption and emission spectra of the donor and the acceptor matched so that FRET should be observed (see **Appendix A.5**). FRET systems between organic dyes and quantum dots have already been used for sensing in the past [383, 384].

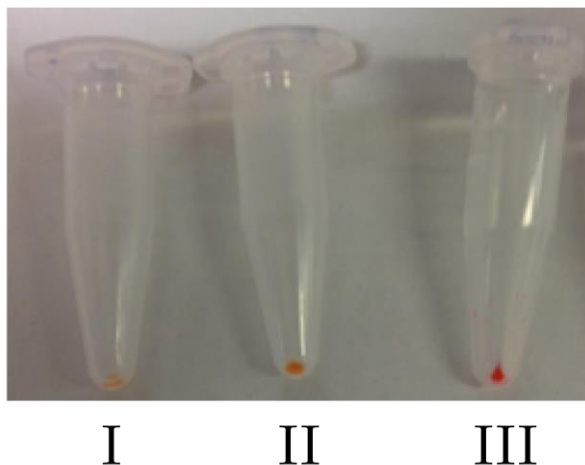


Figure 6.2: Quantum dots (QD540) before and after attachment of DNA (Seq1-Cy3) with EDC/Sulfo-NHS coupling. I: QD540 without DNA, II: QD540 coupled with phosphate buffer, III: QD540 coupled with MES buffer. The pink colour indicates the presence of Seq1-Cy3 on the nanoparticle surface.



Figure 6.3: Quantum dots (QD540) illuminated with UV-A light after EDC/Sulfo-NHS coupling. Left: QD540 without DNA; Middle: QD540 coupled with phosphate buffer; Right: QD540 coupled with MES buffer.

Secondly, UV-Visible spectroscopy was employed. Cy3 as an organic dye has a specific absorption spectrum with a peak extinction at  $\lambda_{ext}^{max} = 550$  nm and a shoulder at higher energies (see **Appendix A.5**) [385]. This allows for checking the functionalisation of the nanoparticles by UV-Vis spectroscopy. **Figure 6.4** shows UV-Vis spectra of quantum dots (QD540) after DNA coupling with phosphate and MES buffer. Unmodified QDs in water were used as a reference. The extinction spectrum of QDs incubated in MES buffer showed the signature of the Cy3 dye, which indicated the attachment of the DNA. On the other hand, there was only a small increase in the extinction after EDC/Sulfo-NHS coupling in phosphate buffer.

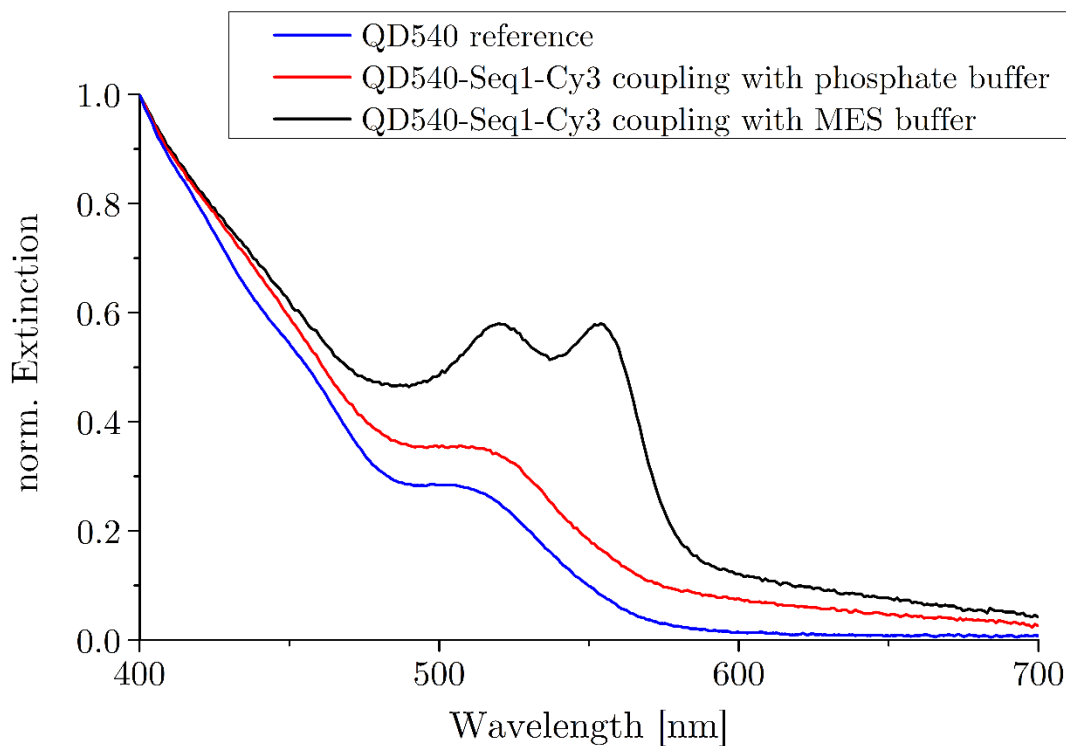


Figure 6.4: Extinction spectra of QD540 before and after coupling with Seq1-Cy3 using phosphate buffer or MES buffer.

Thirdly, the nanoparticles were analysed by fluorescence spectroscopy. The samples were excited at 400 nm where Cy3 has a very low extinction coefficient and almost no fluorescence from direct excitation of the dye was obtained. Figure 6.5 shows the fluorescence spectra of quantum dots (QD540) functionalised with Seq1-Cy3 using PBS or MES buffer. The spectra show that quantum dots coupled with Seq1-Cy3 using MES buffer were almost completely quenched and that the spectrum follows the Cy3 emission instead. On the other hand, there was only a small shoulder present when phosphate buffer was used. As a reference, the spectrum of quantum dots in water is displayed as well.

From these coupling experiments it can be concluded that the EDC/Sulfo-NHS coupling works a lot better at slightly acidic conditions for this system. Similar results regarding the coupling performance were found with the upconversion nanoparticles. When MES buffer was used the nanoparticle pellet was pink in colour after centrifugation, which indicated the successful coupling of Seq1-Cy3 to the UCNPs. In the following, the quantum dots with an emission at 580 nm (QD580) were used because of their larger extinction coefficients in the near-UV.

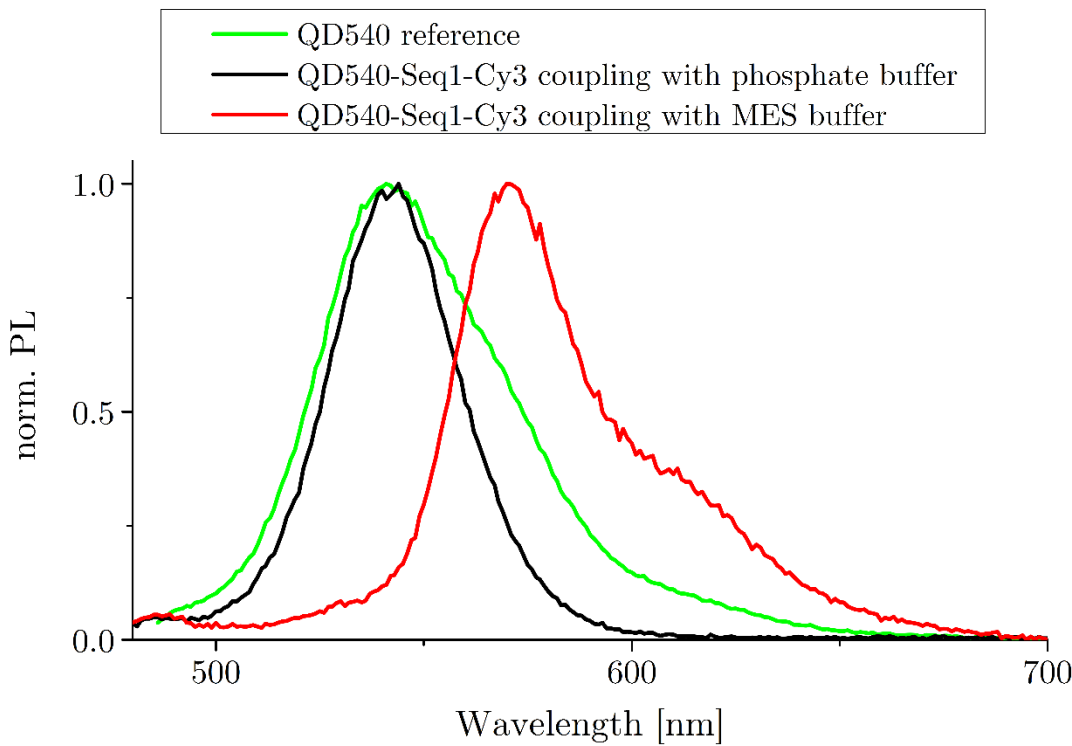


Figure 6.5: Fluorescence spectra of QD540 with Cy3-DNA coupling by two different methods via EDC/NHS chemistry.

Before the hybridisation experiments, potential reabsorption by the quantum dots (QD580), i.e. photons emitted by the UCNPs are absorbed by the QDs, was checked. This was done by mixing both types of nanoparticles without DNA functionalisation in the upconversion set-up (see [section 3.4.2](#)). Two different ratios with UCNP:QDs of 1:100 and 1:10<sup>5</sup> and with a concentration of 1 nM UCNP were tested. The results are displayed in [Figure 6.6](#). While reabsorption was detected at high concentrations of QDs, there was no such measurable interaction for a 100x excess of QDs. This was expected because of the low emission efficiency of the UCNPs and the short path length in the cuvette. The lower ratio corresponds to the highest ratio used in the hybridisation experiments. From the emission spectra it is clear that the blue emission is largely quenched at high quantum dot concentrations because of the absorption of blue light. On the other hand, the emission spectrum of the quantum dots (QD580) with a peak wavelength at 580 nm appeared and showed that the photons are absorbed by the quantum dots. Therefore, a high concentration of quantum dots was needed for a significant reabsorption effect.

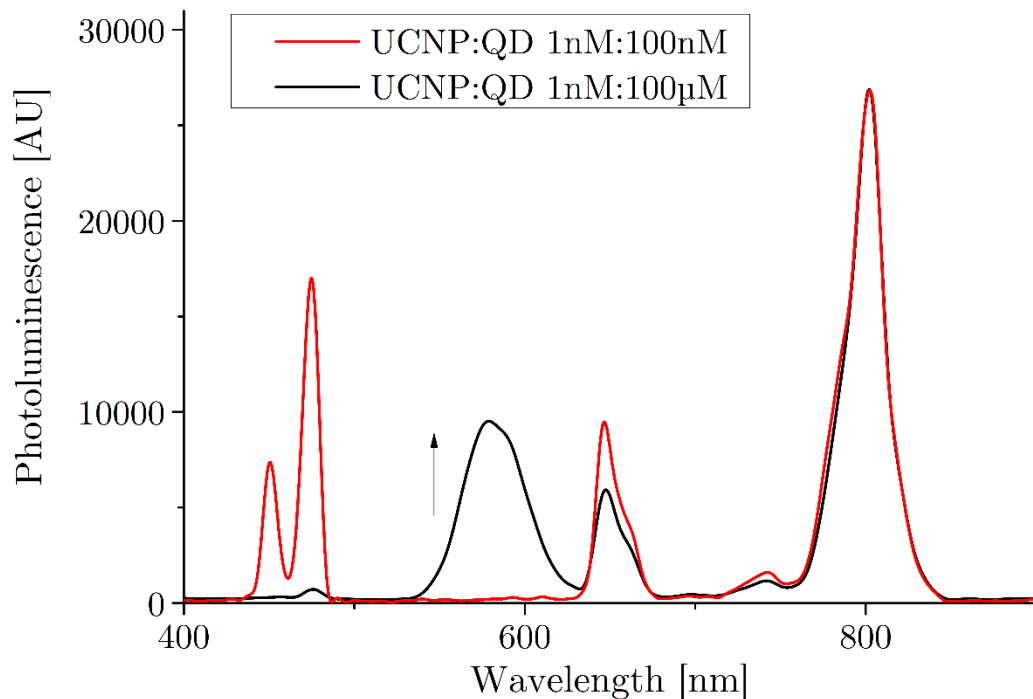


Figure 6.6: Photoluminescence spectra of UCNPs ( $\text{NaYF}_4$ :Yb,Tm) mixed with QDs (QD580) and without DNA functionalisation to determine potential reabsorption from the QDs. The UCNPs concentration was 1 nM. At a ratio of UCNP:QD of 1:100, there is no emission from the QDs (red curve). At a ratio of UCNP:QD of 1:10<sup>5</sup>, the QD spectrum is clearly obtained and the blue emission of the UCNPs is quenched (red curve).

In the next step, the quantum dots (QD580) and upconversion nanoparticles were functionalised with oligonucleotides **Seq1** and **Seq2**, respectively. The quantum dots were placed in the upconversion set-up to verify that there is no detectable luminescence due to two-photon absorption. As expected, there was no signal obtained due to two-photon absorption because the power density of the laser diode was too low (Figure 6.7, black curve). Then, the two different nanoparticles were hybridised using different ratios of UCNPs:QDs and luminescence spectra were acquired under illumination with light of 980 nm. The results are presented in Figure 6.7. The hybridised samples all show different photoluminescence intensities from the quantum dots. This indicates that the nanoparticles successfully hybridised and that there was FRET between the nanoparticles. With increasing quantum dot concentrations, the peak intensity increased from 4000 (1:10) to 7000 (1:25) and 11000 (1:100). This behaviour indicated that not all hybridisation sites on the upconversion nanoparticles were occupied by the quantum dots at lower concentrations. Nevertheless, there seems to be a saturation at the highest ratio because the intensity was significantly smaller than a linear extrapolation would

suggest. Even though quantification was not possible in this set of experiments, the saturation seemed reasonable. The UCNP were functionalised using 50 DNA strands per particle. Assuming that in the case of the 1:10 ratio all QDs are bound, an estimated number of roughly 30 DNA strands would be present on the UCNP. However, further experiments are needed to quantify the number of DNA strands and the resulting luminescence created by energy transfer to the quantum dots. It should be noted that the PL signals from the QDs were rather low and the integration time needed to be increased (5-fold). The main reason is that due to the large size of the UCNP, the PL from the inner core was not affected by energy transfer due to the inverse 6<sup>th</sup> power law. Therefore, a much larger portion of the incident light was still emitted instead of transferred.

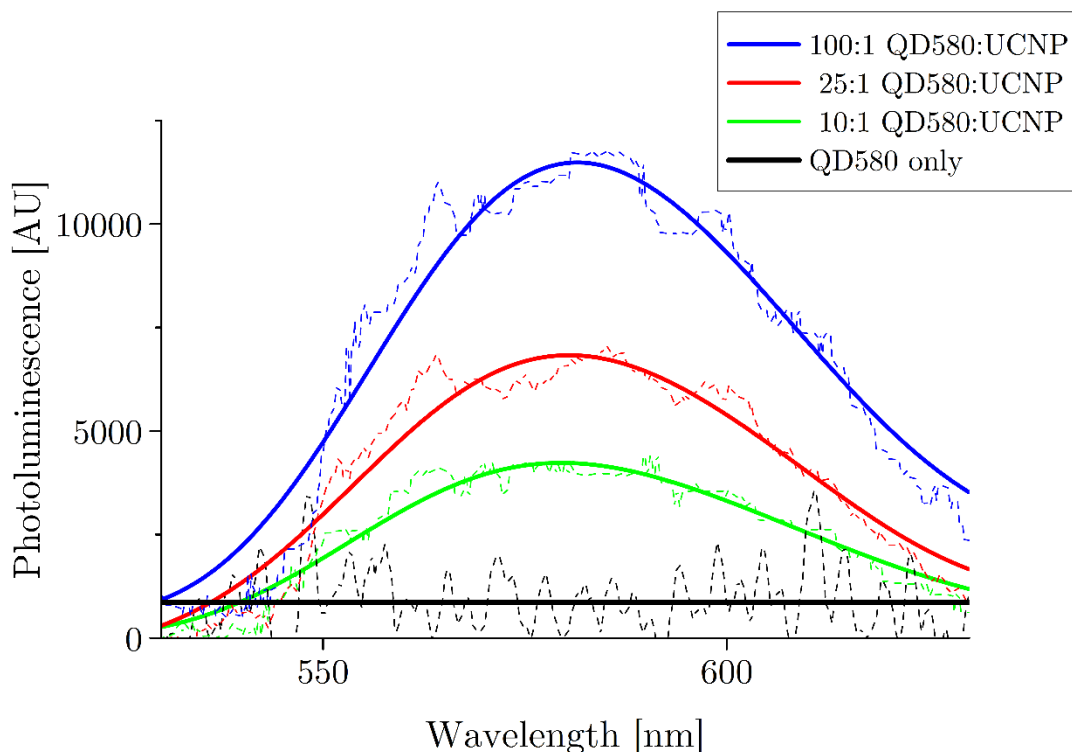


Figure 6.7: Photoluminescence spectra obtained from UCNP-QD580 assemblies. No PL was obtained from QDs under irradiation with 980 nm light (black curve). Hybridised assemblies showed quantum dot PL depending on the ratio UCNP:QD due to energy transfer from the UCNPs (1:10 green, 1:25 red, 1:100 blue).

In conclusion, the successful self-assembly of upconversion nanoparticles and quantum dots using DNA was demonstrated. The system was analysed in terms of FRET between the two nanoparticles. While there was no emission from the QDs themselves or mixtures of both nanoparticles without DNA functionalisation, photoluminescence from the QDs was obtained after hybridisation. With increasing

quantum dot concentrations, the PL intensity increased non-linearly indicating a saturation of the UCNP binding sites. This proof of concept study shows the feasibility of creating hetero-assemblies with short oligonucleotides and combined properties from both nanoparticle types. Therefore, it would be of interest to carry out further research in order to quantify the FRET efficiency and to gain a general understanding of the properties of larger hetero-assemblies. The formation of different other hetero-assemblies would also be interesting. Especially, a combination of plasmonic nanoparticles (e.g. gold nanorods or copper chalcogenide nanoparticles ( $\text{Cu}_2\text{S}$ )) and upconversion nanoparticles could be investigated focussed on plasmonic enhancement of photoluminescence.

## Chapter 7. Summary and Outlook

The field of nanotechnology has rapidly evolved in the last two decades and will certainly become part of everyday life in the near future. The rich library of nanoparticles with different sizes, shapes and compositions is the foundation for the creation of novel materials and devices [262]. The seminal work from Alivisatos and Mirkin on DNA-nanoparticle hybrids created a large stimulus in the field of self-assembling nanoparticles [13, 14]. While a lot of progress has been made in this area and many interesting results were obtained, there are still many challenges to be overcome [17]. In this work, the method of nanoparticle self-assembly with DNA was further developed. A summary of the results will be given in **section 7.1**. Following the summary, suggestions and ideas for future work will be presented in **section 7.2**.

### 7.1 Summary of results

Several different types of nanoparticles were synthesised and characterised in order to use them as building blocks for self-assembly (**Chapter 4**). Plasmonic gold and silver nanoparticles were synthesised with the standard Turkevich method [58]. Fluorescent CdSe/ZnS semiconductor quantum dots and NaYF<sub>4</sub>:Yb,Tm upconversion nanoparticles were synthesised by solvothermal methods in high boiling point organic solvents [106]. The nanoparticles were rendered water-soluble by ligand exchange with molecules containing terminal carboxyl groups allowing the attachment of oligonucleotides [266]. A novel protocol for the synthesis of lead halide nanoparticles was established by replacing octylamine with CTAB. These particles exhibit a higher stability and allow for complete removal of DMF improving spin-coating results significantly. Different techniques were employed for the characterisation of the nanoparticles. UV-Visible spectroscopy, fluorescence spectroscopy, TEM as well as zeta-potential measurements validated the stability of the nanoparticle dispersions.

In **Chapter 5**, oligonucleotides with different modifications were analysed and employed for the self-assembly gold nanoparticle structures. The DNA approach towards nanoparticle assembly is still the most promising for the creation of well-defined structures. Different from other self-assembly techniques, the recognition of the building blocks via Watson-Crick base pairing allows for the design of complex structures. The oligonucleotides were designed in such a way that they fold into a tetrahedral structure [249]. In order to stabilise the assemblies, the oligonucleotides

were functionalised with either azide and bicyclononyne (BCN) groups or 3-cyanovinyl carbazole [213]. This was done in order to tackle the inherent disadvantage of DNA-based assembly, which is the reversible nature of the DNA hybridisation. Stable DNA nano-constructs that maintain their structure in low ionic strength media are important for the application with nanoparticles [386]. The first combination forms a covalent bond between two DNA strands by spontaneously reacting in a strain-promoted azide-alkyne click reaction (SPAAC). The latter molecule reacts with an opposite thymine base in dsDNA when illuminated with UV-A light and can be reversed using UV-B light. While the unmodified and carbazole-modified oligonucleotides showed the expected hybridisation behaviour and formed different assemblies depending on the DNA mixture, PAGE analysis of the hybridisation behaviour of the differently modified oligonucleotides revealed that azide/BCN-modified oligonucleotides form large assemblies, which do not pass through the gel. Similarly, gold nanoparticle assemblies contained large clusters when azide/BCN-modified DNA was used. These results were unexpected because the SPAAC reaction has been applied successfully before [22, 213]. However, in these examples there has only been one clicking moiety per oligonucleotide. Therefore, these findings suggest that either BCN is too reactive in order to be used as multiple modification in oligonucleotides or that the use of several clicking groups per DNA strand is not possible generally.

On the other hand, 3-cyanovinyl carbazole was shown to overcome these problems and to provide an effective way of ligating complex structures such as tetrahedral assemblies of gold nanoparticles [24, 315]. The advantage of this molecule is that there is only a crosslinking reaction upon UV irradiation. Besides the effective crosslinking, the reversibility of the interstrand bonds provides a new functionality, which is not present in other crosslinking techniques. While the crosslinked gold nanoparticle assemblies were stable under denaturing conditions, the de-crosslinked assemblies broke apart into their individual building blocks. Furthermore, it was found that the crosslinked nanoparticle assemblies could be efficiently purified to a high purity of up to 90% with gel electrophoresis. In comparison, the non-crosslinked assemblies were partially dissociating after centrifugation. This technique can be applied to trigger the reactions time- and spatially controlled, which might be of interest in superlattices and for the design of switchable nanostructures [387].

One of the major problems of nanoparticle self-assembly is the yield of the final product [303]. A range of different hybridisation conditions were employed in order to improve the yield. Nevertheless, no conclusive answer can be given on the best reaction conditions and why the product yield seems to be limited. Therefore, further research should be conducted in this direction in the future.

In **Chapter 6**, the assembly of hetero-structures is presented.  $\text{NaYF}_4:\text{Yb,Tm}$  upconversion nanoparticles and  $\text{CdSe/ZnS}$  quantum dots functionalised with two completely complementary 15 mer oligonucleotides were employed as building blocks. EDC/Sulfo-NHS coupling was used for the attachment of amine-modified DNA to the nanoparticles bearing carboxyl group on their surfaces [300]. Since there are many different coupling conditions for different applications, the best choice of buffer was determined first. It was found that MES buffer with slightly acidic pH (6-6.5) provided much more efficient coupling than phosphate buffer. Due to the short length of the DNA, the hybridisation of the two different nanoparticles led to a detectable energy transfer from the upconversion nanoparticles to the quantum dots. A similar system has been investigated where instead of DNA, avidin and streptavidin were employed to assemble the nanoparticles [379]. While a direct comparison between the two systems was not possible due to a lack of analysis equipment, it is clear that there has been a significant energy transfer from the upconversion nanoparticles to the quantum dots in the DNA-based system. The advantage of using DNA is that it is a more versatile material as it can be modified in manifold ways. Especially in the context of superlattices, these first results show the feasibility of combining differently composed nanoparticles using short oligonucleotides in order to create new interactions [31].

## 7.2 Outlook to future work

In the last years, the complexity of self-assembled nanoparticle structures increased tremendously [9, 17]. Nevertheless, there are still several challenges, which prevent a wide use of this technology in applications [17]. While DNA nanotechnology is already capable of creating very advanced structures (e.g. DNA origami), the implementation of design rules for DNA in nanoparticle assembly has just begun [17, 263]. Hybridisation simulations are focussed on nanoparticles with a dense layer of oligonucleotides [388]. However, it would be of interest to analyse the hybridisation of NP-monoconjugates in order to improve the reaction yields. Potential experiments

could include the hybridisation of nanoparticle dimers with oligonucleotides containing only one BCN or highly reactive cyclooctyne [227]. This system would allow to gather information about the hybridisation process of nanoparticles because once clicked, the dimers will not be available for further hybridisation and could be analysed subsequently without breaking. It would also be interesting to compare pre-formed DNA structure templates onto with nanoparticles are bound in order to understand if this process is giving higher product yields than the direct hybridisation of nanoparticles. Such a comparative study would be interesting to determine the limitations of the different approaches.

The results obtained in this work could be a starting point for further research. The oligonucleotides modified with two BCN groups proved to be unsuitable for the system explored in this work. However, it was not possible to determine the exact cause. The hybridisation of oligonucleotides additionally modified with well-established FRET pairs like Cy3 and Cy5 could be used to determine if the wrong groups reacted [389]. Furthermore, the BCN group could be replaced with less reactive cyclooctynes like DIBO in order to find out if the problem of clustering still occurs [227].

The presented crosslinking technique using 3-cyanovinyl carbazole could be a way to improve DNA templates for the assembly of nanoparticles. DNA scaffolds, which are already used in DNA origamis could be permanently linked and would therefore readily be available for the use with nanoparticles. Typically, these origamis need high ionic strength media, which is unsuitable for nanoparticles because of aggregation problems [386]. It would be interesting to conduct nanoparticle assembly experiments exploiting the orthogonality of the carbazole chemistry with click chemistry [213]. The smart design and modification with reversible and irreversible crosslinkers could allow to create switchable systems, which change their states triggered by an external stimulus [390]. Recently, gold nanoparticle superlattices with DNA and RNA bonds were formed making them responsive to enzymatic digestion by ribonuclease [387]. The reversibility of 3-cyanovinyl carbazole could introduce a UV-responsiveness, which further increases the design possibilities in terms of dynamic structures.

Besides the improvement of the assembly process, lots of research is needed on the development and characterisation of hetero- and homo-assemblies [31]. The UCNP-

QD system presented in this work could be further developed and analysed by using smaller upconversion nanoparticles or plasmonic nanoparticles [30]. It is known that photoluminescence properties can be improved by plasmonic enhancement [391, 392]. The DNA-mediated assembly allows to control the spacing between the nanoparticles in a defined way and could therefore be a reasonable approach to investigate such systems in solution. The determination of the FRET intensity and the potential of plasmonic light harvesting could be interesting factors for the application in photovoltaics.



## A. Appendix

### A.1 List of reagents and suppliers

All chemicals were used without further purification.

**Sigma-Aldrich:** Acridine orange, Ammonium persulfate, Boric acid, Bis(p-sulfonatophenyl)phenylphosphine dihydrate dipotassium salt (BSPP), Cadmium oxide, *N*-(3-Dimethylaminopropyl)-*N'*-ethylcarbodiimide hydrochloride (EDC), Ethylenediaminetetraacetic acid (EDTA), Ficoll-400, Formamide, *N*-hydroxysulfosuccinimide (sulfo-NHS), Lipoic acid, Lead bromide, Lead chloride, Lead iodide, Methylamine, MES sodium salt, 1-Octadecene, Octylamine, Oleic acid, Rhodamine 6G, Sodium borohydride, Sodium chloride, Sodium tetrachloroaurate(III) dehydrate, Selenium, Silver nitrate, Sodium hydroxide, Sulfur, Tannic acid, *N,N,N',N'*-tetramethylethylenediamine, Trisodium citrate, Tris base, Zinc acetate.

**Fisher Scientific:** Acrylamide:bis-acrylamide 1:29 solution (40%), Ammonia solution (35%), *N,N*-Dimethylformamide (DMF), Ethanol, Hydrochloric acid (conc.), Methanol, Nitric acid (conc.), Potassium carbonate, Toluene.

**ATDBio:** All oligonucleotides were obtained from ATDBio with HPLC grade purity.

### A.2 Calculation of nanoparticle concentration

In this section the estimation of nanoparticle concentrations will be explained.

*Gold and silver nanoparticles:*

The concentration of gold nanoparticles was calculated according to the following method based on UV-Vis spectroscopy. For the determination of nanoparticle concentrations, three UV-Vis spectra were measured with different dilutions in order to obtain a reliable mean value. The extinction coefficients for the gold nanoparticles were taken from a table, which was published by Haiss *et al.* containing nanoparticle sizes from 5 nm to 100 nm [60]. The concentration was then calculated using Beer-Lambert's law as follows (section 3.4.1):

$$c = \frac{A \cdot D}{\varepsilon \cdot l}$$

where  $\varepsilon$  is the molar extinction coefficient, D the dilution factor, A the absorbance and l the path length. The extinction coefficients are:  $\varepsilon(5 \text{ nm AuNP}) = 9.14 \cdot 10^6 \text{ L mol}^{-1} \text{ cm}^{-1}$ ,  $\varepsilon(15 \text{ nm AuNP}) = 3.55 \cdot 10^8 \text{ L mol}^{-1} \text{ cm}^{-1}$  and  $\varepsilon(30 \text{ nm AuNP}) = 3.64 \cdot 10^9 \text{ L mol}^{-1} \text{ cm}^{-1}$ . For example, if a 15 nm gold nanoparticle solution has an absorbance of 0.5 with a dilution factor of 1000 and has been measured using a 1 cm cuvette, the concentration would be:

$$c = \frac{0.5 \cdot 1000}{3.55 \cdot 10^8 \text{ L mol}^{-1} \text{ cm}^{-1} \cdot 1 \text{ cm}} = 141 \cdot 10^{-7} \frac{\text{mol}}{\text{L}} = 140 \text{ nM}$$

In the same way, the concentration of silver nanoparticles can be estimated as Paramelle *et al.* have published a table of extinction coefficients for these nanoparticles [393].

*Quantum dots:*

The concentration of semiconductor quantum dots can be determined in a similar way with a few more calculations following the method of Yu *et al.* [268]. First, the wavelength of the first exciton peak and the absorbance at that point are determined by UV-Visible spectroscopy. Then, the diameter of the CdSe core can be calculated using the empirically fitting function

$$D[\text{nm}] = (1.6122 \cdot 10^{-9}) \cdot \lambda^4 - (2.6575 \cdot 10^{-6}) \cdot \lambda^3 + (1.6242 \cdot 10^{-3}) \cdot \lambda^2 - 0.4277 \cdot \lambda + 41.57,$$

where  $\lambda$  is the wavelength of the first exciton peak. From the size of the CdSe core the molar extinction coefficient can be calculated with the fitting function

$$\varepsilon = 5857 \cdot D^{2.65},$$

where  $\varepsilon$  is the molar extinction coefficient and D is the diameter in nanometres. Finally, by employing the calculated  $\varepsilon$  the concentration can be determined using Beer-Lamberts law. It should be noted that the same procedure can be used for both, hydrophilic and hydrophobic quantum dots as discussed in the report of Yu *et al.* [268].

As an example, the UV-Visible spectrum of water-soluble quantum dots (QD520) shown in **Figure A1** will be considered. Then, the calculations yield the following values for D,  $\varepsilon$  and the concentration c:

$$D = (1.6122 \cdot 10^{-9}) \cdot 503^4 - (2.6575 \cdot 10^{-6}) \cdot 503^3 + (1.6242 \cdot 10^{-3}) \cdot 503^2 -$$

$$0.4277 \cdot 503 + 41.57 = 2.37 \text{ nm}$$

$$\varepsilon = 5857 \cdot 2.39^{2.65} \frac{\text{L}}{\text{mol} \cdot \text{cm}} = 57644 \frac{\text{L}}{\text{mol} \cdot \text{cm}}$$

$$c = \frac{0.04}{57644 \frac{\text{L}}{\text{mol} \cdot \text{cm}} \cdot 1 \text{ cm}} = 694 \text{ nM}$$

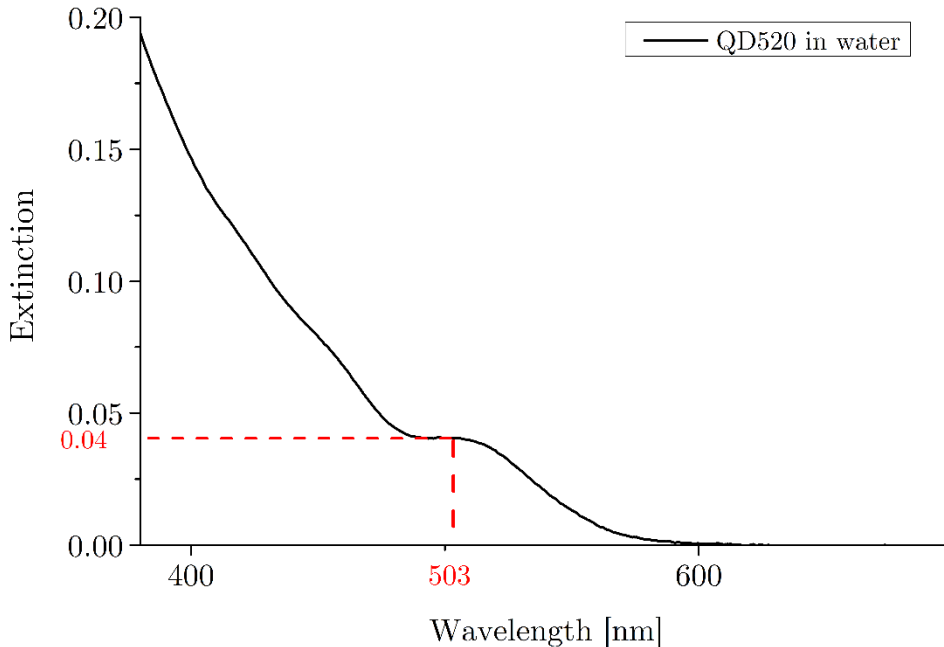


**Figure A1:** Extinction spectrum of QD520 in water. The first exciton peak is used to determine the concentration of the quantum dots.

*Upconversion nanoparticles:*

For upconversion nanoparticles there is no spectroscopic procedure for determining the molar concentration. However, an estimate can be made by considering the nanoparticle size as well as the density of the host crystal [394]. First, the volume of one nanoparticle is calculated from its dimensions obtained by TEM. Then, the mass of one particle can be obtained using literature values for the crystal density. The weight concentration of the sample in mg/mL is then converted to a molar

concentration using Avogadro's number. An example calculation for the nanoparticles used in this work will be given in the following.

The diameter of the upconversion nanoparticles determined from TEM was 32 nm (section 4.3). Therefore, the volume of one nanoparticle is  $V = \frac{4}{3}\pi \left(\frac{d}{2}\right)^3 = 1.7 \cdot 10^{-17} \text{ cm}^3$ . Assuming a density of  $\rho = 4.2 \text{ g/cm}^3$  for the NaYF<sub>4</sub> crystal [394], the mass per particle is:  $m_p = \rho \cdot V = 7.2 \cdot 10^{-17} \text{ g}$ . Now, the molar concentration of nanoparticles  $c_{\text{molar}}$  can be calculated from the weight concentration  $c_{\text{weight}}$  as follows:  $c_{\text{molar}} = \frac{c_{\text{weight}}}{m_p \cdot N_A}$ .  $N_A$  denotes Avogadro's number. For the nanoparticles considered in this example, 1 mg/mL weight concentration corresponds to a molar concentration of 23 nM.

### A.3 Sequences of unmodified and Azide/BCN-modified DNA

The sequences of the oligonucleotides without a cross-linker group are displayed in **Table A1**.

Strand SA1	<b>TTT</b> GCC TGG AGA TAC ATG CAC ATT ACG GC <b>TTT</b> C CCT ATT AGA AGG TCT CAG GTG CGC G <b>TTT</b> CG GTA AGT AGA CGG GAC CAG TTC GCC
Strand SA2	<b>TTT</b> CGC GCA CCT GAG ACC TTC TAA TAG GG <b>TTT</b> G CGA CAG TCG TTC AAC TAG AAT GCC C <b>TTT</b> GG GCT GTT CCG GGT GTG GCT CGT CGG
Strand SA3	<b>TTT</b> GGC CGA GGA CTC CTG CTC CGC TGC GG <b>TTT</b> G GCG AAC TGG TCC CGT CTA CTT ACC G <b>TTT</b> CC GAC GAG CCA CAC CCG GAA CAG CCC
Strand SA4	<b>TTT</b> GCC GTA ATG TGC ATG TAT CTC CAG GC <b>TTT</b> C CGC AGC GGA GCA GGA GTC CTC GGC C <b>TTT</b> GG GCA TTC TAG TTG AAC GAC TGT CGC

Table A1: Oligonucleotide sequences without cross-linker modifications.

The sequences of the azide and BCN containing sequences are shown in **Table A2**. The azide moieties are marked as **X** and the BCN moieties are marked as **Y**. Furthermore, the TTT spacers are marked in bold.

Strand SB1	<b>TTT</b> GCC TGG AGA GAC <b>A</b> XG CAC AGT ACG GC <b>TTT</b> C CCT ATT AGA AGG TCT CAG GTG CGC G <b>TTT</b> CG GTA AGT AGA CGG <b>X</b> AC CAG TTC GCC
Strand SB2	<b>TTT</b> CGC GCA CCT GAG ACC TTC TAA TAG GG <b>TTT</b> G CGA CAG TCG <b>X</b> AC GAC TAG AAT GCC C <b>TTT</b> GG GCT GTT CCG GAX GTG GCT CGT CGG
Strand SB3	<b>TTT</b> GGC CGA GGA CTC CTG CTC CGC TGC GG <b>TTT</b> G GCG AAC TGG <b>Y</b> AC CGT CTA CTT ACC G <b>TTT</b> CC GAC GAG CCA CAY CCG GAA CAG CCC
Strand SB4	<b>TTT</b> GCC GTA CTG TGC AYG TCT CTC CAG GC <b>TTT</b> C CGC AGC GGA GCA GGA GTC CTC GGC C <b>TTT</b> GG GCA TTC TAG TCG <b>Y</b> AC GAC TGT CGC

Table A2: Oligonucleotide sequences modified with azide (labelled with X) and BNC moieties (labelled with Y).

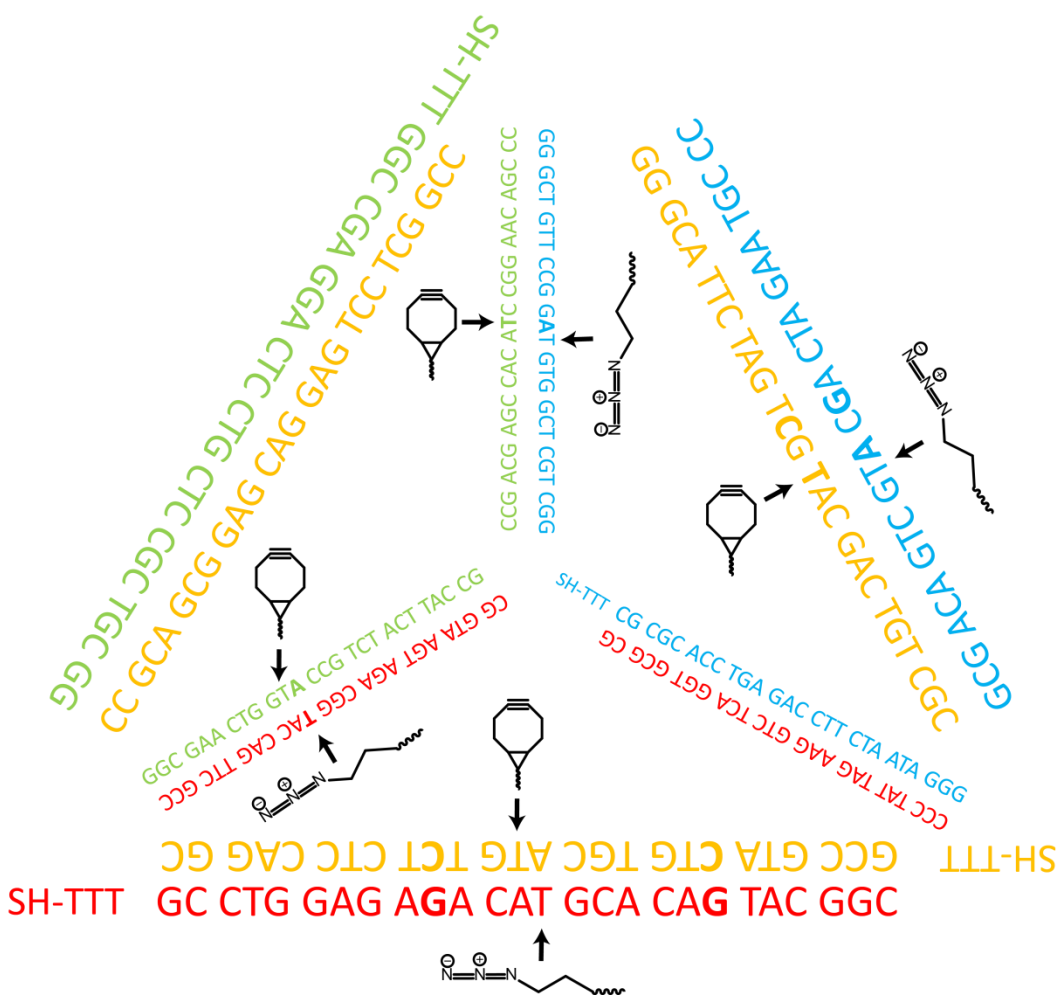


Figure A2: Three-dimensional representation of the tetrahedron formed by hybridisation of all four oligonucleotides SB1-SB4 and the positions of the clicking groups (see Table A2).

**Figure A2** depicts the tetrahedron formed by hybridisation of all four oligonucleotides SC1-SC4. The azide and alkyne moieties were placed in such a way that they are in direct proximity to each other.

#### A.4 Determination of the PLQY

In this part, the procedure for the determination of the photoluminescence quantum yield (PLQY) will be described. The measurement of PLQYs is rather difficult because there are many potential sources of errors [395-397]. A detailed report about the quantification of PLQYs was recently published by Würth *et al.* and suggests best practices for minimising errors [398].

The PLQY is defined as the fraction of the number of emitted photons over the number of absorbed photons and has values between 0% and 100%:

$$\Phi = \frac{\# \text{ emitted photons}}{\# \text{ absorbed photons}}$$

Equation A1: Definition of the photoluminescence quantum yield.

The idea for the quantification is that all emitted photons are counted and correlated to the number of absorbed photons. Except if an integrating sphere is used, both quantities are typically unknown [399]. Therefore, a reference with a known quantum yield needs to be utilised. Several organic dyes like rhodamine 6G or Fluorescein have proven to be reliable as standards and are often used for PLQY measurements.

In order to calculate the PLQY, absorption and emission spectra of the sample and the reference are taken. Then, the following formula is applied:

$$\Phi_s = \Phi_R \cdot \frac{I_s}{I_R} \frac{1 - 10^{-A_R}}{1 - 10^{-A_s}} \frac{n_s^2}{n_R^2}$$

Equation A2: Formula for the calculation of the quantum yield  $\phi$ .

where  $I$  denotes the integrated intensity of the whole emission spectrum,  $A$  the absorbance at the excitation wavelength and  $n$  the refractive index of the solvent. The indices  $s$  and  $R$  refer to sample and reference, respectively. The refractive indices are correcting the different optical geometries caused by refraction.

The quantum yields were determined using rhodamine 6G and fluorescein as reference dyes. The procedure was first verified by cross-checking the quantum yields of both dyes with each other. Then, the quantum yields of the nanoparticles was measured (**Table A3**). The solvents were 0.1 M NaOH (fluorescein), ethanol (Rhodamine 6G), hexane (QDs) and toluene (Perovskite NP). The excitation wavelength was 470 nm for all samples. The calculated values are the average from two independent samples with a deviation smaller than 0.07 between both measurements.

Sample	Calc. PLQY	Lit. PLQY
Rhodamine 6G	-	0.91 [398]
Fluorescein	0.87	0.89 [398]
QD520	0.68	0.6-0.8 [118]
QD580	0.45	0.6-0.8 [118]
$\text{CH}_3\text{NH}_3\text{PbBr}_3$ NP (CTAB)	0.58	>0.5 [154]

Table A3: Calculated and literature quantum yields for different nanoparticles.

### A.5 Extinction and PL spectral overlap

As explained in **chapter 6**, FRET is only possible when the absorption of the acceptor spectrally overlaps with the emission of the donor. **Figure A3** visualises the emission spectrum of QD540 and the absorption and emission spectrum of Cy3. This combination was used for the determination of DNA attachment (**section 6.2**). The emission spectrum of QD540 almost completely matches the absorption of the Cy3 dye, which makes this donor-acceptor pair suitable for FRET. Cy3 emission is obtained after energy transfer. Likewise, the absorption of QD580 overlaps completely with the emission of thulium-doped upconversion nanoparticles (**Figure A4**). This leads to an emission around 580 nm from the quantum dots due to energy transfer.

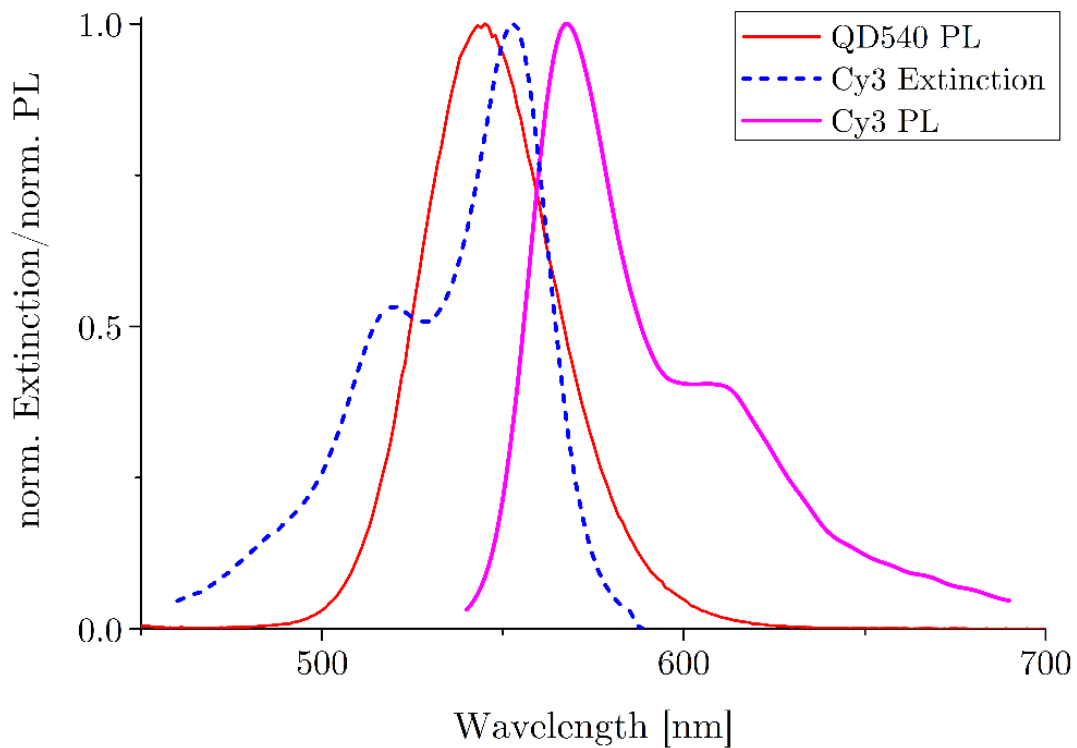


Figure A3: The emission spectrum of QD540 (red curve) and the absorption of Cy3 (blue curve) have a large overlap allowing FRET to occur, which results in emission from the Cy3 dye (pink curve).

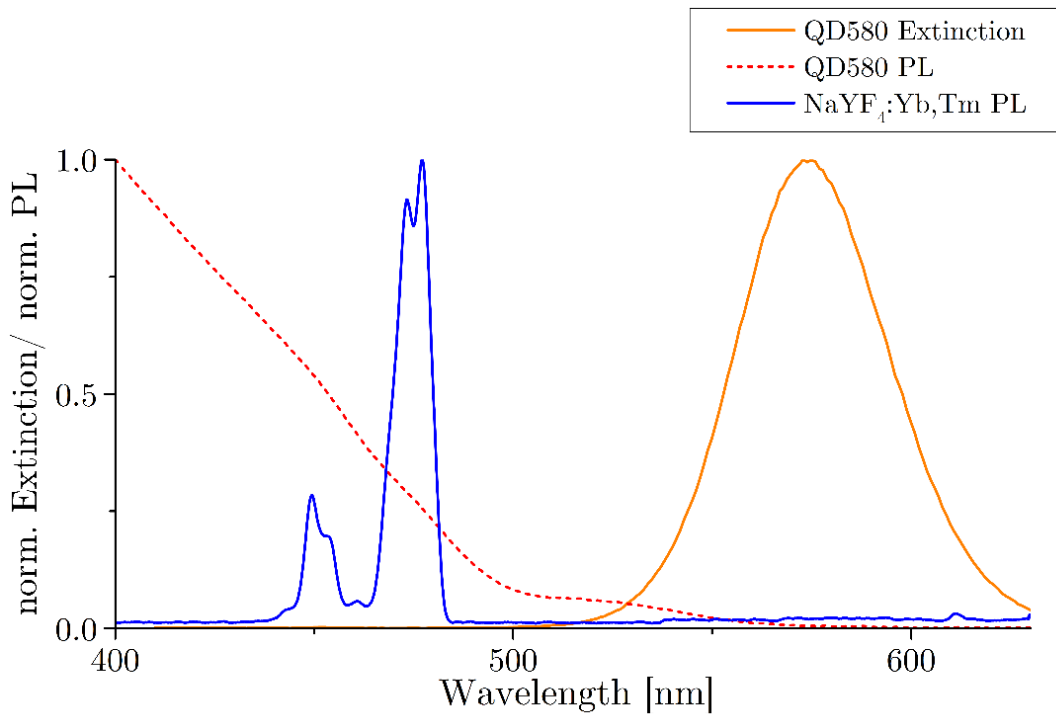


Figure A4: The emission spectrum of NaYF<sub>4</sub>:Yb,Tm UCNP (blue curve) and the absorption of QD580 (red curve) have a complete overlap allowing FRET to occur, which results in emission from QD580 (orange curve).

## References

1. 'Plenty of room' revisited. *Nat Nano*, 2009. **4**(12): p. 781-781.
2. Liu X., Lu C.-H., Willner I., *Switchable Reconfiguration of Nucleic Acid Nanostructures by Stimuli-Responsive DNA Machines*. *Accounts of Chemical Research*, 2014. **47**(6): p. 1673-1680.
3. Weller H., *Colloidal Semiconductor Q-Particles: Chemistry in the Transition Region Between Solid State and Molecules*. *Angewandte Chemie International Edition in English*, 1993. **32**(1): p. 41-53.
4. Toshima N., Yonezawa T., *Bimetallic nanoparticles-novel materials for chemical and physical applications*. *New Journal of Chemistry*, 1998. **22**(11): p. 1179-1201.
5. Sun Y., Xia Y., *Shape-Controlled Synthesis of Gold and Silver Nanoparticles*. *Science*, 2002. **298**(5601): p. 2176-2179.
6. Tao A. R., Habas S., Yang P., *Shape Control of Colloidal Metal Nanocrystals*. *Small*, 2008. **4**(3): p. 310-325.
7. Wu Z., Yang S., Wu W., *Shape control of inorganic nanoparticles from solution*. *Nanoscale*, 2016. **8**(3): p. 1237-1259.
8. Grzelczak M., Vermant J., Furst E. M., Liz-Marzán L. M., *Directed Self-Assembly of Nanoparticles*. *ACS Nano*, 2010. **4**(7): p. 3591-3605.
9. Nie Z., Petukhova A., Kumacheva E., *Properties and emerging applications of self-assembled structures made from inorganic nanoparticles*. *Nat Nano*, 2010. **5**(1): p. 15-25.
10. Jones M. R., Osberg K. D., Macfarlane R. J., Langille M. R., Mirkin C. A., *Templated Techniques for the Synthesis and Assembly of Plasmonic Nanostructures*. *Chemical Reviews*, 2011. **111**: p. 3736-3827.
11. Bao N., Gupta A., *Self-assembly of superparamagnetic nanoparticles*. *Journal of Materials Research*, 2011. **26**(02): p. 111-121.
12. Fan Z., Govorov A. O., *Plasmonic Circular Dichroism of Chiral Metal Nanoparticle Assemblies*. *Nano Letters*, 2010. **10**(7): p. 2580-2587.
13. Alivisatos A. P., Johnsson K. P., Peng X., Wilson T. E., Loweth C. J., Bruchez M. P., Schultz P. G., *Organization of 'nanocrystal molecules' using DNA*. *Nature*, 1996. **382**(6592): p. 609-611.
14. Mirkin C. A., Letsinger R. L., Mucic R. C., Storhoff J. J., *A DNA-based method for rationally assembling nanoparticles into macroscopic materials*. *Nature*, 1996. **382**(6592): p. 607-609.
15. Seeman N. C., *Structural DNA Nanotechnology: An Overview*. *Methods in molecular biology* (Clifton, NJ), 2005. **303**: p. 143-166.
16. Kolny J., Kornowski A., Weller H., *Self-Organization of Cadmium Sulfide and Gold Nanoparticles by Electrostatic Interaction*. *Nano Letters*, 2002. **2**(4): p. 361-364.
17. Rogers W. B., Shih W. M., Manoharan V. N., *Using DNA to program the self-assembly of colloidal nanoparticles and microparticles*. *Nature Reviews Materials*, 2016. **1**: p. 16008.
18. Sharma J., Chhabra R., Andersen C. S., Gothelf K. V., Yan H., Liu Y., *Toward Reliable Gold Nanoparticle Patterning On Self-Assembled DNA Nanoscaffold*. *Journal of the American Chemical Society*, 2008. **130**(25): p. 7820-7821.
19. Fernandez Y. D., Sun L., Gschneidtner T., Moth-Poulsen K., *Research Update: Progress in synthesis of nanoparticle dimers by self-assembly*. *APL Mater*, 2014. **2**(1): p. 010702.

20. Abdallah H. O., Ohayon Y. P., Chandrasekaran A. R., Sha R., Fox K. R., Brown T., Rusling D. A., Mao C., Seeman N. C., *Stabilisation of self-assembled DNA crystals by triplex-directed photo-cross-linking*. Chemical Communications, 2016. p.

21. Rajendran A., Endo M., Katsuda Y., Hidaka K., Sugiyama H., *Photo-Cross-Linking-Assisted Thermal Stability of DNA Origami Structures and Its Application for Higher-Temperature Self-Assembly*. Journal of the American Chemical Society, 2011. **133**(37): p. 14488-14491.

22. Heuer-Jungemann A., Kirkwood R., El-Sagheer A. H., Brown T., Kanaras A. G., *Copper-free click chemistry as an emerging tool for the programmed ligation of DNA-functionalised gold nanoparticles*. Nanoscale, 2013. **5**(16): p. 7209-7212.

23. El-Sagheer A. H., Brown T., *Click chemistry with DNA*. Chemical Society Reviews, 2010. **39**(4): p. 1388-1405.

24. Yoshimura Y., Fujimoto K., *Ultrafast Reversible Photo-Cross-Linking Reaction: Toward in Situ DNA Manipulation*. Organic Letters, 2008. **10**(15): p. 3227-3230.

25. Chen G., Qiu H., Prasad P. N., Chen X., *Upconversion Nanoparticles: Design, Nanochemistry, and Applications in Theranostics*. Chemical Reviews, 2014. **114**(10): p. 5161-5214.

26. Alivisatos A. P., *Perspectives on the Physical Chemistry of Semiconductor Nanocrystals*. The Journal of Physical Chemistry, 1996. **100**(31): p. 13226-13239.

27. Frecker T., Bailey D., Arzeta-Ferrer X., McBride J., Rosenthal S. J., *Review—Quantum Dots and Their Application in Lighting, Displays, and Biology*. ECS Journal of Solid State Science and Technology, 2016. **5**(1): p. R3019-R3031.

28. Haase M., Schäfer H., *Upconverting Nanoparticles*. Angewandte Chemie International Edition, 2011. **50**(26): p. 5808-5829.

29. . !!! INVALID CITATION !!! : p.

30. Li L.-L., Lu Y., *Regiospecific Hetero-Assembly of DNA-Functionalized Plasmonic Upconversion Superstructures*. Journal of the American Chemical Society, 2015. **137**(16): p. 5272-5275.

31. Zhang Y., Lu F., Yager K. G., van der Lelie D., Gang O., *A general strategy for the DNA-mediated self-assembly of functional nanoparticles into heterogeneous systems*. Nat Nano, 2013. **8**(11): p. 865-872.

32. Green M. A., Ho-Baillie A., Snaith H. J., *The emergence of perovskite solar cells*. Nat Photon, 2014. **8**(7): p. 506-514.

33. Stranks S. D., Snaith H. J., *Metal-halide perovskites for photovoltaic and light-emitting devices*. Nat Nano, 2015. **10**(5): p. 391-402.

34. Song J., Li J., Li X., Xu L., Dong Y., Zeng H., *Quantum Dot Light-Emitting Diodes Based on Inorganic Perovskite Cesium Lead Halides (CsPbX<sub>3</sub>)*. Advanced Materials, 2015. **27**(44): p. 7162-7167.

35. Mulvaney P., *Surface Plasmon Spectroscopy of Nanosized Metal Particles*. Langmuir, 1996. **12**(3): p. 788-800.

36. Liz-Marzán L. M., *Nanometals: Formation and color*. Materials Today, 2004. **7**(2): p. 26-31.

37. Fricker S. P., *Medical uses of gold compounds: Past, present and future*. Gold Bulletin, 1996. **29**(2): p. 53-60.

38. Eustis S., El-Sayed M. A., *Why gold nanoparticles are more precious than pretty gold: Noble metal surface plasmon resonance and its enhancement of the radiative and nonradiative properties of nanocrystals of different shapes*. Chemical Society Reviews, 2006. **35**(3): p. 209-217.

39. Daniel M.-C., Astruc D., *Gold Nanoparticles: Assembly, Supramolecular Chemistry, Quantum-Size-Related Properties, and Applications toward Biology, Catalysis, and Nanotechnology*. Chemical Reviews, 2004. **104**(1): p. 293-346.

40. Turkevich J., Stevenson P. C., Hillier J., *A study of the nucleation and growth processes in the synthesis of colloidal gold*. Discussions of the Faraday Society, 1951. **11**(0): p. 55-75.

41. Frens G., *Particle size and sol stability in metal colloids*. Kolloid-Zeitschrift und Zeitschrift für Polymere, 1972. **250**(7): p. 736-741.

42. Frens G., *Controlled Nucleation for the Regulation of the Particle Size in Monodisperse Gold Suspensions*. Nature Physical Science, 1973. **241**: p. 20-22.

43. Xia H., Bai S., Hartmann J., Wang D., *Synthesis of Monodisperse Quasi-Spherical Gold Nanoparticles in Water via Silver(I)-Assisted Citrate Reduction*. Langmuir, 2010. **26**(5): p. 3585-3589.

44. Turkevich J., *Colloidal gold. Part I*. Gold Bulletin, 1985. **18**(3): p. 86-91.

45. Chow M. K., Zukoski C. F., *Gold Sol Formation Mechanisms: Role of Colloidal Stability*. Journal of Colloid and Interface Science, 1994. **165**(1): p. 97-109.

46. Pei L., Mori K., Adachi M., *Formation Process of Two-Dimensional Networked Gold Nanowires by Citrate Reduction of AuCl<sub>4</sub><sup>-</sup> and the Shape Stabilization*. Langmuir, 2004. **20**(18): p. 7837-7843.

47. Privman V., Goia D. V., Park J., Matijević E., *Mechanism of Formation of Monodispersed Colloids by Aggregation of Nanosize Precursors*. Journal of Colloid and Interface Science, 1999. **213**(1): p. 36-45.

48. Li G., Lauer M., Schulz A., Boettcher C., Li F., Fuhrhop J.-H., *Spherical and Planar Gold(0) Nanoparticles with a Rigid Gold(I)-Anion or a Fluid Gold(0)-Acetone Surface†*. Langmuir, 2003. **19**(16): p. 6483-6491.

49. Kumar S., Gandhi K. S., Kumar R., *Modeling of Formation of Gold Nanoparticles by Citrate Method†*. Industrial & Engineering Chemistry Research, 2007. **46**(10): p. 3128-3136.

50. LaMer V. K., Dinegar R. H., *Theory, Production and Mechanism of Formation of Monodispersed Hydrosols*. Journal of the American Chemical Society, 1950. **72**(11): p. 4847-4854.

51. Wu X., Redmond P. L., Liu H., Chen Y., Steigerwald M., Brus L., *Photovoltage Mechanism for Room Light Conversion of Citrate Stabilized Silver Nanocrystal Seeds to Large Nanoprisms*. Journal of the American Chemical Society, 2008. **130**(29): p. 9500-9506.

52. Redmond P. L., Wu X., Brus L., *Photovoltage and Photocatalyzed Growth in Citrate-Stabilized Colloidal Silver Nanocrystals†*. The Journal of Physical Chemistry C, 2007. **111**(25): p. 8942-8947.

53. Ojea-Jiménez I., Bastús N. G., Puntes V., *Influence of the Sequence of the Reagents Addition in the Citrate-Mediated Synthesis of Gold Nanoparticles*. The Journal of Physical Chemistry C, 2011. **115**(32): p. 15752-15757.

54. Ji X., Song X., Li J., Bai Y., Yang W., Peng X., *Size Control of Gold Nanocrystals in Citrate Reduction: The Third Role of Citrate*. Journal of the American Chemical Society, 2007. **129**(45): p. 13939-13948.

55. Schulz F., Homolka T., Bastús N. G., Puntes V., Weller H., Vossmeye T., *Little Adjustments Significantly Improve the Turkevich Synthesis of Gold Nanoparticles*. Langmuir, 2014. **30**(35): p. 10779-10784.

56. Pong B.-K., Elim H. I., Chong J.-X., Ji W., Trout B. L., Lee J.-Y., *New Insights on the Nanoparticle Growth Mechanism in the Citrate Reduction of Gold(III) Salt: Formation of the Au Nanowire Intermediate and Its Nonlinear Optical Properties*. The Journal of Physical Chemistry C, 2007. **111**(17): p. 6281-6287.

57. Polte J., Ahner T. T., Delissen F., Sokolov S., Emmerling F., Thünemann A. F., Krahnert R., *Mechanism of Gold Nanoparticle Formation in the Classical Citrate Synthesis Method Derived from Coupled In Situ XANES and SAXS Evaluation*. *Journal of the American Chemical Society*, 2010. **132**(4): p. 1296-1301.

58. Wuithschick M., Birnbaum A., Witte S., Sztucki M., Vainio U., Pinna N., Rademann K., Emmerling F., Krahnert R., Polte J., *Turkevich in New Robes: Key Questions Answered for the Most Common Gold Nanoparticle Synthesis*. *ACS Nano*, 2015. **9**(7): p. 7052-7071.

59. Brown K. R., Walter D. G., Natan M. J., *Seeding of Colloidal Au Nanoparticle Solutions. 2. Improved Control of Particle Size and Shape*. *Chemistry of Materials*, 2000. **12**(2): p. 306-313.

60. Haiss W., Thanh N. T. K., Aveyard J., Fernig D. G., *Determination of Size and Concentration of Gold Nanoparticles from UV-Vis Spectra*. *Analytical Chemistry*, 2007. **79**(11): p. 4215-4221.

61. Ziegler C., Eychmüller A., *Seeded Growth Synthesis of Uniform Gold Nanoparticles with Diameters of 15–300 nm*. *The Journal of Physical Chemistry C*, 2011. **115**(11): p. 4502-4506.

62. Bastús N. G., Comenge J., Puntes V., *Kinetically Controlled Seeded Growth Synthesis of Citrate-Stabilized Gold Nanoparticles of up to 200 nm: Size Focusing versus Ostwald Ripening*. *Langmuir*, 2011. **27**(17): p. 11098-11105.

63. Deraedt C., Salmon L., Gatard S., Ciganda R., Hernandez R., Ruiz J., Astruc D., *Sodium borohydride stabilizes very active gold nanoparticle catalysts*. *Chemical Communications*, 2014. **50**(91): p. 14194-14196.

64. Brust M., Walker M., Bethell D., Schiffrin D. J., Whyman R., *Synthesis of thiol-derivatised gold nanoparticles in a two-phase Liquid-Liquid system*. *Journal of the Chemical Society, Chemical Communications*, 1994. (7): p. 801-802.

65. Lee P. C., Meisel D., *Adsorption and surface-enhanced Raman of dyes on silver and gold sols*. *The Journal of Physical Chemistry*, 1982. **86**(17): p. 3391-3395.

66. Dadash T., *Synthesis of uniform silver nanoparticles with a controllable size*. *Materials Letters*, 2009. **63**(26): p. 2236-2238.

67. Rainville L., Dorais M.-C., Boudreau D., *Controlled synthesis of low polydispersity Ag@SiO<sub>2</sub> core-shell nanoparticles for use in plasmonic applications*. *RSC Advances*, 2013. **3**(33): p. 13953-13960.

68. Bastús N. G., Merkoçi F., Piella J., Puntes V., *Synthesis of Highly Monodisperse Citrate-Stabilized Silver Nanoparticles of up to 200 nm: Kinetic Control and Catalytic Properties*. *Chemistry of Materials*, 2014. **26**(9): p. 2836-2846.

69. Krutyakov Y. A. K., A. A.; Olenin, A. Yu; Lisichkin, G. V., *Synthesis and properties of silver nanoparticles: advances and prospects*. *Russian Chemical Reviews*, 2008. **77**(3): p. 233-257.

70. Janata E., Henglein A., Ershov B. G., *First Clusters of Ag<sup>+</sup> Ion Reduction in Aqueous Solution*. *The Journal of Physical Chemistry*, 1994. **98**(42): p. 10888-10890.

71. Pillai Z. S., Kamat P. V., *What Factors Control the Size and Shape of Silver Nanoparticles in the Citrate Ion Reduction Method?* *The Journal of Physical Chemistry B*, 2004. **108**(3): p. 945-951.

72. Link S., El-Sayed M. A., *Size and Temperature Dependence of the Plasmon Absorption of Colloidal Gold Nanoparticles*. *The Journal of Physical Chemistry B*, 1999. **103**(21): p. 4212-4217.

73. Faraday M., *The Bakerian Lecture: Experimental Relations of Gold (and Other Metals) to Light*. Philosophical Transactions of the Royal Society of London, 1857. **147**: p. 145-181.

74. Willets K. A., Van Duyne R. P., *Localized Surface Plasmon Resonance Spectroscopy and Sensing*. Annual Review of Physical Chemistry, 2007. **58**(1): p. 267-297.

75. Kelly K. L., Coronado E., Zhao L. L., Schatz G. C., *The Optical Properties of Metal Nanoparticles: The Influence of Size, Shape, and Dielectric Environment*. The Journal of Physical Chemistry B, 2003. **107**(3): p. 668-677.

76. Noguez C., *Surface Plasmons on Metal Nanoparticles: The Influence of Shape and Physical Environment*. The Journal of Physical Chemistry C, 2007. **111**(10): p. 3806-3819.

77. Link S., El-Sayed M. A., *Spectral Properties and Relaxation Dynamics of Surface Plasmon Electronic Oscillations in Gold and Silver Nanodots and Nanorods*. The Journal of Physical Chemistry B, 1999. **103**(40): p. 8410-8426.

78. Underwood S., Mulvaney P., *Effect of the Solution Refractive Index on the Color of Gold Colloids*. Langmuir, 1994. **10**(10): p. 3427-3430.

79. Fan X., Zheng W., Singh D. J., *Light scattering and surface plasmons on small spherical particles*. Light Sci Appl, 2014. **3**: p. e179.

80. Bohren C. F., Huffman D. R. *Absorption and Scattering of Light by Small Particles*. New York: Wiley; 1983.

81. Fröhlich H. *Theory of Dielectrics: Dielectric Constant and Dielectric Loss*. Oxford: Clarendon Press; 1949.

82. Liz-Marzán L. M., Giersig M., Mulvaney P., *Synthesis of Nanosized Gold–Silica Core–Shell Particles*. Langmuir, 1996. **12**(18): p. 4329-4335.

83. Averitt R. D., Sarkar D., Halas N. J., *Plasmon Resonance Shifts of Au-Coated Au<sub>2</sub>S Nanoshells: Insight into Multicomponent Nanoparticle Growth*. Physical Review Letters, 1997. **78**(22): p. 4217-4220.

84. Palomba S., Novotny L., Palmer R. E., *Blue-shifted plasmon resonance of individual size-selected gold nanoparticles*. Optics Communications, 2008. **281**(3): p. 480-483.

85. Kreibig U., Genzel L., *Optical absorption of small metallic particles*. Surface Science, 1985. **156**: p. 678-700.

86. Kreibig U., Vollmer M. *Optical Properties of Metal Clusters*. Berlin: Springer; 1995.

87. Alvarez M. M., Khouri J. T., Schaaff T. G., Shafiqullin M. N., Vezmar I., Whetten R. L., *Optical Absorption Spectra of Nanocrystal Gold Molecules*. The Journal of Physical Chemistry B, 1997. **101**(19): p. 3706-3712.

88. Johnson P. B., Christy R. W., *Optical Constants of the Noble Metals*. Physical Review B, 1972. **6**(12): p. 4370-4379.

89. *Optical Properties of Metal Vol. 2*. Weaver J. H., Kafka C., Lynch D. W., Koch E. E., editors. Karlsruhe: Fachinformationszentrum; 1981.

90. Mie G., *Beiträge zur Optik trüber Medien, speziell kolloidaler Metallösungen*. Annalen der Physik, 1908. **330**(3): p. 377-445.

91. Stratton J. A. *Electromagnetic Theory*. New York and London: McGraw-Hill; 1941.

92. Link S., El-Sayed M. A., *Shape and size dependence of radiative, non-radiative and photothermal properties of gold nanocrystals*. International Reviews in Physical Chemistry, 2000. **19**(3): p. 409-453.

93. Myroshnychenko V., Rodriguez-Fernandez J., Pastoriza-Santos I., Funston A. M., Novo C., Mulvaney P., Liz-Marzan L. M., Garcia de Abajo F. J., *Modelling*

*the optical response of gold nanoparticles.* Chemical Society Reviews, 2008. **37**(9): p. 1792-1805.

94. Gans R., *Über die Form ultramikroskopischer Goldteilchen.* Annalen der Physik, 1912. **342**(5): p. 881-900.

95. Gans R., *Über die Form ultramikroskopischer Silberteilchen.* Annalen der Physik, 1915. **352**(10): p. 270-284.

96. Sprünken D. P., Omi H., Furukawa K., Nakashima H., Sychugov I., Kobayashi Y., Torimitsu K., *Influence of the Local Environment on Determining Aspect-Ratio Distributions of Gold Nanorods in Solution Using Gans Theory.* The Journal of Physical Chemistry C, 2007. **111**(39): p. 14299-14306.

97. Link S., Mohamed M. B., El-Sayed M. A., *Simulation of the Optical Absorption Spectra of Gold Nanorods as a Function of Their Aspect Ratio and the Effect of the Medium Dielectric Constant.* The Journal of Physical Chemistry B, 1999. **103**(16): p. 3073-3077.

98. Stone J., Jackson S., Wright D., *Biological applications of gold nanorods.* Wiley Interdisciplinary Reviews: Nanomedicine and Nanobiotechnology, 2011. **3**(1): p. 100-109.

99. Huang X., Neretina S., El-Sayed M. A., *Gold Nanorods: From Synthesis and Properties to Biological and Biomedical Applications.* Advanced Materials, 2009. **21**(48): p. 4880-4910.

100. Shi C., Soltani S., Armani A. M., *Gold Nanorod Plasmonic Upconversion Microlaser.* Nano Letters, 2013. **13**(12): p. 5827-5831.

101. Chen H., Shao L., Li Q., Wang J., *Gold nanorods and their plasmonic properties.* Chemical Society Reviews, 2013. **42**(7): p. 2679-2724.

102. Stamplecoskie K. G., Scaiano J. C., Tiwari V. S., Anis H., *Optimal Size of Silver Nanoparticles for Surface-Enhanced Raman Spectroscopy.* The Journal of Physical Chemistry C, 2011. **115**(5): p. 1403-1409.

103. Fan M., Brolo A. G., *Silver nanoparticles self assembly as SERS substrates with near single molecule detection limit.* Physical Chemistry Chemical Physics, 2009. **11**(34): p. 7381-7389.

104. Dabbousi B. O., Rodriguez-Viejo J., Mikulec F. V., Heine J. R., Mattossi H., Ober R., Jensen K. F., Bawendi M. G., *(CdSe)ZnS Core-Shell Quantum Dots: Synthesis and Characterization of a Size Series of Highly Luminescent Nanocrystallites.* The Journal of Physical Chemistry B, 1997. **101**(46): p. 9463-9475.

105. Steigerwald M. L., Brus L. E., *Semiconductor crystallites: a class of large molecules.* Accounts of Chemical Research, 1990. **23**(6): p. 183-188.

106. Murray C. B., Norris D. J., Bawendi M. G., *Synthesis and characterization of nearly monodisperse CdE (E = sulfur, selenium, tellurium) semiconductor nanocrystallites.* Journal of the American Chemical Society, 1993. **115**(19): p. 8706-8715.

107. Moudrikoudis S., Liz-Marzán L. M., *Oleylamine in Nanoparticle Synthesis.* Chemistry of Materials, 2013. **25**(9): p. 1465-1476.

108. Yu W. W., Peng X., *Formation of High-Quality CdS and Other II-VI Semiconductor Nanocrystals in Noncoordinating Solvents: Tunable Reactivity of Monomers.* Angewandte Chemie International Edition, 2002. **41**(13): p. 2368-2371.

109. Talapin D. V., Rogach A. L., Kornowski A., Haase M., Weller H., *Highly Luminescent Monodisperse CdSe and CdSe/ZnS Nanocrystals Synthesized in a Hexadecylamine-Trioctylphosphine Oxide-Trioctylphosphine Mixture.* Nano Letters, 2001. **1**(4): p. 207-211.

110. de Mello Donegá C., Liljeroth P., Vanmaekelbergh D., *Physicochemical Evaluation of the Hot-Injection Method, a Synthesis Route for Monodisperse Nanocrystals*. *Small*, 2005. **1**(12): p. 1152-1162.
111. Wise F. W., *Lead Salt Quantum Dots: the Limit of Strong Quantum Confinement*. *Accounts of Chemical Research*, 2000. **33**(11): p. 773-780.
112. Veamatahau A., Jiang B., Seifert T., Makuta S., Latham K., Kanehara M., Teranishi T., Tachibana Y., *Origin of surface trap states in CdS quantum dots: relationship between size dependent photoluminescence and sulfur vacancy trap states*. *Physical Chemistry Chemical Physics*, 2015. **17**(4): p. 2850-2858.
113. Hines M. A., Guyot-Sionnest P., *Synthesis and Characterization of Strongly Luminescing ZnS-Capped CdSe Nanocrystals*. *The Journal of Physical Chemistry*, 1996. **100**(2): p. 468-471.
114. Jang E., Jun S., Chung Y., Pu L., *Surface Treatment to Enhance the Quantum Efficiency of Semiconductor Nanocrystals*. *The Journal of Physical Chemistry B*, 2004. **108**(15): p. 4597-4600.
115. Reiss P., Protière M., Li L., *Core/Shell Semiconductor Nanocrystals*. *Small*, 2009. **5**(2): p. 154-168.
116. Chen X., Lou Y., Samia A. C., Burda C., *Coherency Strain Effects on the Optical Response of Core/Shell Heteronanostructures*. *Nano Letters*, 2003. **3**(6): p. 799-803.
117. de Mello Donegá C., Hickey S. G., Wuister S. F., Vanmaekelbergh D., Meijerink A., *Single-Step Synthesis to Control the Photoluminescence Quantum Yield and Size Dispersion of CdSe Nanocrystals*. *The Journal of Physical Chemistry B*, 2003. **107**(2): p. 489-496.
118. Bae W. K., Char K., Hur H., Lee S., *Single-Step Synthesis of Quantum Dots with Chemical Composition Gradients*. *Chemistry of Materials*, 2008. **20**(2): p. 531-539.
119. Bae W. K., Padilha L. A., Park Y.-S., McDaniel H., Robel I., Pietryga J. M., Klimov V. I., *Controlled Alloying of the Core–Shell Interface in CdSe/CdS Quantum Dots for Suppression of Auger Recombination*. *ACS Nano*, 2013. **7**(4): p. 3411-3419.
120. Bawendi M. G., Steigerwald M. L., Brus L. E., *The Quantum Mechanics of Larger Semiconductor Clusters ("Quantum Dots")*. *Annual Review of Physical Chemistry*, 1990. **41**(1): p. 477-496.
121. Scholes G. D., Rumbles G., *Excitons in nanoscale systems*. *Nat Mater*, 2006. **5**(9): p. 683-696.
122. Kittel C. *Introduction to Solid State Physics*: John Wiley & Sons; 2005.
123. de L. Kronig R., Penney W. G., *Quantum Mechanics of Electrons in Crystal Lattices*. *Proceedings of the Royal Society of London A: Mathematical, Physical and Engineering Sciences*, 1931. **130**(814): p. 499-513.
124. Meier C., Gondorf A., Lüttjohann S., Lorke A., Wiggers H., *Silicon nanoparticles: Absorption, emission, and the nature of the electronic bandgap*. *Journal of Applied Physics*, 2007. **101**(10): p. 103112.
125. Canham L. T., *Silicon quantum wire array fabrication by electrochemical and chemical dissolution of wafers*. *Applied Physics Letters*, 1990. **57**(10): p. 1046-1048.
126. Pavesi L., Dal Negro L., Mazzoleni C., Franzo G., Priolo F., *Optical gain in silicon nanocrystals*. *Nature*, 2000. **408**(6811): p. 440-444.
127. Xin Y., Nishio K., Saitow K.-i., *White-blue electroluminescence from a Si quantum dot hybrid light-emitting diode*. *Applied Physics Letters*, 2015. **106**(20): p. 201102.

128. Norris D. J., Bawendi M. G., *Measurement and assignment of the size-dependent optical spectrum in CdSe quantum dots*. Physical Review B, 1996. **53**(24): p. 16338-16346.

129. Brus L. E., *Electron-electron and electron-hole interactions in small semiconductor crystallites: The size dependence of the lowest excited electronic state*. The Journal of Chemical Physics, 1984. **80**(9): p. 4403-4409.

130. Krauss T. D., Peterson J. J. *Colloidal Quantum Dot Optoelectronics and Photovoltaics*. Konstantatos G., Sargent E. H., editors. Cambridge: Cambridge University Press; 2013.

131. Brus L., *Electronic wave functions in semiconductor clusters: experiment and theory*. The Journal of Physical Chemistry, 1986. **90**(12): p. 2555-2560.

132. Resch-Genger U., Grabolle M., Cavaliere-Jaricot S., Nitschke R., Nann T., *Quantum dots versus organic dyes as fluorescent labels*. Nat Meth, 2008. **5**(9): p. 763-775.

133. Carey G. H., Abdelhady A. L., Ning Z., Thon S. M., Bakr O. M., Sargent E. H., *Colloidal Quantum Dot Solar Cells*. Chemical Reviews, 2015. **115**(23): p. 12732-12763.

134. Algar W. R., Tavares A. J., Krull U. J., *Beyond labels: A review of the application of quantum dots as integrated components of assays, bioprobes, and biosensors utilizing optical transduction*. Analytica Chimica Acta, 2010. **673**(1): p. 1-25.

135. Zhang Y.-W., Sun X., Si R., You L.-P., Yan C.-H., *Single-Crystalline and Monodisperse LaF<sub>3</sub> Triangular Nanoplates from a Single-Source Precursor*. Journal of the American Chemical Society, 2005. **127**(10): p. 3260-3261.

136. Ye X., Collins J. E., Kang Y., Chen J., Chen D. T. N., Yodh A. G., Murray C. B., *Morphologically controlled synthesis of colloidal upconversion nanophosphors and their shape-directed self-assembly*. Proceedings of the National Academy of Sciences, 2010. **107**(52): p. 22430-22435.

137. Li Z., Zhang Y., *An efficient and user-friendly method for the synthesis of hexagonal-phase NaYF<sub>4</sub> :Yb, Er/Tm nanocrystals with controllable shape and upconversion fluorescence*. Nanotechnology, 2008. **19**(34): p. 345606.

138. Wang F., Liu X., *Upconversion Multicolor Fine-Tuning: Visible to Near-Infrared Emission from Lanthanide-Doped NaYF<sub>4</sub> Nanoparticles*. Journal of the American Chemical Society, 2008. **130**(17): p. 5642-5643.

139. Ansari A. A., Yadav R., Rai S. B., *Enhanced luminescence efficiency of aqueous dispersible NaYF<sub>4</sub>:Yb/Er nanoparticles and the effect of surface coating*. RSC Advances, 2016. **6**(26): p. 22074-22082.

140. Zheng W., Huang P., Tu D., Ma E., Zhu H., Chen X., *Lanthanide-doped upconversion nano-bioprobes: electronic structures, optical properties, and biodetection*. Chemical Society Reviews, 2015. **44**(6): p. 1379-1415.

141. Vivas M. G., Cury J. F., Schiavon M. A., Mendonca C. R., *Two-Photon Absorption of ZnS Quantum Dots: Interpreting the Nonlinear Spectrum*. The Journal of Physical Chemistry C, 2013. **117**(16): p. 8530-8535.

142. Chen S. L., Stehr J., Reddy N. K., Tu C. W., Chen W. M., Buyanova I. A., *Efficient upconversion of photoluminescence via two-photon absorption in bulk and nanorod ZnO*. Applied Physics B, 2012. **108**(4): p. 919-924.

143. Auzel F., *Upconversion and Anti-Stokes Processes with f and d Ions in Solids*. Chemical Reviews, 2004. **104**(1): p. 139-174.

144. Suyver J. F., Grimm J., van Veen M. K., Biner D., Krämer K. W., Güdel H. U., *Upconversion spectroscopy and properties of NaYF<sub>4</sub> doped with Er<sup>3+</sup>, Tm<sup>3+</sup> and/or Yb<sup>3+</sup>*. Journal of Luminescence, 2006. **117**(1): p. 1-12.

145. Quintanilla M., Nunez N. O., Cantelar E., Ocana M., Cusso F., *Tuning from blue to magenta the up-converted emissions of YF<sub>3</sub>:Tm<sup>3+</sup>/Yb<sup>3+</sup> nanocrystals*. *Nanoscale*, 2011. **3**(3): p. 1046-1052.
146. Smith A. M., Mancini M. C., Nie S., *Bioimaging: Second window for in vivo imaging*. *Nat Nano*, 2009. **4**(11): p. 710-711.
147. Park Y. I., Lee K. T., Suh Y. D., Hyeon T., *Upconverting nanoparticles: a versatile platform for wide-field two-photon microscopy and multi-modal in vivo imaging*. *Chemical Society Reviews*, 2015. **44**(6): p. 1302-1317.
148. van Sark W., de Wild J., Rath J., Meijerink A., Schropp R. E., *Upconversion in solar cells*. *Nanoscale Research Letters*, 2013. **8**(1): p. 81.
149. Zhou B., Shi B., Jin D., Liu X., *Controlling upconversion nanocrystals for emerging applications*. *Nat Nano*, 2015. **10**(11): p. 924-936.
150. Snaith H. J., *Perovskites: The Emergence of a New Era for Low-Cost, High-Efficiency Solar Cells*. *The Journal of Physical Chemistry Letters*, 2013. **4**(21): p. 3623-3630.
151. Song T.-B., Chen Q., Zhou H., Jiang C., Wang H.-H., Yang Y., Liu Y., You J., Yang Y., *Perovskite solar cells: film formation and properties*. *Journal of Materials Chemistry A*, 2015. **3**(17): p. 9032-9050.
152. Kojima A., Teshima K., Shirai Y., Miyasaka T., *Organometal Halide Perovskites as Visible-Light Sensitizers for Photovoltaic Cells*. *Journal of the American Chemical Society*, 2009. **131**(17): p. 6050-6051.
153. Schmidt L. C., Pertegás A., González-Carrero S., Malinkiewicz O., Agouram S., Mínguez Espallargas G., Bolink H. J., Galian R. E., Pérez-Prieto J., *Nontemplate Synthesis of CH<sub>3</sub>NH<sub>3</sub>PbBr<sub>3</sub> Perovskite Nanoparticles*. *Journal of the American Chemical Society*, 2014. **136**(3): p. 850-853.
154. Gonzalez-Carrero S., Galian R. E., Perez-Prieto J., *Maximizing the emissive properties of CH<sub>3</sub>NH<sub>3</sub>PbBr<sub>3</sub> perovskite nanoparticles*. *Journal of Materials Chemistry A*, 2015. **3**(17): p. 9187-9193.
155. Zhang F., Zhong H., Chen C., Wu X.-g., Hu X., Huang H., Han J., Zou B., Dong Y., *Brightly Luminescent and Color-Tunable Colloidal CH<sub>3</sub>NH<sub>3</sub>PbX<sub>3</sub> (X = Br, I, Cl) Quantum Dots: Potential Alternatives for Display Technology*. *ACS Nano*, 2015. **9**(4): p. 4533-4542.
156. Protesescu L., Yakunin S., Bodnarchuk M. I., Krieg F., Caputo R., Hendon C. H., Yang R. X., Walsh A., Kovalenko M. V., *Nanocrystals of Cesium Lead Halide Perovskites (CsPbX<sub>3</sub>, X = Cl, Br, and I): Novel Optoelectronic Materials Showing Bright Emission with Wide Color Gamut*. *Nano Letters*, 2015. **15**(6): p. 3692-3696.
157. Nedelcu G., Protesescu L., Yakunin S., Bodnarchuk M. I., Grotevent M. J., Kovalenko M. V., *Fast Anion-Exchange in Highly Luminescent Nanocrystals of Cesium Lead Halide Perovskites (CsPbX<sub>3</sub>, X = Cl, Br, I)*. *Nano Letters*, 2015. **15**(8): p. 5635-5640.
158. Akkerman Q. A., D'Innocenzo V., Accornero S., Scarpellini A., Petrozza A., Prato M., Manna L., *Tuning the Optical Properties of Cesium Lead Halide Perovskite Nanocrystals by Anion Exchange Reactions*. *Journal of the American Chemical Society*, 2015. **137**(32): p. 10276-10281.
159. Filip M. R., Eperon G. E., Snaith H. J., Giustino F., *Steric engineering of metal-halide perovskites with tunable optical band gaps*. *Nat Commun*, 2014. **5**: p.
160. Kulkarni S. A., Baikie T., Boix P. P., Yantara N., Mathews N., Mhaisalkar S., *Band-gap tuning of lead halide perovskites using a sequential deposition process*. *Journal of Materials Chemistry A*, 2014. **2**(24): p. 9221-9225.
161. Sichert J. A., Tong Y., Mutz N., Vollmer M., Fischer S., Milowska K. Z., García Cortadella R., Nickel B., Cardenas-Daw C., Stolarczyk J. K., Urban A. S.,

Feldmann J., *Quantum Size Effect in Organometal Halide Perovskite Nanoplatelets*. Nano Letters, 2015. **15**(10): p. 6521-6527.

162. Chen J., Zhou S., Jin S., Li H., Zhai T., *Crystal organometal halide perovskites with promising optoelectronic applications*. Journal of Materials Chemistry C, 2016. **4**(1): p. 11-27.

163. Sperling R. A., Parak W. J., *Surface modification, functionalization and bioconjugation of colloidal inorganic nanoparticles*. Philosophical Transactions of the Royal Society of London A: Mathematical, Physical and Engineering Sciences, 2010. **368**(1915): p. 1333-1383.

164. Hakkinen H., *The gold-sulfur interface at the nanoscale*. Nat Chem, 2012. **4**(6): p. 443-455.

165. Fairbanks M. C., Benfield R. E., Newport R. J., Schmid G., *An exafs study of the cluster molecule Au55(PPh<sub>3</sub>)<sub>12</sub>Cl<sub>6</sub>*. Solid State Communications, 1990. **73**(6): p. 431-436.

166. Loweth C. J., Caldwell W. B., Peng X., Alivisatos A. P., Schultz P. G., *DNA-Based Assembly of Gold Nanocrystals*. Angewandte Chemie International Edition, 1999. **38**(12): p. 1808-1812.

167. Schmid G., Lehnert A., *The Complexation of Gold Colloids*. Angewandte Chemie International Edition in English, 1989. **28**(6): p. 780-781.

168. Wang M., Abbineni G., Clevenger A., Mao C., Xu S., *Upconversion Nanoparticles: Synthesis, Surface Modification, and Biological Applications*. Nanomedicine : nanotechnology, biology, and medicine, 2011. **7**(6): p. 710-729.

169. Lévy R., Thanh N. T. K., Doty R. C., Hussain I., Nichols R. J., Schiffrian D. J., Brust M., Fernig D. G., *Rational and Combinatorial Design of Peptide Capping Ligands for Gold Nanoparticles*. Journal of the American Chemical Society, 2004. **126**(32): p. 10076-10084.

170. Liu Y., Shipton M. K., Ryan J., Kaufman E. D., Franzen S., Feldheim D. L., *Synthesis, Stability, and Cellular Internalization of Gold Nanoparticles Containing Mixed Peptide-Poly(ethylene glycol) Monolayers*. Analytical Chemistry, 2007. **79**(6): p. 2221-2229.

171. Roux S., Garcia B., Bridot J.-L., Salomé M., Marquette C., Lemelle L., Gillet P., Blum L., Perriat P., Tillement O., *Synthesis, Characterization of Dihydrolipoic Acid Capped Gold Nanoparticles, and Functionalization by the Electroluminescent Luminol*. Langmuir, 2005. **21**(6): p. 2526-2536.

172. Caragheorgheopol A., Chechik V., *Mechanistic aspects of ligand exchange in Au nanoparticles*. Physical Chemistry Chemical Physics, 2008. **10**(33): p. 5029-5041.

173. Gittins D. I., Caruso F., *Spontaneous Phase Transfer of Nanoparticulate Metals from Organic to Aqueous Media*. Angewandte Chemie International Edition, 2001. **40**(16): p. 3001-3004.

174. Thanh N. T. K., Maclean N., Mahiddine S., *Mechanisms of Nucleation and Growth of Nanoparticles in Solution*. Chemical Reviews, 2014. **114**(15): p. 7610-7630.

175. Camargo C. P. H., Rodrigues S. T., da Silva M. A. G., Wang J. *Controlled Synthesis: Nucleation and Growth in Solution*. In: Xiong Y., Lu X., editors. Metallic Nanostructures: From Controlled Synthesis to Applications. Cham: Springer International Publishing; 2015. p. 49-74.

176. Ostwald W., *Über die vermeintliche Isomerie des roten und gelben Quecksilberoxyds und die Oberflächenspannung fester Körper*. Zeitschrift für Physikalische Chemie, 1900. **34**: p. 495-503.

177. Derjaguin B., Landau L., *Theory of the stability of strongly charged lyophobic sols and of the adhesion of strongly charged particles in solutions of electrolytes*. Progress in Surface Science, 1993. **43**(1): p. 30-59.
178. Hamaker H. C., *The London—van der Waals attraction between spherical particles*. Physica, 1937. **4**(10): p. 1058-1072.
179. Stolarszyk J. K., Deak A., Brougham D. F., *Nanoparticle Clusters: Assembly and Control Over Internal Order, Current Capabilities, and Future Potential*. Advanced Materials, 2016. p. n/a-n/a.
180. Stenhammar J., Linse P., Wennerström H., Karlström G., *An Exact Calculation of the van der Waals Interaction between Two Spheres of Classical Dipolar Fluid*. The Journal of Physical Chemistry B, 2010. **114**(42): p. 13372-13380.
181. Tadros T. F. *General Principles of Colloid Stability and the Role of Surface Forces*. In: Tadros T. F., editor. Colloid Stability: The Role of Surface Forces - Part I. Weinheim, Germany: Wiley-VCH; 2006. p. 1-22.
182. Hunter R. J. *Chapter 6 - Applications of the Zeta Potential*. Zeta Potential in Colloid Science: Academic Press; 1981. p. 219-257.
183. Alkilany A. M., Abulataeffeh S. R., Mills K. K., Bani Yaseen A. I., Hamaly M. A., Alkhatib H. S., Aiedeh K. M., Stone J. W., *Colloidal Stability of Citrate and Mercaptoacetic Acid Capped Gold Nanoparticles upon Lyophilization: Effect of Capping Ligand Attachment and Type of Cryoprotectants*. Langmuir, 2014. **30**(46): p. 13799-13808.
184. Romero-Cano M. S., Martín-Rodríguez A., de las Nieves F. J., *Electrosteric Stabilization of Polymer Colloids with Different Functionality*. Langmuir, 2001. **17**(11): p. 3505-3511.
185. Napper D. H., *Steric stabilization*. Journal of Colloid and Interface Science, 1977. **58**(2): p. 390-407.
186. Shalkevich N., Shalkevich A., Si-Ahmed L., Burgi T., *Reversible formation of gold nanoparticle-surfactant composite assemblies for the preparation of concentrated colloidal solutions*. Physical Chemistry Chemical Physics, 2009. **11**(43): p. 10175-10179.
187. Koczkur K. M., Mourdikoudis S., Polavarapu L., Skrabalak S. E., *Polyvinylpyrrolidone (PVP) in nanoparticle synthesis*. Dalton Transactions, 2015. **44**(41): p. 17883-17905.
188. Fang C., Bhattacharai N., Sun C., Zhang M., *Functionalized Nanoparticles with Long-Term Stability in Biological Media*. Small, 2009. **5**(14): p. 1637-1641.
189. Blackburn G. M., Gait M. J., Loakes D., Williams D. M. *Chapter 2 DNA and RNA Structure*. Nucleic Acids in Chemistry and Biology (3). Cambridge: The Royal Society of Chemistry; 2006. p. 13-76.
190. Watson J. D., Crick F. H. C., *Molecular Structure of Nucleic Acids: A Structure for Deoxyribose Nucleic Acid*. Nature, 1953. **171**(4356): p. 737-738.
191. Kool E. T., *Hydrogen Bonding, Base Stacking, and Steric Effects in DNA Replication*. Annual Review of Biophysics and Biomolecular Structure, 2001. **30**(1): p. 1-22.
192. Kolář M., Kubař T., Hobza P., *On the Role of London Dispersion Forces in Biomolecular Structure Determination*. The Journal of Physical Chemistry B, 2011. **115**(24): p. 8038-8046.
193. Chandler D., *Interfaces and the driving force of hydrophobic assembly*. Nature, 2005. **437**(7059): p. 640-647.
194. Yakovchuk P., Protozanova E., Frank-Kamenetskii M. D., *Base-stacking and base-pairing contributions into thermal stability of the DNA double helix*. Nucleic Acids Research, 2006. **34**(2): p. 564-574.

195. Lou C., Dallmann A., Marafini P., Gao R., Brown T., *Enhanced H-bonding and  $\pi$ -stacking in DNA: a potent duplex-stabilizing and mismatch sensing nucleobase analogue*. Chemical Science, 2014. **5**(10): p. 3836-3844.

196. Owczarzy R., Moreira B. G., You Y., Behlke M. A., Walder J. A., *Predicting Stability of DNA Duplexes in Solutions Containing Magnesium and Monovalent Cations*. Biochemistry, 2008. **47**(19): p. 5336-5353.

197. Ansevin A. T., Vizard D. L., Brown B. W., McConathy J., *High-resolution thermal denaturation of DNA. I. Theoretical and practical considerations for the resolution of thermal subtransitions*. Biopolymers, 1976. **15**(1): p. 153-174.

198. D'Abramo M., Castellazzi C. L., Orozco M., Amadei A., *On the Nature of DNA Hyperchromic Effect*. The Journal of Physical Chemistry B, 2013. **117**(29): p. 8697-8704.

199. Ivanov V., Piontковski D., Zocchi G., *Local cooperativity mechanism in the DNA melting transition*. Physical Review E, 2005. **71**(4): p. 041909.

200. SantaLucia J., *A unified view of polymer, dumbbell, and oligonucleotide DNA nearest-neighbor thermodynamics*. Proceedings of the National Academy of Sciences of the United States of America, 1998. **95**(4): p. 1460-1465.

201. Kibbe W. A., *OligoCalc: an online oligonucleotide properties calculator*. Nucleic Acids Research, 2007. **35**(suppl 2): p. W43-W46.

202. Dixon J. M., Taniguchi M., Lindsey J. S., *PhotochemCAD 2: A Refined Program with Accompanying Spectral Databases for Photochemical Calculations*. Photochemistry and Photobiology, 2005. **81**(1): p. 212-213.

203. Biebricher A. S., Heller I., Roijmans R. F. H., Hoekstra T. P., Peterman E. J. G., Wuite G. J. L., *The impact of DNA intercalators on DNA and DNA-processing enzymes elucidated through force-dependent binding kinetics*. Nat Commun, 2015. **6**: p.

204. Zimmerman F., Hossenfelder B., Panitz J. C., Wokaun A., *SERRS study of Acridine Orange and Its Binding to DNA Strands*. The Journal of Physical Chemistry, 1994. **98**(48): p. 12796-12804.

205. Bohr V., Lerche A., *In vitro crosslinking of DNA by 8-methoxypsoralen visualized by electron microscopy*. Biochimica et Biophysica Acta (BBA) - Nucleic Acids and Protein Synthesis, 1978. **519**(2): p. 356-364.

206. Schuster G. B., Chen W., Ma Z., Avirah R. R., *Precise synthesis of conducting polymers by DNA-directed self-assembly*. Chemistry in New Zealand, 2013. **77**(3): p. 69-75.

207. Ma Z., Chen W., Johnson M. C., Schmidt-Krey I., Williams L., Schuster G. B., *Modular-DNA Programmed Molecular Construction of "Fixed" of 2D and 3D-Au Nanoparticle Arrays*. Chemistry of Materials, 2014. **26**(19): p. 5499-5505.

208. Smith S. I., Brodbelt J. S., *Rapid characterization of cross-links, mono-adducts, and non-covalent binding of psoralens to deoxyoligonucleotides by LC-UV/ESI-MS and IRMPD mass spectrometry*. Analyst, 2010. **135**(5): p. 943-952.

209. Hearst J. E., *Psoralen Photochemistry*. Annual Review of Biophysics and Bioengineering, 1981. **10**(1): p. 69-86.

210. Sakamoto T., Tanaka Y., Fujimoto K., *DNA Photo-Cross-Linking Using 3-Cyanovinylcarbazole Modified Oligonucleotide with Threonitol Linker*. Organic Letters, 2015. **17**(4): p. 936-939.

211. Loutfy R. O., Mayo P. D., *Primary Bond Formation in the Addition of Cyclopentenone to Chloroethylenes*. Canadian Journal of Chemistry, 1972. **50**(21): p. 3465-3471.

212. Broeker J. L., Eksterowicz J. E., Belk A. J., Houk K. N., *On the Regioselectivity of Photocycloadditions of Triplet Cyclohexenones to Alkenes*. Journal of the American Chemical Society, 1995. **117**(6): p. 1847-1848.

213. Gerrard S. R., Hardiman C., Shelbourne M., Nandhakumar I., Nordén B., Brown T., *A New Modular Approach to Nanoassembly: Stable and Addressable DNA Nanoconstructs via Orthogonal Click Chemistries*. ACS Nano, 2012. **6**(10): p. 9221-9228.

214. Kolb H. C., Finn M. G., Sharpless K. B., *Click Chemistry: Diverse Chemical Function from a Few Good Reactions*. Angewandte Chemie International Edition, 2001. **40**(11): p. 2004-2021.

215. Tornøe C. W., Christensen C., Meldal M., *Peptidotriazoles on Solid Phase: [1,2,3]-Triazoles by Regiospecific Copper(I)-Catalyzed 1,3-Dipolar Cycloadditions of Terminal Alkynes to Azides*. The Journal of Organic Chemistry, 2002. **67**(9): p. 3057-3064.

216. Rostovtsev V. V., Green L. G., Fokin V. V., Sharpless K. B., *A Stepwise Huisgen Cycloaddition Process: Copper(I)-Catalyzed Regioselective "Ligation" of Azides and Terminal Alkynes*. Angewandte Chemie International Edition, 2002. **41**(14): p. 2596-2599.

217. Castro V., Rodríguez H., Albericio F., *CuAAC: An Efficient Click Chemistry Reaction on Solid Phase*. ACS Combinatorial Science, 2016. **18**(1): p. 1-14.

218. Agard N. J., Prescher J. A., Bertozzi C. R., *A Strain-Promoted [3 + 2] Azide–Alkyne Cycloaddition for Covalent Modification of Biomolecules in Living Systems*. Journal of the American Chemical Society, 2004. **126**(46): p. 15046-15047.

219. Wittig G., Krebs A., *Zur Existenz niedergliedriger Cycloalkine, I*. Chemische Berichte, 1961. **94**(12): p. 3260-3275.

220. Bach R. D., *Ring Strain Energy in the Cyclooctyl System. The Effect of Strain Energy on [3 + 2] Cycloaddition Reactions with Azides*. Journal of the American Chemical Society, 2009. **131**(14): p. 5233-5243.

221. Ning X., Guo J., Wolfert M. A., Boons G.-J., *Visualizing Metabolically Labeled Glycoconjugates of Living Cells by Copper-Free and Fast Huisgen Cycloadditions*. Angewandte Chemie International Edition, 2008. **47**(12): p. 2253-2255.

222. Dommerholt J., Schmidt S., Temming R., Hendriks L. J. A., Rutjes F. P. J. T., van Hest J. C. M., Lefeber D. J., Friedl P., van Delft F. L., *Readily Accessible Bicyclononynes for Bioorthogonal Labeling and Three-Dimensional Imaging of Living Cells*. Angewandte Chemie International Edition, 2010. **49**(49): p. 9422-9425.

223. MacKenzie D. A., Sherratt A. R., Chigrinova M., Cheung L. L. W., Pezacki J. P., *Strain-promoted cycloadditions involving nitrones and alkynes — rapid tunable reactions for bioorthogonal labeling*. Current Opinion in Chemical Biology, 2014. **21**: p. 81-88.

224. Chan T. R., Hilgraf R., Sharpless K. B., Fokin V. V., *Polytriazoles as Copper(I)-Stabilizing Ligands in Catalysis*. Organic Letters, 2004. **6**(17): p. 2853-2855.

225. Gramlich P. M. E., Wirges C. T., Manetto A., Carell T., *Postsynthetic DNA Modification through the Copper-Catalyzed Azide–Alkyne Cycloaddition Reaction*. Angewandte Chemie International Edition, 2008. **47**(44): p. 8350-8358.

226. Hong V., Steinmetz N. F., Manchester M., Finn M. G., *Labeling Live Cells by Copper-Catalyzed Alkyne–Azide Click Chemistry*. Bioconjugate Chemistry, 2010. **21**(10): p. 1912-1916.

227. Jewett J. C., Bertozzi C. R., *Cu-free click cycloaddition reactions in chemical biology*. Chemical Society Reviews, 2010. **39**(4): p. 1272-1279.

228. Ozin G. A., Hou K., Lotsch B. V., Cademartiri L., Puzzo D. P., Scotognella F., Ghadimi A., Thomson J., *Nanofabrication by self-assembly*. Materials Today, 2009. **12**(5): p. 12-23.

229. Lehn J.-M., *Perspectives in Supramolecular Chemistry—From Molecular Recognition towards Molecular Information Processing and Self-Organization*. Angewandte Chemie International Edition in English, 1990. **29**(11): p. 1304-1319.

230. Whitesides G., Mathias J., Seto C., *Molecular self-assembly and nanochemistry: a chemical strategy for the synthesis of nanostructures*. Science, 1991. **254**(5036): p. 1312-1319.

231. Love J. C., Estroff L. A., Kriebel J. K., Nuzzo R. G., Whitesides G. M., *Self-Assembled Monolayers of Thiolates on Metals as a Form of Nanotechnology*. Chemical Reviews, 2005. **105**(4): p. 1103-1170.

232. Ulman A., *Formation and Structure of Self-Assembled Monolayers*. Chemical Reviews, 1996. **96**(4): p. 1533-1554.

233. Celia E., Darmanin T., Taffin de Givenchy E., Amigoni S., Guittard F., *Recent advances in designing superhydrophobic surfaces*. Journal of Colloid and Interface Science, 2013. **402**: p. 1-18.

234. Stratakis E., Mateescu A., Barberoglou M., Vamvakaki M., Fotakis C., Anastasiadis S. H., *From superhydrophobicity and water repellency to superhydrophilicity: smart polymer-functionalized surfaces*. Chemical Communications, 2010. **46**(23): p. 4136-4138.

235. Rahmawan Y., Xu L., Yang S., *Self-assembly of nanostructures towards transparent, superhydrophobic surfaces*. Journal of Materials Chemistry A, 2013. **1**(9): p. 2955-2969.

236. Chen J., Seeman N. C., *Synthesis from DNA of a molecule with the connectivity of a cube*. Nature, 1991. **350**(6319): p. 631-633.

237. Jin R., Wu G., Li Z., Mirkin C. A., Schatz G. C., *What Controls the Melting Properties of DNA-Linked Gold Nanoparticle Assemblies?* Journal of the American Chemical Society, 2003. **125**(6): p. 1643-1654.

238. Elghanian R., Storhoff J. J., Mucic R. C., Letsinger R. L., Mirkin C. A., *Selective Colorimetric Detection of Polynucleotides Based on the Distance-Dependent Optical Properties of Gold Nanoparticles*. Science, 1997. **277**(5329): p. 1078-1081.

239. Macfarlane R. J., Lee B., Jones M. R., Harris N., Schatz G. C., Mirkin C. A., *Nanoparticle Superlattice Engineering with DNA*. Science, 2011. **334**(6053): p. 204-208.

240. Senesi A. J., Eichelsdoerfer D. J., Macfarlane R. J., Jones M. R., Auyeung E., Lee B., Mirkin C. A., *Stepwise Evolution of DNA-Programmable Nanoparticle Superlattices*. Angewandte Chemie International Edition, 2013. **52**(26): p. 6624-6628.

241. Zhang C., Macfarlane R. J., Young K. L., Choi C. H. J., Hao L., Auyeung E., Liu G., Zhou X., Mirkin C. A., *A general approach to DNA-programmable atom equivalents*. Nat Mater, 2013. **12**(8): p. 741-746.

242. Ross M. B., Blaber M. G., Schatz G. C., *Using nanoscale and mesoscale anisotropy to engineer the optical response of three-dimensional plasmonic metamaterials*. Nat Commun, 2014. **5**: p.

243. Lee S., *Colloidal superlattices for unnaturally high-index metamaterials at broadband optical frequencies*. Optics Express, 2015. **23**(22): p. 28170-28181.

244. Park D. J., Zhang C., Ku J. C., Zhou Y., Schatz G. C., Mirkin C. A., *Plasmonic photonic crystals realized through DNA-programmable assembly*. Proceedings of the National Academy of Sciences, 2015. **112**(4): p. 977-981.

245. Pinheiro A. V., Han D., Shih W. M., Yan H., *Challenges and opportunities for structural DNA nanotechnology*. Nat Nano, 2011. **6**(12): p. 763-772.

246. Zanchet D., Micheel C. M., Parak W. J., Gerion D., Alivisatos A. P., *Electrophoretic Isolation of Discrete Au Nanocrystal/DNA Conjugates*. Nano Letters, 2001. **1**(1): p. 32-35.

247. Pellegrino T., Sperling R. A., Alivisatos A. P., Parak W. J., *Gel Electrophoresis of Gold-DNA Nanoconjugates*. Journal of Biomedicine and Biotechnology, 2007. **2007**: p. 26796.

248. Zheng J., Constantinou P. E., Micheel C., Alivisatos A. P., Kiehl R. A., Seeman N. C., *Two-Dimensional Nanoparticle Arrays Show the Organizational Power of Robust DNA Motifs*. Nano Letters, 2006. **6**(7): p. 1502-1504.

249. Mastroianni A. J., Claridge S. A., Alivisatos A. P., *Pyramidal and Chiral Groupings of Gold Nanocrystals Assembled Using DNA Scaffolds*. Journal of the American Chemical Society, 2009. **131**(24): p. 8455-8459.

250. Zanchet D., Micheel C. M., Parak W. J., Gerion D., Williams S. C., Alivisatos A. P., *Electrophoretic and Structural Studies of DNA-Directed Au Nanoparticle Groupings*. The Journal of Physical Chemistry B, 2002. **106**(45): p. 11758-11763.

251. Su K. H., Wei Q. H., Zhang X., Mock J. J., Smith D. R., Schultz S., *Interparticle Coupling Effects on Plasmon Resonances of Nanogold Particles*. Nano Letters, 2003. **3**(8): p. 1087-1090.

252. Ghosh S. K., Pal T., *Interparticle Coupling Effect on the Surface Plasmon Resonance of Gold Nanoparticles: From Theory to Applications*. Chemical Reviews, 2007. **107**(11): p. 4797-4862.

253. Barrow S. J., Funston A. M., Wei X., Mulvaney P., *DNA-directed self-assembly and optical properties of discrete 1D, 2D and 3D plasmonic structures*. Nano Today, 2013. **8**(2): p. 138-167.

254. Nordlander P., Oubre C., Prodan E., Li K., Stockman M. I., *Plasmon Hybridization in Nanoparticle Dimers*. Nano Letters, 2004. **4**(5): p. 899-903.

255. Liu N., Hentschel M., Weiss T., Alivisatos A. P., Giessen H., *Three-Dimensional Plasmon Rulers*. Science, 2011. **332**(6036): p. 1407-1410.

256. Hill R. T., Mock J. J., Hucknall A., Wolter S. D., Jokerst N. M., Smith D. R., Chilkoti A., *Plasmon Ruler with Angstrom Length Resolution*. ACS Nano, 2012. **6**(10): p. 9237-9246.

257. Jun Y.-w., Sheikholeslami S., Hostetter D. R., Tajon C., Craik C. S., Alivisatos A. P., *Continuous imaging of plasmon rulers in live cells reveals early-stage caspase-3 activation at the single-molecule level*. Proceedings of the National Academy of Sciences, 2009. **106**(42): p. 17735-17740.

258. Wang H., Li Z., Zhang H., Wang P., Wen S., *Giant local circular dichroism within an asymmetric plasmonic nanoparticle trimer*. Scientific Reports, 2015. **5**: p. 8207.

259. Yan W., Xu L., Xu C., Ma W., Kuang H., Wang L., Kotov N. A., *Self-Assembly of Chiral Nanoparticle Pyramids with Strong R/S Optical Activity*. Journal of the American Chemical Society, 2012. **134**(36): p. 15114-15121.

260. Kuzyk A., Schreiber R., Fan Z., Pardatscher G., Roller E.-M., Hogele A., Simmel F. C., Govorov A. O., Liedl T., *DNA-based self-assembly of chiral plasmonic nanostructures with tailored optical response*. Nature, 2012. **483**(7389): p. 311-314.

261. Thacker V. V., Herrmann L. O., Sigle D. O., Zhang T., Liedl T., Baumberg J. J., Keyser U. F., *DNA origami based assembly of gold nanoparticle dimers for surface-enhanced Raman scattering*. Nat Commun, 2014. **5**: p.

262. Macfarlane R. J., O'Brien M. N., Petrosko S. H., Mirkin C. A., *Nucleic Acid-Modified Nanostructures as Programmable Atom Equivalents: Forging a New "Table of Elements"*. *Angewandte Chemie International Edition*, 2013. **52**(22): p. 5688-5698.

263. Rothemund P. W. K., *Folding DNA to create nanoscale shapes and patterns*. *Nature*, 2006. **440**(7082): p. 297-302.

264. Quan Z., Xu H., Wang C., Wen X., Wang Y., Zhu J., Li R., Sheehan C. J., Wang Z., Smilgies D.-M., Luo Z., Fang J., *Solvent-Mediated Self-Assembly of Nanocube Superlattices*. *Journal of the American Chemical Society*, 2014. **136**(4): p. 1352-1359.

265. Zhang T., Chen P., Sun Y., Xing Y., Yang Y., Dong Y., Xu L., Yang Z., Liu D., *A new strategy improves assembly efficiency of DNA mono-modified gold nanoparticles*. *Chemical Communications*, 2011. **47**(20): p. 5774-5776.

266. Aldeek F., Hawkins D., Palomo V., Safi M., Palui G., Dawson P. E., Alabugin I., Matoussi H., *UV and Sunlight Driven Photoligation of Quantum Dots: Understanding the Photochemical Transformation of the Ligands*. *Journal of the American Chemical Society*, 2015. **137**(7): p. 2704-2714.

267. Liu C., Wang Z., Wang X., Li Z., *Surface modification of hydrophobic NaYF<sub>4</sub>:Yb,Er upconversion nanophosphors and their applications for immunoassay*. *Science China Chemistry*, 2011. **54**(8): p. 1292-1297.

268. Yu W. W., Qu L., Guo W., Peng X., *Experimental Determination of the Extinction Coefficient of CdTe, CdSe, and CdS Nanocrystals*. *Chemistry of Materials*, 2003. **15**(14): p. 2854-2860.

269. Clark A. H., Ross-Murphy S. B. *Structural and mechanical properties of biopolymer gels*. *Biopolymers*. Berlin, Heidelberg: Springer Berlin Heidelberg; 1987. p. 57-192.

270. Schneider C. A., Rasband W. S., Eliceiri K. W., *NIH Image to ImageJ: 25 years of image analysis*. *Nat Meth*, 2012. **9**(7): p. 671-675.

271. Silberberg M. *Principles of General Chemistry (2)*: McGraw-Hill Publishing Company; 2010.

272. Barreto Â., Luis L. G., Girão A. V., Trindade T., Soares A. M. V. M., Oliveira M., *Behavior of colloidal gold nanoparticles in different ionic strength media*. *Journal of Nanoparticle Research*, 2015. **17**(12): p. 1-13.

273. Mayer K. M., Hafner J. H., *Localized Surface Plasmon Resonance Sensors*. *Chemical Reviews*, 2011. **111**(6): p. 3828-3857.

274. Manson J., Kumar D., Meenan B. J., Dixon D., *Polyethylene glycol functionalized gold nanoparticles: the influence of capping density on stability in various media*. *Gold Bulletin*, 2011. **44**(2): p. 99-105.

275. Bidault S., Polman A., *Water-Based Assembly and Purification of Plasmon-Coupled Gold Nanoparticle Dimers and Trimers*. *International Journal of Optics*, 2012. **2012**: p. 5.

276. Xu B., Gonella G., DeLacy B. G., Dai H.-L., *Adsorption of Anionic Thiols on Silver Nanoparticles*. *The Journal of Physical Chemistry C*, 2015. **119**(10): p. 5454-5461.

277. Battocchio C., Meneghini C., Fratoddi I., Venditti I., Russo M. V., Aquilanti G., Maurizio C., Bondino F., Matassa R., Rossi M., Mobilio S., Polzonetti G., *Silver Nanoparticles Stabilized with Thiols: A Close Look at the Local Chemistry and Chemical Structure*. *The Journal of Physical Chemistry C*, 2012. **116**(36): p. 19571-19578.

278. Steinbrück A., Csaki A., Ritter K., Leich M., Köhler J. M., Fritzsche W., *Gold-silver and silver-silver nanoparticle constructs based on DNA hybridization of*

*thiol- and amino-functionalized oligonucleotides.* Journal of Biophotonics, 2008. **1**(2): p. 104-113.

279. Zhang X., Servos M. R., Liu J., *Fast pH-assisted functionalization of silver nanoparticles with monothiolated DNA.* Chemical Communications, 2012. **48**(81): p. 10114-10116.

280. Wang Y., Newell B. B., Irudayaraj J., *Folic Acid Protected Silver Nanocarriers for Targeted Drug Delivery.* Journal of Biomedical Nanotechnology, 2012. **8**(5): p. 751-759.

281. Rahme K., Chen L., Hobbs R. G., Morris M. A., O'Driscoll C., Holmes J. D., *PEGylated gold nanoparticles: polymer quantification as a function of PEG lengths and nanoparticle dimensions.* RSC Advances, 2013. **3**(17): p. 6085-6094.

282. Chan W. C. W., Nie S., *Quantum Dot Bioconjugates for Ultrasensitive Nonisotopic Detection.* Science, 1998. **281**(5385): p. 2016-2018.

283. Misiak M., Prorok K., Cichy B., Bednarkiewicz A., Stręk W., *Thulium concentration quenching in the up-converting  $\alpha$ -Tm<sup>3+</sup>/Yb<sup>3+</sup> NaYF<sub>4</sub> colloidal nanocrystals.* Optical Materials, 2013. **35**(5): p. 1124-1128.

284. Muhr V., Wilhelm S., Hirsch T., Wolfbeis O. S., *Upconversion Nanoparticles: From Hydrophobic to Hydrophilic Surfaces.* Accounts of Chemical Research, 2014. **47**(12): p. 3481-3493.

285. Schubert S., Delaney J. J. T., Schubert U. S., *Nanoprecipitation and nanoformulation of polymers: from history to powerful possibilities beyond poly(lactic acid).* Soft Matter, 2011. **7**(5): p. 1581-1588.

286. Mićić O. I., Cheong H. M., Fu H., Zunger A., Sprague J. R., Mascarenhas A., Nozik A. J., *Size-Dependent Spectroscopy of InP Quantum Dots.* The Journal of Physical Chemistry B, 1997. **101**(25): p. 4904-4912.

287. Müller-Buschbaum P., Gutmann J. S., Wolkenhauer M., Kraus J., Stamm M., Smilgies D., Petry W., *Solvent-Induced Surface Morphology of Thin Polymer Films.* Macromolecules, 2001. **34**(5): p. 1369-1375.

288. Niu G., Guo X., Wang L., *Review of recent progress in chemical stability of perovskite solar cells.* Journal of Materials Chemistry A, 2015. **3**(17): p. 8970-8980.

289. Klíčová L. u., Šebej P., Štacko P., Filippov S. K., Bogomolova A., Padilla M., Klán P., *CTAB/Water/Chloroform Reverse Micelles: A Closed or Open Association Model?* Langmuir, 2012. **28**(43): p. 15185-15192.

290. Muthu C., Nagamma S. R., Nair V. C., *Luminescent hybrid perovskite nanoparticles as a new platform for selective detection of 2,4,6-trinitrophenol.* RSC Advances, 2014. **4**(99): p. 55908-55911.

291. Bain C. D., Biebuyck H. A., Whitesides G. M., *Comparison of self-assembled monolayers on gold: coadsorption of thiols and disulfides.* Langmuir, 1989. **5**(3): p. 723-727.

292. Cleland W. W., *Dithiothreitol, a New Protective Reagent for SH Groups\*.* Biochemistry, 1964. **3**(4): p. 480-482.

293. Dmitrenko O., Thorpe C., Bach R. D., *Mechanism of S<sub>N</sub>2 Disulfide Bond Cleavage by Phosphorus Nucleophiles. Implications for Biochemical Disulfide Reducing Agents.* The Journal of Organic Chemistry, 2007. **72**(22): p. 8298-8307.

294. Burns J. A., Butler J. C., Moran J., Whitesides G. M., *Selective reduction of disulfides by tris(2-carboxyethyl)phosphine.* The Journal of Organic Chemistry, 1991. **56**(8): p. 2648-2650.

295. Sweetman B., Maclare J., *The reduction of wool keratin by tertiary phosphines*. Australian Journal of Chemistry, 1966. **19**(12): p. 2347-2354.

296. Busson M. P., Rolly B., Stout B., Bonod N., Larquet E., Polman A., Bidault S., *Optical and Topological Characterization of Gold Nanoparticle Dimers Linked by a Single DNA Double Strand*. Nano Letters, 2011. **11**(11): p. 5060-5065.

297. Xue C., Métraux G. S., Millstone J. E., Mirkin C. A., *Mechanistic Study of Photomediated Triangular Silver Nanoprism Growth*. Journal of the American Chemical Society, 2008. **130**(26): p. 8337-8344.

298. Lu L., Burkey G., Halaciuga I., Goia D. V., *Core-shell gold/silver nanoparticles: Synthesis and optical properties*. Journal of Colloid and Interface Science, 2013. **392**: p. 90-95.

299. Nakajima N., Ikada Y., *Mechanism of Amide Formation by Carbodiimide for Bioconjugation in Aqueous Media*. Bioconjugate Chemistry, 1995. **6**(1): p. 123-130.

300. Fischer M. J. E. *Amine Coupling Through EDC/NHS: A Practical Approach*. In: Mol J. N., Fischer E. M. J., editors. Surface Plasmon Resonance: Methods and Protocols. Totowa, NJ: Humana Press; 2010. p. 55-73.

301. Hermanson G. *Bioconjugate Techniques*: Academic Press; 2013.

302. Castro C. E., Kilchherr F., Kim D.-N., Shiao E. L., Wauer T., Wortmann P., Bathe M., Dietz H., *A primer to scaffolded DNA origami*. Nat Meth, 2011. **8**(3): p. 221-229.

303. Peng Z., Liu H., *Bottom-up Nanofabrication Using DNA Nanostructures*. Chemistry of Materials, 2016. **28**(4): p. 1012-1021.

304. Frank R., Köster H., *DNA chain length markers and the influence of base composition on electrophoretic mobility of oligodeoxyribonucleotides in polyacrylamide-gels*. Nucleic Acids Research, 1979. **6**(6): p. 2069-2087.

305. Debets M. F., van Hest J. C. M., Rutjes F. P. J. T., *Bioorthogonal labelling of biomolecules: new functional handles and ligation methods*. Organic & Biomolecular Chemistry, 2013. **11**(38): p. 6439-6455.

306. de Almeida G., Sletten E. M., Nakamura H., Palaniappan K. K., Bertozzi C. R., *Thiacycloalkynes for Copper-Free Click Chemistry*. Angewandte Chemie International Edition, 2012. **51**(10): p. 2443-2447.

307. Ballari R. V., Martin A., *Assessment of DNA degradation induced by thermal and UV radiation processing: Implications for quantification of genetically modified organisms*. Food Chemistry, 2013. **141**(3): p. 2130-2136.

308. Flett F., Interthal H., *Separation of DNA Oligonucleotides Using Denaturing Urea PAGE*. In: Makovets S., editor. DNA Electrophoresis: Methods and Protocols. Totowa, NJ: Humana Press; 2013. p. 173-185.

309. Blake R. D., Delcourt S. G., *Thermodynamic Effects of Formamide on DNA Stability*. Nucleic Acids Research, 1996. **24**(11): p. 2095-2103.

310. Höglberg B., Helmersson J., Holm S., Olin H., *Study of DNA coated nanoparticles as possible programmable self-assembly building blocks*. Applied Surface Science, 2006. **252**(15): p. 5538-5541.

311. Avigail S., Dvir R., Inna P., Danny P., *Quasi 3D imaging of DNA-gold nanoparticle tetrahedral structures*. Journal of Physics: Condensed Matter, 2012. **24**(16): p. 164203.

312. Piantanida L., Naumenko D., Lazzarino M., *Highly efficient gold nanoparticle dimer formation via DNA hybridization*. RSC Advances, 2014. **4**(29): p. 15281-15287.

313. Li F., Zhang H., Dever B., Li X.-F., Le X. C., *Thermal Stability of DNA Functionalized Gold Nanoparticles*. Bioconjugate Chemistry, 2013. **24**(11): p. 1790-1797.

314. Vieregg J. R., Nelson H. M., Stoltz B. M., Pierce N. A., *Selective Nucleic Acid Capture with Shielded Covalent Probes*. Journal of the American Chemical Society, 2013. **135**(26): p. 9691-9699.

315. Tagawa M., Shohda K.-i., Fujimoto K., Suyama A., *Stabilization of DNA nanostructures by photo-cross-linking*. Soft Matter, 2011. **7**(22): p. 10931-10934.

316. Sheng Q.-L., Liu R.-X., Zheng J.-B., Zhu J.-J., *Reversible switches of DNA nanostructures between "Closed" and "Open" states and their biosensing applications*. Nanoscale, 2013. **5**(16): p. 7505-7511.

317. Abi A., Lin M., Pei H., Fan C., Ferapontova E. E., Zuo X., *Electrochemical Switching with 3D DNA Tetrahedral Nanostructures Self-Assembled at Gold Electrodes*. ACS Applied Materials & Interfaces, 2014. **6**(11): p. 8928-8931.

318. Pocoví-Martínez S., Parreño-Romero M., Agouram S., Pérez-Prieto J., *Controlled UV-C Light-Induced Fusion of Thiol-Passivated Gold Nanoparticles*. Langmuir, 2011. **27**(9): p. 5234-5241.

319. Zhou Y., Wang C. Y., Zhu Y. R., Chen Z. Y., *A Novel Ultraviolet Irradiation Technique for Shape-Controlled Synthesis of Gold Nanoparticles at Room Temperature*. Chemistry of Materials, 1999. **11**(9): p. 2310-2312.

320. Lan X., Chen Z., Liu B.-J., Ren B., Henzie J., Wang Q., *DNA-Directed Gold Nanodimers with Tunable Sizes and Interparticle Distances and Their Surface Plasmonic Properties*. Small, 2013. **9**(13): p. 2308-2315.

321. Smekal A., *Zur Quantentheorie der Dispersion*. Naturwissenschaften, 1923. **11**(43): p. 873-875.

322. Raman C. V., Krishnan K. S., *A New Type of Secondary Radiation*. Nature, 1928. **121**: p. 501-502.

323. Landsberg G., Mandelstam L., *Eine neue Erscheinung bei der Lichtzerstreuung in Krystallen*. Naturwissenschaften, 1928. **16**(28): p. 557-558.

324. Das R. S., Agrawal Y. K., *Raman spectroscopy: Recent advancements, techniques and applications*. Vibrational Spectroscopy, 2011. **57**(2): p. 163-176.

325. Krause M., Rösch P., Radt B., Popp J., *Localizing and Identifying Living Bacteria in an Abiotic Environment by a Combination of Raman and Fluorescence Microscopy*. Analytical Chemistry, 2008. **80**(22): p. 8568-8575.

326. Young A. T., *Rayleigh scattering*. Applied Optics, 1981. **20**(4): p. 533-535.

327. Hendra P. J., Stratton P. M., *Laser-Raman spectroscopy*. Chemical Reviews, 1969. **69**(3): p. 325-344.

328. Kim H., Kosuda K. M., Van Duyne R. P., Stair P. C., *Resonance Raman and surface- and tip-enhanced Raman spectroscopy methods to study solid catalysts and heterogeneous catalytic reactions*. Chemical Society Reviews, 2010. **39**(12): p. 4820-4844.

329. Asher S. A. *Handbook of Vibrational Spectroscopy*. Chalmers J. M., Griffiths P. R., editors. Chichester: John Wiley & Sons Ltd; 2002.

330. Schmid E. D., Derner H., Berthold G., *Resonance Raman effect of anthracene in the pre-resonance region*. Journal of Raman Spectroscopy, 1976. **4**(3): p. 329-337.

331. Albrecht A. C., *On the Theory of Raman Intensities*. The Journal of Chemical Physics, 1961. **34**(5): p. 1476-1484.

332. Fleischmann M., Hendra P. J., McQuillan A. J., *Raman spectra of pyridine adsorbed at a silver electrode*. Chemical Physics Letters, 1974. **26**(2): p. 163-166.

333. Albrecht M. G., Creighton J. A., *Anomalously intense Raman spectra of pyridine at a silver electrode*. Journal of the American Chemical Society, 1977. **99**(15): p. 5215-5217.

334. Otto A., Mrozek I., Grabhorn H., Akemann W., *Surface-enhanced Raman scattering*. Journal of Physics: Condensed Matter, 1992. **4**(5): p. 1143.

335. Moskovits M., *Surface-enhanced Raman spectroscopy: a brief retrospective*. Journal of Raman Spectroscopy, 2005. **36**(6-7): p. 485-496.

336. Nie S., Emroy S. R., *Probing Single Molecules and Single Nanoparticles by Surface-Enhanced Raman Scattering*. Science, 1997. **275**(5303): p. 1102-1106.

337. Michaels A. M., Nirmal M., Brus L. E., *Surface Enhanced Raman Spectroscopy of Individual Rhodamine 6G Molecules on Large Ag Nanocrystals*. Journal of the American Chemical Society, 1999. **121**(43): p. 9932-9939.

338. Stiles P. L., Dieringer J. A., Shah N. C., Van Duyne R. P., *Surface-Enhanced Raman Spectroscopy*. Annual Review of Analytical Chemistry, 2008. **1**(1): p. 601-626.

339. Sharma B., Frontiera R. R., Henry A.-I., Ringe E., Van Duyne R. P., *SERS: Materials, applications, and the future*. Materials Today, 2012. **15**(1-2): p. 16-25.

340. Tian Z.-Q., Ren B., Wu D.-Y., *Surface-Enhanced Raman Scattering: From Noble to Transition Metals and from Rough Surfaces to Ordered Nanostructures*. The Journal of Physical Chemistry B, 2002. **106**(37): p. 9463-9483.

341. Talley C. E., Jackson J. B., Oubre C., Grady N. K., Hollars C. W., Lane S. M., Huser T. R., Nordlander P., Halas N. J., *Surface-Enhanced Raman Scattering from Individual Au Nanoparticles and Nanoparticle Dimer Substrates*. Nano Letters, 2005. **5**(8): p. 1569-1574.

342. Cintra S., Abdelsalam M. E., Bartlett P. N., Baumberg J. J., Kelf T. A., Sugawara Y., Russell A. E., *Sculpted substrates for SERS*. Faraday Discussions, 2006. **132**(0): p. 191-199.

343. Natan M. J., *Concluding Remarks Surface enhanced Raman scattering*. Faraday Discussions, 2006. **132**(0): p. 321-328.

344. Lin X.-M., Cui Y., Xu Y.-H., Ren B., Tian Z.-Q., *Surface-enhanced Raman spectroscopy: substrate-related issues*. Analytical and Bioanalytical Chemistry, 2009. **394**(7): p. 1729-1745.

345. Lal S., Grady N. K., Goodrich G. P., Halas N. J., *Profiling the Near Field of a Plasmonic Nanoparticle with Raman-Based Molecular Rulers*. Nano Letters, 2006. **6**(10): p. 2338-2343.

346. Saute B., Narayanan R., *Solution-based direct readout surface enhanced Raman spectroscopic (SERS) detection of ultra-low levels of thiram with dogbone shaped gold nanoparticles*. Analyst, 2011. **136**(3): p. 527-532.

347. Rivas L., Murza A., Sánchez-Cortés S., García-Ramos J. V., *Adsorption of acridine drugs on silver: surface-enhanced resonance Raman evidence of the existence of different adsorption sites*. Vibrational Spectroscopy, 2001. **25**(1): p. 19-28.

348. Rost F. W. D. *Fluorescence Microscopy*. Cambridge: University Press; 1995.

349. Tomita G., *Fluorescence-excitation spectra of acridine orange-DNA and -RNA systems*. Biophysik, 1967. **4**(1): p. 23-29.

350. Seballos L., Olson T. Y., Zhang J. Z., *Effects of chromophore orientation and molecule conformation on surface-enhanced Raman scattering studied with alkanoic acids and colloidal silver nanoparticles*. The Journal of Chemical Physics, 2006. **125**(23): p. 234706.

351. Zhang Y., Walkenfort B., Yoon J. H., Schlucker S., Xie W., *Gold and silver nanoparticle monomers are non-SERS-active: a negative experimental study with silica-encapsulated Raman-reporter-coated metal colloids*. Physical Chemistry Chemical Physics, 2015. **17**(33): p. 21120-21126.

352. Yin H. J., Liu L., Shi C. A., Zhang X., Lv M. Y., Zhao Y. M., Xu H. J., *Study of surface-enhanced Raman scattering activity of DNA-directed self-assembled gold nanoparticle dimers*. Applied Physics Letters, 2015. **107**(19): p. 193106.

353. Wang H., Fang J., Xu J., Wang F., Sun B., He S., Sun G., Liu H., *A hanging plasmonic droplet: three-dimensional SERS hotspots for a highly sensitive multiplex detection of amino acids*. Analyst, 2015. **140**(9): p. 2973-2978.

354. Li X., Lee H. K., Phang I. Y., Lee C. K., Ling X. Y., *Superhydrophobic-Oleophobic Ag Nanowire Platform: An Analyte-Concentrating and Quantitative Aqueous and Organic Toxin Surface-Enhanced Raman Scattering Sensor*. Analytical Chemistry, 2014. **86**(20): p. 10437-10444.

355. Pazos-Perez N., Wagner C. S., Romo-Herrera J. M., Liz-Marzán L. M., García de Abajo F. J., Wittemann A., Fery A., Alvarez-Puebla R. A., *Organized Plasmonic Clusters with High Coordination Number and Extraordinary Enhancement in Surface-Enhanced Raman Scattering (SERS)*. Angewandte Chemie International Edition, 2012. **51**(51): p. 12688-12693.

356. Urban A. S., Shen X., Wang Y., Large N., Wang H., Knight M. W., Nordlander P., Chen H., Halas N. J., *Three-Dimensional Plasmonic Nanoclusters*. Nano Letters, 2013. **13**(9): p. 4399-4403.

357. Shiohara A., Wang Y., Liz-Marzán L. M., *Recent approaches toward creation of hot spots for SERS detection*. Journal of Photochemistry and Photobiology C: Photochemistry Reviews, 2014. **21**: p. 2-25.

358. Fan X., White I. M., *Optofluidic microsystems for chemical and biological analysis*. Nat Photon, 2011. **5**(10): p. 591-597.

359. Kim D., Campos A. R., Datt A., Gao Z., Rycenga M., Burrows N. D., Greeneltch N. G., Mirkin C. A., Murphy C. J., Van Duyne R. P., Haynes C. L., *Microfluidic-SERS devices for one shot limit-of-detection*. Analyst, 2014. **139**(13): p. 3227-3234.

360. Liu M., Wang Z., Zong S., Zhang R., Zhu D., Xu S., Wang C., Cui Y., *SERS-based DNA detection in aqueous solutions using oligonucleotide-modified Ag nanoprisms and gold nanoparticles*. Analytical and Bioanalytical Chemistry, 2013. **405**(18): p. 6131-6136.

361. Bethell D., Schiffrian D. J., *Nanotechnology and nucleotides*. Nature, 1996. **382**(6592): p. 581-581.

362. Liu J., Lu Y., *A Colorimetric Lead Biosensor Using DNAzyme-Directed Assembly of Gold Nanoparticles*. Journal of the American Chemical Society, 2003. **125**(22): p. 6642-6643.

363. Storhoff J. J., Elghanian R., Mucic R. C., Mirkin C. A., Letsinger R. L., *One-Pot Colorimetric Differentiation of Polynucleotides with Single Base Imperfections Using Gold Nanoparticle Probes*. Journal of the American Chemical Society, 1998. **120**(9): p. 1959-1964.

364. Förster T., *Zwischenmolekulare Energiewanderung und Fluoreszenz*. Annalen der Physik, 1948. **437**(1-2): p. 55-75.

365. Dexter D. L., *A Theory of Sensitized Luminescence in Solids*. The Journal of Chemical Physics, 1953. **21**(5): p. 836-850.

366. Heer S., Kömpe K., Güdel H. U., Haase M., *Highly Efficient Multicolour Upconversion Emission in Transparent Colloids of Lanthanide-Doped NaYF<sub>4</sub> Nanocrystals*. Advanced Materials, 2004. **16**(23-24): p. 2102-2105.

367. Yao L., Zhou J., Liu J., Feng W., Li F., *Iridium-Complex-Modified Upconversion Nanophosphors for Effective LRET Detection of Cyanide Anions in Pure Water*. Advanced Functional Materials, 2012. **22**(13): p. 2667-2672.

368. Liu Q., Peng J., Sun L., Li F., *High-Efficiency Upconversion Luminescent Sensing and Bioimaging of Hg(II) by Chromophoric Ruthenium Complex-Assembled Nanophosphors*. ACS Nano, 2011. **5**(10): p. 8040-8048.

369. Xiong L.-Q., Chen Z.-G., Yu M.-X., Li F.-Y., Liu C., Huang C.-H., *Synthesis, characterization, and in vivo targeted imaging of amine-functionalized rare-earth up-converting nanophosphors*. Biomaterials, 2009. **30**(29): p. 5592-5600.

370. Ma X., Ni X., *Using upconversion nanoparticles to improve photovoltaic properties of poly(3-hexylthiophene)-TiO<sub>2</sub> heterojunction solar cell*. Journal of Nanoparticle Research, 2013. **15**(4): p. 1-7.

371. Zhou Z., Wang J., Nan F., Bu C., Yu Z., Liu W., Guo S., Hu H., Zhao X.-Z., *Upconversion induced enhancement of dye sensitized solar cells based on core-shell structured  $\beta$ -NaYF<sub>4</sub>:Er<sup>3+</sup>, Yb<sup>3+</sup>@SiO<sub>2</sub> nanoparticles*. Nanoscale, 2014. **6**(4): p. 2052-2055.

372. Zou W., Visser C., Maduro J. A., Pshenichnikov M. S., Hummelen J. C., *Broadband dye-sensitized upconversion of near-infrared light*. Nat Photon, 2012. **6**(8): p. 560-564.

373. Kim J., Lee J. E., Lee J., Jang Y., Kim S.-W., An K., Yu J. H., Hyeon T., *Generalized Fabrication of Multifunctional Nanoparticle Assemblies on Silica Spheres*. Angewandte Chemie International Edition, 2006. **45**(29): p. 4789-4793.

374. Zhang H., Dong B., Zhou T., Li C. Y., *Directed self-assembly of hetero-nanoparticles using a polymer single crystal template*. Nanoscale, 2012. **4**(24): p. 7641-7645.

375. Jiang S., Zhang Y., *Upconversion Nanoparticle-Based FRET System for Study of siRNA in Live Cells*. Langmuir, 2010. **26**(9): p. 6689-6694.

376. Ding Y., Zhu H., Zhang X., Zhu J.-J., Burda C., *Rhodamine B derivative-functionalized upconversion nanoparticles for FRET-based Fe<sup>3+</sup>-sensing*. Chemical Communications, 2013. **49**(71): p. 7797-7799.

377. Donald L. K., Sarah M. R., Brittany L. C., Paul H. D., Elton G., Jeunghoon L., Bernard Y., William B. K., *DNA-mediated excitonic upconversion FRET switching*. New Journal of Physics, 2015. **17**(11): p. 115007.

378. Chen Y., Liang H., *Applications of quantum dots with upconverting luminescence in bioimaging*. Journal of Photochemistry and Photobiology B: Biology, 2014. **135**: p. 23-32.

379. Mattsson L., Wegner K. D., Hildebrandt N., Soukka T., *Upconverting nanoparticle to quantum dot FRET for homogeneous double-nano biosensors*. RSC Advances, 2015. **5**(18): p. 13270-13277.

380. Shi J., Tian F., Lyu J., Yang M., *Nanoparticle based fluorescence resonance energy transfer (FRET) for biosensing applications*. Journal of Materials Chemistry B, 2015. **3**(35): p. 6989-7005.

381. Sehgal D., Vijay I. K., *A Method for the High Efficiency of Water-Soluble Carbodiimide-Mediated Amidation*. Analytical Biochemistry, 1994. **218**(1): p. 87-91.

382. Bartczak D., Kanaras A. G., *Preparation of Peptide-Functionalized Gold Nanoparticles Using One Pot EDC/Sulfo-NHS Coupling*. Langmuir, 2011. **27**(16): p. 10119-10123.

383. Medintz I. L., Clapp A. R., Mattoussi H., Goldman E. R., Fisher B., Mauro J. M., *Self-assembled nanoscale biosensors based on quantum dot FRET donors*. Nat Mater, 2003. **2**(9): p. 630-638.

384. Hohng S., Ha T., *Single-Molecule Quantum-Dot Fluorescence Resonance Energy Transfer*. *ChemPhysChem*, 2005. **6**(5): p. 956-960.

385. Mujumdar R. B., Ernst L. A., Mujumdar S. R., Lewis C. J., Waggoner A. S., *Cyanine dye labeling reagents: Sulfoindocyanine succinimidyl esters*. *Bioconjugate Chemistry*, 1993. **4**(2): p. 105-111.

386. Zhao J., Chandrasekaran A. R., Li Q., Li X., Sha R., Seeman N. C., Mao C., *Post-Assembly Stabilization of Rationally Designed DNA Crystals*. *Angewandte Chemie International Edition*, 2015. **54**(34): p. 9936-9939.

387. Barnaby S. N., Thaner R. V., Ross M. B., Brown K. A., Schatz G. C., Mirkin C. A., *Modular and Chemically Responsive Oligonucleotide "Bonds" in Nanoparticle Superlattices*. *Journal of the American Chemical Society*, 2015. **137**(42): p. 13566-13571.

388. Randeria P. S., Jones M. R., Kohlstedt K. L., Banga R. J., Olvera de la Cruz M., Schatz G. C., Mirkin C. A., *What Controls the Hybridization Thermodynamics of Spherical Nucleic Acids?* *Journal of the American Chemical Society*, 2015. **137**(10): p. 3486-3489.

389. Lee W., von Hippel P. H., Marcus A. H., *Internally labeled Cy3/Cy5 DNA constructs show greatly enhanced photo-stability in single-molecule FRET experiments*. *Nucleic Acids Research*, 2014. **42**(9): p. 5967-5977.

390. Jha P. K., Kuzovkov V., Grzybowski B. A., Olvera de la Cruz M., *Dynamic self-assembly of photo-switchable nanoparticles*. *Soft Matter*, 2012. **8**(1): p. 227-234.

391. Fischer S., Hallermann F., Eichelkraut T., von Plessen G., Krämer K. W., Biner D., Steinkemper H., Hermle M., Goldschmidt J. C., *Plasmon enhanced upconversion luminescence near gold nanoparticles – simulation and analysis of the interactions: Errata*. *Optics Express*, 2013. **21**(9): p. 10606-10611.

392. Wu D. M., García-Etxarri A., Salleo A., Dionne J. A., *Plasmon-Enhanced Upconversion*. *The Journal of Physical Chemistry Letters*, 2014. **5**(22): p. 4020-4031.

393. Paramelle D., Sadovoy A., Gorelik S., Free P., Hobley J., Fernig D. G., *A rapid method to estimate the concentration of citrate capped silver nanoparticles from UV-visible light spectra*. *Analyst*, 2014. **139**(19): p. 4855-4861.

394. Jeong S., Won N., Lee J., Bang J., Yoo J., Kim S. G., Chang J. A., Kim J., Kim S., *Multiplexed near-infrared *in vivo* imaging complementarily using quantum dots and upconverting  $NaYF_4:Yb^{3+},Tm^{3+}$  nanoparticles*. *Chemical Communications*, 2011. **47**(28): p. 8022-8024.

395. Brouwer A. M., *Standards for photoluminescence quantum yield measurements in solution (IUPAC Technical Report)*. *Pure and Applied Chemistry*, 2011. **83**(12): p. 2213-2228.

396. Birks J. B., *Fluorescence Quantum Yield Measurements*. *Journal of Research of the National Bureau of Standards - A Physics and Chemistry*, 1976. **80A**(3): p. 389-399.

397. Fery-Forgues S., Lavabre D., *Are Fluorescence Quantum Yields So Tricky to Measure? A Demonstration Using Familiar Stationery Products*. *Journal of Chemical Education*, 1999. **76**(9): p. 1260.

398. Würth C., Grabolle M., Pauli J., Spieles M., Resch-Genger U., *Relative and absolute determination of fluorescence quantum yields of transparent samples*. *Nat Protocols*, 2013. **8**(8): p. 1535-1550.

399. Würth C., Pauli J., Lochmann C., Spieles M., Resch-Genger U., *Integrating Sphere Setup for the Traceable Measurement of Absolute Photoluminescence Quantum Yields in the Near Infrared*. *Analytical Chemistry*, 2012. **84**(3): p. 1345-1352.

